ALS ACTIVITY REPORT 2005

June 2006
LBNL-55917 (2005)

Ernest Orlando Lawrence Berkeley National Laboratory
University of California • Berkeley, California, 94720

EDITORS:
Lori Tamura
Arthur Robinson
Elizabeth Moxon

Design, layout, photography, and additional writing provided by the Creative Services Office and the Communications Department of Berkeley Lab's Public Affairs Department.

The editors gratefully acknowledge the ALS users and staff for their contributions, advice, and patience.

Available to DOE and DOE Contractors from the Office of Scientific and Technical Communication, P.O. Box 62, Oak Ridge, TN 37831. Prices available from (615) 576-8401.

Available to the public from the National Technical Information Service, U.S. Department of Commerce, 5285 Port Royal Road, Springfield, VA 22161.

Ernest Orlando Lawrence Berkeley National Laboratory is an equal opportunity employer.

CSO 11977

ALS ACTIVITY REPORT 2005

This work was sponsored by the Director, Office of Science, Office of Basic Energy Sciences, of the U.S. Department of Energy under Contract No. DE-AC02-05CH11231.

Office of Science
U.S. DEPARTMENT OF ENERGY

BERKELEY LAB

JUNE 2006
LBNL-55917 (2005)

ERNEST ORLANDO LAWRENCE BERKELEY NATIONAL LABORATORY
UNIVERSITY OF CALIFORNIA • BERKELEY, CALIFORNIA, 94720

DEDICATED TO THE MEMORY OF

NEVILLE SMITH

(1942–2006)

The ALS community mourns the loss of Neville Smith, scientific director for the ALS, who died at his home in Berkeley of cancer on August 18, 2006. He was 64.

Neville had a long association with the ALS, including a number of "firsts." A native of England and a graduate of the University of Cambridge, he became a leading authority in the field of photoemission spectroscopy while a member of the scientific staff of AT&T Bell Laboratories. Accordingly, he was tapped to serve on the original ALS Users' Executive Committee, where he oversaw the development of the ALS user policy, steering a careful balance between the interests of PRTs and general users, as well as the Users' Association charter. Subsequently, he was chair of the first Program Review Panel that selected the first PRTs. In 1994 after 25 years at Bell Labs, he came to the ALS as the first scientific program head.

Under his leadership, the ALS scientific program has thrived. Said Patricia Dehmer, Associate Director of Science for DOE's Office of Basic Energy Sciences, "As its scientific director, Neville shepherded the Advanced Light Source to international prominence making it one of the most scientifically productive and important facilities in the world. Moreover, his wisdom, maturity, innovativeness, and diplomacy made him a leader in the national and international light source community."

Contents

Welcome iv

Note from the UEC Chair v

SCIENCE HIGHLIGHTS 1

Feature: Combustion Research Heats Up at the ALS 2

Condensed Matter Physics 12

Nano and Materials Science 22

Environmental and Earth Science 35

Structural Biology 45

X-Ray Microscopy 63

Atomic and Molecular Science 70

FACILITY REPORT 81

Operations 82

Accelerator Physics 87

Experimental Systems 96

Scientific Support 107

User Services 119

SPECIAL EVENTS 125

Meetings and Workshops 126

Distinguished Visitors 133

Education 135

ABOUT THE ALS 137

ALS Staff 138

ALS Advisory Panels 140

Facts and Figures 142

Publications 146

Acronyms and Abbreviations 171

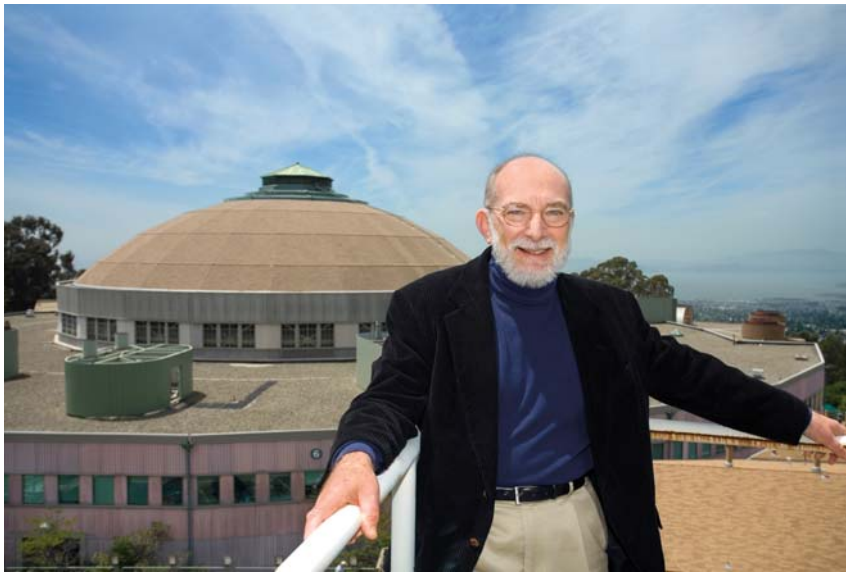

Welcome

Janos Kirz, Acting ALS Director

The year 2005 was in many ways one of transition in the life of the ALS. The Department of Energy's triennial ALS review, conducted in early February by a team organized by Office of Basic Energy Sciences (BES) Facilities Division Director Pedro Montano, found the ALS not only in fine shape, but that it "serves as a model for how a user facility should operate." However, while "recognizing the enormous contributions of Daniel Chemla," the review did recommend that a search for a new, permanent director be launched. Daniel, who continues his recovery from surgery, stepped down from his position as director in July. A search committee, chaired by Paul Alivisatos, has been at work to identify a short list of candidates for Berkeley Lab Director Steve Chu's consideration. I expect to welcome the new director in the near future. (As I approach my 69th birthday, I see the need for a younger person to take on the job and have made it clear that I am not a candidate.)

The University of California was retained by the Department of Energy as the contractor to run Berkeley Lab. The new Lab management team includes former ALS Division Deputy for Planning Jim Krupnick, who was appointed Director of Institutional Assurance. Jim continues to attend some of our ALS management meetings but has for the most part moved to the fourth floor of Building 50A, where Berkeley Lab management is located. His departure forced a change in the ALS organization. Deputy Director Ben Feinberg agreed to take on Jim's responsibilities in planning and budget. Neville Smith is now Scientific Director, with Gary Krebs as Deputy. David Robin became Deputy for Operations; Howard Padmore, Deputy for Experimental Systems; and Zahid Hussain, Deputy for Scientific Support.

The year also brought new highs. The number of users passed the 2000 mark for the first time. The number of participants at the annual Users' Meeting continues to grow as well. We had 12 very well attended workshops connected with this event. I am most grateful to the Users' Executive Committee, especially Jinghua Guo and Simon Morton, for their excellent job of organizing it all, with the usual able support of the User Services Office staff.

We completed the new ALS Strategic Plan, and put it on the ALS Web site (http://www-als.lbl.gov/als/ourorg/strategicplan.html). While it is a living document that is being updated to reflect our changing priorities, it provides a blueprint for where we believe the ALS is going in the next decade. For the period beyond that, Berkeley Lab Deputy Director Graham Fleming has assembled a working group to plan for the longer-term future. Through it all, our mission, "to support users in doing outstanding science in a safe environment," remains constant.

Note from the UEC Chair

Greg Denbeaux, UEC Chair for 2005

It has been my pleasure to have the opportunity to serve as chair of the ALS Users' Executive Committee (UEC) during the past year. In addition to the exciting science that was performed by the growing number of users of the ALS this year, there were two notable changes. The number of user proposals for beam time has grown so fast that a new, expanded system for review of proposals was required, and a project to build a user guest house for on-site housing has been approved.

Due to the success of the ALS and the increase in the number of users and the resultant increase in the number of proposals for beam time, the responsibilities for the members of the proposal study panel to provide an in-depth review of all proposals became overly time consuming. In order to solve this problem, a new system of proposal review has been implemented that will use external reviewers to provide analysis of each proposal. This should also help to ensure that each proposal gets the full attention that it deserves.

The location of the ALS on the hills of Berkeley has many benefits, but one of the drawbacks has been the lack of affordable housing for visiting scientists that is in close proximity to the ALS. Due in large part to the support of Director Chu and the years of effort by Gary Krebs, a project to build a user guest house that will provide affordable housing for visiting scientists within walking distance of the ALS to help make visits as scientifically productive as possible has been approved.

As always, the Users' Executive Committee of the Advanced Light Source is here to help the scientific community of users. So, feel free to contact us with any questions, comments, or concerns. For 2006, the chair of the UEC is Clemens Heske (heske@unlv.nevada.edu) and the vice chair is Tony van Buuren (vanbuuren1@llnl.gov). Please contact them or any of the other UEC members (www.als.lbl.gov/als/uec/index.html).


11
C
10
C

SCIENCE HIGHLIGHTS

Combustion Research

Craig A. Taatjes, Combustion Research Facility, Sandia National Laboratories
Terrill A. Cool, School of Applied and Engineering Physics, Cornell University

FIGURE 1
Right: The low-pressure flame apparatus in operation at the ALS. The luminous zone of the flame is visible as the bright blue line on the left. The tip of the quartz sampling cone is glowing red. The burner can be moved horizontally to place the sampling tip at any point in the flame. Photograph by Daniel Strong, courtesy of Sandia National Laboratories.

Combustion produces an incredibly complicated chemical (and fluid-dynamical) system. Even with a single pure fuel like n-heptane (C_7H_{16}), thousands of reactions involving hundreds of chemical species take place. A "real fuel" like gasoline contains hundreds of single-fuel components. Moreover, the combustion chemistry of minor constituents is critical in some of the most pressing technical challenges in combustion science today, pollutant formation and ignition behavior to name two. Validation of the chemical kinetic models for such processes relies largely on measurements of chemical species in well-characterized research flames. Recently, our experiments at the ALS have produced measurements of the chemical intermediates of combustion with unprecedented detail, enabling the discovery of new species never before observed in flames.

Fire fascinates almost everyone, and combustion is one of the most commercially important processes in the world. The study of flame chemistry stretches back more than 150 years, to the work of pioneers like Robert Bunsen and Michael Faraday. In the time since then, our understanding of combustion has progressed enormously, but significant uncertainties remain in the details of combustion chemistry. Our experiments at the ALS that combine synchrotron radiation with a novel flame apparatus aim

Heats Up at the ALS

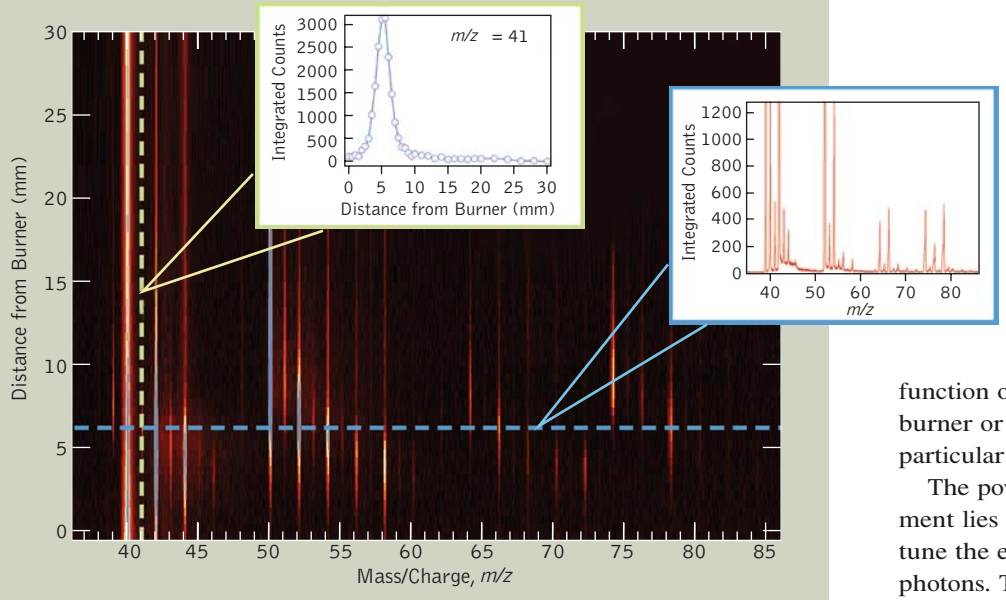

FIGURE 2
A section of photoionization mass spectrometric data from molecules sampled out of a rich ethene (C_2H_4) flame. The main panel shows the ion signal as a function of mass-to-charge ratio *m/z* and distance from the burner face. Slices through these data are also shown. A vertical slice gives the profile of a particular species in the flame, in this case the allyl radical at *m/z* = 41. A horizontal slice gives the mass spectrum of molecules at any point in the flame.

to fill in some of the gaps.

The flame apparatus used at ALS Beamline 9.0.2 was developed by scientists from the Combustion Research Facility of Sandia National Laboratories, Cornell University, and the University of Massachusetts (see sidebar, "Controlled Burning at the ALS"). It combines the powerful technique of synchrotron photoionization with the method of molecular beam mass sampling (MBMS) through a quartz cone of molecules from a laminar, premixed, low-pressure flame (Figure 1). The flame is designed to have very simple fluid mechanics, essentially one-dimensional flow, in order to isolate the chemistry of the combustion process. The ALS flame instrument is designed so that a complete mass spectrum can be taken at any point in the flame.

Representative data from this apparatus are shown in Figure 2 for a fuel-rich ethylene (C_2H_4) flame. The three-dimensional data show the observed photoion signal as a function of the mass-to-charge ratio (*m/z*) and the distance from the burner to the sampling cone. Slices through these data can give the profile of a particular mass as a function of distance from the burner or the mass spectrum at a particular position in the flame.

The power of the ALS instrument lies in the ability to easily tune the energy of the ionizing photons. This allows a second kind of data to be obtained, showing the signal taken at a particular position in the flame as a function of mass and photon energy (Figure 3). A slice through these data at a particular value of *m/z* gives what is called the photoionization efficiency (PIE) spectrum. The PIE spectrum is a valuable tool for determining the chemical identity of species that may share the same mass. In this way, the tunable photoionization method can distinguish isomers,

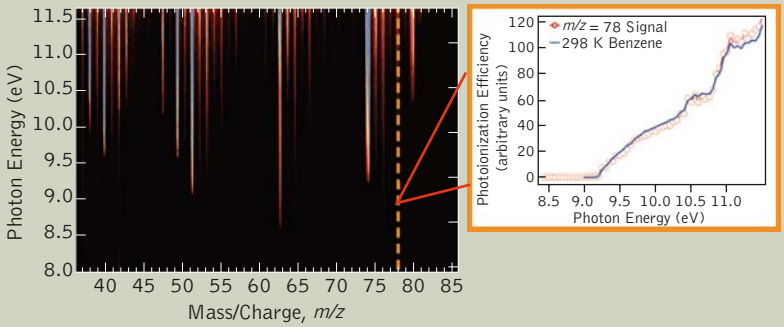

FIGURE 3
Photoionization efficiency measurements of molecules sampled from a cyclohexane flame 0.65 mm from the burner face. The main panel shows the ion signal measured as a function of photon energy and mass-to-charge ratio. A vertical slice through these data gives the photoionization efficiency of molecules of a particular mass at this point in the flame; *m/z* = 78 at this position can be identified as benzene from the observed photoionization efficiency curve.

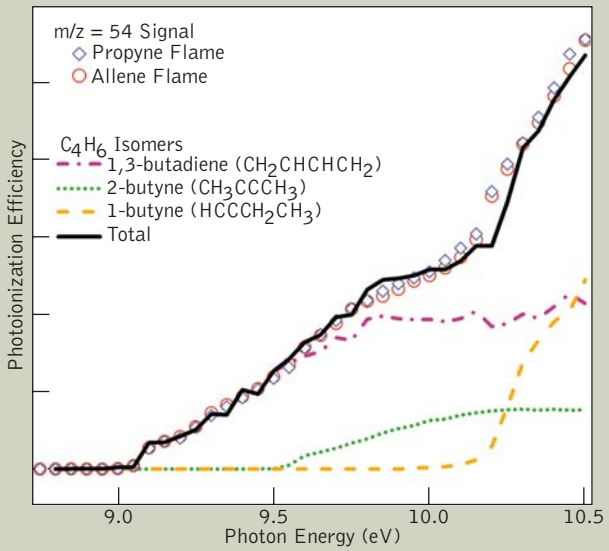

FIGURE 4
Photoionization efficiency measurements of *m/z* = 54 signals from propyne and allene flames show a mix of C_4H_6 isomers that can be identified from reference spectra.

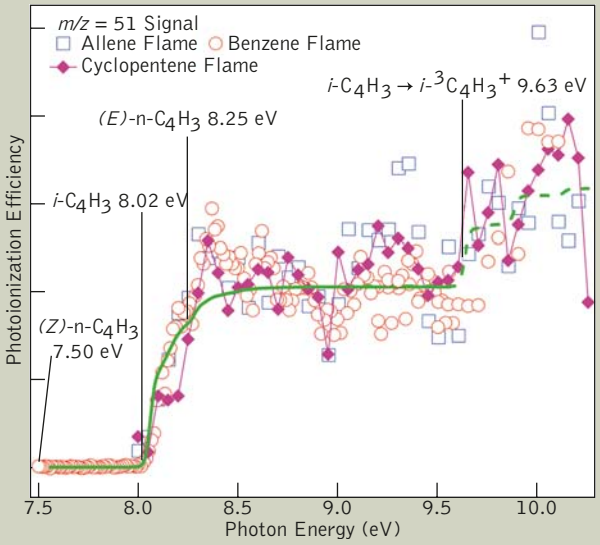

FIGURE 5
Photoionization efficiency measurements of C_4H_3 molecules from flames show clear evidence for the *i*-isomer, but no apparent signal from the *n*-isomers that have been proposed as soot precursors. The vertical lines show the adiabatic ionization energies of the C_4H_3 isomers. The solid and dashed lines are calculated ionization signals arising solely from *i*-C_4H_3. The benzene data at low photon energy is taken from the low-pressure flame machine in Fei Qi's group at the National Synchrotron Radiation Laboratory in Hefei, China.

molecules made of the same constituent atoms in different arrangements (Figure 4). Isomeric species can have very different chemical behaviors, for example, in soot formation (see sidebar, "Chemical Kinetic Models of Soot Formation").

The formation of soot is one of the outstanding chemical issues in combustion science today. Soot is largely made up of carbon ring structures, and much attention has been focused on the "first ring," that is, production of the first aromatic ring species from a straight-chain fuel. The reaction of two propargyl radicals (C_3H_3) to form benzene (C_6H_6) is generally acknowledged to be the most important route to the first ring, but controversy remains about other routes, for example those involving "even-carbon" precursors like C_4H_3 and C_4H_5.

The *n*-isomers of these radicals (•CH=CH–C≡CH and •CH=CH–CH=CH_2) have been proposed to react with acetylene to form aromatic ring species. But our measurements at the ALS of C_4H_3 and C_4H_5 from several different flames have revealed that the concentration of other isomers of these radicals, particularly the *i*-isomers (CH_2=C•–C≡CH↔CH_2–C=C=•CH and •CH_2–CH=C=CH_2↔CH_2=CH–•C=CH_2), are in fact dominant (Figure 5). These results suggest that reactions of *i*-C_4H_3 and *i*-C_4H_5 with acetylene should be given more attention in soot-formation models.

Measurements in cyclopentene flames at the ALS also allowed us to determine the isomeric composition of another important species in soot formation, the C_3H_2 radical. Singlet cyclopropenylidene, the most stable C_3H_2 isomer, is abundant in interstellar space. Triplet HCCCH (prop-2-ynylidene or propargylene) is the second most stable isomer, lying about 47 kJ/mol higher in energy. This isomer is a product of reactions of the propargyl radical (C_3H_3), the dominant radical responsible for formation of the first ring, and may itself be involved in the chemistry of soot formation. C_3H_2 had been observed in several rich hydrocarbon flames; however, our ALS measurements were the first to prove the presence of the propargylene isomer (and to measure its ionization energy).

More surprisingly, the capability

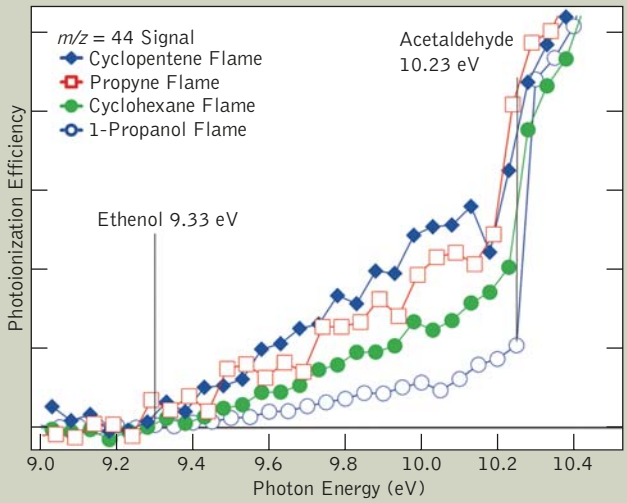

FIGURE 6
Photoionization efficiency measurements of *m/z* = 44 molecules sampled from four flames. The threshold near 9.33 eV clearly identifies ethenol in all these flames. Ethenol had never been observed in flames before the work at the ALS.

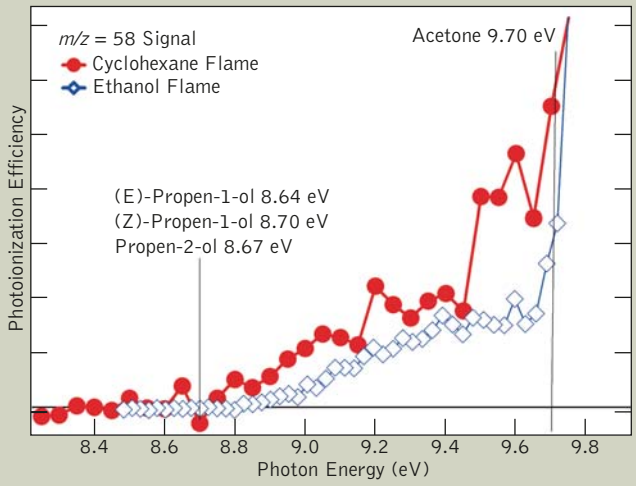

FIGURE 7
Photoionization efficiency measurements of *m/z* = 58 molecules sampled from two flames. Propenols, enols with three carbon atoms, are identified by the threshold near 8.7 eV.

of the ALS instrument enabled the discovery that a whole class of molecules absent from combustion chemistry models, the enols, appear in substantial concentrations in flames. Enols are hydrocarbon molecules with an OH group adjacent to a carbon–carbon double bond; the more stable keto isomers of enols are well-known combustion intermediates, aldehydes and ketones. Enols were predicted to be transient chemical intermediates by Erlenmeyer in 1880, but it took 96 years to observe the simplest enol, vinyl alcohol, in the gas phase!

Because of their instability, and perhaps owing to their experimental elusiveness, enols have not been included in detailed combustion chemistry models. However, our results from the ALS have shown substantial concentrations of 2-, 3-, and 4-carbon enols in low-pressure flames of many elementary fuels. The enols have ionization energies well below those of their aldehyde or ketone counterparts and can be readily distinguished in the PIE spectra (Figures 6 and 7). It is remarkable that an entire class of molecules should have remained undetected in the long history of combustion research. Hydrocarbon oxidation mechanisms must be modified to account for formation and removal of these unexpected compounds.

Enols are present in concentrations 10 to100 times what would be expected by simple keto–enol isomerization, indicating separate formation mechanisms for the isomers. Modeling of enols in flames has so far concentrated on reactions of hydroxyl radicals (OH) with alkenes like ethene (C_2H_4) and propene (C_3H_6) as the source for enols. These reactions are predicted to produce enols, but this has not yet been confirmed by experiments. For some flames, like a fuel-rich ethene flame, modeling with calculated rate coefficients for ethenol production is very successful (Figure 8). The concentration profiles of the enols as a function of position in the flame demonstrate that their removal cannot be dominated by isomerization to the more stable keto form. In the model, the removal reactions of ethenol have been assumed to take place with the same rate constants as for the acetaldehyde isomer.

Enols should react rather differently from aldehyde or ketone isomers, but very little is yet known about gas-phase neutral enol reactions. A new apparatus just beginning operation at the ALS is designed to probe individual chemical reactions with the same isomeric selectivity that has proved so valuable in the flame experiments. These kinetics experiments, also at Beamline 9.0.2, initiate reactions in a controlled fashion by pulsed laser photolysis and measure the photoionization

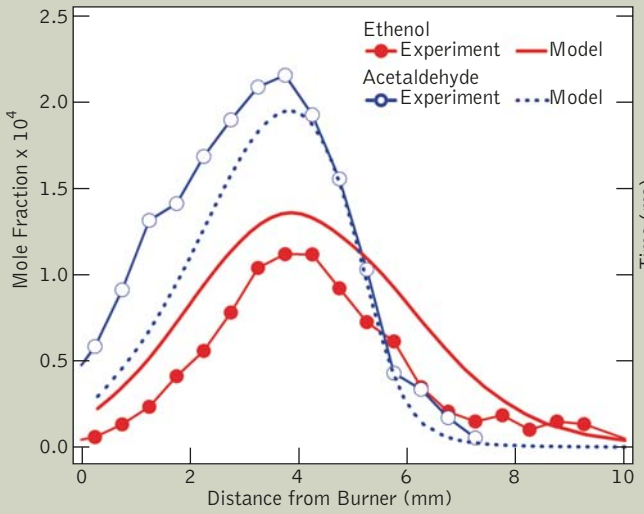

FIGURE 8
Comparison of experimental profiles of ethenol (CH_2CHOH) and acetaldehyde (CH_3CHO) in a rich ethene flame with a model based on ab initio calculations of ethenol production from the OH + ethene reaction.

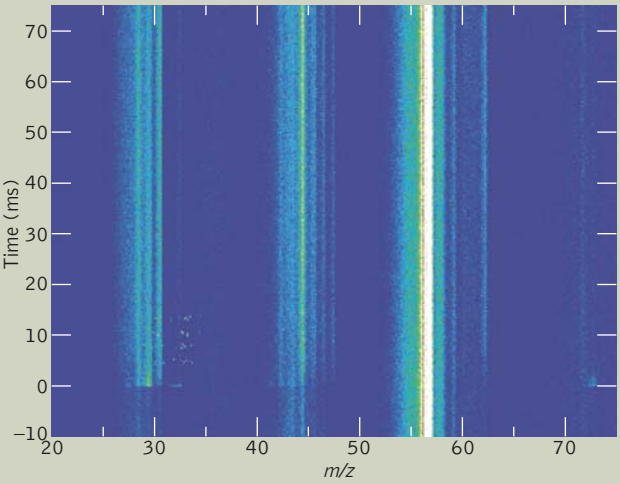

FIGURE 9
Time-resolved photoionization mass spectra of the reaction of ethyl radicals (C_2H_5) with O_2. The reaction is initiated at time = 0 by laser photolysis of diethyl ketone in the presence of oxygen. The mass spectrum of the reacting mixture shows the appearance of primary and secondary products, and can be measured as a function of photon energy to gain isomeric identification of species.

mass spectra of the reacting mixture as a function of time after the initiating laser pulse. Representative data are shown in Figure 9 for the reaction of ethyl radicals (C_2H_5) with oxygen molecules, a key reaction in hydrocarbon ignition.

Measurements of elementary rate coefficients for reactions of enols and other combustion intermediates using the new instrument will be combined with detailed flame component measurements to improve the chemical kinetic models of combustion, thereby aiding in the quest to improve combustion efficiency and reduce pollution by mastering combustion at the molecular level.

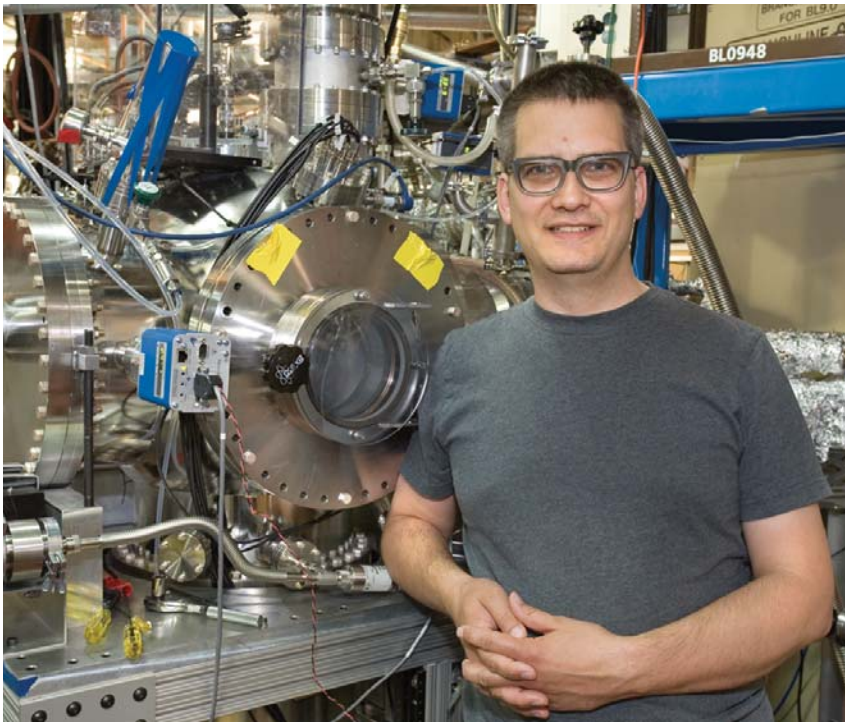

Craig Taatjes (Sandia National Laboratories).

PUBLICATIONS

T.A. Cool, K. Nakajima, T.A. Mostefaoui, F. Qi, A McIlroy, P.R. Westmoreland, M.E. Law, L. Poisson, D.S. Peterka, and M. Ahmed, "Selective detection of isomers with photoionization mass spectrometry for studies of hydrocarbon flame chemistry," *J. Chem. Phys.* **119,** 8356 (2003).

C.A. Taatjes, D.L. Osborn, T.A. Cool, and K. Nakajima, "Synchrotron photoionization of combustion intermediates: The photoionization efficiency of HONO," *Chem. Phys. Lett.* **394,** 19 (2004).

T.A. Cool, K. Nakajima, C.A. Taatjes, A. McIlroy, P.R. Westmoreland, M.E. Law, and A. Morel, "Studies of a fuel-rich propane flame with photoionization mass spectrometry," *Proc. Combust. Inst.* **30,** 1631 (2004).

C.A. Taatjes, S.J. Klippenstein, N. Hansen, J.A. Miller, T.A. Cool, J. Wang, M.E. Law, and P.R. Westmoreland, "Synchrotron photoionization of combustion intermediates: The photoionization efficiency of C_3H_2 isomers," *Phys. Chem. Chem. Phys.* **7,** 806 (2005).

C.A. Taatjes, N. Hansen, A. McIlroy, J.A. Miller, J.P. Senosiain, S.J. Klippenstein, F. Qi, L. Sheng, Y. Zhang, T.A. Cool, J. Wang, P.R. Westmoreland, M.E. Law, T. Kasper, and K. Kohse-Höinghaus, "Enols are common intermediates in hydrocarbon oxidation," *Science* **308,** 1887 (2005).

T.A. Cool, A. McIlroy, F. Qi, P.R. Westmoreland, L. Poisson, D.S. Peterka, and M. Ahmed, "A photoionization mass spectrometer for studies of flame chemistry with a synchrotron light source," *Rev. Sci. Instrum.* **76,** 094102 (2005).

T.A. Cool, J. Wang, K. Nakajima, C.A. Taatjes, and A. McIlroy, "Photoionization cross sections for reaction intermediates in hydrocarbon combustion," *Int. J. Mass. Spectrom.* **247,** 18 (2005).

C.A. Taatjes, N. Hansen, J.A. Miller, T.A. Cool, J. Wang, P.R. Westmoreland, M.E. Law, T. Kasper, and K. Kohse-Höinghaus, "Combustion chemistry of enols: Possible ethenol precursors in flames," *J. Phys. Chem. A* **110,** 3254 (2006).

N. Hansen, S.J. Klippenstein, C.A. Taatjes, J.A. Miller, J. Wang, T.A. Cool, B. Yang, R. Yang, L. Wei, C. Huang, J. Wang, F. Qi, M.E. Law, and P.R. Westmoreland, "The identification and chemistry of C_4H_3 and C_4H_5 isomers in fuel-rich flames," *J. Phys. Chem. A* **110,** 3670 (2006).

FUNDING

U.S. DOE BES, U.S. DOE National Nuclear Security Administration, U.S. Army Research Office, Chinese Academy of Sciences, National Natural Science Foundation of China, and German Research Foundation.

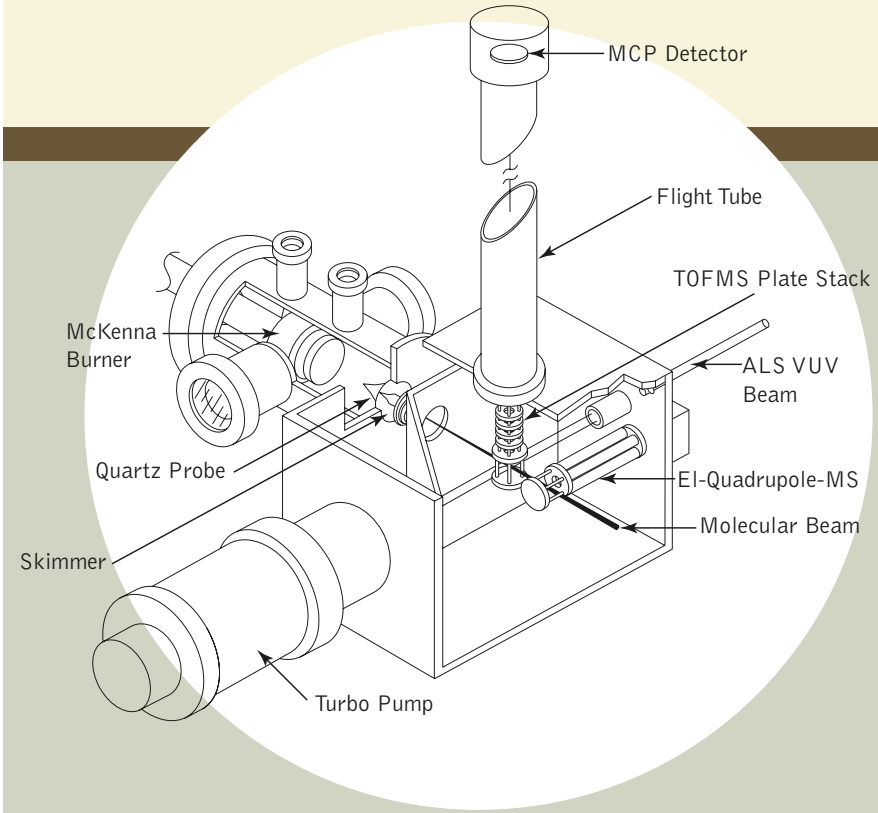

FIGURE 1
Schematic drawing of the ALS flame apparatus.

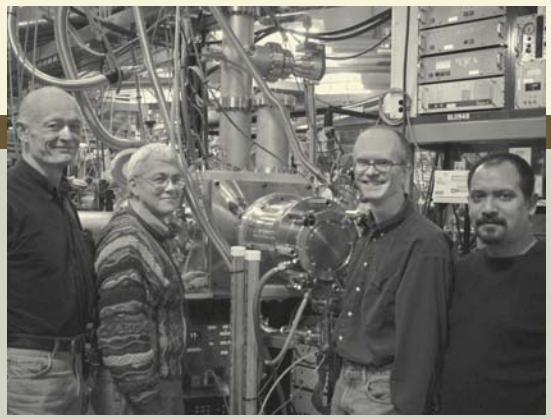

FIGURE 2
Terrill Cool, Philip Westmoreland, Andrew McIlroy, and Musa Ahmed pose in front of the ALS flame apparatus during its inaugural beam cycle at Beamline 9.0.2.

Controlled Burning at the ALS

TERRILL A. COOL, SCHOOL OF APPLIED AND ENGINEERING PHYSICS, CORNELL UNIVERSITY
CRAIG A. TAATJES, COMBUSTION RESEARCH FACILITY, SANDIA NATIONAL LABORATORIES

Flame chemistry experiments at the ALS were born in meetings held in the spring of 2000 between Tomas Baer (University of North Carolina and then interim director of the Chemical Dynamics Beamline 9.0.2), Terrill Cool (Cornell University), Philip Westmoreland (University of Massachusetts), and Andrew McIlroy (a principal investigator at Sandia National Laboratories' Combustion Research Facility). Cool, Westmoreland, and McIlroy were all well-versed in the use of molecular-beam mass sampling to investigate the composition of low-pressure flames. Cool and McIlroy used laser-generated vacuum-ultraviolet light to perform photoionization on molecules sampled from flames. Baer suggested that the tunable synchrotron radiation available at the ALS would offer great advantages over lasers and proposed that the researchers form a team to design and build a low-pressure flame apparatus for the ALS.

The machine they designed, in collaboration with Berkeley Lab scientists Musa Ahmed, Darcy Peterka, Lionel Poisson, and Fei Qi, is depicted in Figure 1. It consists of a low-pressure flame chamber, a two-stage differentially pumped flame-sampling system, a time-of-flight mass spectrometer (TOFMS), and a low-resolution quadrupole mass spectrometer. Premixed fuel/oxygen/argon flames are stabilized at pressures ranging from 20 to 40 Torr on a 6-cm-diameter flat-flame burner located inside the cylindrical flame chamber. Flame gases are sampled along the flow axis with a quartz cone and collimated by a nickel skimmer to form a molecular beam at the entrance to the main test chamber. The burner may be moved towards or away from the fixed sampling cone to record mass spectra at any desired position in the flame, from immediately in front of the burner face, through the luminous zone, and out into the burned gases.

The molecular beam passes horizontally through the gap between the repeller and extraction plates of a conventional Wiley-McLaren linear TOFMS, where it intersects the tunable vacuum ultraviolet (VUV) beam from the ALS at the ionization source region. Pulsed gating of the voltage of the repeller plate is used to propel ions up the flight tube to a multichannel plate detector. A multichannel scaler records the TOFMS data, with a typical mass resolution of $m/\Delta m = 400$. The quadrupole mass spectrometer is used to measure the ion signals from background gases (H_2, O_2, N_2, H_2O) present in the main test chamber.

The ALS flame apparatus became operational in March 2002 (Figure 2 shows Cool, Westmoreland, McIlroy, and Ahmed during the instrument's first beam cycle). One of the first flames investigated was a fuel-rich ethene flame for which a signal for ethenol was recorded in July 2002, the first identification of an enol in a hydrocarbon flame. This powerful combustion chemistry tool has already generated one friendly competitor: Qi, now at the University of Science and Technology of China, has built a nearly identical flame apparatus at the National Synchrotron Radiation Laboratory in Hefei.

Under the present direction of Stephen Leone (Berkeley Lab), the Chemical Dynamics Beamline is extending its investigations of combustion chemistry to probes of the elementary kinetics of important combustion reactions. A new apparatus, designed by David Osborn and Craig Taatjes of Sandia's Combustion Research Facility, again in collaboration with Ahmed and Peterka at Berkeley Lab, uses photoionization and a miniature magnetic sector mass spectrometer to measure time-resolved mass spectra of a mixture following reaction initiation by a pulsed ultraviolet laser.

Chemical Kinetic Models of Soot Formation

JAMES A. MILLER, COMBUSTION RESEARCH FACILITY, SANDIA NATIONAL LABORATORIES

Combustion chemists seek to develop chemical kinetic models that quantitatively describe the oxidation of fuels and the formation of pollutants. Understanding fuel oxidation is important for predicting flame propagation rates and the details of ignition phenomena, particularly the cool-flame chemistry that leads to auto-ignition and "knock" in internal combustion engines. But combustion chemists meet their greatest challenge in trying to predict the small quantities (usually measured in parts per million) of pollutants that are formed as by-products of combustion. Such pollutants include NO_x (NO and NO_2), SO_x (SO_2 and SO_3), polycyclic aromatic hydrocarbons (PAHs), and soot.

Perhaps the most demanding problem of this type is quantitatively predicting concentrations of aromatic compounds (containing aromatic carbon rings), PAHs, and their precursors in flames burning aliphatic (i.e., noncyclic) fuels. This topic has long been of concern because of its connection with soot formation, but interest in it has increased since the Clean Air Act Amendments of 1990 in the United States regulated the emissions of many such compounds from industrial burners, calling them "air toxic species." Examples of air toxics include benzene, toluene, and 1,3-butadiene, among others.

The accurate modeling of such species in flames requires dealing with a degree of complexity not encountered in other combustion problems. Consequently, many of the important issues are only beginning to take focus, and few have been resolved satisfactorily.

Current conventional wisdom has it that PAH and soot are formed from a "first ring," probably benzene (C_6H_6) or phenyl ($-C_6H_5$) but perhaps some other six-membered ring. This first ring serves as the nucleus for the formation of PAH, perhaps by a mechanism that involves sequentially adding acetylene molecules. At a molecular weight of about 2000 amu, it becomes better to think about the PAHs as solid particles instead of molecules—this is soot!

Clearly, the formation of the first ring is a critical part of this process. It has even been conjectured that this step may control the overall rate of PAH and soot formation, at least under some conditions. Consequently, a significant amount of effort has been devoted to understanding how the first ring is formed. Knowledge of both radical and stable-species concentrations *in their various isomeric forms* is crucial to developing kinetic models for these processes. For example, it is important to know whether the C_6H_6 detected in flames is benzene, fulvene (a five-membered ring), or some benign linear isomer. It is also important to know the isomeric distribution of C_4H_3 radicals, only one of which is likely to lead directly to the formation of phenyl by adding acetylene. The flame experiments at the ALS are beginning to shed light on these important issues.

Pseudogaps, Polarons, and the Mystery of High-Temperature Superconductivity

Superconductivity is a state in which certain superchilled metals lose all electrical resistance, but the need to cool them to within 10 to 20 degrees of absolute zero has limited them to niche markets. Beginning in 1986, a class of ceramics called cuprates was discovered to be superconducting at much higher temperatures. Initially, these "high-temperature superconductors" created enormous excitement over the possibility of one day developing room-temperature superconductors. Moreover, the mechanism behind high-temperature superconductivity remains unexplained. If found, such an explanation would not only answer a foundational question in modern solid state physics, but it could provide more precise hints on where to search for the elusive room-temperature superconductor. Mannella et al. have made a significant advance by showing that a phenomenon of solid state physics known as a "pseudogap with a nodal–antinodal dichotomy," suspected by some scientists of playing a key role in the mystery of high-temperature superconductors, has now been found to occur in materials of a completely different nature. This discovery casts new doubts on any direct link between this phenomenon and high-temperature superconductivity.

Working at the ALS, a multi-institutional collaboration led by researchers from the ALS and Stanford University has identified a pseudogap phase with a nodal–antinodal dichotomy in ferromagnetic manganese oxide materials (manganites). Even though ferromagnetism and superconductivity do not exist together, the pseudogap state found in these manganites is remarkably similar to that found in high-temperature superconducting copper oxide materials (cuprates). This discovery casts new doubts on any direct link between the pseudogap phase and high-temperature superconductivity and adds fire to the debate over one of the great scientific mysteries of our time: What causes high-temperature superconductivity?

Beginning in 1986, the cuprates were discovered to have much higher superconducting transition temperatures (T_c) than known metallic superconductors. Among the possible explanations for high-T_c superconductivity, the pseudogap state has played a prominent role. In metals, electrons occupy a continuous spectrum of quantum states up to a maximum energy known as the Fermi level. When the metal is superchilled to become a superconductor, a forbidden energy gap opens up at the Fermi energy.

Experiments in recent years have shown that the spectrum in the superconducting state of high-T_c cuprates is characterized by a "nodal–antinodal dichotomy." When plotted in reciprocal (momentum) space, the spectrum is shaped like a cloverleaf, exhibiting a gap in the so-called antinodal direction (parallel to the copper–oxygen bonds), which vanishes along the nodal direction (from the origin running diagonal to the bonds). This dichotomous character of the excitation spectrum is generally assumed to be linked to the "d-wave" symmetry of the superconducting state.

In the high-T_c cuprates, this dichotomous gap structure persists even above T_c and gives rise to the so-called "pseudogap state" with finite "Fermi arcs" replacing the original nodal points of the superconducting state. More intriguingly, the pseudogap appears to have two energy scales, with a low-energy pseudogap comparable to that of the superconducting gap and a much larger high-energy pseudogap. Naturally, the high-energy pseudogap is taken to represent the dominating physics.

The investigators used angle-resolved photoemission spectroscopy (ARPES) at ALS Beamline 10.0.1 to study a two-layer manganite compound called LSMO that consists of a mixture of lanthanum, strontium, manganese, and oxygen (Figure 1). Such manganese oxide materials become ferromagnetic below a certain critical temperature and display colossal magnetoresistance (CMR), meaning their electrical resistance can change by orders of magnitude in the presence of a magnetic field.

The investigators were quite surprised when the LSMO man-

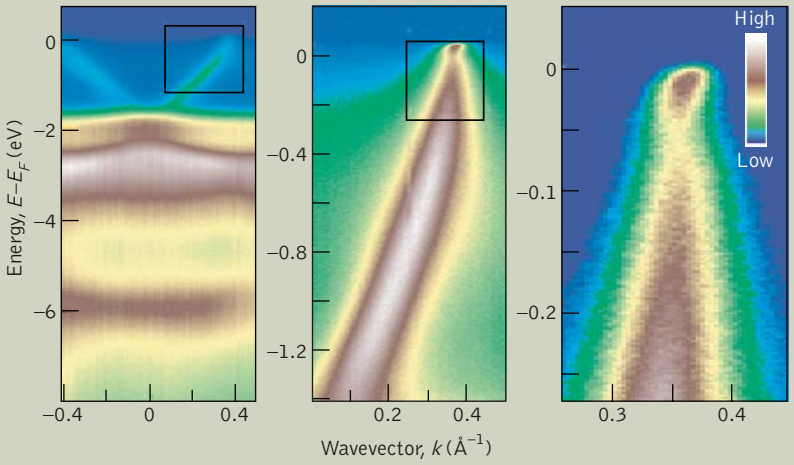

FIGURE 1
ARPES data for three magnifications plot photoelectron intensity variation with energy (relative to the Fermi level) and momentum in the nodal direction. Momentum is determined from the angle of emission. The need for high energy and angular resolution is apparent upon realizing that the data analyzed in this experiment are those contained in the right arm of the light blue "V" in the left low-magnification image.

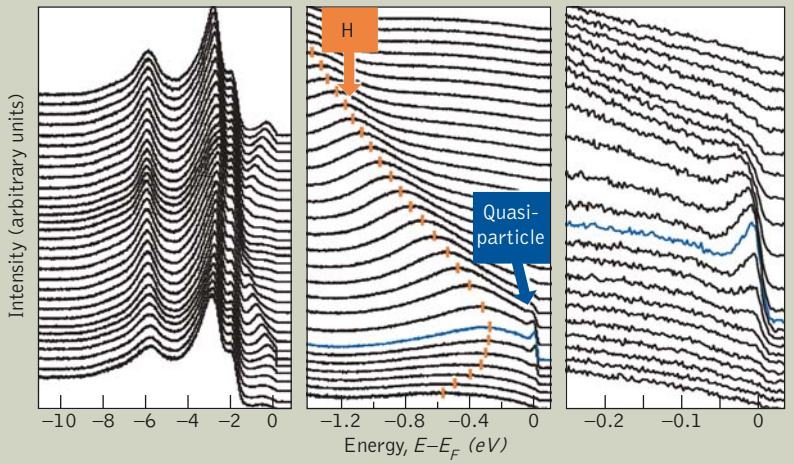

FIGURE 2
Energy distribution curves (EDCs) plot the variation in photoelectron intensity with energy for a fixed momentum. The set of EDCs is obtained by taking vertical line scans through the ARPES data at various momenta. The two features labeled "H" (red) and "Quasiparticle" (blue) are associated respectively with a particular electron band (designated e_g) and a small quasiparticle peak with polaronic features visible both as its small spectral weight (intensity) and its very narrow dispersion (variation of energy with momentum).

ganites displayed the characteristic signatures of the pseudogap state as found in the cuprates, including the nodal and antinodal dichotomy (Figures 2 and 3). These findings therefore cast doubt on the assumption that the pseudogap state and the nodal–antinodal dichotomy are hallmarks of the superconductivity state and suggests they are a more general phenomenon characteristic of transition-metal oxides.

Moreover, these ARPES experiments suggest the occurrence of a polaronic metal with anisotropic band structure (Figure 4). A polaron is a "quasiparticle" formed when an electron causes a large distortion around it in the atomic lattice of a crystal. Since the surrounding atoms are much more massive than the bare electron, the polaron behaves as a negatively charged particle with a larger mass and lower mobility than an isolated electron. Earlier research at the ALS had linked the formation of polarons in LSMO to the CMR effect.

This latest research goes further and indicates that polaron formation is crucial to CMR. What might be even more interesting is the now-emerging picture that polarons are the basic constituents of a poorly understood mysterious metallic phase that is present in both CMR materials and so-called underdoped high-T_c cuprates and is likely ubiquitous to all transition-metal oxides. A proper understanding of this new phase will go a long way in capturing the essence of important phenomena such as colossal magnetoresistance and high-temperature superconductivity.

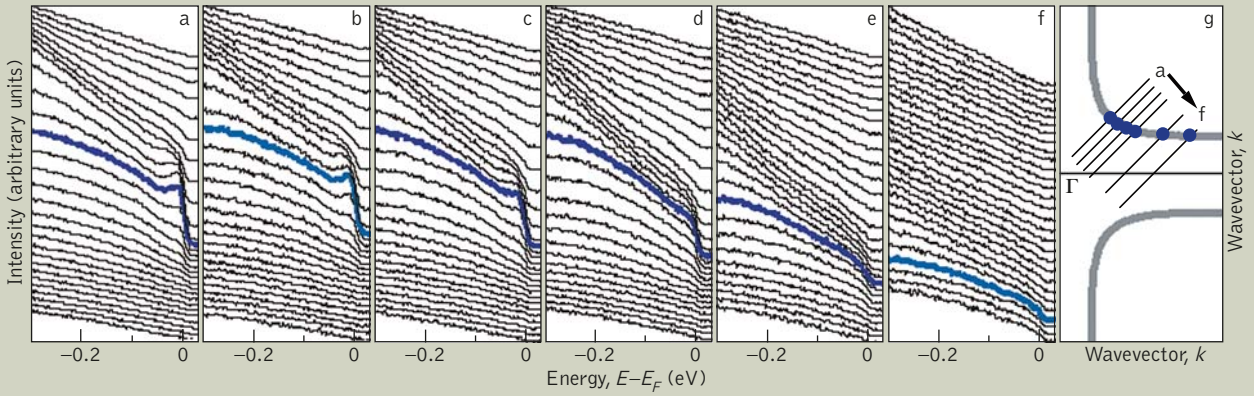

FIGURE 3
The locus of the momenta corresponding to a crossing of the Fermi level ("Fermi momenta") defines a Fermi surface in momentum space (curved lines in g). Γ marks the origin of momentum space. Here, a series of EDC sets for angular scans crossing the Fermi surface displays the nodal–antinodal dichotomy: the quasiparticle peak in the nodal direction (a) loses its intensity rather quickly while moving towards the antinodal direction (f).

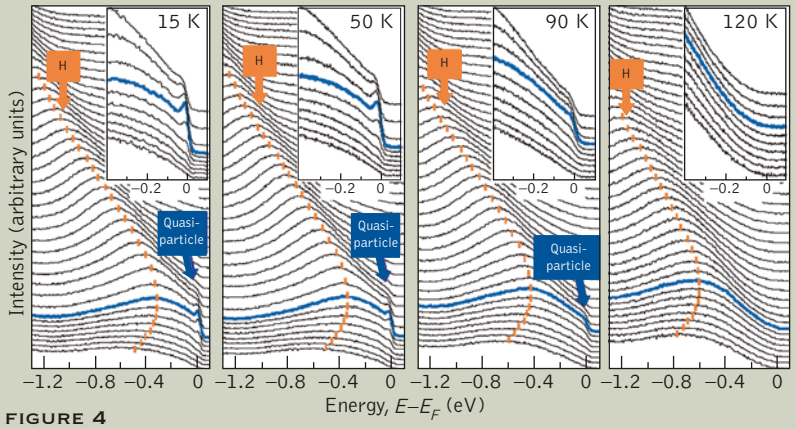

FIGURE 4
A series of EDC sets taken at temperatures from 15 to 120 K shows that the nodal quasiparticle feature disappears as the temperature is raised to the ferromagnetic transition temperature (Curie temperature) at which LSMO also becomes insulating. The H feature does not show a dramatic temperature dependence, as predicted by recent theoretical models describing a polaronic scenario.

INVESTIGATORS
N. Mannella, W. Yang, and X.J. Zhou (Stanford University, Stanford Synchrotron Radiation Laboratory, and ALS); H. Zheng and J.F. Mitchell (Argonne National Laboratory); J. Zaanen (Stanford University, Stanford Synchrotron Radiation Laboratory, and Leiden University, The Netherlands); T.P. Devereaux (University of Waterloo, Canada); N. Nagaosa (University of Tokyo and Correlated Electron Research Center, Tsukuba, Japan); Z. Hussain (ALS); and Z.X. Shen (Stanford University and Stanford Synchrotron Radiation Laboratory).

PUBLICATIONS
N. Mannella, W. Yang, X.J. Zhou, H. Zheng, J.F. Mitchell, J. Zaanen, T.P. Devereaux, N. Nagaosa, Z. Hussain, and Z.X. Shen, "Nodal quasiparticles in pseudo-gapped colossal magnetoresistive manganites," *Nature* **438,** 474 (2005).

FUNDING
U.S. DOE BES, National Science Foundation, and Office of Naval Research.

Fermi Surface Evolution with Sodium Concentration in Na_xCoO_2

Despite the best efforts of thousands of researchers around the world invoking an impressive array of experimental and theoretical techniques, exactly why certain ordinarily insulating ceramic compounds called cuprates (because they contain copper and oxygen) become superconducting when their composition is altered slightly has been a mystery since their initial discovery 20 years ago. One promising avenue is to hunt for clues in other classes of materials that exhibit similar structural and behavioral features, such as atoms arrayed in two-dimensional planes and superconductivity induced by small compositional changes (doping). Yang et al. have taken this approach in their investigation of a different group of compounds (cobaltates) based on cobalt and oxygen. In this case, the addition of sodium and water makes the cobaltates superconducting. By studying the angular distribution, energy, and intensity of x-ray-induced electrons (photoelectrons) emitted from the surface as the amount of sodium is varied, the investigators were able to unravel a key signature of metallic solids known as the Fermi surface that is involved in the transition to a superconductive state.

Although high-transition-temperature (high-T_c) superconductivity is found in many copper oxides (cuprates), superconductivity at any temperature rarely occurs in transition-metal oxides. Owing to the many similarities between cuprates and cobaltates, the discovery of superconductivity in the hydrated cobaltate $Na_xCoO_2 \cdot yH_2O$ ($T_c \sim 5$ K) stirred up the hope that cobaltates might help solve the long-standing mystery of the origin of high-T_c superconductivity. Researchers from Boston College and the ALS working at ALS Beamline 12.0.1 and at the University of Wisconsin Synchrotron Radiation Center have contributed important new information with a systematic angle-resolved photoemission (ARPES) study that exposed new details about the Fermi surface, a crucial factor in superconductivity.

Electrons in metals occupy quantum states in energy bands up to a maximum energy, the Fermi energy, that depends on the number of electrons. The Fermi surface (FS), the most basic attribute of a metal, is the contour in reciprocal or momentum space of the Fermi energy. Electrons near the FS are affected by the common features of both cobaltates and cuprates, including a layered structure, strong electron correlations, and superconductivity induced by doped carriers.

Controversy still shrouds the nature of the Fermi surface in cobaltates. Local density approximation (LDA) band calculations have predicted two kinds of FS sheets: a large hexagonal shape centered around the center of the Brillouin zone (unit cell in reciprocal space whose shape depends on the crystal symmetry) and six small elliptical pockets near the zone corners. However, initial ARPES measurements in $Na_{0.7}CoO_2$ revealed only one large FS sheet.

To resolve the discrepancy, the researchers studied a wide range of carrier concentrations by varying the sodium concentration ($0.3<x<0.72$). They found that there is only one FS sheet centered around the zone center (Figure 5). The enclosed area of the FS shrinks as sodium concentration is reduced, so that the Luttinger theorem (effective carrier concentration equals the sodium concentration) is obeyed in this material. In addition, at $x \sim 1/3$ (the sodium doping level for maximum superconductivity), they observed that the hexagonal FS almost coincides with the new zone boundary that results from a symmetry-changing commensurate charge ordering, indicating the importance of charge fluctuations to the superconductivity in this material.

An accurate FS determination over a large momentum span (Figure 6) allowed the researchers to observe a strong kink in the variation of the carrier energy with momentum (dispersion) about 100 meV below the Fermi energy. A similar dispersion kink has been also observed in high-T_c cuprates, with the implication of strong coupling between electrons and a bosonic mode (lattice vibration or spin wave), a possible signature of

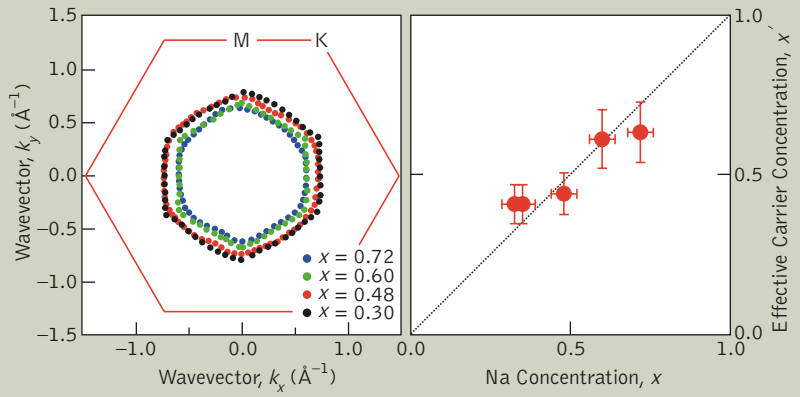

FIGURE 5
Fermi surface evolution in Na_xCoO_2. Left: Fermi surfaces at four carrier concentrations show only a single FS sheet in each case. Right: Effective carrier concentration x', derived from the FS area as a function of sodium concentration x, indicates agreement with Luttinger's theorem (diagonal line).

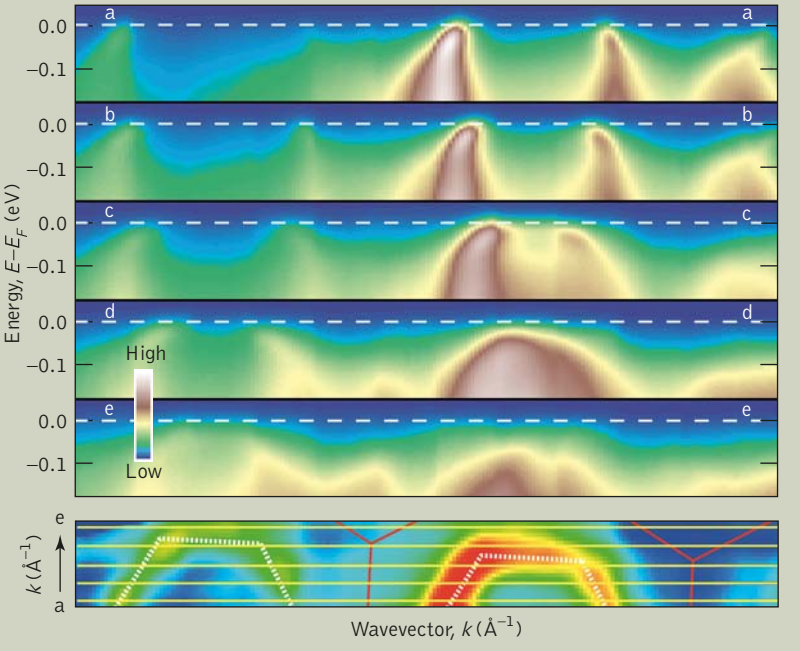

FIGURE 6
An example of FS mapping for $Na_{0.48}CoO_2$. Energy-momentum (wavevector) plots (a–e) of the photoemission intensity along the long cuts indicated by the yellow solid lines in the bottom panel, where FS contours obtained from the intensity at E_F are shown. The energy-momentum dispersion is obtained from the momenta at which the intensity is maximum for a sequence of energies.

the "glue" that causes carrier pairing in superconductivity. However, the group recently concluded that the kink observed in the cobaltate is probably due to orbital hybridization.

Regarding the disappearance of the small FS pockets, the researchers showed that this is due to a lowered energy in a branch (e_g') of the t_{2g} band complex (Figure 7). Instead of crossing the Fermi energy, the e_g' band "sinks" below the Fermi "sea level." This sinking is not due to the opening of an energy gap, as the leading edge does not show gap closing at high temperatures. Neither is it due to a surface effect, since no FS pocket was observed when the photon energy was raised to make ARPES much more bulk sensitive.

Observation of "sinking" FS pockets has motivated a reexamination of LDA calculations. Most promising, a calculation based on the Gutzwiller approximation has predicted vanishing FS pockets at all carrier concentrations under the condition of strong correlations. In principle, the fate of small Fermi surfaces in this kind of multi-orbital system depends on a delicate balance of electron correlations, Hund's coupling, and crystal field splitting, and so does the superconductivity.

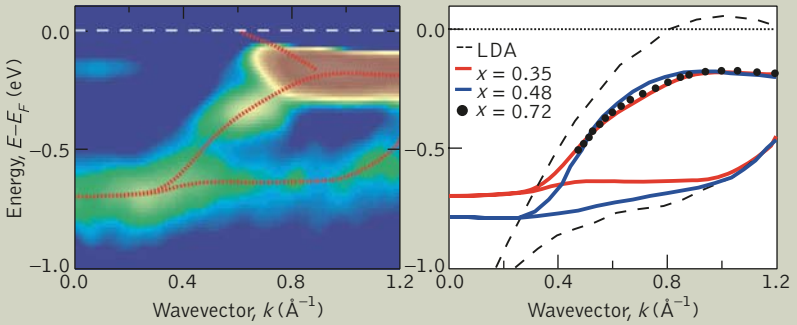

FIGURE 7
"Sinking" pockets near Brillouin zone corners. Left: Second derivative of the intensity spectra for $Na_{0.3}CoO_2$ along the principal axis Γ-K measured using 30-eV photons. Right: The measured e_g' band at three different carrier concentrations shows that the measured bands do not cross the Fermi energy, whereas a calculated band (dashed lines) does.

INVESTIGATORS
H. Ding, H.B. Yang, Z.H. Pan, A.K.P. Sekharan, and Z. Wang (Boston College); A.V. Fedorov (ALS); T. Sato, S. Souma, and T. Takahashi (Tohoku University, Japan); and R. Jin, B.C. Sales, and D. Mandrus (Oak Ridge National Laboratory).

PUBLICATIONS
H.B. Yang, Z.H. Pan, A.K.P. Sekharan, T. Sato, S. Souma, T. Takahashi, R. Jin, B.C. Sales, D. Mandrus, A.V. Fedorov, Z. Wang, and H. Ding, "Fermi surface evolution and Luttinger theorem in Na_xCoO_2: A systematic photoemission study," *Phys. Rev. Lett.* **95,** 146401 (2005).

FUNDING
National Science Foundation, U.S. DOE BES, Petroleum Research Fund, and Japanese Ministry of Education, Culture, Sports, Science and Technology.

Tuning the Metal–Insulator Transition via Alkali Adsorption

Illumination at the flick of a switch. Instant communication across vast distances. A universe of information accessible from your desktop. We now enjoy a practically endless list of technological advances that owe their existence to understanding how electrons behave in the solid state. To put it simply, in certain metals, electrons in the atoms' outer orbitals are free to wander throughout the material and thus conduct electricity. This highly simplified picture, however, does not take into account the effect that electrons have on each other, an effect known as "electron correlation." Materials with electrons that are strongly correlated are expected to provide the basis of major new technologies as we begin to exploit, not just electron charge, but the interplay of electron charge, spin, and orbital properties. Such interactions often result in dramatic effects: superconductivity, for example, or extreme sensitivity to slight changes in magnetic field (colossal magnetoresistance). Rossnagel et al. have found a way to observe, "live," the changes in the electronic structure of a strongly correlated electron material as it transforms from a metal into an insulator.

Turning a material from an insulator to a metal, or vice versa, by light irradiation, exposure to electric or magnetic fields, or applying small changes in temperature, pressure, or doping—such intriguing control of a material's electronic properties is possible by exploiting strongly interacting or "correlated" electrons. Now a team of researchers from the University of Kiel in Germany and the ALS has found a novel, surprising way to continuously transform a layered metallic transition-metal compound, TaS_2, into an insulator. Using angle-resolved photoemission spectroscopy (ARPES), they have demonstrated that adsorption of alkali atoms onto this material's surface gradually makes it more insulating, although in general, alkali adsorption should lead to more metallic behavior, as alkali atoms easily give away their loosely bound outermost electron.

How can a correlated material undergo a metal-to-insulator transition? Suppose we have a crystal with a simple band structure consisting of a single half-filled valence band, and we start to increase the lattice spacing between the atoms (Figure 8). Band theory then predicts metallic

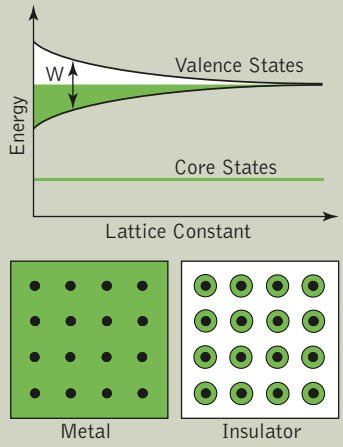

FIGURE 8
Top: Schematic representation of the lattice-constant dependence of a simple band structure. Band theory predicts metallic conduction, no matter how narrow the band becomes. Bottom: At a critical lattice constant, itinerant electrons become mostly localized at individual sites, but can still hop from site to site with a non-negligible probability.

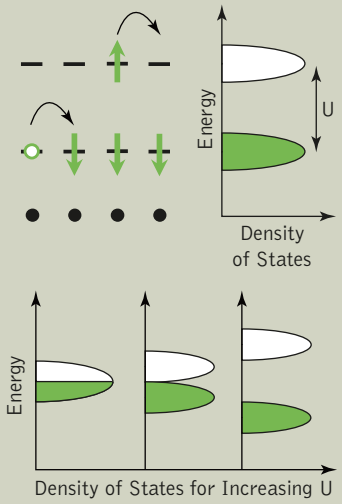

FIGURE 9
Top: Hopping of a spin-up electron and a spin-down hole on the background of spin-down electrons gives rise to the so-called Hubbard subbands, separated by the Hubbard interaction term U. Bottom: The Hubbard subbands form gradually as the ratio U/W is increased.

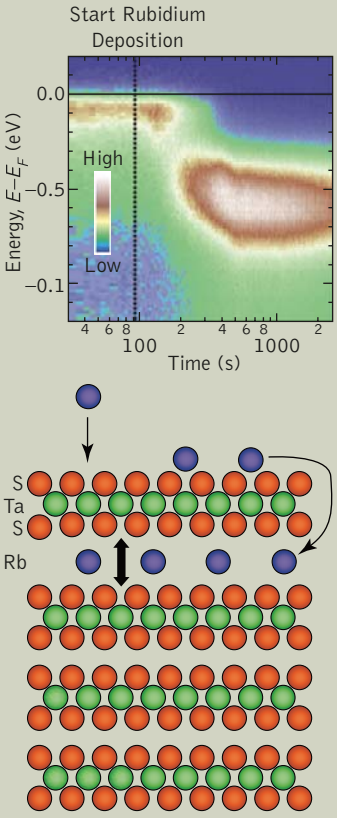

FIGURE 10
Top: Evolution of ARPES data recorded during the deposition of rubidium atoms on the surface of the layered transition-metal compound TaS_2. Bottom: An artist's impression of the rubidium intercalation process in TaS_2.

conduction, no matter how narrow the valence band becomes (as measured by the band width W).

What happens instead, at some critical band width, is that the itinerant (delocalized) valence electrons become mostly localized at individual atomic sites, such that they only hop from site to site with a small, but nonnegligible probability. This breakdown of metallic conduction is reflected in the formation of the so-called Hubbard subbands, which are separated by U, the energy cost an electron has to pay when it hops on an already occupied atom. Quite generally, these Hubbard subbands form gradually as the ratio U/W is increased (Figure 9).

To reveal such drastic changes in the electronic structure of a material, ARPES is the ideal tool, since it directly probes the valence-electron distribution in momentum space. The Kiel–Berkeley collaboration performed their ARPES measurements at the Electronic Structure Factory on ALS Beamline 7.0.1. Clean surfaces of layered TaS_2 were prepared by cleavage in ultrahigh vacuum, and an alkali, rubidium in this case, was evaporated live during the photoemission measurements.

A "photoemission movie" recorded during the deposition process shows the intriguing evolution of the valence spectra as a function of deposition time (Figure 10). At the beginning of the movie, the high spectral intensity near the highest occupied electron energy, the Fermi energy E_F, identifies TaS_2 as a metal. Then rubidium deposition is started and spectral weight is continuously removed away from E_F, gradually transforming the material into an insulator. The similarity of these results with the simple sketch of Hubbard subbands strongly supports the interpretation as a correlation-driven metal-to-insulator transition (note that ARPES can only probe the lower Hubbard subband). But what is the reason for this transition, as alkali adsorption onto metallic systems usually causes an increased

band filling and thus more metallic behavior?

The possible solution lies in the characteristic layer structure of TaS_2. Remarkably, alkali deposition on such a material can result in the intercalation of some alkali atoms in the gaps between the layers, which increases the layer separation and thereby reduces the electronic band width perpendicular to the layers. Thus, the ratio U/W can be driven through the critical value for the metal-to-insulator transition.

Besides electronic correlations, there are more facets of this particular metal-to-insulator transition, namely, disorder introduced by the rubidium atoms, charge transfer from rubidium to TaS_2, and electron–lattice coupling, as TaS_2 also undergoes a charge-density-wave reconfiguration. But electron–electron interaction appears as the dominant cause in this case, making the rubidium/TaS_2 system an ideal test object to study in detail the continuous evolution of the valence electron structure of a correlated material across the passage from the metallic to the insulating regime.

Kai Rossnagel (University of Kiel).

Investigators

K. Rossnagel and L. Kipp (University of Kiel, Germany) and H. Koh, E. Rotenberg, and N. Smith (ALS).

Publications

K. Rossnagel, H. Koh, E. Rotenberg, N.V. Smith, and L. Kipp, "Continuous tuning of electronic correlations by alkali adsorption on layered 1T-TaS_2," *Phys. Rev. Lett.* **95,** 126403 (2005).

Funding

German Research Foundation, Alexander von Humboldt Foundation, and U.S. DOE BES.

Coupling of Multiple Phonons to Electrons in High-Temperature Superconductors

Why do some materials become superconducting (lose electrical resistance) at much higher temperatures (above the boiling point of liquid nitrogen, 77 K) than others (typically 20 K or below)? To form a superconducting state, electrons need to pair up by forming an attractive force between them that overcomes their natural inclination to repulse each other. In the low-temperature conventional superconductors, this attractive force is realized through interactions of these electrons with phonons (lattice vibrations). But in high-temperature superconductors, the nature of the glue for the pairing and whether it is still electron–phonon coupling remain unclear. In this study, Zhou et al. have found that, by taking high-quality photoemission spectra, they could identify signatures of fine structure in the electron "self-energy" that correspond well with the phonon spectra measured directly from other techniques (such as neutron scattering). This correlation indicates that the entity that couples to electrons is indeed phonons. Furthermore, it indicates that phonons of many frequencies can participate in the coupling, in contrast to earlier suggestions that only one phonon frequency is involved.

Unraveling the mechanism of high-temperature superconductivity is one of the prominent issues in condensed matter physics. As an essential step in the transition to the superconducting state, the electrons involved must form pairs, but how they do this has been controversial. An international collaboration from the United States, Japan, and China has now provided strong evidence from angle-resolved photoemission spectroscopy (ARPES) of the superconductor $(La_{2-x}Sr_x)CuO_4$ (LSCO) that interactions between electrons and phonons are the key players. Their approach will open a new path for investigating electron–boson coupling, not only in high-temperature superconductors, but also in all other materials.

According to the traditional BCS theory (named after John Bardeen,

Leon Cooper, and Robert Schrieffer) for conventional low-temperature superconductors like metals and alloys, the electrons are paired (form Cooper pairs) by exchanging phonons. The theory predicts an isotropic superconducting gap (energy needed to break a Cooper pair) and a limit to the superconducting transition temperature (T_c) below 40 K. Therefore, the high T_c (highest at ambient pressure is 134 K) and the anisotropic superconducting gap found in high-temperature superconductors indicate that the BCS theory can not be directly applied. These observations, together with transport and other measurements, have led physicists to the dominant view that electron–phonon coupling is weak and irrelevant in high-temperature superconductivity.

To shed light on the pairing mechanism, the group used ARPES to measure the electrons' energy distribution (intensity as a function of electron energy) at different angles in real space, which yields information about the electronic state inside the solid. The relationship between two quantities (electron energy and momentum) provides important information about the electron dynamics, such as the speed of the electrons and their effective mass. In particular, if the electrons are coupled with other entities like phonons, it will show up as a modified energy-momentum relation (dispersion). The difference between the measured dispersion and that calculated for a noncoupling case gives the so-called electron self-energy, which contains information about the coupling. However, this effect of coupling is usually very small, so it can only be revealed with high energy resolution and high data statistics. For this reason, the experiment was done with the High-Energy-Resolution Spectrometer (HERS) endstation at ALS Beamline 10.0.1.

Recently, in high-T_c superconductors, it has been observed that the energy-momentum dispersion exhibits a kink. This kink is an indication of electron–boson coupling, but the nature of the boson is controversial. There are two leading possibilities: a magnetic resonance mode and a phonon. Because the energy scale of these two is close, it is hard to distinguish between them. From their high-quality LSCO data, the group was able to observe some fine structure in the kink (Figure 11). The energy scale of the fine structure well matches the phonon structure measured from neutron scattering from the same material. This finding is important evidence that (1) the kink in the dispersion of LSCO is caused by phonons, and (2) multiple phonon energies are involved in the electron–phonon

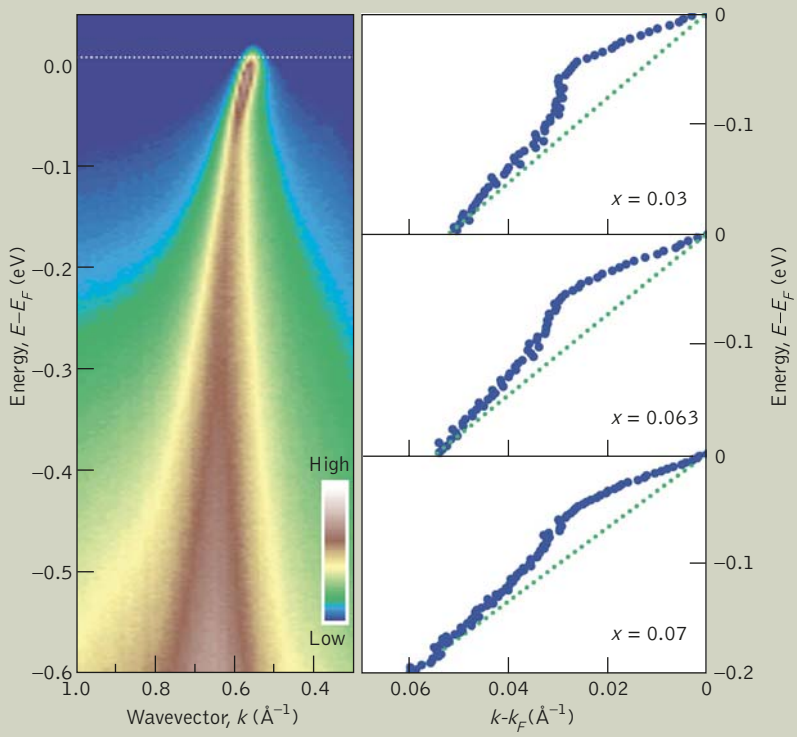

FIGURE 11
Left: Two-dimensional photoemission "image" showing the photoelectron intensity as a function of momentum and energy for a LSCO sample with x = 0.063. The measurement was taken along the (0,0)–(π,π) nodal direction (direction in momentum space where the anisotropic superconducting gap is minimum) at a temperature of about 20 K. Right: The energy-momentum relation obtained from such data for LSCO with compositions x = 0.03, x = 0.063, and x = 0.07. The green dashed lines connecting the two points at the Fermi energy and –0.2 eV are examples of a simple way to obtain the bare band for electrons without coupling.

coupling, not just one, as previously assumed.

These new results also provide a promising way to measure the Eliashberg function, $\alpha^2F(\omega)$, which is an important parameter that describes electron–phonon coupling in materials. The fact that this quantity, extracted from tunneling experiments in conventional superconductors, was consistent with the density of phonon modes as a function of frequency, $F(\omega)$, measured directly from neutron scattering, played an important role in establishing that the superconductivity was realized through the exchange of phonons. There have been attempts to measure $\alpha^2F(\omega)$ in high-T_c superconductors, but so far they have not been fruitful. In the new work, the group demonstrated that it is possible to obtain $\alpha^2F(\omega)$ from angle-resolved photoemission measurements (Figures 12 and 13). Even better, the parameter is momentum resolved, which provides an even more detailed look.

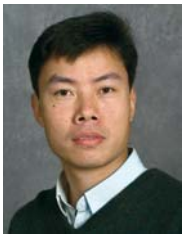

Xingjiang Zhou (Stanford University and ALS).

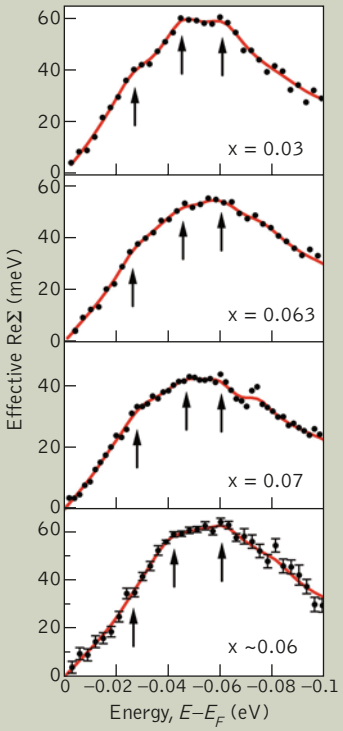

FIGURE 12
The effective real part of the electron self-energy (ReΣ) for LSCO samples with x = 0.03, 0.063, 0.07, and ~0.06. The arrows in the figure mark possible fine structures in the self-energy. The data are fitted using the maximum entropy method (solid red lines).

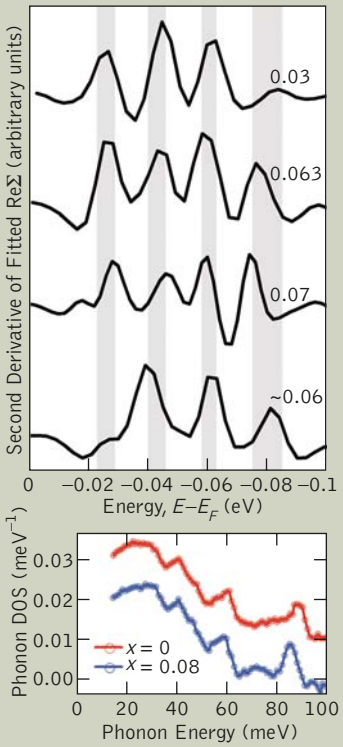

FIGURE 13
Top: The second-order derivative of the calculated ReΣ highlights the fine structure. The four shaded areas correspond to energies where the fine features fall. Bottom: The phonon density of states (DOS) $F(\omega)$ for LSCO with x = 0 (red) and x = 0.08 (blue) measured from neutron scattering matches the structure in the second derivative of ReΣ.

INVESTIGATORS

X.J. Zhou, W.L. Yang, V. Brouet, and N. Mannella (Stanford University and ALS); J.R. Shi (Oak Ridge National Laboratory), T. Yoshida, T. Sasagawa, and H. Eisaki (Stanford University and University of Tokyo); T. Cuk, J. Nakamura, Z.X. Shen, and R.B. Laughlin (Stanford University); S. Komiya and Y. Ando (Central Research Institute of Electric Power Industry, Japan); F. Zhou, W.X. Ti, J.W. Xiong, and Z.X. Zhao (Institute of Physics, Chinese Academy of Science); T. Kakeshita, S. Uchida, and A. Fujimori (University of Tokyo); Z.Y. Zhang and E.W. Plummer (Oak Ridge National Laboratory and University of Tennessee); and Z. Hussain (ALS).

PUBLICATIONS

X.J. Zhou, J.R. Shi, T. Yoshida, T. Cuk, W.L. Yang, V. Brouet, J. Nakamura, N. Mannella, S. Komiya, Y. Ando, F. Zhou, W.X. Ti, J.W. Xiong, Z.X. Zhao, T. Sasagawa, T. Kakeshita, H. Eisaki, S. Uchida, A. Fujimori, Z.Y. Zhang, E.W. Plummer, R.B. Laughlin, Z. Hussain, and Z.X. Shen, "Multiple bosonic mode coupling in the electron self-energy of $(La_{2-x}Sr_x)CuO_4$," *Phys. Rev. Lett.* **95,** 117001 (2005).

FUNDING

U.S. DOE BES; National Science Foundation; Office of Naval Research; Japanese Ministry of Education, Culture, Sports, Science and Technology; Japanese New Energy and Industrial Technology Development Organization; Natural Science Foundation of China; and Chinese Ministry of Science and Technology.

Hydrogen Storage in Carbon Nanotubes Through the Formation of C–H Bonds

The twin specters of an energy shortage and global climate change loom over our energy-hungry modern civilization. Currently, fossil hydrocarbons from coal, oil, and natural gas are the main source of energy powering today's world, but their availability is dwindling. Moreover, their intensive use has led to increasing emissions of greenhouse gases, causing an already measurable global warming. The main debate concerns how large the warming will be and how it will affect our climate. Substituting hydrogen for fossil hydrocarbons is one way address both issues. To avoid greenhouse gases, hydrogen can be produced from the electrolysis of water using renewable energy, from direct photolysis using sunlight, and from thermal cracking using the heat from nuclear reactors. The hydrogen can then be consumed in fuel cells, without harmful emissions, to generate electricity in power plants or vehicles. To realize hydrogen-powered transport, it is necessary to find ways to store hydrogen onboard efficiently and safely. Nikitin et al. have demonstrated with x-ray spectroscopy techniques that nanometer-sized structures known as carbon nanotubes can indeed store a useful amount of hydrogen and can also be made to release it.

Two of the major challenges for humanity in the next 20 years are the shrinking availability of fossil fuels and the global warming and potential climate changes that result from their ever-increasing use. One possible solution to these problems is to use an energy carrier such as hydrogen, and ways to produce and store hydrogen in electric power plants and vehicles is a major research focus for materials scientists and chemists. To realize hydrogen-powered transport, for example, it is necessary to find ways to store hydrogen onboard vehicles efficiently and safely. Nanotechnology in the form of single-walled carbon nanotubes provides a candidate storage medium. A U.S., German, and Swedish collaboration led by researchers from SSRL used ALS Beamline 11.0.2 and SSRL Beamline 5-1 to investigate the chemical interaction of hydrogen with single-walled carbon nanotubes (SWCNs). Their findings demonstrate that substantial hydrogen storage is both feasible and reversible.

Since hydrogen exists in the form of gas at ambient pressure and temperature, the most appropriate way to store hydrogen is in an adsorbed form on media capable of absorbing and releasing large quantities of this element easily and reliably. Carbon nanotubes are one of the most promising materials, and hydrogen storage through both physisorption and chemisorption mechanisms has been proposed. While most previous studies have focused on the potential of physisorption of molecular hydrogen, there is no direct reliable evidence of high hydrogen storage capacity at room temperature. It has been predicted that the chemisorption mechanism could provide hydrogen storage capacity that fulfills the technological requirement through the saturation of C–C π bonds with atomic hydrogen. However, direct experimental evidence of the feasibility of hydrogen storage through chemisorption has not yet been demonstrated.

The Stanford group studied as-grown SWCN films and SWCNs hydrogenated in situ by means of an atomic hydrogen beam. The team used x-ray photoelectron spectroscopy (XPS) and x-ray absorption spectroscopy (XAS) to observe the formation of C–H bonds through the modification of the local electronic structure around specific carbon atoms. With XPS and XAS, the researchers could also quantify the relative amount of hydrogen per carbon atom that was chemically adsorbed.

Hydrogenation leads to the breaking of C–C π bonds and C–H bond formation, as seen from the decrease in intensity of the π^* resonance and the increase in the intensity of C–H* and σ^* resonances in the XAS spectra (Figure 1). Of the two peaks in the carbon 1s XPS spectrum of hydrogenated SWCN (Figure 2), the higher-energy peak was assigned to nonhydrogenated carbon atoms and the lower-energy peak to hydrogenated carbon atoms. The assignment is supported by the theoretical calculation for the carbon 1s chemical shifts. Based on the intensity ratio between the two peaks, the amount of hydrogenated

carbon atoms was estimated to be 5.1 ± 1.2 weight percent of the hydrogen capacity of SWCNs. This value is close to the 6 weight percent required by the U.S. DOE for media to be used as an onboard hydrogen-storage system. The investigators also found that all C–H bonds in hydrogenated SWCN break at temperatures above 600 °C, demonstrating the reversibility of the hydrogenation (Figure 3).

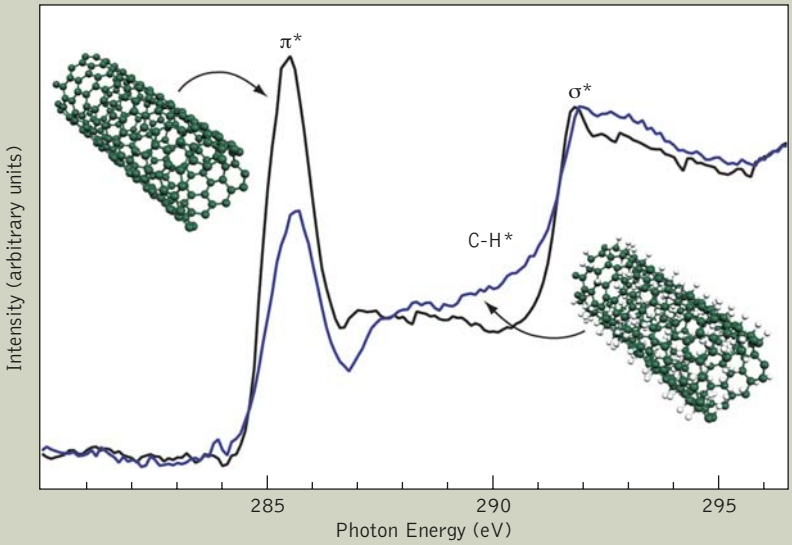

FIGURE 1
Carbon K-edge XAS spectra of a clean SWCN film (black) and a SWCN film (blue) after hydrogenation. The decrease of the π* resonance intensity and increase of the intensity in the energy range of C–H* and σ* indicate that the hydrogenation causes the rehybridization of the carbon atoms in the SWCN film from sp^2 to sp^3 form along with the formation of C–H bonds.

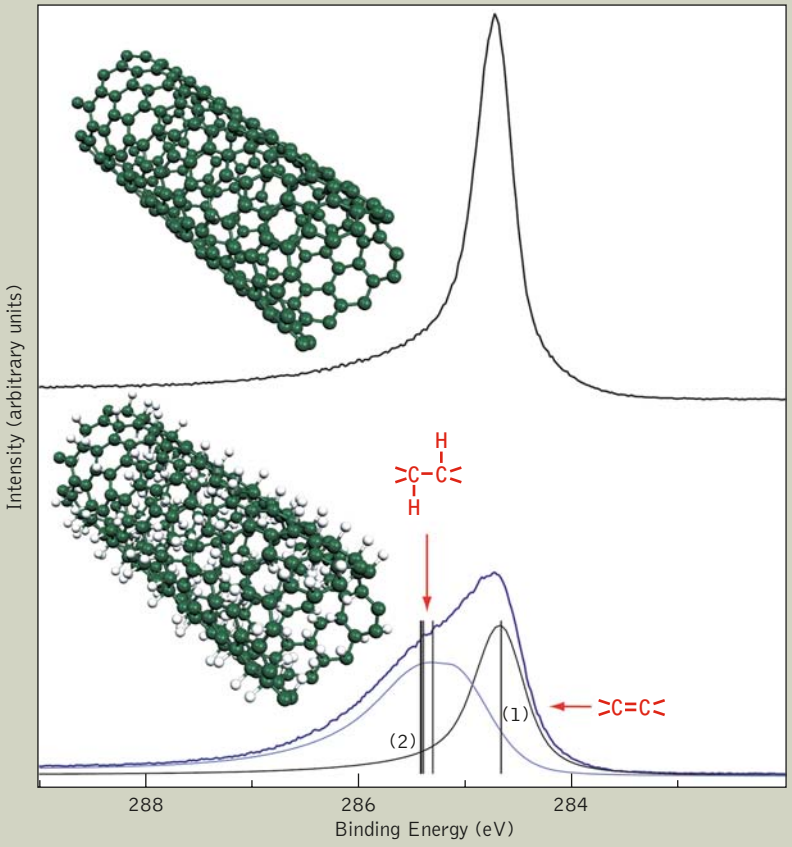

FIGURE 2
Carbon 1s XPS spectra of a clean SWCN film (black) and SWCN film (blue) after hydrogenation. Peak 1 at higher energy (lower binding energy) corresponds to the signal from carbon atoms unaffected by hydrogenation, whereas peak 2 at lower energy is due to hydrogen-coordinated carbon atoms. The theoretical values of the carbon 1s core-level chemical shifts due to C–H bond formation for different types of SWCNs are shown as vertical lines.

The present results indicate that it is possible to store hydrogen chemically in SWCNs through hydrogenation. The group thinks that the hydrogenated SWCNs provide a storage capacity close to the technologically required values, but it is essential to find means to hydrogenate SWCN efficiently and to fine-tune the energetics of the C–H bonds to allow for hydrogen release at 50 to 100°C. A hydrogenation metal catalyst can address the former, and the latter can be accomplished by using SWCNs with an appropriate diameter distribution.

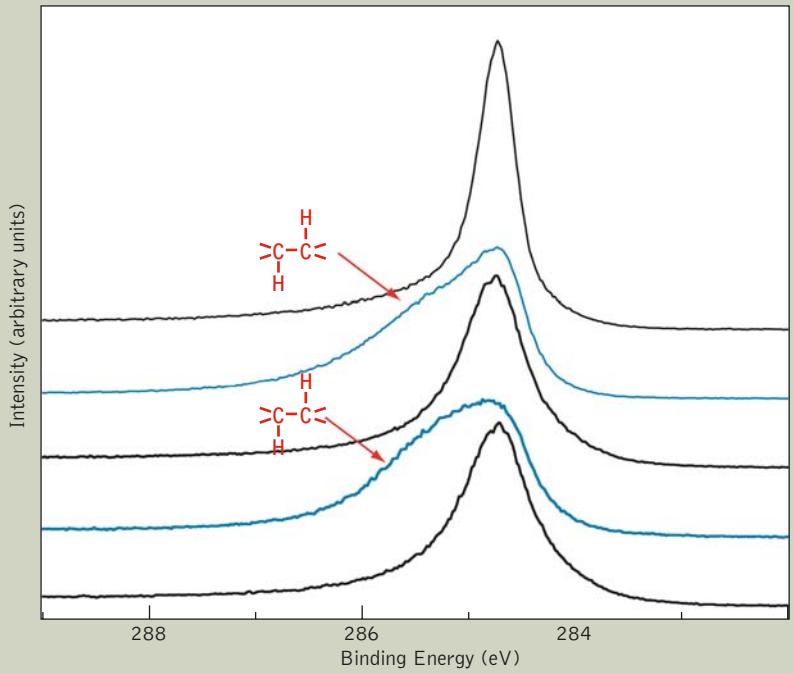

FIGURE 3
Carbon 1s XPS spectra of a SWCN film exposed to two cycles of hydrogenation and dehydrogenation. From top to bottom: Clean SWCN film (black), hydrogenated SWCN film (blue), SWCN annealed at 600 °C (black), hydrogenated SWCN film (blue), SWCN annealed at 600 °C (black). It is clear that the second hydrogenation led to the restoration of the shoulder that is due to the signal from C–H bonded carbon atoms.

INVESTIGATORS
A. Nikitin and H. Ogasawara (Stanford Synchrotron Radiation Laboratory); D. Mann (Stanford University); R. Denecke (Stanford Synchrotron Radiation Laboratory and Universität Erlangen-Nürnberg, Germany); Z. Zhang, H. Dai, and K. Cho (Stanford University); and A. Nilsson (Stanford Synchrotron Radiation Laboratory and Stockholm University).

PUBLICATIONS
A. Nikitin, H. Ogasawara, D. Mann, R. Denecke, Z. Zhang, H. Dai, K. Cho, and A. Nilsson, "Hydrogenation of single-walled carbon nanotubes," *Phys. Rev. Lett.* **95,** 225507 (2005).

FUNDING
U.S. DOE BES and the Global Climate Energy Project operated by Stanford University.

Engineering Metal Impurities in Multicrystalline Silicon Solar Cells

Solar energy is often touted as the most promising and secure alternative energy source, capable of reducing both our dependence on foreign fuels and the emission of dangerous pollutants that alter the world's climate. Although its current market share is small, it could substantially increase, if the cost of installed residential systems decreased from the current price of approximately $16,000–$25,000. One way to lower the cost is to use less expensive, low-grade silicon instead of ultrahigh-purity, electronic-grade material, which is currently in short supply, owing to the parallel growth of the semiconductor and solar cell industries. Buonassisi et al. used an x-ray analytical technique to find and analyze metal clusters as small as a few tens of nanometers, dispersed tens of micrometers apart in solar cells. Based on the correlations between the size and distribution of the nanoscale clusters and the efficiency of the cells, they suggested a novel concept of metal defect engineering to decrease the negative impact by transforming the metal clusters to a less harmful state. This approach may lead to the production of cheaper solar cells from inexpensive low-grade silicon.

Transition metals are one of the main culprits in degrading the efficiency of multicrystalline solar cells. With a suite of x-ray microprobe techniques, a multi-institutional collaboration led by researchers from UC Berkeley and Berkeley Lab studied the distribution of metal clusters in a variety of multicrystalline solar cells before and after processing. Their discovery that the size, spatial distribution, and chemical binding of metals within clusters is just as important as the total metal concentration in limiting the performance of multicrystalline silicon solar cells led to the concept of defect engineering by optimizing growth and processing sequences to trap metals in their least harmful state.

Materials alternatives for solar cells range from single-crystal electronic-grade silicon, which yields solar cells with efficiencies close to the theoretical limit but at a prohibitive price, to dirty metallurgical-grade silicon, which has failed to produce working solar cells. Some manufacturers experiment with blending semiconductor-grade silicon and metallurgical-grade silicon; others discuss the concept of cheap "solar-grade silicon" that is purified only to the extent necessary to make working solar cells. In practice, nearly 90 percent of commercial solar cells are made of highly purified silicon.

The key factor that determines the quality of raw silicon used for crystal growth is its transition-metal content. Multicrystalline silicon (mc-Si) solar cells can tolerate iron, copper, or nickel in concentrations up to 10^{14}–10^{15} cm^{-3} because metals in mc-Si are often found in less electrically active inclusions, or they precipitate at structural defects (e.g., grain boundaries) rather than being atomically dissolved. Since there is no simple correlation between the total metal content and cell efficiency, there is a strong need to understand the physics and the properties of metal clusters in solar cells.

The researchers used a combination of micro x-ray fluorescence (μ-XRF), x-ray absorption, and x-ray-beam-induced-current techniques at ALS Beamline 10.3.2 and APS SRICAT and PNCCT beamlines to study the distribution, chemical state, and electron-hole recombination activity of metal clusters in mc-Si (Figure 4). Two types of metal clusters were found: large inclusions greater than a micron in size, often containing a variety of metals in oxidized chemical states, and small metal-silicide precipi-

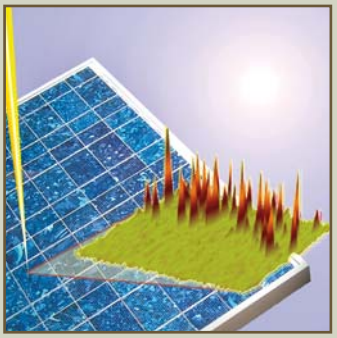

FIGURE 4
Artist's impression of an intense beam of synchrotron light striking a solar cell and the resulting fluorescence image of the distribution of iron impurities.

tates several tens of nanometers in size (Figure 5).

Metal clusters were found predominantly at boundaries between grains, dislocations, and, in some types of materials, at defect clusters within grains. Materials that had metal clusters confined to specific structural defects performed better in solar cells than materials in which metals were dispersed through the wafer. This led the researchers to the conclusion that the impact of metals on solar cells is determined not only by the total metal content but also by their distribution within the cell.

The existing technologies of gettering (removal from the wafers) and hydrogen passivation, routinely used to reduce the impact of metals on cell efficiency, can improve the cell performance by several percent, but they are insufficient if low-grade silicon is used. The researchers suggested that instead of taking the impurities out, one can manipulate them in a way that reduces their detrimental impact on the solar cell efficiency. This concept was dubbed "defect engineering of metal nanodefects."

For example, a simple variation of the cooling sequence of a sample that was intentionally contaminated with iron, copper, and nickel to simulate low-grade mc-Si improved the minority carrier diffusion length, the parameter directly linked to the cell efficiency, by a factor of four (Figure 6). This improvement was caused by a

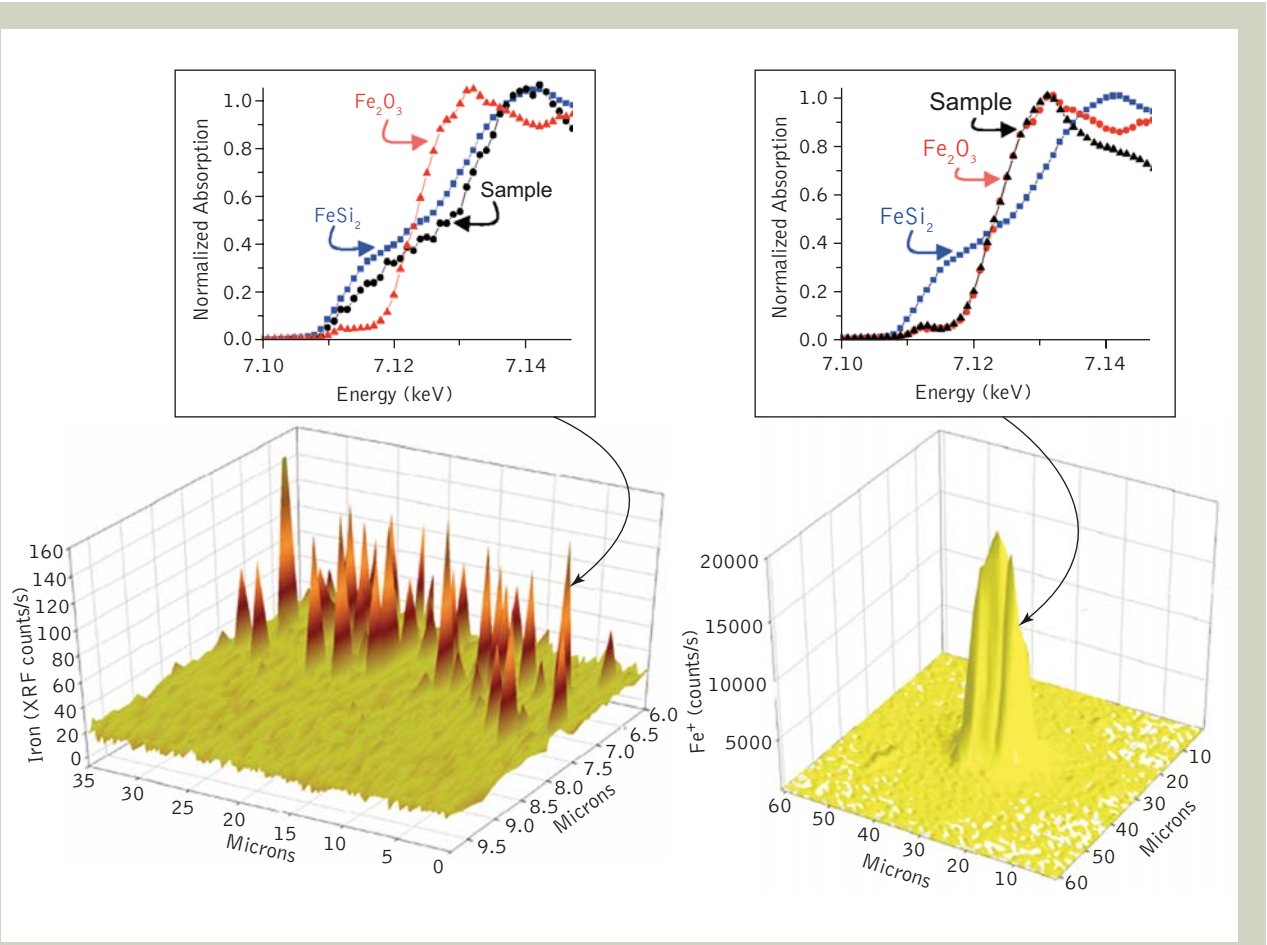

FIGURE 5
Two types of metal defects in commercial solar cell material. Left: Iron silicide nanoprecipitates with radii of about 20–30 nm. Right: Iron oxide inclusion, several microns in diameter. X-ray fluorescence (bottom) maps the defect distribution, while x-ray absorption spectra (top) determine their chemical states.

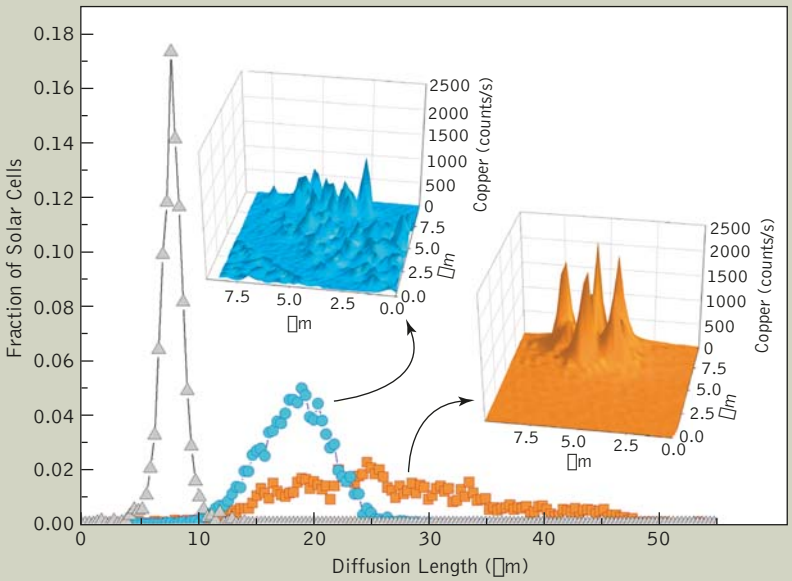

FIGURE 6
Material performance as measured by minority carrier diffusion length in three differently cooled samples (gray = quench, blue = quench and re-anneal, orange = slow cool) and size and spatial distributions of metal defects (insets). The slowly cooled material with microdefects in lower spatial densities clearly outperforms materials with smaller nanodefects in higher spatial densities, even though all materials contain the same total amount of metals.

Matthew Marcus (ALS) and Andrei Istratov, Eicke Weber, and, holding a multicrystalline silicon wafer, Tonio Buonassisi (UC Berkeley and Berkeley Lab).

change in metal distribution from a high density of small clusters and complexes to a low density of larger but isolated precipitates. Defect engineering of metal clusters, when optimized, could lead to new cost-efficient solar cell technologies.

INVESTIGATORS
T. Buonassisi, A.A. Istratov, and E.R. Weber (UC Berkeley and Berkeley Lab); M.A. Marcus (ALS); B. Lai and Z. Cai (Argonne National Laboratory); and S.M. Heald (Pacific Northwest National Laboratory).

PUBLICATIONS
T. Buonassisi, A.A. Istratov, M.A. Marcus, B. Lai, Z. Cai, S.M. Heald, and E.R. Weber, "Engineering metal-impurity nanodefects for low-cost solar cells," *Nature Materials* **4,** 676 (2005).

T. Buonassisi, A.A. Istratov, M. Heuer, M.A. Marcus, R. Jonczyk, J. Isenberg, B. Lai, Z. Cai, S. Heald, W. Warta, R. Schindler, and E.R. Weber, "Synchrotron-based investigations of the nature and impact of iron contamination in multicrystalline silicon solar cell materials," *J. Appl. Phys.* **97,** 074901 (2005).

T. Buonassisi, M.A. Marcus, A.A. Istratov, M. Heuer, T.F. Ciszek, B. Lai, Z. Cai, and E.R. Weber, "Analysis of copper-rich precipitates in silicon: Chemical state, gettering, and impact on multicrystalline silicon solar cell material," *J. Appl. Phys.* **97,** 063503 (2005).

FUNDING
National Renewable Energy Laboratory and U.S. DOE BES.

Vacancy-Induced Nanoscale Wire Structure in Gallium Selenide Layers

We live in a three-dimensional world, but finding ways to exploit the novel properties that result when one or more of the dimensions shrinks to the size of a few atoms (one nanometer on down) is a frontier of today's solid state physics and materials science. Developing techniques to controllably fabricate structures at the nanoscale is the necessary foundation for studying so-called low-dimensional materials, such as two-dimensional, nanometer-thick layers (a technology now well in hand) and one-dimensional, nanometer-wide wires (a skill just beginning to be acquired). Many of the approaches to growing nanowires rely on naturally occurring structures in bulkier materials to provide a kind of one-dimensional template. Ohta et al. have taken advantage of atomic defects called vacancies that occur in most metals and semiconductors. In the case of the semiconductor compound gallium selenide, the vacancies line up in rows along specific directions in the crystal lattice, and these rows guide the growth of wire-like structures less than one nanometer thick.

Low-dimensional materials have gained much attention not only because of the nonstop march toward miniaturization in the electronics industry but also for the exotic properties that are inherent in their small size. One approach to creating low-dimensional structures is to exploit the nanoscale or atomic-scale features that exist naturally in the three-dimensional (bulk) form of materials. By this means, a group from the University of Washington has demonstrated a new way of creating one-dimensional nanoscale structures (nanowires) in the compound gallium selenide. In short, ordered lines of structural vacancies in the material stimulate the growth of "one-dimensional" structures less than 1 nanometer in width.

A structural vacancy is a vacant atomic position in the crystal lattice. Introduction of chemical impurities (doping) can result in vacancy generation as the crystal seeks an equilibrium between local charge balance, bonding coordination, and valency around the impurity. Thermal energy can create vacancies even in ultrapure materials at temperatures above absolute zero. Structural vacancies are a source of numerous interesting structural, electronic, and optical properties, and materials scientists often rely them as an important building block for constructing the desired behavior.

As a semiconductor formed from group III (gallium) and VI (selenium) elements, gallium selenide (Ga_2Se_3) exhibits still another way to generate vacancies. So-called III–V semiconductors consisting of group III and group V elements or II–VI semiconductors consisting of group II and group VI elements typically exhibit tetrahedral sp^3 bonding to accommodate the eight electrons per cation–anion pair and crystallize in either zinc blende or wurzite structures. But Ga_2Se_3 has nine valence electrons per cation–anion pair, resulting in a competition between the desire to retain tetrahedral sp^3 bonding and the need to accommodate the extra electron. So, the compound stabilizes itself by incorporating structural vacancies. In particular, Ga_2Se_3 crystallizes in a "defected" zinc blende structure with one-third of the cation (gallium) sites vacant (Figure 7). In β-Ga_2Se_3, these sites are ordered in one dimension. These ordered vacancy arrays yield anisotropic optical transmission and photoluminescence and are predicted by theory to yield nondispersing electronic bands (energy is flat in momentum space), which is a signature of one-dimensional materials.

The Washington researchers studied a heteroepitaxial layer of

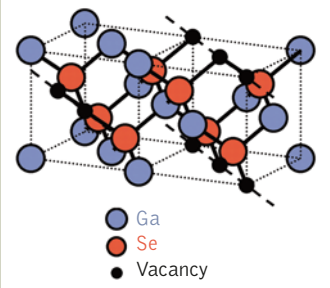

FIGURE 7
Crystal structure of Ga_2Se_3. One-third of the gallium sites are vacant along the <110> direction of the zinc blende lattice.

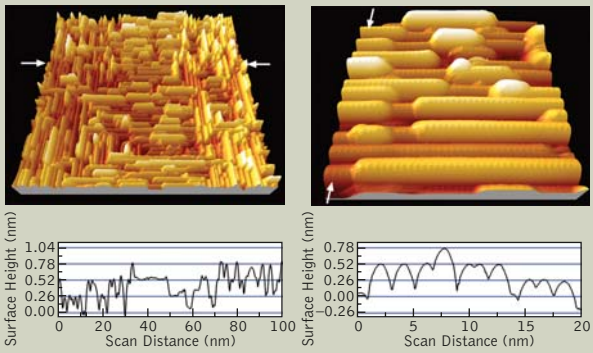

FIGURE 8
STM images of the growth morphology of 0.9-nm-thick Ga_2Se_3 on a Si(001) substrate. Left: 100 × 100 nm^2 three-dimensional image and cross section of surface height along the line between the white arrows. Right: Higher-magnification 20 × 20 nm^2 image and cross section of surface height between the white arrows.

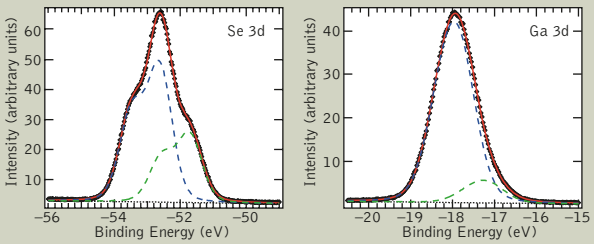

FIGURE 9
PES of 0.8-nm-thick Ga_2Se_3 film reflects that of bulk Ga_2Se_3. Selenium 3d and gallium 3d spectra (photon energy hν = 246 eV, normal emission geometry).

Ga_2Se_3 on a silicon (001) substrate covered by a single monolayer of arsenic by means of scanning tunneling microscopy (STM), core-level photoemission spectroscopy (PES), and photoemission diffraction (PED). They used STM to observe surface morphology and PES and PED to probe the chemical bonding and the bonding configuration. All PES and PED measurements were performed at the Electronic Structure Factory endstation of ALS Beamline 7.0.1.

STM of Ga_2Se_3 films revealed nanoscale, wire-like structures less than 1 nm wide and up to 30 nm long covering the surface in parallel lines (Figure 8). Core-level PES and PED showed the local structure of gallium and selenium atoms to reflect that of bulk Ga_2Se_3 (Figures 9 and 10). The <110> direction of the wire structure also coincided with the ordered vacancy direction usually seen in β-Ga_2Se_3. The researchers attributed the anisotropic growth of Ga_2Se_3 to passivation of the side walls of the wire structure by fully occupied lone-pair (nonbonding) orbitals of selenium atoms that arise due to the extra electron, so

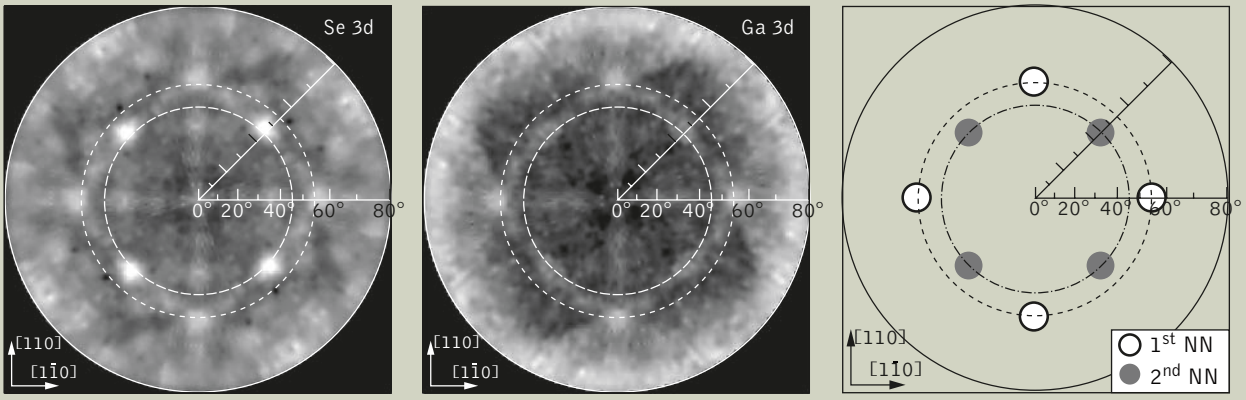

FIGURE 10
PED of 0.8-nm-thick Ga_2Se_3 film reflects that of bulk Ga_2Se_3. Selenium 3d and gallium 3d scanned-angle stereographic projections of photoemission intensities (magnesium Kα x-ray source, hν = 1253 eV) and characteristic angles for the first-nearest and second-nearest neighbor directions in a zinc blende lattice.

that adsorbing atoms during the growth process (adatoms) attach at the ends of the wires rather than on their chemically inert sides. Another way of looking at it is that the observed anisotropic morphology is a coalescence of the vacancies at the surface.

The formation of wire structures results from the strongly anisotropic growth of Ga_2Se_3, driven by intrinsic structural vacancies. To the group's knowledge, this mechanism has not been previously observed, and its understanding opens new opportunities for controlled growth or self-assembly of nanoscale structures in other materials containing structural vacancies.

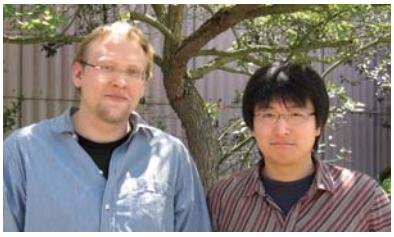

Aaron Bostwick and Taisuke Ohta (University of Washington).

INVESTIGATORS

T. Ohta, D.A. Schmidt, S. Meng, A. Klust, A. Bostwick, Q. Yu, M.A. Olmstead, and F.S. Ohuchi (University of Washington).

PUBLICATIONS

T. Ohta, D.A. Schmidt, S. Meng, A. Klust, A. Bostwick, Q. Yu, M.A. Olmstead, and F.S. Ohuchi, "Intrinsic vacancy-induced nanoscale wire structure in heteroepitaxial Ga_2Se_3/Si(001)," *Phys. Rev. Lett.* **94,** 116102 (2005).

FUNDING

National Science Foundation, M.J. Murdock Charitable Trust, University of Washington, UW/PNNL Joint Institute for Nanoscience, and Alexander von Humboldt Foundation.

Depth Profile of Uncompensated Spins in an Exchange-Bias System

Location, location, location! Consider the quantum mechanical spins that make some atoms magnetic. In a ferromagnet, the spins are aligned in parallel but are free to rotate, whereas in an antiferromagnet, the spins are antiparallel. Interactions across the interface between a ferromagnet and an antiferromagnet result in "exchange bias," which locks the ferromagnet spins, thereby forming a reference layer with a fixed direction of magnetization that is one key to modern magnetic devices. Despite years of effort, the details of how exchange bias occurs remain incomplete. Roy et al. have combined two experimental techniques, one based on reflection of x rays from an exchange-biased sample consisting of iron difluoride (the antiferromagnet) and cobalt (the ferromagnet) and the other relying on reflection of neutrons to obtain the distribution of spins of both iron and cobalt with distance away from the interface between the ferromagnetic and antiferromagnetic layers. Their spin profiles allowed them to determine the distributions of free and pinned spins and of spin orientation, thereby providing atomic-level insights into the mechanism of exchange bias.

The phenomenon known as exchange bias at the interface between a ferromagnet and an antiferromagnet is currently a subject of intense research because of its applications in the magnetic recording and read-head industries. An international collaboration headed by researchers from UCSD has used resonant x-ray scattering and polarized-neutron reflectometry to determine the depth-dependent magnetization in an exchange-biased sample. These results provide atomic-level insights into the mechanism of exchange bias, specifically the involvement of mutual interactions between two kinds of uncompensated spins in the antiferromagnet and spins in the ferromagnet.

In modern nanolayer magnetic devices, the shifted hysteresis loop

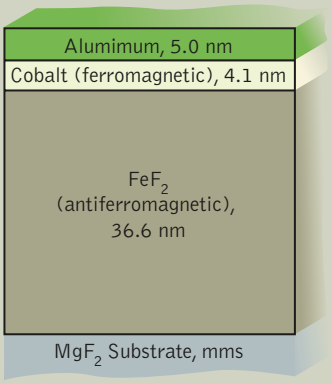

FIGURE 11
Multilayered sample consisted of antiferromagnetic iron, ferromagnetic cobalt, and aluminum on a substrate of magnesium fluoride.

centered on a nonzero magnetic field that characterizes exchange bias makes the ferromagnet an excellent magnetic reference layer because it is difficult to reverse the magnetization. Although exchange bias has been extensively studied over the years, fundamental questions remain unanswered or inadequately answered. For example, photoemission electron microscope (PEEM) images and x-ray circular magnetic dichroism (XMCD) studies have revealed the existence of uncompensated moments (spins in one direction not matched by an opposite spin) at the antiferromagnetic interface. What is the nature of the uncompensated spins? What are their lateral and depth distributions? How do they interact with the spins in the ferromagnet?

To address these issues, the collaboration used circularly polarized soft x-ray and spin-polarized neutron beams in small-angle reflection geometry with a sample consisting of a trilayer of antiferromagnetic FeF_2, ferromagnetic cobalt, and aluminum epitaxially grown onto a single-crystal MgF_2 substrate (Figure 11). Resonant x-ray measurements at the L edges of the magnetic atoms provided the variation of the element-specific magnetization, while neutron measurements yielded the variation of the vector magnetization. With the two techniques, the group was able to determine, in an element-specific way, the depth dependence of the magnetic density in absolute units.

Soft x-ray resonant magnetic reflectivity at ALS Beamline 4.0.2 was used to measure hysteresis loops at the L_3 edges of cobalt and iron in a 1-tesla field at 20 K (Figure 12, left). The measurements showed that both elements exhibited hysteresis, indicating that some cobalt and some iron spins were unpinned or free to rotate with the applied field. Both loops were shifted along the positive-field axis, with a similar bias field resulting from the shifted loops. The spin-density profiles obtained from analyzing the reflectivity as a function of wave vector transfer revealed a thin interfacial layer (about 17 Å thick) in FeF_2 with unpinned iron spins that were aligned opposite to cobalt spins in the bulk cobalt (Figure 12, right). Pinned, uncompensated iron

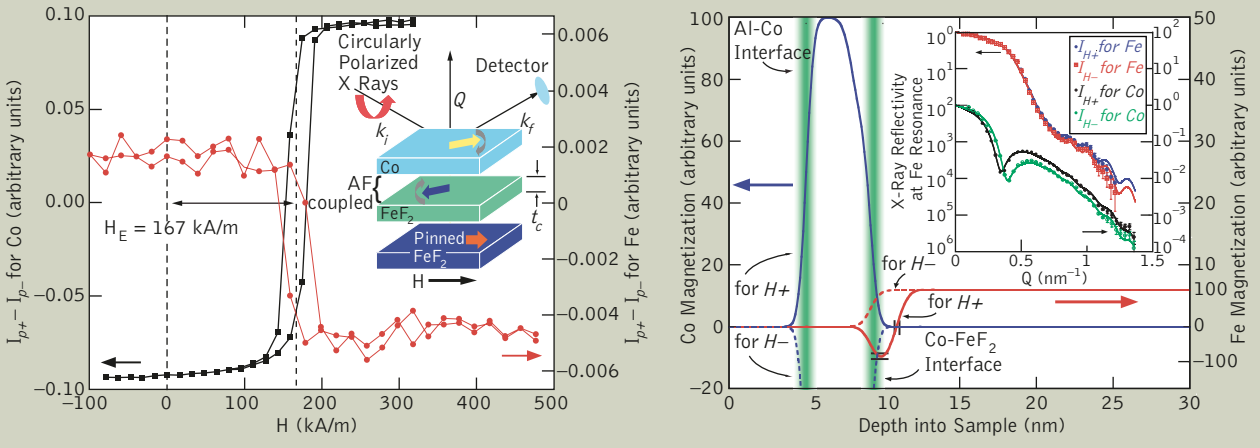

FIGURE 12
Left: Hysteresis loops measured from the difference in the reflectivity for left- and right-circularly polarized x rays ($I_{p+} - I_{p-}$) at a fixed angle of incidence for cobalt (black) and iron (red). The inset shows the scattering geometry and the spin model used to fit reflectivity data. Right: Depth-dependent magnetic-density profiles of cobalt (blue) and iron (red) as obtained by fitting the reflectivity data (inset). The vertical green lines mark the physical interface between Al/Co and Co/FeF_2, respectively. The two curves correspond to magnetizations when the external field is parallel to the direction of the field in which the sample was cooled; dashed curves represent the field-reversed case.

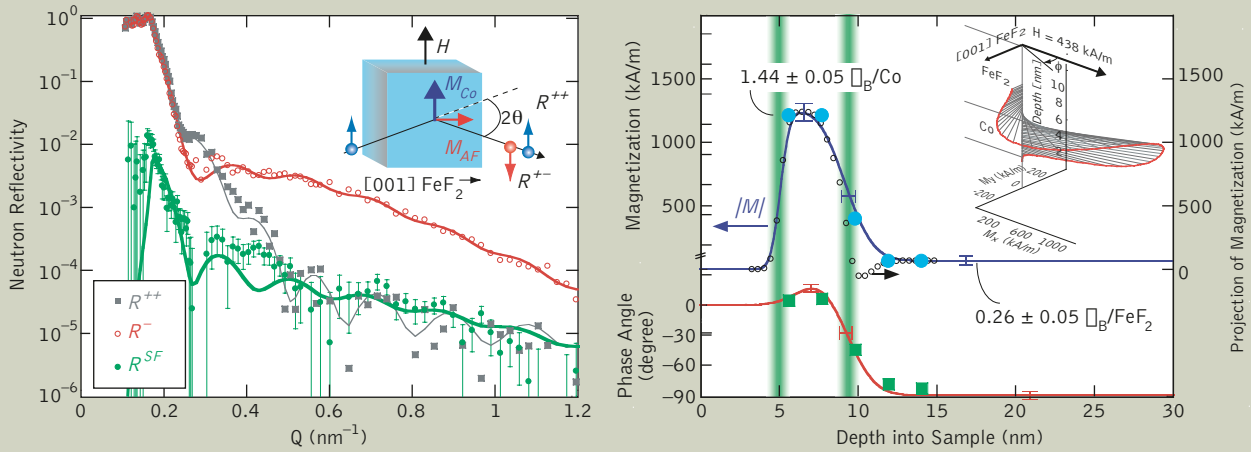

FIGURE 13
Left: Polarized neutron reflectivity data (symbols) and fit (continuous line). Inset shows the experimental geometry. Right: Depth dependence magnitude (blue) and phase angle (red) of the vector magnetization. The inset shows the twist in the magnetization near the Co/FeF_2 interface. Cyan and green dots are magnetization magnitudes and phases obtained from a micromagnetic simulation. The sum of the iron and cobalt spin density profiles from Figure 12 are shown in absolute units (open circles).

spins were also found throughout the depth of the antiferromagnet.

To probe the depth profile of the pinned magnetization, the group turned to the Manuel Lujan Jr. Neutron Scattering Center at Los Alamos National Laboratory for polarized-neutron reflectometry measurements in a cooled sample in a 0.7-tesla field (Figure 13, left). The oscillations of the reflectivity with wave vector transfer indicated the presence of pinned moments in the bulk of the FeF_2 at distances greater than about 3.5 nm from the interface (Figure 13, right). Further analysis showed that near the Co/FeF_2 interface, the angular dependence of the magnetization relative to the applied field is consistent with an antiferromagnetic coupling across an interface.

From these results, the collaborators concluded that the antiferromagnet has a net magnetization made up of two types of spins: those in a thin (about 2-nm) interfacial layer at the interface, which are strongly coupled to the magnetic spins of the ferromagnetic cobalt (and respond with them to an applied field) and those in the bulk of the FeF_2, which do not respond to an external field. It is the coupling of these spins to the ferromagnetic spins via the interfacial spins that gives rise to the exchange bias.

INVESTIGATORS
S. Roy, M. Dorn, Z.P. Li, I.V. Roshchin, and I.K. Schuller (UCSD); O. Petracic (UCSD and Universität Duisburg-Essen, Germany); X. Batlle (UCSD and Universitat de Barcelona, Spain); R. Morales (UCSD and Universidad de Olviedo, Spain); K. Chesnel (ALS); J.B. Kortright (Berkeley Lab); S. Park, M.R. Fitzsimmons, A. Mishra, and X. Zhang (Los Alamos National Laboratory); and S.K. Sinha (UCSD and Los Alamos National Laboratory).

PUBLICATIONS
S. Roy, M.R. Fitzsimmons, S. Park, M. Dorn, O. Petracic, I.V. Roshchin, Z.P. Li, X. Batlle, R. Morales, A. Mishra, X. Zhang, K. Chesnel, J.B. Kortright, S.K. Sinha, and I.K. Schuller, "Depth profile of uncompensated spins in an exchange bias system," *Phys. Rev. Lett.* **95,** 047201 (2005).

FUNDING
U.S. DOE BES; National Science Foundation; University of California; Alexander von Humboldt Foundation; Spanish Ministry of Education, Culture, and Sport; Fulbright Commission; Catalan Dursi; and Swiss National Science Foundation.

Time-Resolved Study of Bonding in Liquid Carbon

There are nearly ten million known carbon compounds in addition to the elemental forms we know as diamond and graphite. Key to carbon's versatility is its proclivity to form strong bonds, whether with two atoms in a linear chain, three atoms in a layer as in graphite, or four atoms in a crystal like diamond. Liquid carbon is yet another incarnation, one that can exist only in environments of extremely high temperatures and pressures. Johnson et al. have found a way to combine the use of an ultrafast laser with an x ray "probe" to study liquid carbon samples within the very short times in which the required conditions can be achieved in the laboratory. This allowed them to discern how the atoms in liquid carbon are arranged. Such investigations of so-called "warm dense matter" may lead to improved methods for synthesizing new materials, a better understanding of cooler astrophysical objects such as gas-giant planets like Uranus and Neptune and brown dwarfs, and more accurate models to help us predict the dynamics of carbon bonds under a variety of conditions.

We are accustomed to observing carbon in its elemental form as a solid, ranging from the soft "lead" in pencils to the precious gemstone in diamond rings (Figure 14). While considerable attention has been focused on solid forms of carbon, the properties of liquid carbon are much more difficult to measure accurately. The very strong bonding between carbon atoms that gives diamonds their hardness also makes carbon very difficult to melt, requiring temperatures above 5000 K at pressures above 100 bar (Figure 15). Maintaining such conditions in a laboratory is a challenge that has hampered efforts to fully understand the chemical bonding properties of this biologically, industrially, and environmentally important element. At the ALS, researchers have found a way to rapidly heat a carbon sample and contain the resulting liquid long enough to perform picosecond time-resolved x-ray absorption spectroscopy. The technique provides a way to measure the bonding properties of liquid carbon at near-solid densities that can then be compared with results from molecular dynamics simulations.

Even the most basic properties of liquid carbon have long been debated because of the challenge of studying the material at the required temperatures and pressures. Liquid carbon is volatile and thus inherently transient in an unconstrained environment. Most experiments involve the rapid melting of a solid sample, followed by observation of the liquid in the short time before it expands and vaporizes. The transient nature of these experiments limits the methods that can be used to probe the liquid properties, with inconsistent results. For example, although the most recent and reliable measure-

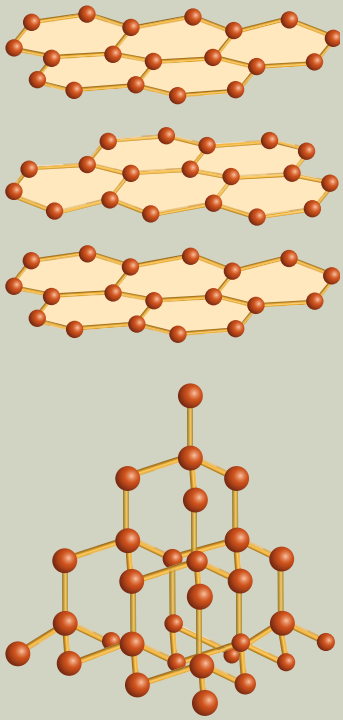

FIGURE 14
Two possible geometries for carbon bonds: graphite-like planar structure in which each carbon atom bonds to three others (top) and diamond-like crystal structure in which each carbon atom bonds to four others (bottom).

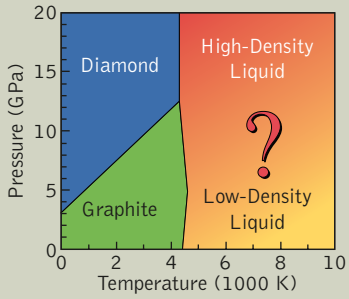

FIGURE 15
Carbon phase diagram. The properties of the liquid phase have remained unclear because of the difficulty in performing experiments at the required temperatures and pressures.

ments show that liquid carbon is metallic, reported conductivity values vary by more than an order of magnitude. This may be due to a strong dependence of the liquid properties on temperature and density, but so far no single experiment has demonstrated such a relationship. In addition to experiments, first-principles molecular dynamics simulations have been used to explore the properties of the liquid as a function of temperature and density. The results suggest that the local bonding structure of the liquid varies continuously from twofold to fourfold coordination as the density increases.

To investigate this intriguing result, the researchers performed ultrafast x-ray absorption spectroscopy at ALS Beamline 5.3.1. Thin (500-Å) foils of solid carbon were rapidly heated by a femtosecond laser pulse and then probed by a broadband soft x-ray pulse. A grating spectrograph then measured the spectrum of the transmitted x rays in the vicinity of the carbon K edge, providing information about the local bonding environment of the carbon atoms (Figure 16, left). By varying the relative timing of the x-ray and laser pulses, the (nearly instantaneous) melting process and the subsequent expansion dynamics of the liquid could be probed with 70-ps resolution. To delay the expansion and allow accurate measurements, the foil was "tamped" by a thick (3500-Å) LiF coating on both sides. The large optical band gap of LiF makes it essentially transparent to the laser, and the mechanical stiffness of the tamping layers prevents the foil from expanding on a time scale of about 100 ps, allowing

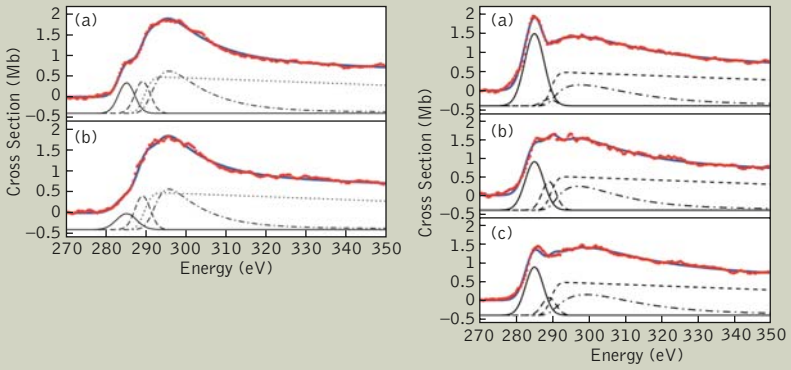

FIGURE 16
Left: K-edge absorption spectra of the unheated solid carbon foils; (a) amorphous carbon prepared by evaporation from an arc source and (b) diamond-like carbon. The red circles are the data. The black curves show the results of fitting the spectrum to various components corresponding to antibonding states. The blue curve is the sum of the fit components. Right: K-edge absorption spectra of liquid carbon at various densities, 100 ps after heating; (a) untamped, (b) 2.0 g/cm^3, and (c) 2.6 g/cm^3. The red circles are the data. The black curves show the fit results as in figure above.

observation of the liquid at densities very near that of the initial solid.

By fitting the resulting absorption spectra and comparing them to a reference spectrum of carbon-60, the researchers were able to establish that low-density liquid carbon contains predominantly twofold-coordinated chain structures (*sp* hybridization). As the density increased to that of solid forms (Figure 16, right), bond hybridization increased and threefold-coordinated (graphite-like) and fourfold-coordinated (diamond-like) bonds become more prevalent (indicating sp^2 and sp^3 hybridization, respectively). These observations are consistent with molecular dynamics calculations that rely on a tight-binding model of interatomic bonding. The fits also suggest that the bond length between carbon atoms in the liquid is significantly shorter than those in the solid, an observation also consistent with simulations.

INVESTIGATORS
S.L. Johnson (UC Berkeley, currently at the Paul Scherrer Institut, Switzerland), P.A. Heimann and O.R. Monteiro (Berkeley Lab), A.G. MacPhee and A.M. Lindenberg (UC Berkeley), Z. Chang (Kansas State University), R.W. Lee (Lawrence Livermore National Laboratory), and R.W. Falcone (UC Berkeley and Berkeley Lab).

PUBLICATIONS
S.L. Johnson, P.A. Heimann, A.G. MacPhee, A.M. Lindenberg, O.R. Monteiro, Z. Chang, R.W. Lee, and R.W. Falcone, "Bonding in liquid carbon studied by time-resolved x-ray absorption spectroscopy," Phys. Rev. Lett. **94,** 057407 (2005).

FUNDING
U.S. DOE BES, U.S. DOE High Energy Density Science Grants Program, and Institute for Laser Science and Applications, Lawrence Livermore National Laboratory.

Ultrafast Dynamics in Water

Even the stillest of waters, at the molecular level, contain a surprisingly turbulent, dynamic universe. The water molecules constantly form and break bonds under the influence of several weak interactions, balancing both cooperative and anticooperative effects. The situation gets further complicated when you add ionizing x-ray radiation to the mix: the energy from the radiation is enough to eject an electron from the core of the molecule, immediately resulting in the stretching and, sometimes, breaking of bonds. This process of radiolysis is commonly encountered in many fields and technologies, including biophysics, radiation physics, waste remediation, environmental cleanup, medical diagnosis, and radiation therapy. The detailed study of substances in the condensed and dynamic liquid state poses unique challenges that aren't an issue with isolated gas molecules or solids with rigid structures. Only recently have experimental techniques capable of probing the dynamics of liquid water become available. Odelius et al. have applied a combination of approaches, both experimental and theoretical, to gain a better understanding of how the fate of a given water molecule can be decided in a split second by tiny radiation-induced jiggles.

A thorough understanding of the chemical processes that are initiated when radiation interacts with aqueous systems is essential for many diverse fields, from condensed matter physics to medicine to environmental science. An incoming photon with enough energy to produce a core hole in a water molecule sets off motions that can affect bonding configurations, which in turn affect subsequent chemical-reaction pathways. However, it is a fundamental challenge for the radiation chemistry community to unravel the early time dynamics of electronically excited states in water because their short (femtosecond) time scales are difficult to access directly with pump–probe measurements. Using a combination of isotope substitution experiments and molecular dynamics simulations, researchers from Sweden, Germany, and the U.S. have shown that the ultrafast (0- to 10-fs) dissociation dynamics of liquid water can be successfully probed with x-ray emission spectroscopy.

X-ray emission spectroscopy (XES) is an element-specific tool capable of probing the local electronic structure of the occupied electronic states in complex systems. In the XES of water, the fluorescence from an electron reoccupying the oxygen 1s core level is measured. For hydrogen-bonded systems such as liquid water, ultrafast dynamics that occur during the lifetime of the core-excited state complicate the interpretation of the XES in terms of molecular structures but open a unique opportunity to study femtosecond reaction dynamics (Figure 1). This primary event of excitation or ionization of a water molecule in the radiolysis of aqueous systems governs all the subsequent steps in the radiolytic process.

The molecular dynamics are strongly dependent on the nature of the electronic core-excited state, and by scanning through the x-ray absorption excitation energy, from preedge through postedge, different reaction dynamics can be probed. In addition, by performing the same measurements using molecules of different nuclear masses, any differences in the dynamics will become apparent, and an observed isotope effect in the XES would provide direct evidence of the importance of such processes.

High-brightness radiation from ALS Beamline 8.0.1 was used to excite both normal and deuterated liquid water in a custom-designed copper liquid cell with a 100-nm-thick silicon nitride membrane that enables the study of liquid water under ultrahigh vacuum conditions (see "Soft X-Ray Liquid-Flow Cell at Beamline 8.0.1" in the SSG section of the Facility Report). The subsequent x-ray emission was recorded in the beamline's soft x-ray fluorescence endstation with

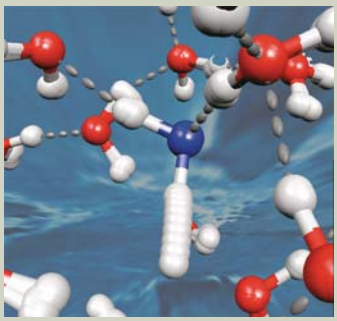

FIGURE 1
Simplified representation of the core-hole dissociation process. Excitation of a core electron in the blue oxygen atom leads to stretching of the O–H bonds and the ultimate dissociation of one of the OH groups, whose trajectories are represented by a "multiple-exposure" effect.

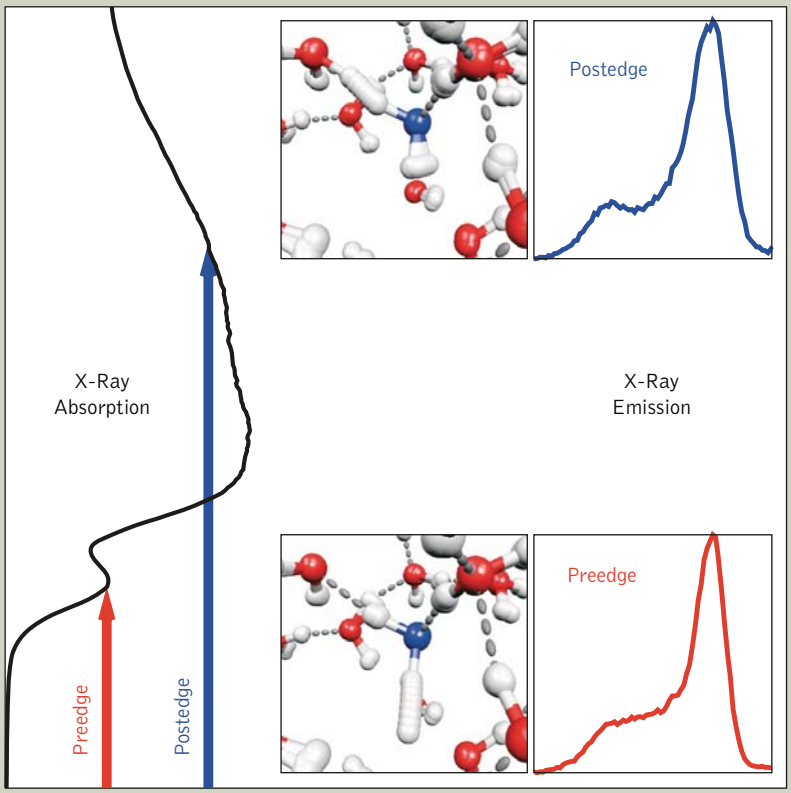

FIGURE 2
By controlling the excitation energy of the initial x-ray absorption, the ultrafast dissociation of hydrogen-bonded or uncoordinated OH groups can be selectively probed in liquid water in the x-ray emission spectrum.

a high-resolution Rowland-circle spectrograph. The temperature of the copper liquid cell was kept slightly above the freezing point of water to minimize temperature-induced effects.

The researchers found both an isotope effect and significant differences between the preedge and postedge XES (Figure 2). The preedge and postedge differences were explained in terms of the localization of the (lower-energy) preedge excitations, possible anisotropy in the direction of the emitted x rays, and differing hydrogen-bond arrangements between the preedge and postedge cases. The researchers then used ab initio molecular dynamics simulations to model the effects of the finite lifetime of the core hole. In these simulations, the isotope effect due to the inertia difference between hydrogen and deuterium is apparent, with an especially striking difference in dynamics for the two different excited states: the postedge excitation results in dissociation of the hydrogen-bonded OH group(s), whereas for the preedge excitation the uncoordinated OH group dissociates.

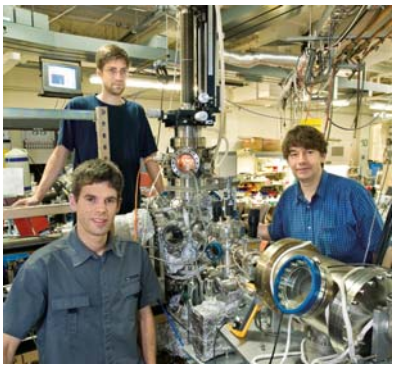

Oliver Fuchs and Lothar Weinhardt (Würzburg University) and Jonathan Denlinger (ALS).

In summary, experimental XES for normal and deuterated liquid water was analyzed against the background of ab initio molecular dynamics simulations. The excitation energy dependence in the XES data is explained in terms of differences in excited-state dynamics. Because of the inertia difference between hydrogen and deuterium, excited-state dynamics on the same time scale as the decay of the core-excited state will result in an isotope effect in the XES. The experimentally observed isotope effect is the key to unravelling the excited-state dynamics, but theoretical simulations were essential for proving the feasibility of the proposed mechanism.

Investigators

M. Odelius, D. Nordlund, and L.G.M. Pettersson (Stockholm University); H. Ogasawara (Stanford Synchrotron Radiation Laboratory); O. Fuchs, L. Weinhardt, F. Maier, and E. Umbach (Würzburg University); C. Heske (University of Nevada, Las Vegas); Y. Zubavichus and M. Grunze (Heidelberg University); J.D. Denlinger (ALS); and A. Nilsson (Stockholm University and Stanford Synchrotron Radiation Laboratory).

Publications

M. Odelius, H. Ogasawara, D. Nordlund, O. Fuchs, L. Weinhardt, F. Maier, E. Umbach, C. Heske, Y. Zubavichus, M. Grunze, J.D. Denlinger, L.G.M. Pettersson, and A. Nilsson, "Ultrafast core-hole-induced dynamics in water probed by x-ray emission spectroscopy," *Phys. Rev. Lett.* **94,** 227401 (2005).

Funding

Swedish Foundation for Strategic Research, Swedish Research Council, Swedish National Supercomputer Center, Center for Parallel Computers (Sweden), and German Federal Ministry of Education and Research.

Electron Spectroscopy of Aqueous Solutions Reveals Surface Enhancement of Halides

Many atmospheric phenomena are driven by reactions with the surface of sea-salt aerosols (tiny droplets of liquid), but the reactions depend on what is at the surface. Scientists have had to rely on theory and indirect observations to explain how charged ions in salt grains rearrange themselves when the salt liquefies after absorbing water vapor from the surrounding air. Conventional spectroscopy experiments have revealed that there are just as many negative ions as positive ions on the surface of a dry salt grain, but what happens when it is wet? Hemminger et al. used a unique photoelectron spectroscopy chamber that can make measurements under pressures and humidities similar to those faced in the everyday world. They found that positively charged potassium ions sink a few atomic layers, while the negatively charged iodine and bromine ions rise to the surface. Their work paves the way for a better understanding of the role played by tiny airborne salt particles, emitted into the air by crashing waves and sea spray, in a slew of atmospheric and environmental processes, including the destruction of the ozone layer.

Reaction chemistry at the interfaces of aqueous solutions plays an important role in atmospheric and environmental chemistry. In particular, reactions between gas-phase pollutant molecules and the surfaces of sea-salt aerosol droplets have been proposed as an important source of reactive halogens in the marine troposphere. Researchers from UC Irvine, Berkeley Lab, the ALS, and the Universidad Nacional de la Plata in Argentina have directly measured the ion concentration at the vapor–liquid interface of potassium halide solutions. These experiments validate the suggestions of the classical molecular dynamics simulations that predict enhanced anion concentrations at the vapor–liquid interface for aqueous solutions of alkali halides.

In aerosols, the concentration of ions at the vapor–liquid interface strongly influences reaction rates between gas-phase molecules and the ions in the aerosol droplet. The conventional view, based on Onsager's theory of ionic solutions, has been that the vapor–liquid interface is devoid of ions, owing to image-charge repulsion. However, recent classical molecular dynamics simulations of sodium halide solutions have predicted that large, polarizable anions, such as Br^- and I^-, segregate to the surface, while the sodium ions remain in the bulk of the solution, essentially forming a dynamic electric double layer at the vapor–liquid interface. In particular, the results of the molecular dynamics simulations suggest that for a KBr or KI solution, the anion–cation stoichiometry at the vapor–liquid

interface deviates from the bulk value of 1 in favor of the anion.

The ambient-pressure photoelectron spectroscopy endstations at ALS Beamlines 11.0.2 and 9.3.2 provide unique experimental capabilities that allowed the group to investigate samples at pressures up to 10 Torr. When a salt sample is exposed to water vapor, at a certain humidity it reaches its deliquescence point where the solid salt, water vapor, and a layer of saturated solution on the salt surface are in equilibrium. For KBr and KI, the deliquescence point is reached at a relative humidity (RH) of 81% and 75%, respectively. In their experiments, the investigators exposed cleaved KBr and KI single crystals to water vapor at a pressure of 1.5 Torr, varying the RH at the surface by changing the sample temperature.

Photoemission spectra for KBr were measured at the same kinetic energy (160 eV), which assures that the effects of scattering of electrons by gas molecules and the experimental probe depth are the same for both postassium 3p and bromine 3d photoelectrons (Figure 3). The bromine/potassium ratio remained constant around an average value of 1 ± 0.1 as the relative humidity increased to just below the deliquescence point (Figure 4). However, at the deliquescence point, when a visible droplet of KBr solution forms at the surface, the bromine/potassium ratio increased to 2.5 ± 0.2. A similar change was also observed in the case of KI, where the potassium/iodine ratio increased from 1 below the deliquescence point to 3.4 at the deliquescence point. These results provide direct experimental evidence that anions are present at

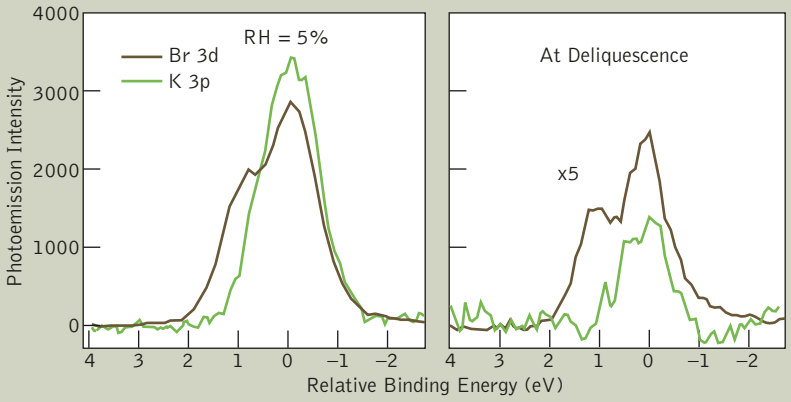

FIGURE 3
The bromine 3d and potassium 3p photoemission spectra for RH 5% and at the deliquescence point. All spectra were taken for a kinetic energy of 160 eV and are normalized for incident photon flux and photoemission cross section, so that the peak areas of the bromine 3d and potassium 3p spectra can be compared directly. The intensity of the spectra at deliquescence is multiplied by a factor of 5. The attenuation of the bromine 3d and potassium 3p signal for the deliquesced sample is due to the adsorption of water at the surface.

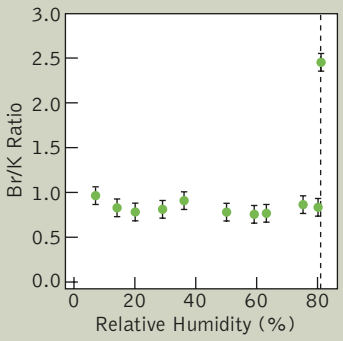

FIGURE 4
Bromine/potassium ratio as a function of RH for a KBr(100) surface. At 5% RH, the ratio shows the expected value of 1.0 ± 0.1 and does not change significantly until the deliquescence point is reached. At deliquescence, the ratio shows a strong increase to a value of 2.5 ± 0.1.

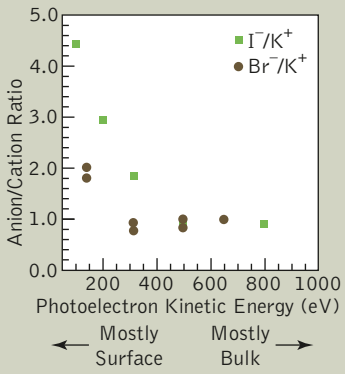

FIGURE 5
Measured anion/cation atomic ratio as a function of the photoelectron kinetic energy. Since the escape depth for photoelectrons varies with the kinetic energy, spectra taken at different photon energies (and hence different kinetic energies) provide a way to obtain depth profiles. The squares are the values of iodine/potassium for KI. The circles are the bromine/potassium ratios for KBr.

the vapor–liquid interface and therefore are likely participants in chemical reactions between gas molecules and aqueous surface ions.

Photoemission spectra taken at different photon energies, which results in different photoelectron kinetic energies, permitted the team to determine concentration depth profiles for deliquesced KBr and KI samples (Figure 5). Both KI and KBr show significant enhancement of the halide ion concentration in the more surface-sensitive experiments (low photoelectron kinetic energy) and the expected anion/cation ratio of 1 ± 0.1 for the experiments at higher photoelectron kinetic energy that probe the bulk of the solution.

In addition to the previously mentioned importance to gas–surface reactions of aerosols in the marine troposphere, enhanced ion concentrations at the surfaces of ionic aqueous solutions are likely to be very important in a variety of other heterogeneous chemistry systems, for example, water transport in environmental systems such as soils and clays and even at interfaces in biological systems.

Investigators

J.C. Hemminger and S. Ghosal (UC Irvine); H. Bluhm, E.L.D. Hebenstreit, G. Ketteler, D.F. Ogletree, and M. Salmeron (Berkeley Lab); B.S. Mun (ALS); and F.G. Requejo (Universidad Nacional de la Plata, Argentina).

Publications

S. Ghosal, J.C. Hemminger, H. Bluhm, B.S. Mun, E.L.D. Hebenstreit, G. Ketteler, D.F. Ogletree, F.G. Requejo, and M. Salmeron, "Electron spectroscopy of aqueous solution interfaces reveals surface enhancement of halides," *Science* **307,** 563 (2005).

Funding

National Science Foundation, Alexander von Humboldt Foundation, Consejo Nacional de Investigaciones Cientificas y Tecnicas (Argentina), and U.S. DOE BES.

Soft X-Ray Spectromicroscopy of Nanoscale Microbe–Mineral Interactions

Microorganisms, omnipresent in our environment, can influence natural processes. For example, the degradation of minerals such as silicates (compounds of metal, silicon, and oxygen) by microorganisms—a process known as bioweathering—contributes to soil formation, plays a key role in the global carbon cycle, and influences the composition of natural waters. Microbes dramatically speed up silicate dissolution, promoting a dynamic cycle of the elements released, including essential nutrients for plant growth as well as elements detrimental to human health. But the mechanisms by which microbes interact with minerals in nature and the resulting weathering products are poorly documented, making uncertain any quantitative estimation of the actual impact of life on rock weathering. Fortunately, the tools necessary for characterizing, at the submicrometer scale, complexes containing organic compounds and minerals and heterogeneous samples like soils have recently become available. Benzerara et al. have combined one of these, soft x-ray spectromicroscopy, with transmission electron microscopy to clarify, at the nanometer scale, various microbially driven geochemical transformations of an iron–magnesium silicate in a meteorite that had fallen in the southern Tunisian desert 70 years ago under arid conditions, so that nonmicrobial processes were minimized.

The degradation of minerals by microorganisms, a process known as bioweathering, plays a key role in environmental processes, including soil formation, the global cycling of carbon, and the release of plant nutrients as well as elements detrimental to human health. Although the capability of microbes to alter minerals has been abundantly demonstrated by experimental studies, a clear picture of what happens in nature at the interface between a microbe and a mineral surface has yet to be drawn at the nanometer scale. A French–Korean–American collaboration working at the ALS focused on a specific natural sample, the Tatahouine meteorite, which offers a particularly pertinent model case. In addition to documenting geochemical reactions catalyzed by a microorganism at the surface of a natural mineral, their work sets a methodological framework, coupling soft x-ray spectromicroscopy and transmission electron microscopy, that might

contribute in the near future to a comprehensive view of interactions between microorganisms and minerals in the environment.

For their study, the collaborators observed the surface of an iron–magnesium (Fe^{2+}–Mg) silicate (orthopyroxene) that was colonized by a microorganism less than 70 years ago. The silicate is a fragment of a meteorite that fell in the southern Tunisian desert, near the village of Tatahouine, in 1931. Some fragments of the meteorite were collected the day after its fall and others were collected in 2000. This meteorite provided a unique opportunity to examine microbially driven processes that occurred during a well-known time frame and under defined conditions at the surface of an initially sterile rock in which bioweathering was far more important than abiotic (nonbiological) weathering.

The researchers used scanning electron microscopy (SEM) to select a particular meteorite fragment collected in 2000 that had been colonized by a terrestrial filamentous microorganism. The microorganism was in contact with the orthopyroxene and bordered by a cluster of $CaCO_3$ crystals with an unusual morphology and crystallography. Transmission electron microscopy (TEM) of an ultrathin (80-nm) cross section through the microorganism, the $CaCO_3$ crystals, and the orthopyroxene, prepared by focused gallium-ion-beam methods, demonstrated the presence of a 100-nm-deep depression in the orthopyroxene adjacent to the microorganism, suggesting an enhanced dissolution mediated by the microbe (Figure 6).

Crucial information was obtained by scanning transmission x-ray microscopy (STXM) observations on the same sample at the Molecular Environmental Science endstation at ALS Beamline 11.0.2. STXM provides both clear chemical state-specific images at a spatial resolution of about 25 nm and high-energy-resolution (about 0.1-eV) near-edge x-ray absorption fine-structure spectroscopy (NEXAFS) at the same spatial scale. This combination allows the chemical characterization of nano-objects.

NEXAFS spectra at the carbon K edge near 300 eV showed that the cluster of $CaCO_3$ crystals adjacent to the microorganism was pervasively associated with polysaccharides that display a specific spectroscopic signature and were likely excreted by the microbe (Figure 7). Those biological polymers are known to

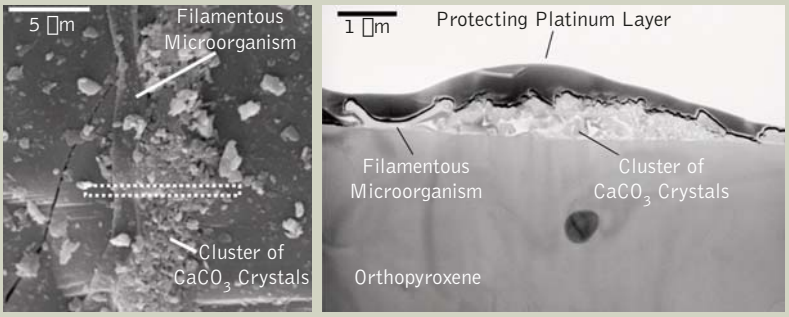

FIGURE 6
Left: SEM observation of a Tatahouine meteorite fragment collected in 2000. The pyroxene (dark background) is colonized by a filamentous microorganism that is bordered by a cluster of nanometer-sized $CaCO_3$ crystals. The dotted rectangle indicates the position from which an ultrathin cross section was extracted by focused ion-beam milling. Right: TEM image of the cross section showing the platinum protective layer deposited for milling, the filamentous microorganism, the cluster of $CaCO_3$ crystals, and the orthopyroxene.

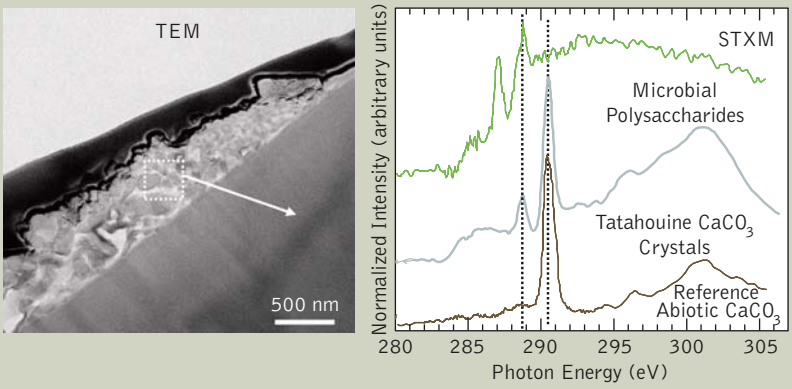

FIGURE 7
Left: TEM image of the cluster of $CaCO_3$ nanocrystals. Right: Carbon K-edge NEXAFS spectra from the calcite cluster outlined in Figure 6, and reference calcite and microbial polysaccharide spectra. Dashed lines at 288.6 and 290.2 eV reflect the mixture of calcite and polysaccharides in the Tatahouine $CaCO_3$ cluster.

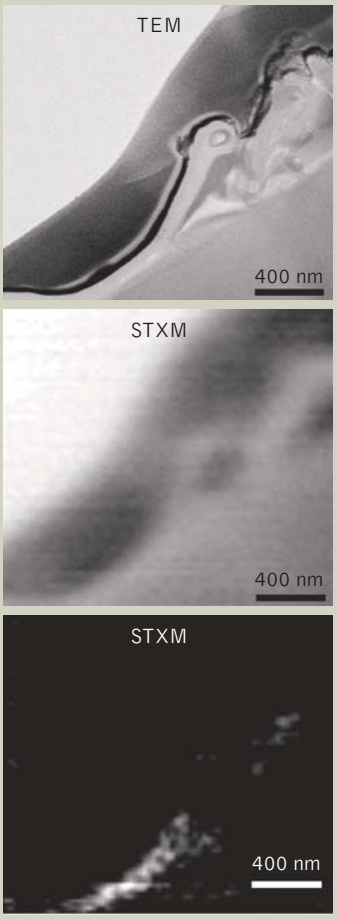

FIGURE 8
Top: TEM image of the microorganism. Center: Corresponding STXM image at 1572 eV. Bottom: Aluminum elemental map obtained from the subtraction of the images of the microorganism taken above and below the aluminum K edge (at 1572 and 1560 eV, respectively), showing high enrichment in aluminum preferentially beneath the microorganism.

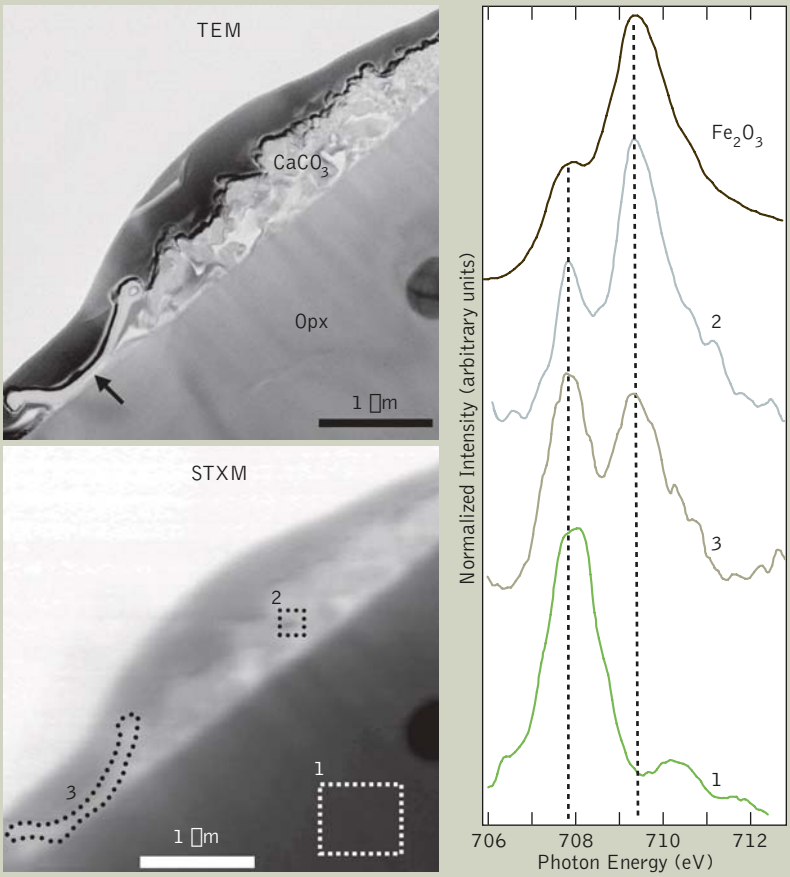

FIGURE 9
Left: TEM image (top) of the cross section showing the microorganism (arrow), the $CaCO_3$ cluster, and the orthopyroxene (Opx) and the equivalent STXM image (bottom) at 707.8 eV. Right: Iron L_3-edge NEXAFS spectra from the orthopyroxene (area 1), the $CaCO_3$ cluster (area 2), the microorganism (area 3), and reference hematite, representing the Fe^{3+} end member. Dashed lines represent the positions of iron L_3 maxima for Fe^{2+} and Fe^{3+} at 707.8 and 709.5 eV, respectively.

affect the nucleation and growth of calcite crystals, and their pervasiveness may explain the very unusual morphology and crystallography of the crystals.

STXM imaging at the aluminum K edge (1560 eV, Figure 8) in the same area showed that aluminum is preferentially concentrated beneath the microorganism, in agreement with TEM observations of an amorphous aluminum-rich silicate layer at the same location. This layer is a weathering product of the orthopyroxene, and its preferential association with the microorganism suggests once more that the latter modifies weathering processes occurring at the surface of the Tatahouine meteorite.

This idea was further supported by observation at the iron L_3 edge, which allowed the determination of the iron oxidation state in the microorganism–calcite–pyroxene microcosm (Figure 9). It showed the development of submicrometer-scale regions surrounding the microorganism with different iron oxidation states, mostly Fe^{2+} in the pyroxene, Fe^{3+} in the calcite cluster, and a mixture of Fe^{2+} and Fe^{3+}

near the microorganism. Whatever mechanisms are involved in changing the iron oxidation, the microorganism heavily influences iron-oxidation dynamics in a microenvironment, possibly through metabolic processes, resulting in a major modification of the pyroxene weathering rate as compared to that in a purely abiotic environment.

Investigators

K. Benzerara and N. Menguy (Institut de Minéralogie et de Physique des Milieux Condensés, France), T.H. Yoon (Hanyang University, Korea), T. Tyliszczak (ALS), and G.E. Brown, Jr. (Stanford University and Stanford Linear Accelerator Center).

Publications

K. Benzerara, T.H. Yoon, N. Menguy, T. Tyliszczak, and G.E. Brown, Jr., "Nanoscale environments associated with bioweathering of a Mg-Fe-pyroxene," *Proc. Natl. Acad. Sci. USA* **102,** 979 (2005).

Funding

National Science Foundation; U.S. DOE, Office of Biological and Environmental Research; Woods Institute for the Environment (Stanford University); and the French Foreign Ministry.

Mechanism of Bacterial Oxidation of Mn(II)

Among its many virtues, the element manganese plays an important role in one stage of the photosynthesis process, it is a trace element vital to our health, and it is essential for the production of steel. It is no surprise then that earth scientists have a keen interest in the global manganese cycle that traces the pathway taken by manganese through the environment. It turns out that several types of bacteria are crucial players in this cycle via their ability to dramatically enhance the rate at which the manganese immobilized in minerals is converted into soluble forms. In the ocean, this process helps to regulate the concentration of dissolved manganese, which is required for the growth of plankton (the foundation on which much of the ocean food web rests), and is responsible for the production of natural manganese oxides that undergo myriad reactions with both nutrients and contaminants in terrestrial and marine environments. Tebo et al. have combined optical and x-ray techniques to identify the specific molecular species in bacteria that drives the oxidation.

Although the biochemical mechanism has never been conclusively demonstrated, an enzyme or enzyme complex involving a multicopper oxidase (MCO) is believed to drive the oxidation of Mn(II) to Mn(IV), an important oxidative segment of the global biogeochemical manganese cycle. Researchers from SSRL and the Scripps Institution of Oceanography have combined in situ trapping chemistry with spatially resolved x-ray spectroscopy (microspectroscopy) to conclude that bacterial oxidation of Mn(II) involves a unique MCO system that produces complex Mn(III) intermediates, a possible source for environmental Mn(III), a strong oxidant.

Bacterial oxidation of Mn(II) to Mn(IV) helps to regulate the concentration of dissolved Mn(II) in the oceanic water column, where it is required for plankton growth, and is responsible for the production of natural manganese oxides, fine-grained materials that undergo myriad reactions with both nutrients and contaminants in terrestrial and marine environments (Figure 10). This process and its products play antagonistic roles in the global biogeochemical cycling of carbon, sulfur, and iron, and are important to natural and engineered contaminant remediation in soils and watersheds. Bacteriogenic manganese oxides also have potential technological applications.

Bacterial oxidation driven by MCO is enigmatic, however, since known MCOs oxidize their substrates by one electron, whereas oxidation of Mn(II) to Mn(IV) requires the transfer of two electrons. Demonstrating the involvement of Mn(III) would be of fundamental importance to this putative reaction mechanism. The Stanford–Scripps team investigated the involvement of Mn(III) complexes during bacterial oxidation of Mn(II) by the exosporium (the exfoliated outer cell coat) of the marine *Bacillus* sp., strain SG-1.

Trapping experiments (one chemical species is used to "trap" another that is otherwise difficult to observe) with the strong Mn(III)-

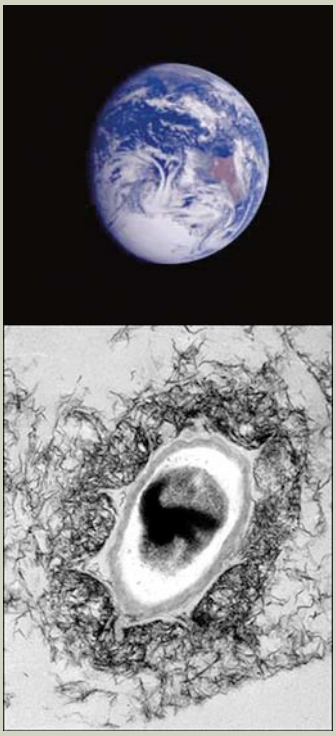

FIGURE 10
Top: Bacterial oxidation of Mn(II) is an important driver of the global biogeochemical manganese cycle, which helps regulate chemical balances in the oceans, as well as in soils and watersheds. Bottom: Fine-grained manganese oxides precipitated around a cell of the bacterium, *Bacillus* sp., strain SG-1. This cell is about 0.5 μm in diameter (small axis).

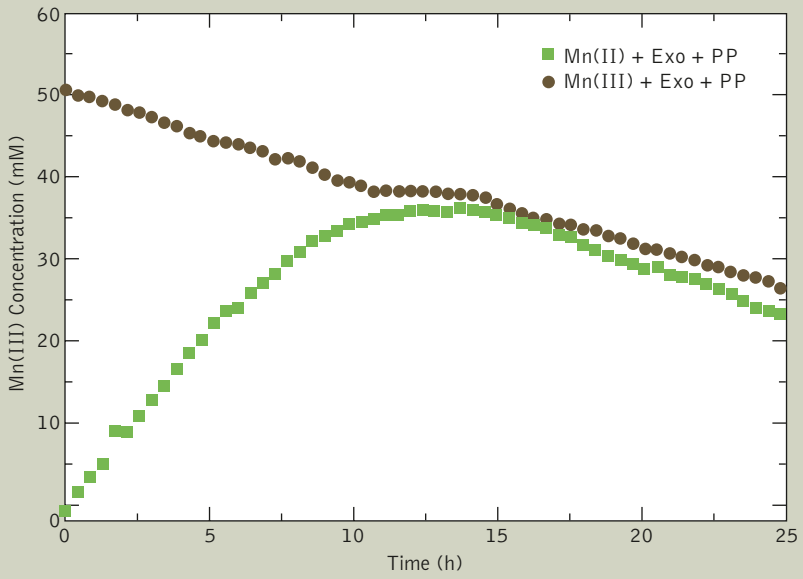

FIGURE 11
Production and decay of Mn(III)–PP complexes during oxidation of Mn(II) by the exosporium of *Bacillus* SG-1 (squares) and degradation of Mn(III) when added to the experiment as Mn(III)–PP (circles).

complexing ligand pyrophosphate (P_2O_7 or PP), monitored with continuous in situ UV–visible spectroscopy, verified the formation of a Mn(III)–PP complex during oxidation of Mn(II) by the exosporium (Figure 11). The Mn(III)–PP complex then began to decay at about 13-15 h. Abiotic controls showed that the decay cannot be attributed to inherent instability of the complex. The decay implied an enzymatically mediated reaction step from Mn(III) to Mn(IV), which acts as a reaction loss term for Mn(III). The presence of enzymatically mediated Mn(II)→(III) and Mn(III)→(IV) steps strongly implies that Mn(III) is a true intermediate.

Manganese K-edge micro-x-ray absorption near-edge spectroscopy (μ-XANES, also known as NEXAFS) measurements were performed at ALS Beamline 10.3.2 to corroborate the existence of Mn(III) complexes during oxidation (Figure 12). To do this, spectra were recorded from numerous small clumps of bacterial cells that contained interstitial water, which may host Mn(III)-siderophore complexes released from the bacteria. A beam spot size of 5 × 5 mm^2 resulted in a nominal probe volume of 200 mm^3. Fluorescence-yield K-edge measurements permitted assignment of a chemical environment even for dilute Mn(II) concentrations.

The spectra were dominated by Mn^{2+}(aq) (source of the prominent absorbance maximum at 6553 eV) and Mn^{4+} in bacteriogenic manganese oxides (absorbance maximum at 6562 eV). Spectra from some cell clumps also exhibited intensity at energies intermediate to these values, suggesting the presence of Mn(III). Fits to the spectra were found to be unsatisfactory unless Mn(III), represented by the Mn(III)–PP spectrum, was included. Further, the method of principal component analysis showed the existence of three significant components. Thus, μ-XANES provides direct observational evidence for the existence of a Mn(III) complex during bacterial Mn(II) oxidation.

The team concluded that oxidation of Mn(II) involves a unique MCO system capable of the overall

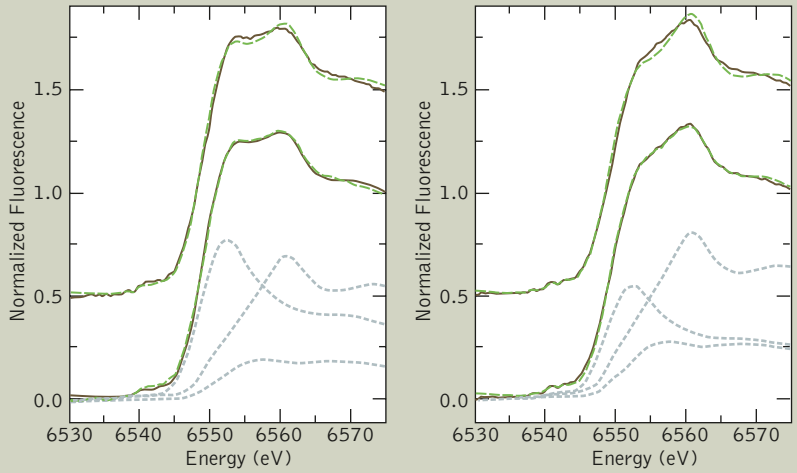

FIGURE 12
Normalized spectra from □-XANES measurements (solid lines) at two different points in the same sample (left and right). Fits to the data (green dashed lines) show that a Mn(III) component is required to match the experimental data: the upper fit includes only Mn^{2+}(aq) and Mn(IV) components (as bacteriogenic manganese oxides), while the lower fit includes Mn^{2+}(aq), Mn(III)–PP, and Mn(IV). The individual components of the latter fits are shown as gray dotted lines below the spectra.

two-electron oxidation of its substrate. That metabolically dormant spores catalyze an important biogeochemical process intimately linked to the carbon, nitrogen, iron, and sulfur cycles requires rethinking the role of spores in the environment.

INVESTIGATORS
S.M. Webb and J.R. Bargar (Stanford Synchrotron Radiation Laboratory), G.J. Dick (Scripps Institution of Oceanography), and B.M. Tebo (Oregon Health and Science University).

PUBLICATIONS
S.M. Webb, G.J. Dick, J.R. Bargar, and B.M. Tebo, "Evidence for the presence of Mn(III) intermediates in the bacterial oxidation of Mn(II)," *Proc. Natl. Acad. Sci. USA* **102,** 5558 (2005).

FUNDING
National Science Foundation.

Highest-Resolution Ribosome Structure

In 1999, the first structure of the intact ribosome—a very large, asymmetric protein that functions as a cellular protein factory found in all forms of life—was solved by x-ray crystallography at the ALS. Since then, scientists have developed quite an extensive photo gallery of ribosomes from various organisms and in various configurations. More importantly, they have sharpened the focus significantly, going from a resolution of 7.8 Å in 1999, to 5.5 Å in 2001, to an amazing 3.5 Å in this latest work by Schuwirth et al. What was initially seen as fuzzy "fingers" of electron density can now be resolved into individual nucleotides in the RNA strands. Serendipitously, the crystals used in this particular study contained two versions of the ribosome, each one in a different "pose," allowing the researchers to compare the positions of the various parts and deduce how they work. With these sharper images, scientists are now better able to interpret previous data, test models, and develop new theories, both practical (how do antibiotics that target the ribosome work?) and theoretical (how much has the ribosome evolved from bacteria to human?). Stay tuned.

The last step in converting the genetic information stored in DNA into the major functional parts of cells is protein biosynthesis. Protein synthesis occurs on the ribosome, a cellular factory found in all forms of life. In contrast to most cellular machines, the ribosome contains a functional core of RNA that is enhanced by ribosomal proteins and accessory factors. Two structures of the intact ribosome from the common bacterium *Escherichia coli*, determined by a UC Berkeley–Berkeley Lab–Berlin collaboration to a resolution of 3.5 Å, the highest yet achieved, provide many new insights into how the ribosome factory works.

The ribosome is a multicomponent machine that, in bacteria, is 21 nm in diameter. Given the large size of the ribosome, it has been difficult to determine how it works at a molecular level. To provide a complete picture of the protein synthesis cycle, many groups have been striving to make an atomic-resolution "movie" of the intact ribosome synthesizing a protein. The collaborators determined the first "frames" of this movie by solving the atomic-resolution structures of two intact ribosomes from the model organism, *Escherichia coli*. To determine the ribosome structures, they used x-ray crystallography at ALS Beamlines 8.3.1 and 12.3.1. The researchers' close proximity to the ALS was critical for optimizing x-ray diffraction from the fragile ribosomes that they had crystallized.

The ribosome crystals happened to contain a repeating unit of two ribosomes, which turned out to be an unexpected boon. Each of the two ribosomes adopted a different conformation, providing clues as to how the ribosome moves along messenger RNA (mRNA), the genetic template for protein synthesis. Comparison of the two ribosome structures revealed movement of the "head" of the small ribosomal subunit that the researchers think helps to complete one step along the mRNA, a process called "translocation" (Figure 1). Using models and lower-resolution structures of the ribosome, the group

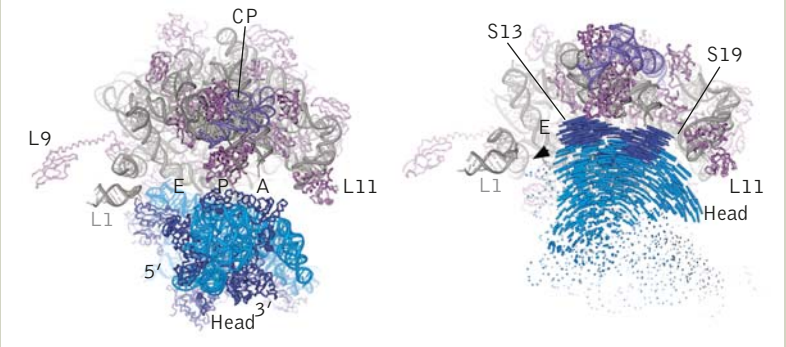

FIGURE 1
Swiveling of the head of the small ribosomal subunit within the intact ribosome. Left: View of the intact ribosome showing the small subunit (dark and light blue) and large subunit (grey and magenta). Right: Swiveling of the head of the small ribosomal subunit (blue difference vectors) determined from the two ribosome structures.

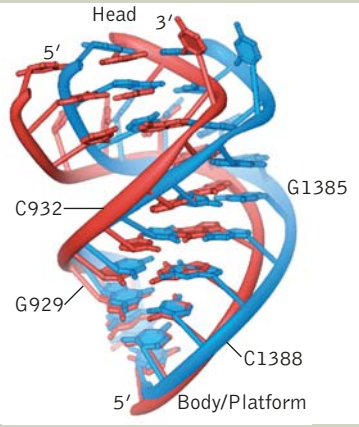

FIGURE 2
Twisting of the neck helix within the small subunit allows swiveling of the head domain. One ribosome is colored red, while the other is blue.

proposed a sequence of steps in translocation that finishes with the swiveling of the small subunit head to allow the mRNA and the transfer RNAs to move by one step. Swiveling of the head may be driven by a protein enzyme called elongation factor G, which burns one guanosine triphosphate (GTP) molecule to catalyze the stepping along the mRNA.

A second intriguing finding from comparison of the two structures is the mode of long-range movements within the ribosome. The researchers were able to identify three long-range motions of 15 Å or more that are concentrated in standard RNA helices within the ribosomal RNA. The researchers think that these may be molecular versions of torsion springs that absorb the strains induced by the rotation of the head domain (Figure 2). The fact that similar neck-helix dynamics have also been identified by biochemical means in human ribosomes suggests that the role of these helices is conserved in all forms of life.

Finally, the researchers found that the interface between the two ribosomal subunits, the 30S and 50S subunits in bacteria, to a large extent consists of salt water. The number of direct interactions between the two subunits, which are primarily RNA, was much lower than expected. This may explain why ribosome function is incredibly sensitive to the salts in the solution around it.

Many commonly used antibiotics target the function of the intact ribosome. Now that intact ribosome crystals that diffract x rays to high resolution have been obtained, the researchers are now working to probe the structural basis for how these antibiotics work. In particular, they are probing how different classes of antibiotic affect three steps of translation. One class of antibiotic blocks translation initiation, whereas a second class degrades accurate mRNA decoding or slows translocation. Yet a third specifically targets translocation by a different mechanism. This future work may potentially open new avenues for antibiotic design.

INVESTIGATORS
B.S. Schuwirth (UC Berkeley and Free University of Berlin, Germany); M.A. Borovinskaya, A. Vila-Sanjurjo, and J.M. Holton (Berkeley Lab); C.W. Hau and Wen Zhang (UC Berkeley); and J.H. Doudna Cate (UC Berkeley and Berkeley Lab).

PUBLICATIONS
B.S. Schuwirth, M.A. Borovinskaya, C.W. Hau, W. Zhang, A. Vila-Sanjurjo, J.M. Holton, and J.H. Doudna Cate, "Structures of the bacterial ribosome at 3.5 Å resolution," *Science* **310,** 827 (2005).

FUNDING
National Institutes of Health and U.S. DOE BES.

Structural Basis for Activation of Cholera Toxin

There have been seven cholera pandemics since we began keeping track in the early 1800s. The ongoing seventh pandemic originated in Indonesia in 1961 and spread rapidly through Asia, Europe, and Africa; it finally reached the New World in 1991, causing over 4000 deaths in 16 Latin American countries that year. A possible eighth pandemic may be incubating in Bangladesh, where a new strain of the bacterium *V. cholerae* was identified in 1992. In the 19th century, the first epidemiologists realized that cholera outbreaks could be traced to a single source of contaminated water. From this simple insight flowed many advances in medicine and improvements in public health. In the 21st century, the world is more aware than ever of the need for similar epiphanies about the molecular mechanisms employed by persistent, resistant scourges like cholera, which can occur even in well-developed areas after natural disaster. With their structures of a key subunit of the cholera toxin bound to a human "activator" molecule, O'Neal et al. have provided both a structural basis for the activation and a starting point for drug development.

Cholera begins when the bacterium *Vibrio cholerae* in the human small intestine secretes cholera toxin, a protein whose A1 subunit (CTA1) triggers a series of events culminating in the massive efflux of electrolytes and water into the intestinal cavity, causing the watery diarrhea characteristic of cholera that can lead to severe dehydration and death. Crystal structures of the CTA1 subunit in complex with its activator molecule (ARF6) obtained by team from the Howard Hughes Medical Institute, the University of Washington, and the University of Colorado Health Sciences Center have revealed that binding of the ARF6 "switch" elicits dramatic changes in CTA1 loop regions, exposing the toxin's active site. The extensive CTA1–ARF6 interface mimics recognition of ARF6's normal cellular protein partners, which suggests that the toxin has evolved to exploit the molecular switch's promiscuous binding properties.

Cholera is a serious disease that claims thousands of victims each year in third-world, war-torn, and disaster-stricken nations. *Vibrio cholerae* is the culprit. It can be ingested through contaminated food or water and then colonizes the mucous membrane of the human small intestine. After a molecule of cholera toxin binds to an epithelial (lining) cell of the human small intestine, CTA1 can enter the cell via several organellar trafficking systems. Once inside, CTA1 interacts with a protein known as adenosine diphosphate (ADP)–ribosylation factor 6 (ARF6), which enhances the activity of the toxin. Almost thirty years ago, ARFs were originally discovered and defined as activators of CTA1. They have since been revealed to also play essential roles in the trafficking of vesicles within cells during normal physiological conditions. While this multispecific binding strategy gives ARF proteins broad flexibility, it also leaves them vulnerable to interaction with unintended partners.

Several crystal structures of both cholera toxin and ARFs have been published; however, it is not clear how these two proteins interact, and more interestingly, how ARF interaction enhances the cholera toxin's activity. To investigate, the researchers turned to ALS Beamline 8.2.2 to determine the 1.8-Å-resolution crystal structure of a CTA1 variant bound to a complex of human ARF6 and guanosine triphosphate (GTP), a mediator of the interaction (Figure 3).

CTA1 makes two large conformational changes when interacting with ARF6-GTP, both in loop regions indicated by previous structures to be flexible (Figure 4). The CTA1 activation loop changes from a structured loop to an amphipathic (polar) helix to make direct contacts to ARF6-GTP. Most strikingly, the active-site loop, which normally occludes the active site and prevents the binding of substrate (target) molecules, swings out of the active site when CTA1 is bound to ARF6-GTP, exposing areas along the active-site cleft implicated in substrate binding.

The active-site loop does not directly contact ARF6-GTP; instead, the presence of the activator is communicated from a distance by several contacts with the activation loop in its altered conformation. The structure thus

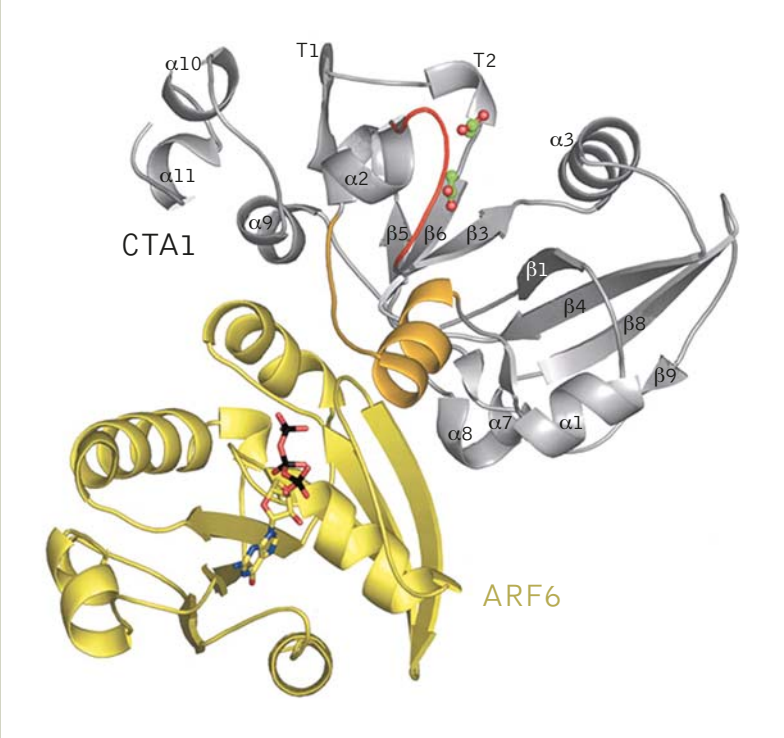

FIGURE 3
The complex between bacterial CTA1 (gray) and human ARF6 (yellow). Important loop regions are delineated in gold (activation loop) and red (active-site loop).

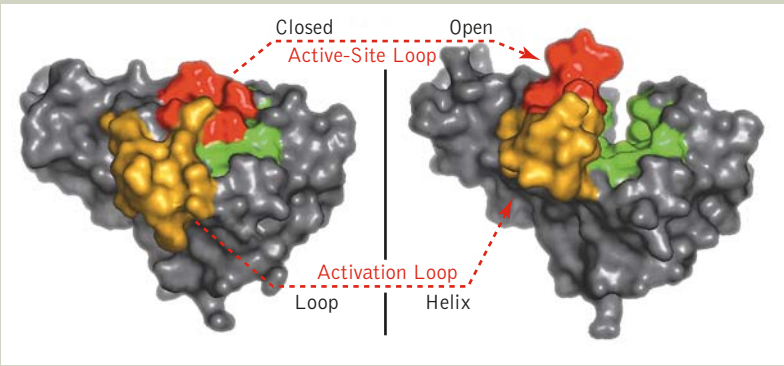

FIGURE 4
CTA1 before (left) and after (right) binding to ARF6-GTP (not shown). ARF6-GTP binding causes conformational changes in the activation loop (gold) and the active-site loop (red), leading to exposure of the active site (green).

implies that ARF6 acts as an allosteric activator of CTA1; that is, it forces the active site open by binding at a site other than the enzymatically active one. This conclusion was confirmed by soaking CTA1:ARF6-GTP crystals with nicotinamide adenine dinucleotide (NAD^+), the substance that binds to the active site. The resultant structure was solved at APS Beamline 19-ID and provides the first glimpse of substrate binding by CTA1.

Further, the open active-site loop conformation creates a knob on the surface of CTA1 near a motif (the "ADP-ribosylating turn-turn" motif) known in functionally related toxins to be involved in binding to the human protein targeted by the toxin (Figure 5). This suggests that, in addition to activation, interaction with ARF6 also generates a surface on CTA1 enabling the toxin to recognize its human protein target. Together,

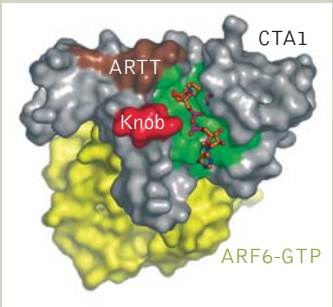

FIGURE 5
The CTA1 active site (green) occupied by NAD^+ (sticks), viewed from above. ARF6-GTP (yellow) binds to CTA1 (gray) far from the active site. The knob formed by the active-site loop (red) when CTA1 is ARF6-bound and the ADP-ribosylating turn-turn (ARTT) motif (brown) form a surface for potential recruitment of the toxin's target protein.

these results elegantly solve the long-standing question of how the human ARF6 protein activates CTA1, while the substrate-bound structure also provides a starting point for structure-based drug design specifically aimed at cholera.

Investigators
C.J. O'Neal (University of Washington), M.G. Jobling and R.K. Holmes (University of Colorado Health Sciences Center), and W.G.J. Hol (Howard Hughes Medical Institute and University of Washington).

Publications
C.J. O'Neal, M.G. Jobling, R.K. Holmes, and W.G.J. Hol, "Structural basis for the activation of cholera toxin by human ARF6-GTP," *Science* **309,** 1093 (2005).

Funding
National Institutes of Health and Howard Hughes Medical Institute.

Crystal Structure of a Protein Kinase A Complex

In mammalian cells, specialized proteins called enzymes drive most of the action by modifying other proteins in a way that changes how they function. Among these ubiquitous enzymes, protein kinase A (PKA) regulates a huge number of processes, including growth, development, memory, metabolism, and gene expression (conversion of the information in DNA into proteins ready to go to work). Failure to keep PKA under control can have disastrous consequences, including diseases such as cancer. The task of riding herd on PKA falls to cyclic adenosine monophosphate (cAMP), a messenger molecule involved in transmitting signals within the cell. Drugs based on inhibiting PKA activity are under development for treating disease, so understanding how cAMP accomplishes this task is of some interest to life scientists. Kim et al. have made a major contribution by determining the structure of PKA in its inactive state. Their structure and its comparison to the structure of cAMP locked in embrace with a key portion of PKA, the regulatory subunit, provides both a molecular mechanism for inhibition of PKA and suggests how cAMP binding leads to activation.

PKA is an enzyme that regulates processes as diverse as growth, memory, and metabolism. In its unactivated state, PKA exists as a tetrameric complex of two catalytic subunits and a regulatory subunit dimer, but when the intracellular signaling molecule cAMP binds to the regulatory subunit, it facilitates dissociation and activation of the catalytic subunits. While separate structures of these subunits were previously known, a group from UC San Diego is the first to determine (to a resolution of 2.0 Å) the structure of the PKA catalytic subunits bound to the regulatory subunit. The structure of the complex clarifies the mechanism for PKA inhibition, and by comparing it to the structure of cAMP bound to the regulatory subunit, the researchers discover hints as to how cAMP binding drives its activation.

The PKA family of enzymes is ubiquitous in mammalian cells (it constitutes approximately 2% of the human genome) and is a prototype for the entire kinase superfamily. Poorly regulated kinase activity can cause many diseases, including cancer. To probe the molecular mechanism of PKA regulation, the group crystallized a complex between the catalytic (C) subunits and the regulatory (R) subunit of PKA. For this purpose, they used a deletion mutant, RIα, that contains key portions of the R subunit. The complex was stabilized against dissociation by crystallizing it in the presence of AMP-PNP, a nonhydrolyzable analog of ATP, and excess Mn^{2+}.

From previous work, it was known that the C subunit consists of a small and large lobe with the active site forming a cleft between the two lobes. The small lobe provides the binding site for adenosine triphosphate (ATP), while the large lobe provides catalytic residues and a docking surface for peptide/protein substrates. In the modular R subunit, two tandem cAMP-binding domains (CBD-A and CBD-B) at the C-terminus are

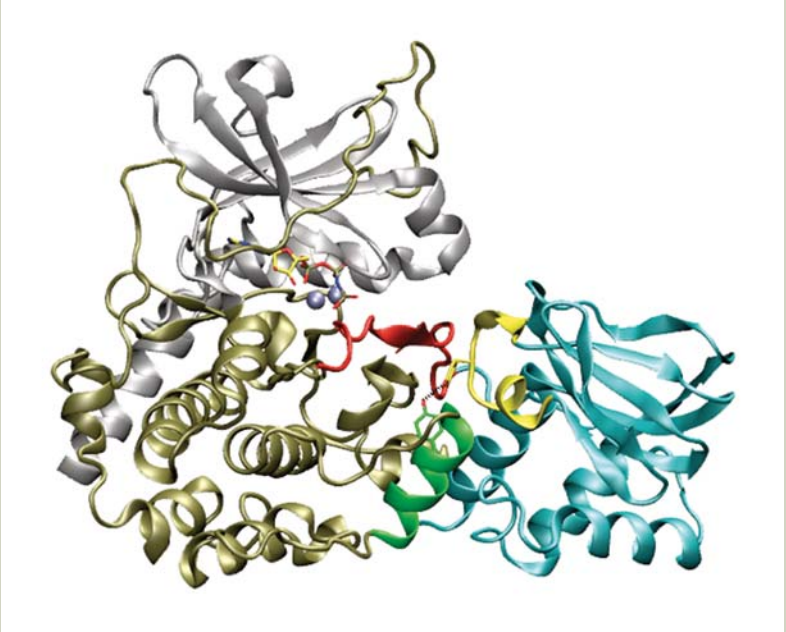

FIGURE 6
Structure of a PKA complex consisting of a catalytically active C subunit (two lobes in gray and tan) and a regulatory R subunit (cyan). The focal point of the complex interface is the hydrogen bond formed between two highly conserved tyrosine residues, one at the G helix (in green) of the C subunit and the other at the phosphate binding cassette (PBC, in yellow) of the R subunit. In the complex, the inhibitor/linker region (red) of the R subunit blocks the active site of the C subunit between the two lobes.

joined to an N-terminal dimerization domain by a flexible linker that includes a substrate-like inhibitor sequence. The inhibitor docks to the active-site cleft of the C subunit in the absence of cAMP. In the presence of cAMP, a phosphate binding cassette (PBC) anchors the cAMP and shields it from solvent.

The architecture of the RIα:C complex reveals an extended interface that covers nearly 3000 Å^2 (Figure 6). Although the C subunit assumes a fully closed conformation with Mn^{2+}AMP-PNP bound at the active site cleft, it does not undergo other major conformational changes as a result of complex formation. The binding surface extends from the inhibitor binding site at the active site-cleft (site 1), across the G helix (site 2) and through to the activation loop (site 3).

In contrast to the C subunit, RIα undergoes major conformational changes upon complex formation (Figure 7). Three general features describe the binding: the inhibitor sequence docks to the active-site cleft; the linker segment that connects the inhibitor peptide to CBD-A becomes ordered; and the helical subdomain within CBD-A docks onto the large lobe of the C subunit. The inhibitor peptide and linker region are disordered in the crystal structure of cAMP-bound RIα, whereas in the complex, this segment binds as an extended chain along the surface of the active-site cleft and closely interacts with the PBC, another important binding site to the C subunit.

The structure of the complex shows that the essence of PKA regulation is in the dynamic nature of its R subunit, which is very flexible and exhibits two distinct structures (noninhibiting and inhibiting) depending on whether it binds cAMP or the C subunit. Comparison of this structure with structures of RIα in its cAMP-bound conformation (Figure 8) provided insight into the structural basis for cAMP-

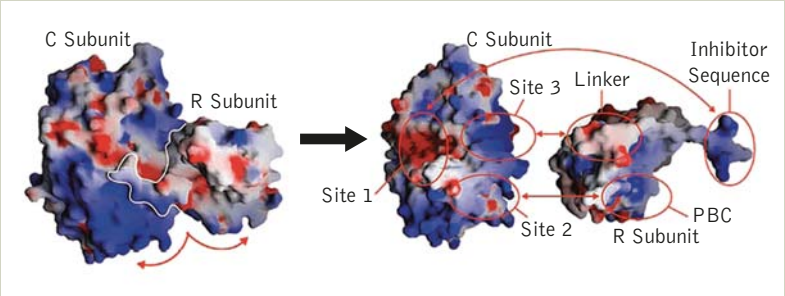

FIGURE 7
Electrostatic surface potential of the entire complex (left) and with its interface opened up to view the surfaces of individual subunits (right). The linker segment complements site 3, the PBC complements site 2, and the inhibitor site complements site 1 of the C subunit.

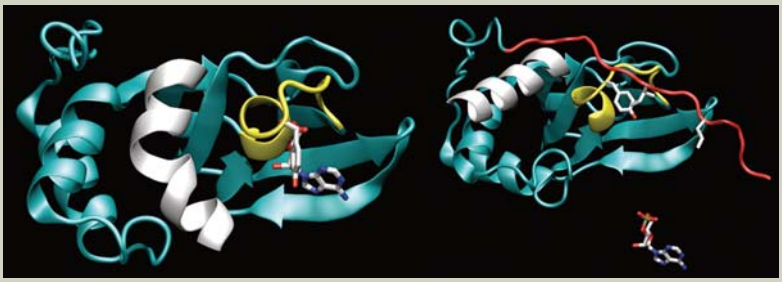

FIGURE 8
Transition of the R subunit from the cAMP-bound (left) to the C-bound (right) conformation. Relative to the cAMP-bound form with the cAMP (ball and stick) anchored by the PBC (yellow), binding of the C subunit accompanies three major changes in the R subunit: (1) the disordered inhibitor peptide and linker region (red) docks to the active-site cleft of the C subunit and becomes ordered; (2) helices rearrange into an extended conformation; and (3) the PBC stretches out, and a tyrosine residue at the center binds tightly to another tyrosine of the C subunit. Competition between cAMP and the C subunit for the PBC lies at the heart of cAMP-dependent regulation of PKA.

induced activation of PKA. The researchers believe that cAMP causes the dissociation of the complex by binding to the PBC, and in winning the binding competition drives away the C subunit from the PBC.

INVESTIGATORS
C. Kim, N.H. Xuong, and S.S. Taylor (UC San Diego).

PUBLICATIONS
C. Kim, N.H. Xuong, and S.S. Taylor, "Crystal structure of a complex between catalytic and regulatory (RIα) subunits of PKA," *Science* **307,** 690 (2005).

FUNDING
National Institutes of Health.

Assembly of a Molecular Needle, From the Bottom Up

Type III secretion systems in bacteria mainline toxins directly into a host cell. Thus, detailed knowledge of the mechanisms involved would definitely tip the balance of power toward us humans in our constant battles with the microorganisms that colonize our bodies. More generally, this "nanoneedle" may be of interest as a possible tool for introducing engineered proteins into almost any type of cultured cell. Such applications would require answers to basic questions such as what triggers injection and how proteins are unfolded before passing through the needle. From an evolutionary standpoint, type III secretion systems provide a fascinating case study. They are found in a broad range of bacteria that are both harmful and beneficial and that affect both plant and animal kingdoms. Genetic sequencing studies seem to indicate that type III secretion systems come from a common ancestor foreign to the bacteria. Crystallographic studies such as the one by Yip et al. contribute key pieces of the puzzle, providing new insights into the assembly of the structure's basic building blocks during the earliest stages of the needle's formation.

Many pathogenic bacteria use a specialized secretion system to inject virulence proteins directly into the cells they infect. The injected proteins, by mimicking host-cell mechanisms, can then subvert normal cellular function. The type III secretion system (TTSS) is a sophisticated protein complex with an overall shape similar to a hypodermic needle. More than twenty unique types of proteins are required for its assembly, most of which are found among a wide variety of animal as well as plant pathogens. Electron microscopy has sketched the broad outlines of TTSS structure, but it does not have sufficient resolution to reveal the details required to understand, and eventually inhibit, the needle's function. At the ALS, researchers from Canada and the U.S. performed crystallo-

graphic studies of EscJ, the protein that makes up the needle's ring-shaped base. Their analysis of the EscJ ring not only presents a snapshot of one of the earliest structures generated in the TTSS assembly process, but also reveals features indicative of its role as the molecular platform for subsequent construction of the secretion apparatus.

The TTSS needle complex is found in gram-negative bacteria (e.g. *Yersinia*, *Shigella*, *Salmonella*, *Pseudomonas*, and *E. coli*), which are all characterized by a double-membrane cell wall. The needle complex spans the two membranes, with the rigid needle protruding outside the cell (Figure 9). The complex has a base of two rings: a larger one anchored to the inner membrane and a smaller one embedded in the outer membrane. While recent electron microscopy images have revealed the gross morphology of the TTSS, a more detailed analysis of the structural characteristics and organization of these protein components within the bacterial membranes is necessary to understand how protein transfer is mediated and regulated.

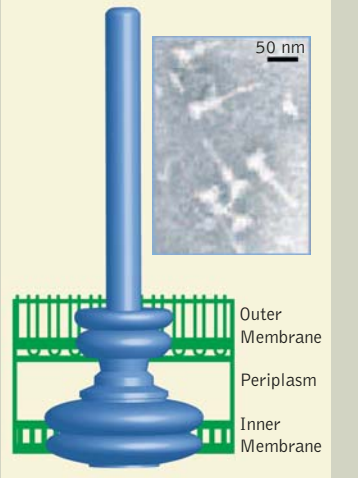

FIGURE 9
Diagram of bacterial TTSS. Inset: Electron micrograph of the needle complex.

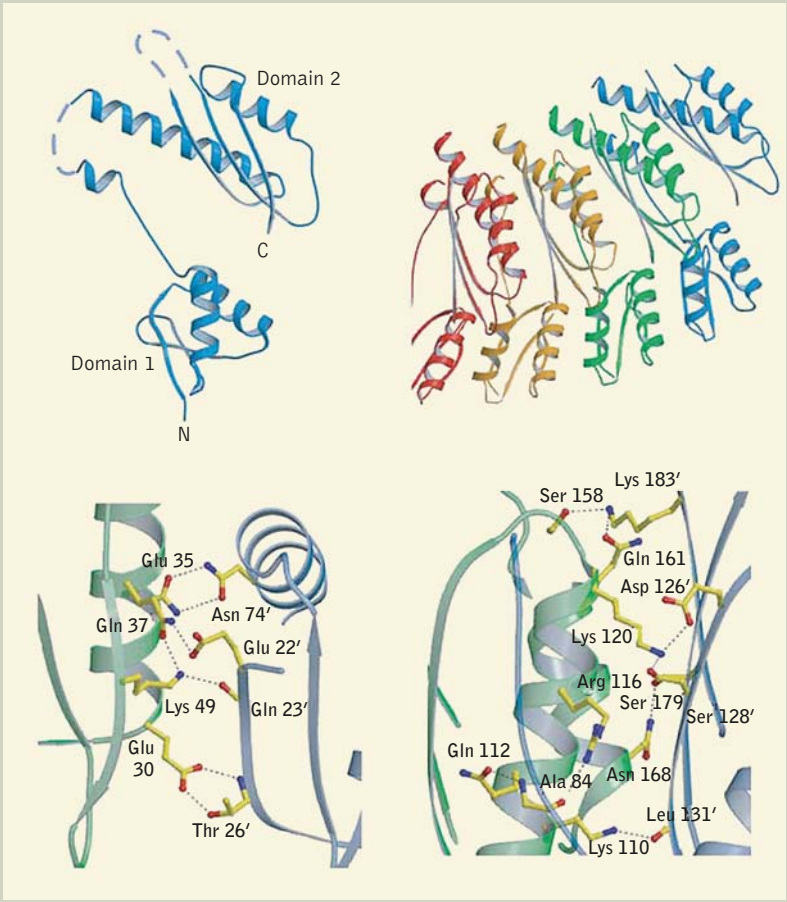

FIGURE 10
Top left: Ribbon representation of the EscJ monomer, showing two domains. Top right: Arc-shaped EscJ tetramer. Bottom left: Interface between domain 1 of two EscJ monomers, colored green and blue. The residues involved in hydrogen-bonding interactions are highlighted with dotted lines. Bottom right: Interface between domain 2 of two EscJ monomers. Residues from two α helices of the green monomer interact with residues from the β sheet of the blue monomer.

To improve the current view of the molecular architecture of the needle complex, the researchers completed the first crystallographic analysis of a basic structural component of the TTSS, that of the protein EscJ from pathogenic *E. coli*, solved to a resolution of 1.8 Å at ALS Beamline 8.2.1 (Figure 10). EscJ belongs to the YscJ/PrgK protein family, members of which are commonly found across many different species of bacteria possessing TTSSs. Most importantly, the self-association ("multimerization") of proteins in this family has been shown to be one of the earliest events in the assembly of the TTSS. The crystal structure of EscJ reveals,

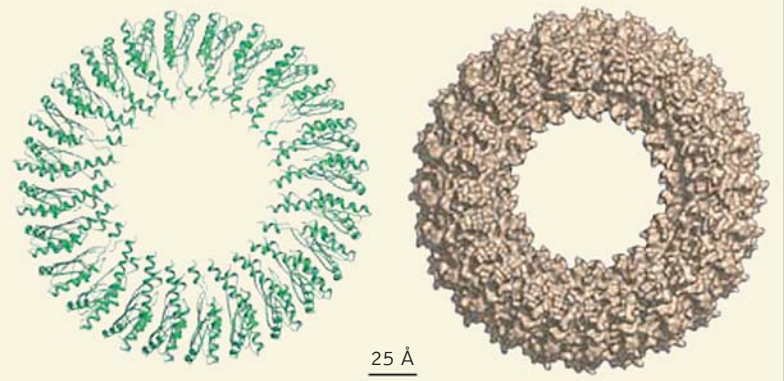

FIGURE 11
Ribbon and surface representation of the modeled 24-subunit EscJ ring.

in atomic detail, how this interaction can occur.

The unique manner in which EscJ molecules pack when in crystalline form strongly suggests the formation of higher-ordered multimers. In addition, the YscJ/PrgK proteins share similarities in their amino-acid sequences with proteins known, based on earlier electron microscopy studies, to form a ring. Using the interaction and symmetry information within the crystal, the researchers were able to construct a ring model containing 24 EscJ molecules and demonstrating several features—including distinctive surface grooves and charged patches—indicative of a role as a docking platform (Figure 11). The researchers believe that the bacterium likely produces such a structure as a platform for assembly of the rest of the needle complex. Several pieces of data have provided validation for this model. The dimensions of the modeled ring (~180 Å in diameter and ~52 Å thick) match those previously estimated by electron microscopy studies. In addition, the number of subunits (24) agrees with results from an extensive labeling and mass spectrometry analysis performed on isolated needle complexes.

This structural analysis of EscJ provides an exciting starting point in the quest to further understand the structure and function of the TTSS. Knowledge of this protein-transfer mechanism will eventually enable the design of novel inhibitors that can combat a broad range of diseases in which the TTSS plays a central role.

INVESTIGATORS
C.K. Yip, M. Vuckovic, N.A. Thomas, R.A. Pfuetzner, E.A. Frey, B.B. Finlay, and N.C.J. Strynadka (University of British Columbia, Canada) and T.G. Kimbrough, H.B. Felise, and S.I. Miller (University of Washington).

PUBLICATIONS
C.K. Yip, T.G. Kimbrough, H.B. Felise, M. Vuckovic, N.A. Thomas, R.A. Pfuetzner, E.A. Frey, B.B. Finlay, S.I. Miller, and N.C.J. Strynadka, "Structural characterization of the molecular platform for type III secretion system assembly," *Nature* **435,** 702 (2005).

FUNDING
Natural Sciences and Engineering Research Council of Canada, Michael Smith Foundation for Health Research, Howard Hughes Medical Institute International Scholar Program, Canadian Institutes of Health Research, Canadian Bacterial Diseases Network, and National Institutes of Health.

Assembly of Activated $G\alpha_q$ and $G\beta\gamma$ Subunits into High-Order Membrane Complexes

G proteins are molecular switches that both initiate and inhibit a vast array of biochemical reactions in cells. The switches are turned on by G-protein-coupled receptors (GPCRs) located in the cell membrane that sense external chemical signals like hormones or neurotransmitters or detect light. The switches are turned off by other proteins known as G-protein-coupled receptor kinases (GRKs). Understanding the molecular basis for signal passage from activated receptors through G proteins and then to downstream targets has been aided by protein crystallography, which yields atomic structures of the respective players, either alone or in concert. Previous atomic models provided the first and last frames, respectively, of a molecular movie that describes the course of the signaling, but the events between the first and last frames of this movie have remained foggy. By solving the structure of a complex formed by subunits of a G protein and GRK2, Tesmer et al. have revealed the configuration of the subunits as they engage a single protein target, thereby providing another snapshot of the events that unfold after G-protein activation by a GPCR.

Many physiological processes initiated in response to external (extracellular) signals such as hormones, neurotransmitters, or light are regulated by a complex dance involving GTP-binding (G) proteins: GPCRs, proteins integral to the cell membrane, sense the signal and activate G proteins in the cellular cytoplasm, but enzymes such as GRK2 keep the G proteins under control. A joint University of Michigan–University of Illinois, Chicago, team has determined the first structure of a particular G-protein–GRK2 complex. The structure, in combination with previous structures of related G-protein complexes, shows how Nature has evolved the G-protein structure to not only propagate activation signals but at the same time directly respond to regulatory proteins that control the duration of the signal.

The G proteins are heterotrimers consisting of three subunits (α, β, and γ). GPCRs activated by the extracellular signal catalyze nucleotide exchange on G proteins, thereby converting the inactive (GDP-bound) $G\alpha\beta\gamma$ heterotrimer into activated $G\alpha\cdot GTP$ and $G\beta\gamma$ subunits. These subunits then interact with downstream proteins called effectors to elicit an appropriate intracellular response. For example, activation of receptors coupled to G_q leads to formation of $G\alpha_q\cdot GTP$ and $G\beta\gamma$, which in turn bind to and stimulate phospholipase Cβ (PLCβ). G_q represents one of the four subfamilies of the Gα subunit ($G\alpha_s$, $G\alpha_t$, $G\alpha_q$, and $G\alpha_{12/13}$).

In order to adapt to new extracellular conditions, G_q-coupled receptors are desensitized by enzymes such as GRK2, which not only add phosphate groups to (phosphorylate) activated GPCRs, initiating their down-regulation, but also sequester activated $G\alpha_q$ and $G\beta\gamma$ subunits from PLCβ. In order to better understand the arrangement of heterotrimeric G proteins in complex with GRK2, the Michigan–Illinois team crystallized the $G\alpha_q$–GRK2–$G\beta\gamma$ complex. After visiting three different beamlines, the team obtained the best diffraction data at ALS Beamline 8.3.1, which allowed them to solve the structure at a resolution of 3.1 Å by the molecular-replacement method.

The $G\alpha_q$–GRK2–$G\beta\gamma$ structure is the first structure obtained to date of $G\alpha_q$; it also reveals for the first time the configuration of activated Gα and $G\beta\gamma$ subunits at the cell membrane. In the $G\alpha_q$–GRK2–$G\beta\gamma$ complex, activated $G\alpha_q$ is completely dissociated from $G\beta\gamma$ and undergoes a dramatic, approximately 105° rotation with respect to its position in the $G\alpha\beta\gamma$ heterotrimer (Figure 12). Because GPCRs also interact with GRK2, the $G\alpha_q$–GRK2–$G\beta\gamma$ structure supports the hypothesis that high-order complexes consisting of receptors, G proteins, and effectors assemble at the cell membrane in response to extracellular stimuli, in this case with GRK2 serving as the scaffold.

GRK2 interacts with $G\alpha_q$ through its regulator of G-protein-signaling (RGS) homology domain. Many other proteins with RGS homology domains function as GTPase-activating proteins (GAPs) for Gα subunits, terminating signal transduction by converting GTP back to GDP. However, the RGS homology domain of GRK2 interacts with $G\alpha_q$ in a manner that is inconsistent with that of a GAP. Instead, the

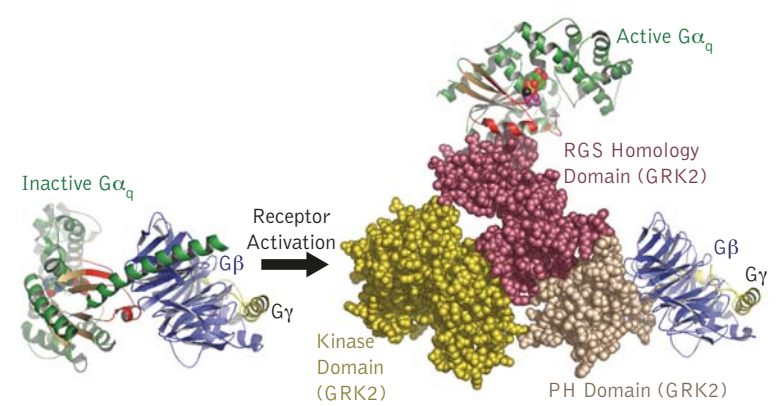

FIGURE 12
Heterotrimeric G proteins (ribbon structures) undergo a dramatic change in configuration as they become activated and bind GRK2 (solid spheres). The view is from the perspective of the membrane surface. The $G\alpha_q$ and $G\beta\gamma$ subunits separate by about 80 Å and the $G\alpha$ subunit rotates more than 100° with respect to $G\beta\gamma$ after GRK2 binding. The so-called "switch" regions of $G\alpha_q$ that undergo conformational change upon binding GTP are shown in red.

GRK2 RGS homology domain binds to an analogous site on $G\alpha_q$ used by the enzymes adenylyl cyclase or cGMP phosphodiesterase to bind $G\alpha_s$ or $G\alpha_t$, respectively. This binding site could mean that GRK2, like PLCβ, is in fact a downstream effector target of $G\alpha_q$. In support of this hypothesis, GRK2 does not appear to impede the binding of RGS4 to $G\alpha_q$. Therefore, RGS proteins such as RGS4 can also participate in the high-order membrane complexes assembled by GRK2.

With the $G\alpha_q$–GRK2–$G\beta\gamma$ structure, each of the $G\alpha$ subunit families has been structurally characterized. Moreover, structures of effector complexes involving each of these subfamilies have been determined. Comparison of these complexes reveals remarkable similarities in how structurally unrelated effectors bind to $G\alpha$ subunits. Remarkably, each of these effector complexes leaves room for the simultaneous binding of a GAP (such as RGS4). This feature explains how $G\alpha$ subunits can propagate signals, while simultaneously directly responding to regulatory proteins that control the duration of the signal.

INVESTIGATORS
V.M. Tesmer, A. Shankaranarayanan, and J.J.G. Tesmer (University of Michigan, Ann Arbor) and T. Kawano and T. Kozasa (University of Illinois, Chicago).

PUBLICATIONS
V.M. Tesmer, T. Kawano, A. Shankaranarayanan, T. Kozasa, and J.J.G. Tesmer, "Snapshot of activated G proteins at the membrane: The $G\alpha_q$–GRK2–$G\beta\gamma$ complex," *Science* **310,** 1686 (2005).

FUNDING
American Heart Association, National Institutes of Health, and American Cancer Society.

Structure of the Kinase Domain of CaMKII and SAXS Analysis of the Holoenzyme

The membranes that separate the inside from the outside of the cells that make up our bodies are neither mechanically rigid nor chemically impenetrable. Nonetheless, they provide an important gate-keeping function by admitting those chemicals that regulate the activity of cellular constituents, such as enzymes that facilitate chemical reactions in the cell. Calcium ions, for example, influence many cellular processes, including fertilization when a sperm fuses with an ovum, the rhythm of the beating heart, and the formation of memories. It turns out that the positively charged calcium enters the cell in waves (oscillating currents), and it is the frequency and the intensity of these waves that are the controlling features. By means of protein crystallography, Rosenberg et al. have obtained atomic-resolution structures of a key portion of the enzyme central to the process. Combining their structure with lower-resolution structural data of the complete enzyme obtained from a technique called small-angle x-ray scattering (SAXS) gave the group a structure-based model for how the cell senses the calcium oscillations and converts them into cellular signals.

The rate and intensity of calcium (Ca^{2+}) currents that oscillate through the plasma membrane around a cell affect such diverse phenomena as fertilization, the cardiac rhythm, and even the formation of memories. How does the cell sense these digital oscillations and transduce them into a cellular signal, such as changes in phosphorylation (addition of a phosphate group to a protein) or gene transcription? A group from UC Berkeley, the Yale University School of Medicine, and Berkeley Lab has combined protein crystallography and SAXS to give a first glimpse into what this conversion may look like as well as the structural consequences of the conversion.

Many years of cell biology and biochemistry have shown that a key player in this process is an enzyme that transfers phosphate groups, the Ca^{2+}/calmodulin-activated protein kinase II (CaMKII). A large protein complex (about 600 kDa), it is made up of twelve individual polypeptide chains (i.e., a dodecamer). Each polypeptide contains a kinase domain, which can phosphorylate downstream targets in the cell, and an "association domain" that links the kinases together in the complete complex (holoenzyme). These two domains are joined by a regulatory segment that binds to the kinase and inhibits its activity, as well as a linker domain of unknown function.

In the absence of Ca^{2+}, the regulatory segment is bound to the kinase, inhibiting its ability to phosphorylate its targets (substrates) including itself (autophosphorylation). When calcium enters the cell, it binds to the small protein calmodulin (CaM), which in turn binds to the regulatory segment, releasing the kinase activity. Underlying the ability of this protein complex to transduce Ca^{2+} signals is a system, based on the autophosphorylation of the regulatory segment, that allows the kinase activity to be initially dependent on Ca^{2+}/CaM and then to become independent in response to an increasing Ca^{2+} oscillation frequency, thereby allowing the phosphorylation to persist even after the calcium signal is over.

The group solved the crystal structure of the isolated kinase domain and regulatory segment of CaMKII from data obtained at ALS Beamline 8.2.2. Members were surprised to find that pairs of neighboring kinase domains form dimers where the active site of the kinase domain is blocked by a coiled-coil (two α-helix coils coiled together) formed by the regulatory segments (Figure 13). The significance of the dimer structure was suggested by biophysical measurements of Ca^{2+}/CaM binding to the holoenzyme. The measurements showed that the activation of the holoenzyme dodecamer is highly cooperative, suggesting that when Ca^{2+}/CaM binds to the kinase, it releases the activity of more than one kinase domain.

The new structure provides an answer for why this happens: When Ca^{2+}/CaM binds to one inhibiting regulatory segment, it releases its dimer pair at the same time. This insight formed the basis for a model of CaMKII activation by Ca^{2+}/CaM. In its resting state, the CaMKII holoenzyme is a tightly

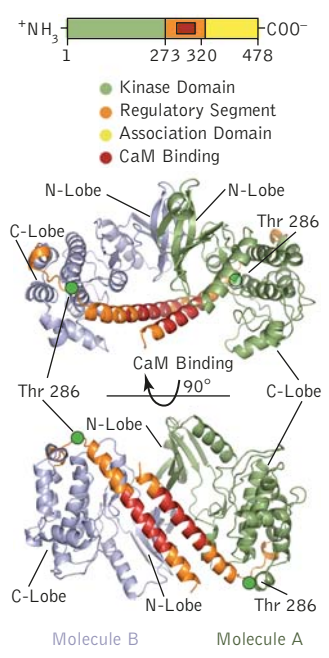

FIGURE 13
The crystal structure of the autoinhibited kinase domain of CaMKII. From top to bottom: The domain organization of CaMKII and two views of the CaMKII dimer, rotated 90° from each other. Molecule A is shown in green and molecule B is shown in blue. The Ca^{2+}/CaM binding residues are shown in magenta and the rest of the regulatory segment is shown in orange. Thr 286 is the residue that is autophosphorylated, leading to Ca^{2+}/CaM independence.

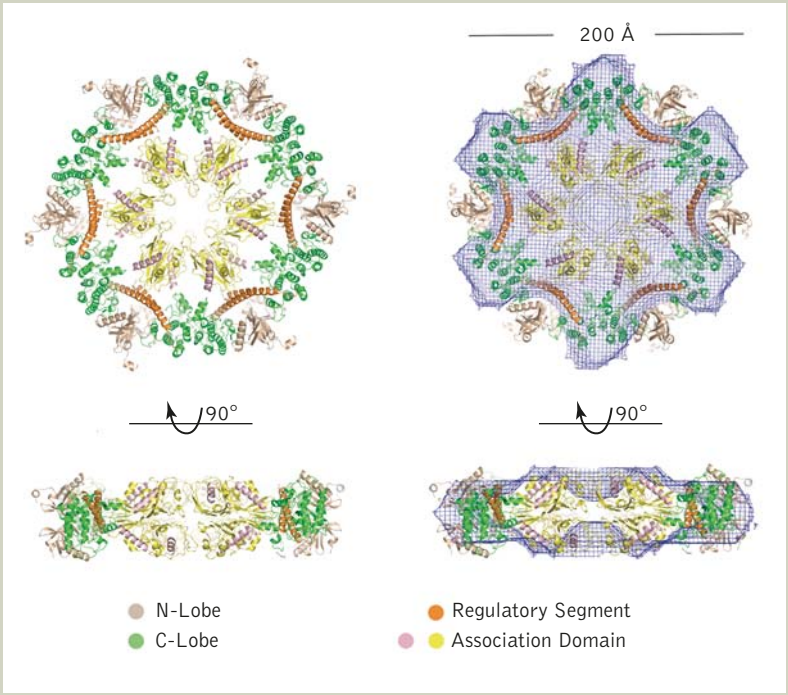

FIGURE 14
Models of the holoenzyme structure and activation using SAXS data. Left: A rigid-body modeling scheme using data from SAXS experiments resulted in a model of the CaMKII holoenzyme. Right: Ab initio models agree well with the rigid modeling results.

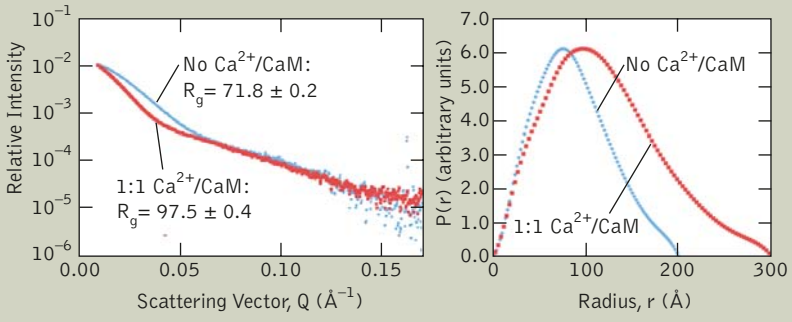

FIGURE 15
Addition of Ca^{2+}/CaM to the holoenzyme causes a dramatic increase in the radius of gyration of the protein complex.

packed and autoinhibited assembly that cannot autophosphorylate. When Ca^{2+}/CaM is added, however, the kinase domains are disrupted and the complex converts into an activated state that is capable of autophosphorylation and Ca^{2+}/CaM-independent activity.

Because the holoenzyme proved resistant to structural characterization by crystallography, the collaborators turned to SAXS at the new SIBYLS facility at ALS Beamline 12.3.1. The combination of high-intensity SAXS and crystallography allowed the group to build a model of the holoenzyme structure that was consistent with their crystal structure and their biochemical results.

The SAXS model revealed that the kinase holoenzyme is a compact flattened disc about 220 Å in diameter (Figure 14). The addition of Ca^{2+}/CaM to the holoenzyme increases the diameter of the complex by almost 25 Å, suggesting that this addition changes the complex into a much looser association of kinase domains (Figure 15).

Investigators

O.S. Rosenberg (UC Berkeley, Howard Hughes Medical Institute, and Yale University School of Medicine), S. Deindl and R.J. Sung (UC Berkeley and Howard Hughes Medical Institute), A.C. Nairn (Yale University School of Medicine), and J. Kuriyan (UC Berkeley, Howard Hughes Medical Institute, and Berkeley Lab).

Publications

O.S. Rosenberg, S. Deindl, R.J. Sung, A.C. Nairn, and J. Kuriyan, "Structure of the autoinhibited kinase domain of CaMKII and SAXS analysis of the holoenzyme," *Cell* **123,** 849 (2005).

Funding

National Institutes of Health through the Yale School of Medicine Medical Scientist Training Program and Howard Hughes Medical Institute.

Protein Flips Lipids across Membranes

In the last few decades, mutant strains of bacteria that are resistant to commonly used antibiotics have emerged. Infections by such strains can be treated with alternative drugs, but an even greater threat is emerging: multiple-drug-resistant bacteria that are no longer susceptible to broad categories of antibiotics, such as certain strains of the bacteria responsible for epidemic dysentery. The effort to develop new antibiotics will benefit from an understanding of the mechanisms by which bacteria expel substances that are toxic to them. One such mechanism can be found in MsbA, a protein that "flips" molecules from one side of a cell membrane to the other, where they can then be jettisoned. In human cells, such transporter proteins play an essential protective role by removing harmful toxins. Unfortunately, this protective action can also reduce the efficacy of certain cancer treatments, whose goal is to selectively destroy cancerous cells. The MsbA structure solved by Chang and Reyes could point the way to a new class of drugs that patients would take in conjunction with antibiotic or chemotherapeutic agents to keep the drugs in the cells and increase their efficacy.

Found ubiquitously in both bacteria and humans, membrane proteins of the adenosine triphosphate (ATP)-binding cassette (ABC) transporter family have been implicated in both antibiotic and cancer-drug resistance. The mechanisms used by these proteins to expel toxins from cells therefore represent key targets for the development of drugs designed to combat the growing problem of multidrug resistance. Toward this end, researchers from The Scripps Research Institute have succeeded in crystallizing MsbA—an ABC transporter protein—together with a substrate (the molecule to be transported) and a hydrolyzed (spent) form of the nucleotide ATP, the transporter's source of chemical energy. The resulting molecular complex is caught at a moment following the transporter's "power stroke," the force-generating part of the transport cycle. This snapshot suggests a mechanism by which the substrate molecule gets flipped head-over-tail from one side of the membrane to the other, on its way out of the cell.

ABC transporters are made up of two subunits, each of which contains a transmembrane domain, where specific substrate molecules can be bound, and a nucleotide-binding domain (the ATP-binding "cassette"), which is conserved across all members of the family. Previous studies have shown MsbA to be extremely flexible, occurring in both open and closed conformations. In the open conformation, the two transmembrane domains connect at their extracellular ends to form an inverted V-shaped molecule. In the closed conformation, both the transmembrane and nucleotide-binding domains are closely packed, and a large chamber accessible from inside the cell is formed. It has also been shown that several members of the ABC transporter family work on both lipids and drug molecules, suggesting a common transport mechanism for these compounds, which are characterized by hydrophilic "heads" and hydrophobic "tails." However, despite attempts to model the

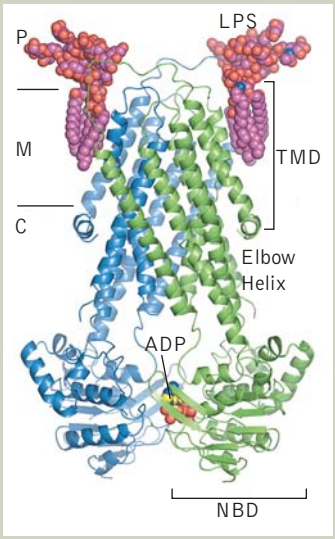

FIGURE 16
Structure of MsbA. TMD = transmembrane domain, NBD = nucleotide-binding domain, P = periplasm (outside membrane), M = membrane, C = cytoplasm (inside membrane), LPS = lipopolysaccharide (the substrate), and ADP = adenosine diphosphate (hydrolyzed ATP).

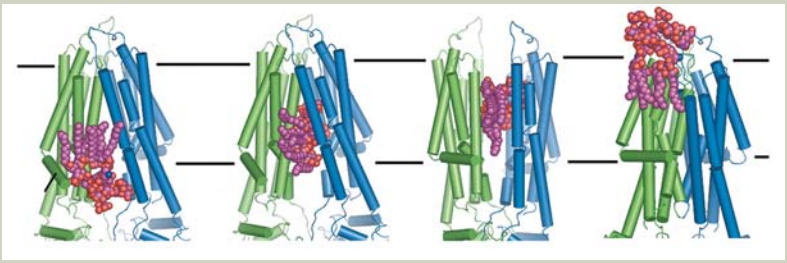

FIGURE 17
Proposed model for lipid flipping (only one LPS shown for clarity). Left to right: Closed MsbA with modeled initial LPS binding; closed MsbA with modeled sequestered LPS; proposed ATP transition state with modeled MsbA and LPS (sequestered LPS flipped 180°); observed post-hydrolysis conformation of MsbA with LPS.

structural changes of MsbA and other multidrug-resistant ABC transporters, a detailed view of conformational rearrangements during ATP hydrolysis and substrate transport has been elusive.

In this work, the researchers obtained for the first time the structure of an intact ABC transporter (bacterial MsbA from *Salmonella typhimurium*) in the presence of a substrate (lipopolysaccharide) and a complex of ADP, inorganic vanadate, and magnesium that mimics the transition state of ATP during hydrolysis (Figure 16). The structure was determined to a resolution of 4.2 Å at ALS Beamline 8.3.1. The results show that the transmembrane domains are tilted 30° relative to the molecular axis, with extensive interdigitation of the helices. Two lipopolysaccharide molecules are bound on the periplasmic (outer-membrane) side, but only one ADP complex is found in the nucleotide-binding domains. A large rotation and translation in the transmembrane domain results in an opening of approximately 15 Å toward the periplasmic end, allowing access to the internal chamber from the periplasm but not from the cytoplasm.

The observations led the researchers to propose a process in which the lipopolysaccharide substrate initially binds near a site in the transmembrane domain (called the elbow helix) with a high affinity for several cationic heavy metals. During the power-stroke step, the hydrophilic heads of the substrate are sequestered within the internal chamber and flipped to the outer membrane by the rigid-body shearing of the transmembrane domains while the hydrophobic tails are dragged through the membrane (Figure 17). The presence of only one ADP complex suggests that the two nucleotide-binding domains act to hydrolyze ATP alternately, while the presence of two lipopolysaccharide molecules suggests that two substrate molecules may be transported per power stroke.

While much work lies ahead before a complete mechanistic model of substrate transport can be achieved, this model (together with previously solved MsbA structures) provides a framework for interpreting functional data concerning ABC "flippases" that confer multidrug resistance to cancer cells and infectious microorganisms.

INVESTIGATORS
C.L. Reyes and G. Chang (The Scripps Research Institute).

PUBLICATIONS
C.L. Reyes and G.A. Chang, "Structure of the ABC transporter MsbA in complex with ADP-vanadate and lipopolysaccharide," *Science* **308,** 1028 (2005).

FUNDING
National Institutes of Health, National Science Foundation, Beckman Young Investigators Grant, Fannie E. Rippel Foundation, Baxter Foundation, and The Skaggs Institute for Chemical Biology.

DNA-Binding Mechanism in Prokaryotic Partition Complex Formation

On the cellular level, self-replication by cell division is a hallmark of life. Bacteria are single-celled creatures without well-defined cell nuclei (technically, they are prokaryotes) in which the DNA is contained both in a single chromosome and in separate smaller molecules called plasmids. For humans, bacteria such as those that inhabit our digestive systems are essential friends, whereas other invaders from outside our bodies can be deadly foes that bring disease and death. In either case, understanding how bacteria multiply and grow not only increases our fundamental knowledge of processes central to life itself but also provides clues for maintaining our health. By determining the atomic structure of a "partition complex" consisting of DNA plus certain workhorse proteins in the bacterium *Escherichia coli,* Schumacher and Funnell have provided new information about a key point in bacterial cell division, the one beginning the process by which the newly replicated DNA is separated so that part can be channelled into the far end of the elongating cell that later pinches off to form parent and daughter cells.

The faithful inheritance of genetic information, essential for all organisms, requires accurate movement and positioning of replicated DNA to daughter cells during cell division. In cells without distinct nuclei (prokaryotes), this process, called partition or segregation, is mediated by *par* systems. The prototype system of prokaryotic partition is the *E. coli* P1 plasmid *par* system, which consists of a centromere site (*parS*) on the plasmid DNA and two proteins, ParA and ParB. The initial formation of the so-called partition complex between ParB and the centromere is a critical step in partition. To understand the DNA-binding mechanism utilized by ParB, Schumacher and Funnell determined crystal structures of the C-terminal region of ParB, known as ParB(142-333), bound to centromere sites.

In prokaryotes, genetic information is contained in the DNA in a single chromosome and in smaller DNA molecules called plasmids, but the P1 plasmid par system is a model for partition in both cases. The ParB–centromere partition complex serves as the docking site for ParA, the enzyme (ATPase) that drives subsequent separation of the plasmid DNA. ParB(142-333) contains all the determinants required for centromere binding and formation of the partition complex.

A *parS-small* centromere site with 25 base pairs and two DNA structural units (motifs) called the A-Box and B-Box is the minimal partition site required for segregation (Figure 18). However, partition efficiency is increased when a full-length, 74-base-pair *parS* centromere is used and the site is bent by the host auxiliary factor IHF whose role is simply to bring together the *parS* arms that contain the A-Box and B-Box. Once the initial complex is formed, additional ParB molecules load onto and spread along the DNA to form large nucleoprotein complexes. These findings indicate a highly complex P1 partition interaction topology and a protein–DNA interaction between ParB and the centromere that is unlike any previously described. In this interaction, ParB must, in some unknown manner, bridge the juxtaposed arms of a looped *parS* centromere site.

Of more than 70 samples in crystallization trials, only two provided data beyond 4.0-Å resolution, and data for these were collected at ALS Beamlines 8.2.1 and 5.0.2. Two structures of the P1 ParB(142-333)–*parS-small* partition complex were determined, the first by multiple-wavelength anomalous diffraction and the second by molecular replacement. Both structures reveal that ParB forms an asymmetric dimer with two flexi-

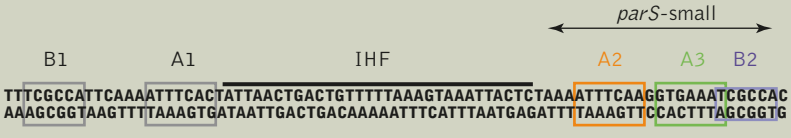

FIGURE 18
The sequences of the *parS-small* centromere site, which is functional for P1 partition, and of the full-length P1 *parS*. The A2-, A3-, and B2-Box DNAs are colored yellow, green, and blue, respectively.

bly linked DNA-binding modules: the extended N-terminal helix-turn-helix (HTH)-containing domains, which contact A-Boxes, and the novel dimerized Dimer domain, which contacts B-Box elements (Figure 19).

In fact, the structures in the two crystal forms, which reveal domain rotations ranging from about 60° to 160° relative to one another, suggest that the flexible linker between the DNA-binding modules allows them to rotate essentially freely. Strikingly, such free rotation would permit these modules to contact direct or inverted arrangements of A- and B-Boxes of the type found in *parS*. Most remarkably, however, each DNA-binding element binds to and thus bridges adjacent DNA duplexes (Figure 20).

The composite and flexibly linked DNA-binding modules and the ability of these flexibly attached elements to bridge adjacent DNA duplexes are unique for a DNA-binding protein and explain how this protein can bind complex arrays of A- and B-Box elements on adjacent DNA arms of the looped centromere site. Moreover, the unique bridging function of ParB may play a role in mediating plasmid pairing. Plasmid pairing is the next crucial step in partition after initial formation of the complex whereby the two DNA molecules are brought together. The paired complexes are then separated by the action of the ParA ATPase. How pairing occurs has been unknown, but the structures suggest that ParB mediates pairing by bridging between the two arms of one parS site and simultaneously binding to a second plasmid parS site.

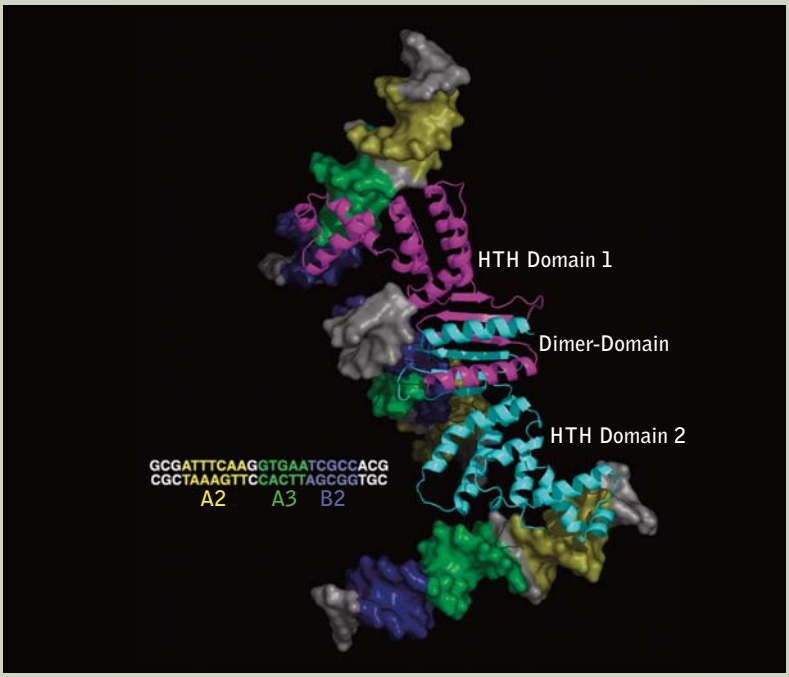

FIGURE 19
Crystal structure of the P1 ParB(142-333)–*parS-small* partition complex. The asymmetric ParB dimer is shown as a ribbon diagram with one subunit colored cyan and the other subunit magenta. Each ParB(142-333) subunit consists of two flexibly attached domains: the HTH domain, which contacts the A-Box DNA, and the Dimer domain, which contacts B-Box DNA. The *parS-small* site is displayed as a surface representation with the A2-, A3-, and B2-Boxes colored yellow, green, and blue, respectively. Next to the structure is the sequence of the *parS-small* centromere site.

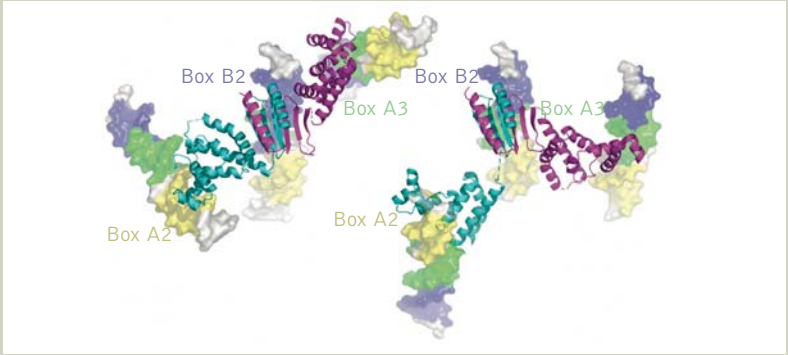

FIGURE 20
P1 ParB is a DNA-bridging factor. Ribbon diagram showing the four distinct DNA bridging interactions observed in two different crystal forms of the complex. ParB and Box motifs are colored as in Figure 19, and the DNA is rendered as a transparent surface. ParB is shown in the same orientation in both crystal forms to underscore the ability of the DNA-binding modules to undergo essentially free rotation, permitting them to contact distinct orientations of Box elements on different DNA duplexes.

INVESTIGATORS

M.A. Schumacher (University of Texas, MD Anderson Cancer Center) and B.E. Funnell (University of Toronto, Canada).

PUBLICATIONS

M.A. Schumacher and B.E. Funnell, "Structures of ParB bound to DNA reveal mechanism of partition complex formation," *Nature* **438,** 516 (2005).

FUNDING

Burroughs Wellcome Career Development Award and Canadian Institutes of Health Research.

X-Ray Microscopy

Biological Imaging by Soft X-Ray Diffraction Microscopy

With wavelengths at least 100 times shorter than that of visible light, x rays offer a path to much finer vision. Indeed, scientists have constructed and now regularly use x-ray microscopes to see into objects opaque to visible light and, with tomographic techniques related to those used in CAT scans, construct three-dimensional images. The rub is that lenses that can focus x rays are difficult to make and have a number of limitations. For this reason, researchers around the world interested in both life and physical sciences have been developing a "lensless" alternative to x-ray microscopy. Lensless imaging uses computational techniques to "reconstruct" an image from diffraction data (the intensities and angles of x rays scattered from the sample rather than transmitted through it). Shapiro et al. have now chimed in with the first lensless imaging of a sample as complex as a eukaryotic cell (a cell with a nucleus). Their reconstructed image of a yeast cell with a spatial resolution of about 30 nm is two-dimensional. Full three-dimensional images are next on the agenda.

Electron and x-ray microscopes are a valuable tool for both the life and materials sciences, but they are limited in their ability to image with nanometer-scale resolution in three dimensions nonperiodic objects that are several microns in size. To fill this gap, the technique of coherent x-ray diffraction imaging now under development takes advantage of the penetrating power of x rays while simultaneously removing the limitations imposed by lens-based optical systems. Researchers from Stony Brook University, in collaboration with scientists at the ALS and Cornell University, have taken a large step in this direction by using a lensless x-ray diffraction microscope to image a freeze-dried yeast cell to better than 30-nm resolution. Images were made at several angular orientations of the cell.

Electron microscopes are limited to biological specimens no thicker than a bacterium, and the technological challenges involved with making high-efficiency diffractive x-ray optics limits the capabilities of current lens-based x-ray microscopes. Coherent x-ray diffraction imaging, also known as x-ray diffraction microscopy (XDM), uses only the scattered intensities in the far field to recover the structure of the scattering object. If the object is nonperiodic, then the far-field intensity pattern is continuous and can be sampled finely enough that the phase, which is lost when intensity measurements are made, can be recovered by iterative computational methods.

In XDM, the action of a lens is replaced by a computational process that recovers the far-field phase information through the iterative application of constraints in both image and diffraction space. These constraints describe a priori knowledge that we have about the object and typically take the form of a support constraint (e.g., a requirement that the sample be finite and isolated) and a Fourier modulus constraint (a requirement that the calculated diffraction intensities match the measurements). This method of imaging a nonperiodic object by phasing its continuous diffraction pattern was first suggested by David Sayre (then at the IBM T.J. Watson Research Center) and first demonstrated with x rays by John Miao (then at Stony Brook University) and others in experiments at NSLS.

The current work represents the first application of XDM to image an object as complex as a eukaryotic cell. The diffraction microscope, developed by researchers at Stony Brook and now stationed at ALS Beamline 9.0.1, is capable of collecting three-dimensional diffraction data sets from dry or frozen hydrated specimens to a scattering angle that corresponds to a reconstructed half-period pixel size of 6 nm for 750-eV x rays. The diffraction pattern that the researchers used for their image reconstruction is a subset (1200 × 1200 pixels) of the full CCD recording and extends to 10-nm resolution (Figure 1). Approximately 400 intensities at low spatial frequencies are missing because of the need to block the brightest part of the pattern to prevent damaging the detector.

The phasing algorithm, developed at Cornell and known as the difference map, controls these intensities and calculates the missing phases. The reconstructed image contains both magnitude and phase information (not the same as the diffraction phases calculated by the algorithm) about the scattered wavefield (Figure 2). An averaging technique was developed

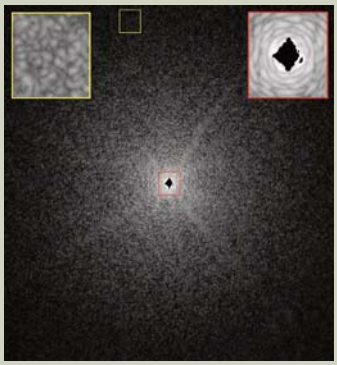

FIGURE 1
Experimental diffraction data used as input to the difference map algorithm. The continuous diffraction pattern, obtained after approximately 60 s of exposure to the x-ray beam, extends to 10-nm resolution at the edges and spans over six decades of intensity. Insets show magnified views of boxed regions.

to minimize the effects of noise on the reconstruction. Similar reconstructions were obtained from eight angular orientations of the cell at 1° rotation intervals (Figure 3). The good agreement between the independently recovered structures provides confidence in the fidelity of the reconstructed images, and a comparison of adjacent reconstructions indicates a spatial resolution of better than 30 nm. This estimate is supported by an analysis of an effective modulation transfer function for the microscope.

Experiments aimed at imaging a frozen hydrated cell in three dimensions are ongoing and will allow us to test our calculations that show the radiation-damage-limited resolution of XDM to be 10 nm for biological specimens.

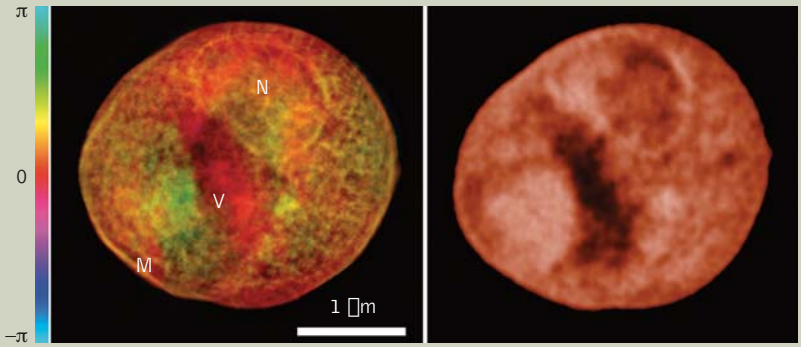

FIGURE 2
Left: Reconstruction of the x-ray wavefield after passage through the cell. The phase information is represented as hue (see color map at left) and the magnitude as brightness. The labels indicate the nucleus (N), vacuole (V), and the cell membrane (M). Right: STXM image of the same cell (obtained at NSLS with 540-eV x rays and an optic with a Raleigh resolution of 42 nm). This image is for comparison only and was not used in the reconstruction process.

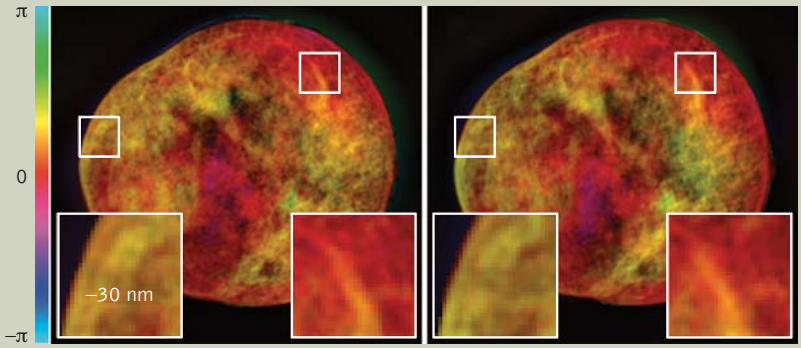

FIGURE 3
Two independent reconstructions after the cell was rotated by 3 and 4 degrees with respect to Figure 1. The insets show that similar structures on the scale of 30 nm can be clearly seen in each.

INVESTIGATORS
D. Shapiro, E. Lima, H. Miao, A.M. Neiman, and D. Sayre (Stony Brook University); P. Thibault and V. Elser (Cornell University); T. Beetz and C. Jacobsen (Stony Brook University and Brookhaven National Laboratory); M. Howells (ALS); and J. Kirz (Stony Brook University and ALS).

PUBLICATIONS
D. Shapiro, P. Thibault, T. Beetz, V. Elser, M. Howells, C. Jacobsen, J. Kirz, E. Lima, H. Miao, A.M. Neiman, and D. Sayre, "Biological imaging by soft x-ray diffraction microscopy," *Proc. Natl. Acad. Sci. USA* **102,** 15343 (2005).

FUNDING
National Institutes of Health, National Science Foundation, and U.S. DOE BES.

New Zone Plate for Soft X-Ray Microscopy at 15-nm Spatial Resolution

X-ray microscopes promise images with 10-nm detail throughout the volume of the sample (three-dimensional imaging). Such a capability would benefit both life scientists peering into cells and materials scientists doing the same for solid materials. For the finest resolution, devices known as Fresnel zone plates have been the choice for the x-ray equivalent of a lens. Looking somewhat like a microscopic archery target, zone plates consist of alternating transparent and opaque concentric "zones" of decreasing width from center to outer edge. X rays passing through a zone plate are diffracted inward to form a spot approximately equal to the width of the outermost zone. Chao et al. have adapted a nanofabrication technique based on the use of a finely focused electron beam to "write" the zone plate pattern. With their "overlay" techniques, they made a zone plate with an outer-zone width of 15 nm and tested it in an x-ray microscope. They foresee refinements of their technique that will result in zone plates with 10-nm zone widths, once regarded as the practical resolution limit for x-ray microscopy.

Analytical tools that combine spatial resolution with elemental and chemical identification at the nanometer scale along with large penetration depth are indispensable for the life and physical sciences. The XM-1 soft x-ray microscope at the ALS produces images that not only reveal structures but can identify their chemical elements and measure magnetic and other properties as well. Now a new method for creating optical devices with nanoscale accuracy has allowed researchers in Berkeley Lab's Center for X-Ray Optics (CXRO), which built and operates the XM-1, to achieve an extraordinary resolution of better than 15 nm, with the promise of even higher resolution in the near future.

Since x rays cannot be focused by conventional refractive lenses, the XM-1 uses Fresnel zone plates, disks of concentric rings of metal of decreasing width that diffract the soft x rays to form an image (Figure 4). An objective lens called a "micro" zone plate (MZP) projects a full-field image of the sample onto a CCD area detector. CXRO fabricates its own zone plates with its Nanowriter electron-beam lithography tool. An energetic beam of electrons just 7 nm wide carves preprogrammed patterns in a resist-coated silicon wafer. The carved-out circular patterns in the resist are then replaced with opaque gold to form an object.

Since the spatial resolution is approximately the width of the outermost zone, high resolution depends on the ability to make narrow outermost zones, with a placement accuracy better than one-third the width of the zones themselves. The Nanowriter is capable of placement accuracy to within 2 nm, but unfortunately, electron scattering spreads even a tightly focused beam when it hits the resist. The exposure due to scattering from neighboring zones, combined with inherent limits in the resist resolution, has made it impossible to maintain high contrast and optical separation for zones narrower than those in the XM-1's earlier objective lens of 25 nm.

To overcome this limit, the

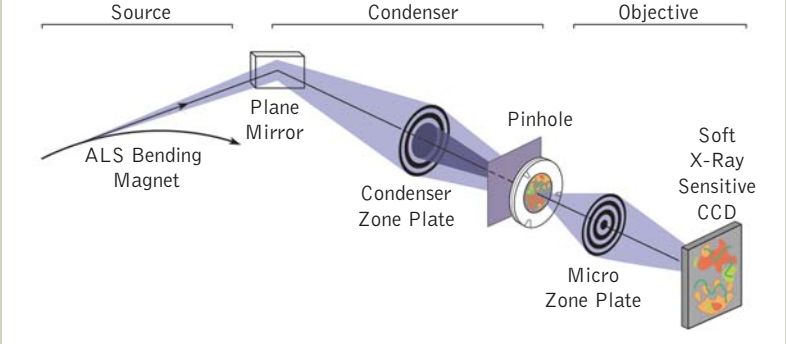

FIGURE 4
Schematic of the CXRO XM-1 full-field imaging microscope at ALS Beamline 6.1.2.

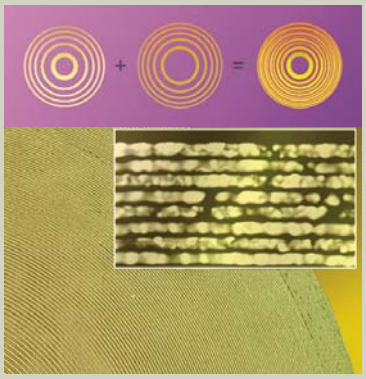

FIGURE 5
Top: In the overlay nanofabrication technique, generating separate electron-beam lithography patterns for alternating opaque zones reduces the smearing due to electron scattering when writing closely spaced features. Bottom: Scanning electron micrograph of an MZP made using the overlay technique demonstrates achievement of a 30-nm zone period (distance from centers of outermost opaque zones) with high quality (e.g., placement accuracy of 1.7 nm).

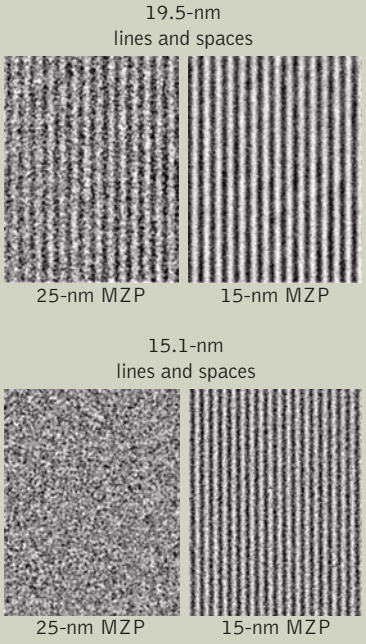

FIGURE 6
Soft x-ray images taken with the XM-1 full-field imaging microscope at Beamline 6.1.2 vividly display the improved resolution achievable when using the new MZP with a 15-nm outer-zone width (Δr_{MZP}).

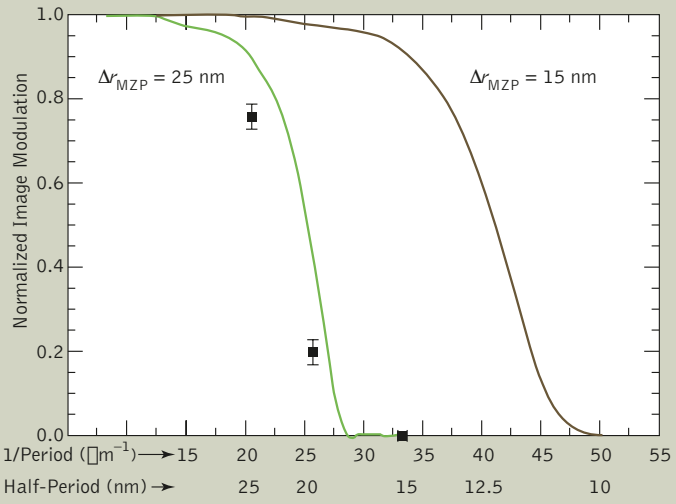

FIGURE 7
The calculated modulation transfer functions of the microscope with an older MZP whose outer-zone width (Δr_{MZP}) is 25 nm (left line) and the new one with Δr_{MZP} = 15 nm (right line). The theoretical resolution for the two lenses are 19 nm and 12 nm, respectively. Squares are experimental data indicating the degree of modulation obtained for various test patterns imaged using the older zone plate.

CXRO researchers adapted an overlay technique used in the semiconductor industry by combining two different zone-plate patterns (Figure 5). Opaque zones are typically given even numbers, so in this scheme the first pattern contains zones 2, 6, 10, 14, and so on, and the second contains zones 4, 8, 12, 16, and so on. The first pattern is carved into the resist-coated wafer; then the zones formed by the electron patterning are filled with gold. The wafer is coated with resist again to make the second pattern.

When combined, the critical outer zones of the combined patterns were less than 15 nm apart, accurately placed to within less than 2 nm. However, the opaque zones were broken by tiny gaps, and they were wider (and the transparent zones between them narrower) than they should have been, somewhat reducing the zone plate's efficiency.

The experimental MZP was then used to obtain images sharper than any previously achieved with an x-ray microscope. Not only were images of test patterns better defined than those made with the XM-1's current 25-nm MZP, the new MZP was able to obtain sharp images of lines a mere 15 nm apart—where the older zone plate had seen only a featureless field of gray (Figure 6). The contrast (modulation) between light and dark features of the pattern was also remarkably good (Figure 7).

The benefits of the advance may not be limited to x-ray microscopes at synchrotron light sources. The CXRO researchers suggest that before too many years, new sources of bright, soft x rays, such as compact, laser-based x-ray sources, will

make it possible to fit x-ray microscopes on the bench top. Nanoscience and nanotechnology will be both the beneficiaries and the driving forces behind the widening horizon for nanoscale analysis.

Weilun Chao (Berkeley Lab and UC Berkeley).

INVESTIGATORS
W. Chao and D.T. Attwood (Berkeley Lab and UC Berkeley) and B.D. Harteneck, J.A. Liddle, and E.H. Anderson (Berkeley Lab).

PUBLICATIONS
W. Chao, B.D. Harteneck, J.A. Liddle, E.H. Anderson, and D.T. Attwood, "Soft x-ray microscopy at a resolution better than 15 nm," *Nature* **435,** 1210 (2005).

FUNDING
National Science Foundation, U.S. DOE BES, and Defense Advanced Research Projects Agency.

First Direct Imaging of Swollen Microgel Particles

Polymers—giant molecules formed by chaining together countless numbers of simpler molecules—can curl back on themselves repeatedly until they resemble a loopy ball of tangled yarn. Moreover, the tangle can have unusual properties that, when controlled, would prove highly useful. For example, the polymer balls found in microgels are known to balloon in size when exposed to certain controllable conditions. Such particles hold the promise of a number of potential applications, including heavy-metal sequestration, dynamically tunable microlenses, and templates for the synthesis of inorganic nanoparticles. In particular, microgels, which are biocompatible, are of great interest as drug-delivery vehicles. Numerous targets for therapeutic drugs, such as tumors and inflammatory tissues, exist at acidic conditions, and many protein-loaded microgels have already been synthesized and investigated. Thus, microgel particles stimulated by an acidic environment should be able to expand on demand to deliver their contents where needed. Realization of that promise, however, requires careful study of the mechanisms involved. Araki et al. have shown that scanning transmission x-ray microscopy at the ALS provides the resolution and contrast necessary to untangle exactly what is going on.

Microgels are soft-material particles consisting of cross-linked polymer networks, 100 nm to 1 μm in diameter, dispersed in a continuous medium such as water. A useful feature of certain types of microgel particles is that they can swell or shrink with changes in external triggers such as pH and temperature. Thus microgel particles can act like "nanosponges" and offer many potential applications in medicine, environmental science, and industry. Because microgels are usually employed in their swollen state, in situ characterization of these particles under such conditions is desirable for understanding their behavior. However, optical microscopy is inadequate to this task, being limited in resolution and by the very small difference in refractive index (i.e., contrast) between the swollen particles and the continuous phase. Now, an international team of researchers from the U.S. and U.K. have obtained the first images of swollen microgel particles directly in aqueous solution using x-ray microscopy at the ALS, which, together with spectroscopic determination of their chemical state, provides insight into the underlying swelling mechanism.

The special properties of microgel particles are due to the presence of covalent bonds between different parts of the polymer chains (i.e., "cross-linking") and the presence of active functional groups. They allow, for example, the polymer network to retain water and the microgels to exhibit interesting physical properties not

seen with common polymer latex microspheres. In this study, the researchers investigated lightly cross-linked poly(4-vinylpyridine)-silica (P4VP-SiO_2) nanocomposite microgel particles synthesized in aqueous solution. Below a critical pH value of around 3.7, the 4-vinylpyridine residues become fully protonated, leading to significant swelling. The hydrodynamic diameter measured by dynamic light scattering changes from around 230 nm (pH 8.8) to 620 nm (pH 3), which indicates a volumetric swelling factor of more than an order of magnitude (Figure 8).

The x-ray microscopy characterization was carried out using the polymer-STXM endstation at ALS Beamline 5.3.2. STXM provides both high spatial resolution imaging (better than 50 nm) with zone-plate focusing and good chemical sensitivity based on NEXAFS spectroscopy. Using the "water window" photon energy region between the carbon and oxygen 1s absorption, the microgel particles can be imaged in their swollen state directly in aqueous solution (Figure 9) through the use of a so-called wet cell, which consists of two thin silicon nitride membranes that are sealed together.

The investigation focused on nitrogen 1s rather than carbon 1s NEXAFS for both STXM imaging and spectroscopic studies. This was partly owing to the ease of handling multicomponent complex samples in wet cells at this particular energy but also because the pH-sensitive chemical environment of the nitrogen atom is of particular interest in this system. The researchers first obtained the nitrogen 1s NEXAFS spectra for both neutral and protonated linear

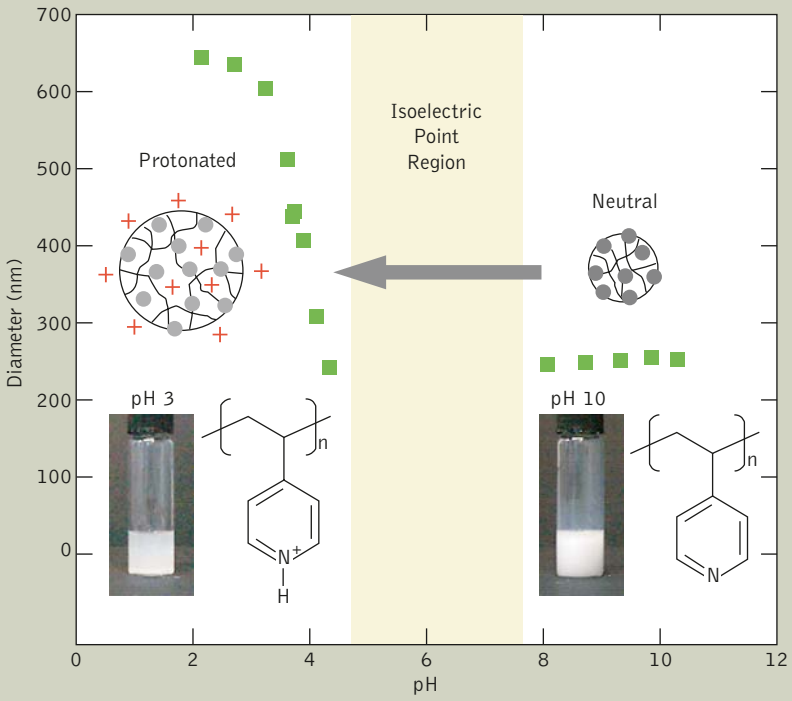

FIGURE 8
Variation of hydrodynamic diameter with solution pH for lightly cross-linked P4VP-SiO_2 nanocomposite microgel particles. The shaded region indicates the pH range in which flocculation (aggregation) was observed. The midpoint of this region corresponds approximately to the isoelectric point (where the particles don't move in an electric field). The digital photographs indicate the visual appearance of this nanocomposite microgel dispersion at pH 3 and pH 10.

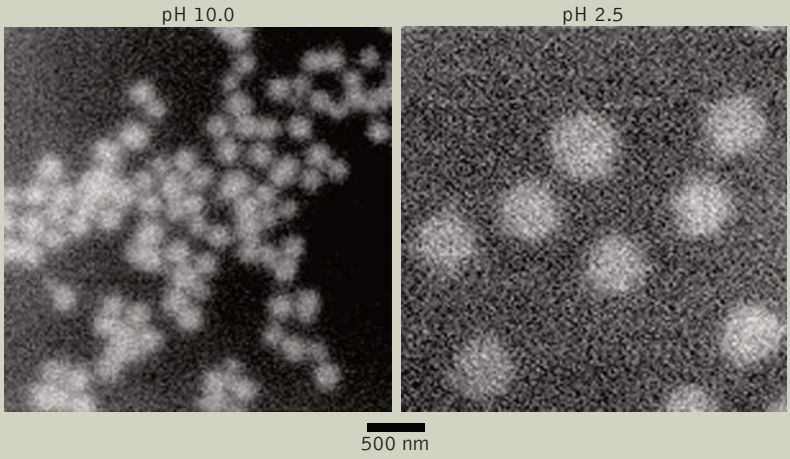

FIGURE 9
STXM optical density images of aqueous dispersions of nanocomposite microgel particles in their nonswollen (pH 10) and swollen (pH 2.5) states.

P4VP homopolymer (Figure 10). These well-resolved lowest-photon-energy peaks served as excellent markers for the protonated and neutral states of the pyridine rings, and the corresponding two photon energies provided sufficient chemical contrast between the microgel particles at high and low pH (neutral form: 398.9 eV, protonated form: 400.4 eV).

The STXM images showed the well-dispersed swollen microgel particles at low pH in contrast to the nonswollen particles at high pH. The average size data of each particle was in good agreement with the dynamic light scattering data. Subsequently, nitrogen 1s NEXAFS spectra were acquired from the individual hydrated microgel particles to estimate their degree of protonation. The resulting spectra at both low and high pH have sharp peaks at the same photon energies as the corresponding reference spectra. From this result, the researchers concluded that the nitrogen atoms of these P4VP-based cationic microgel particles are completely protonated at low pH. The researchers expect that these results will lead to the systematic investigation of a range of microgel particles in the future.

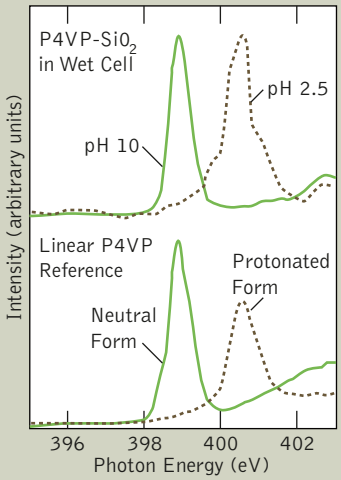

FIGURE 10
Nitrogen 1s NEXAFS spectra of P4VP-SiO_2 nanocomposite microgel particles in the wet cell at pH 10 and 2.5 (top), and linear P4VP homopolymer dried in either its neutral or fully protonated form on Si_3N_4 (bottom).

Harald Ade (North Carolina State University).

INVESTIGATORS
T. Araki and H. Ade (North Carolina State University) and S. Fujii and S.P. Armes (University of Sheffield, U.K.).

PUBLICATIONS
S. Fujii, S.P. Armes, T. Araki, and H. Ade, "Direct imaging and spectroscopic characterization of stimulus-responsive microgels," *J. Am. Chem. Soc.* **127,** 16808 (2005).

FUNDING
U.S. DOE BES, Royal Society/Wolfson Research Merit Award, and U.K. Engineering and Physical Sciences Research Council.

Long-Range Validity of Threshold Laws in Inner-Shell Photodetachment

In physics and chemistry, a threshold refers to the minimum energy required for a reaction to just become observable. A threshold law mathematically describes the reaction yield as the energy varies near the threshold. What is the threshold law when absorption of light causes removal (photodetachment) of an electron from a negatively charged ion (atom with one extra electron)? Not only is the common electrical attraction between oppositely charged particles absent, photodetachment of a tightly bound "inner-shell" electron adds further complications that make adherence to any law problematic. Bilodeau et al. have shown for inner-shell photodetachment of helium and sulfur ions that not only are the appropriate threshold laws valid, they are valid over a wider energy range than predicted by theory. Such fundamental data lead to a deeper understanding of the details of atomic physics. They are also of practical interest because negative ions are important in a number of processes, such as those taking place in stellar atmospheres, molecular clouds, the analytical technique of atomic mass spectrometry, and plasmas.

A threshold law describes the dependence of a reaction yield near a reaction threshold. It is also a signature of the physical forces involved in the reaction, so the agreement of an observed threshold behavior with a threshold law or a departure from it can be a sensitive probe into how well the reaction physics is understood. A collaboration from Western Michigan University, the ALS, and Denison University has now shown that the threshold laws for inner-shell photodetachment of negative ions are not only obeyed but can extend over a much wider energy range than theory had predicted.

Eugene Wigner first derived the general threshold laws for the dissociation of a target into a pair of particles in 1948. In single-electron photodetachment of negative ions where the reaction products (a neutral atom and an electron) interact only in a short-range potential (proportional to $1/r^4$), the threshold behavior is governed by the centrifugal potential—the potential formed by the relative angular momentum of the products—and depends only on the energy (e) and the relative angular momentum (l) of the particles through $e^{l+1/2}$.

This form of the Wigner law has been observed in countless studies, most notably in photodetachment of an outer (valence) electron from negative ions. However, when an inner-shell electron is removed, the neutral atom formed is unstable and quickly emits a second electron (Auger decay). If one considers the final reaction products to be two electrons and a positive ion, the short-range potential threshold law would no longer apply. To investigate whether this is so, the group

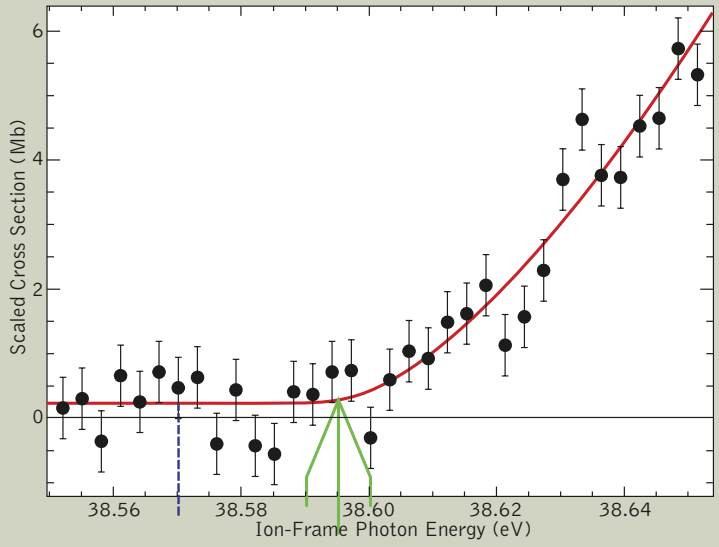

FIGURE 1
He^+-production cross section for 1s photodetachment from He^- closely follows a Wigner p-wave ($l = 1$) threshold law ($e^{3/2}$), despite significant postcollision interaction effects, which appear to effectively shift the observed threshold position (arrow) by about 25 meV from the theoretical position (vertical dashed line).

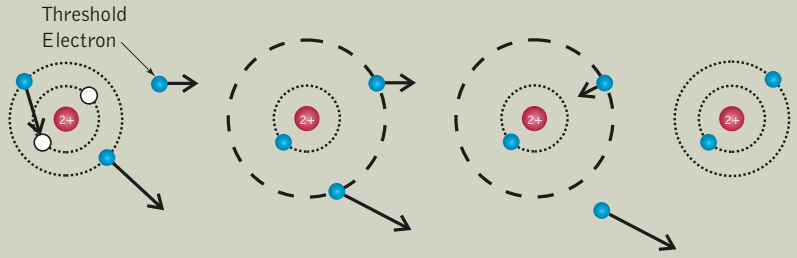

FIGURE 2
Postcollision interaction with recapture is responsible for shifting the observed He^- threshold energy. Left to right: Shortly after the 1s electron is photodetached, the atom ejects a second electron in an Auger decay process. The high-energy Auger electron quickly overtakes the photoelectron. The photoelectron is attracted to the exposed He nucleus. The photoelectron is finally recaptured to form a neutral He atom (shown in an excited state), which does not contribute to the He^+ signal monitored in these experiments.

studied inner-shell photodetachment in two negative ions: He^- and S^-. The experimenters monitored the photodetachment by measuring the positive ion yield (He^+, S^+, S^{2+}, and S^{3+}) at the Ion-Photon Beamline on ALS Beamline 10.0.1.

The ground-state electron configuration of He^- is 1s2s2p. For inner-shell photodetachment, the 1s electron is removed. Since the electron gains one unit of angular momentum by absorbing the photon, the receding photoelectron has angular momentum $l = 1$ and, in the absence of Auger decay, one would expect a p-wave threshold law: $e^{3/2}$. In fact, the measured near-threshold cross section agrees very well with the p-wave law, except that it is shifted in energy by a significant amount—i.e. the Auger decay appears to mainly have the effect of requiring more energy for the photodetached electron to escape (Figure 1). This can be understood in the context of a postcollision interaction effect. Before the photoelectron can fully escape, there is a chance that an Auger process occurs and the fast Auger electron overtakes the slow photoelectron, thus causing the photoelectron to be attracted and possibly recaptured by the suddenly exposed positive core, so that the He^+ signal is suppressed (Figure 2).

To investigate the effect of the angular momentum l, photodetachment of the 2p electron from S^- was also studied. In this case, the absorption of the photon will cause the photoelectron to leave with $l = 1 \pm 1 = 0$ or 2, i.e., an s-wave or d-wave. The d-wave component has always been too weak to be observed, and the s-wave threshold law should be expected: $e^{1/2}$. However, the group observed a change in threshold shape as the d-wave contribution grew (Figure 3).

Furthermore, the wide energy range of agreement of the threshold law to the observed signal was unprecedented; the Wigner law has previously been observed to apply only some 0.01 to 0.1 eV above the threshold, compared to the nearly 3 eV in inner-shell pho-

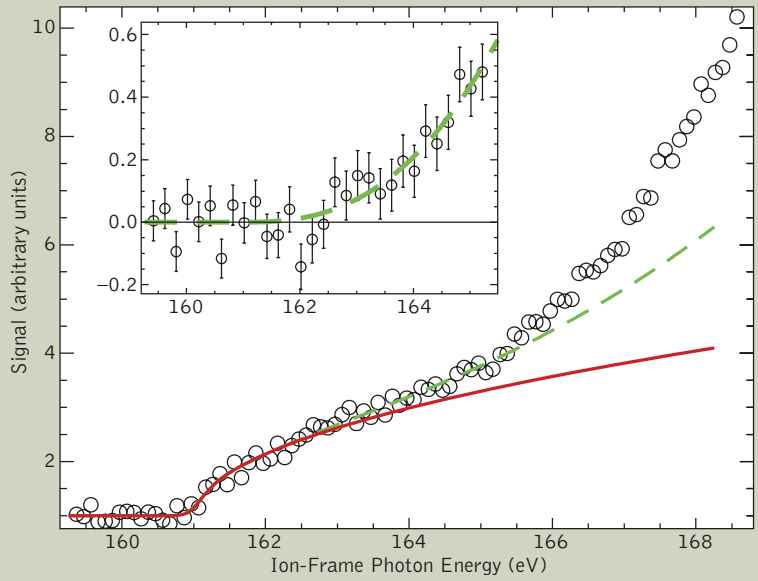

FIGURE 3
Observed S^{2+} signal (S^+ and S^{3+} production is similar) from the photodetachment of a 2p electron from S^-. The s-wave law ($e^{1/2}$) is followed closely up to nearly 3 eV above the threshold (solid curve), after which the inclusion of the weak d-wave is necessary to extend the agreement (dashed curve). In the inset, the s-wave component has been subtracted from the data to make the d-wave law ($e^{5/2}$) apparent. The departure beyond about 166 eV is likely due to the opening of additional detachment channels.

todetachment, a finding that is surprising and remains unexplained. Also surprising is that this range of agreement was further improved with the inclusion of a d-wave component to the fit. This is the first time a d-wave has been observed in this way.

Investigators

R.C. Bilodeau (Western Michigan University and ALS), J.D. Bozek and G.D. Ackerman (ALS), N.D. Gibson and C.W. Walter (Denison University), I. Dumitriu and N. Berrah (Western Michigan University).

Publications

R.C. Bilodeau, J.D. Bozek, N.D. Gibson, C.W. Walter, G.D. Ackerman, I. Dumitriu, and N. Berrah, "Inner-shell photodetachment thresholds: Unexpected long-range validity of the Wigner law," *Phys. Rev. Lett.* **95,** 083001 (2005).

R.C. Bilodeau, N.D. Gibson, J.D. Bozek, C.W. Walter, G.D. Ackerman, P. Andersson, J.G. Heredia, M. Perri, and N. Berrah, "High-charge-state formation following inner-shell photodetachment from S^-," *Phys. Rev. A* **72,** 050701(R) (2005).

R.C. Bilodeau, J.D. Bozek, G.D. Ackerman, A. Aguilar, and N. Berrah, "Photodetachment of He^- near the 1s threshold: Absolute cross-section measurements and postcollision interactions," *Phys. Rev. A* **73,** 034701 (2006).

Funding

U.S. DOE BES.

Rene Bilodeau (Western Michigan University and ALS), Nora Berrah (Western Michigan University), and John Bozek (ALS).

Photoexcitation of a Volume Plasmon in Buckyballs

Plasma is the state of matter in which electrons, ions, and photons mix freely with electrically neutral particles—an ionized gas, if you will. The "electron gas" in a metal can be considered one form of plasma. When such electrons oscillate back and forth to form a wave, the corresponding "quasiparticle" is called a "plasmon." Plasmons confined to the surface of a material can produce obvious effects. A February 22, 2005, article by Kenneth Chang in the New York Times notes that the deep red color in medieval stained-glass windows is actually produced by nanoparticles of gold. The Times calls the stained-glass artisans "the first nanotechnologists." Despite fundamental and practical interest in the interaction between plasmas and radiation, there is very little experimental information available—mainly because experiments have been so technically difficult. At ALS Beamline 10.0.1, specially designed to study the interaction of ions and photons, Scully et al. have found that the geodesic-dome structure of buckyballs makes possible volume plasmons—which exhibit not the back-and-forth oscillation of a surface plasmon but rather an in-and-out contortion, like a beach ball being squeezed.

For molecules made from a single element, buckyballs (carbon-60) are very large. They mark the transition from atoms to solids. In atoms and small molecules, the behavior of electrons is accounted individually; in bulk materials, a sea of innumerable electrons can behave en masse, yielding a very different description of electronic structure. Buckyballs perch on the cusp between these states, as evidenced by the discovery in the early 1990s that, when subject to an excitation energy of about 22 eV, the four valence electrons belonging to each of the 60 carbon atoms in a buckyball, 240 in all, act collectively, resulting in a "surface plasmon." This collective motion is a back-and-forth oscillation of the whole cloud of valence electrons, relative to the effectively rigid cage of carbon cores. Now, the latest results

from a U.S.–German collaboration on the electronic structure of photoexcited buckyball ions show an additional resonance near 40 eV, characterized as a volume plasmon made possible by the special fullerene geometry.

The researchers measured absolute photoionization cross sections for C-60 ions at the Ion-Photon Beamline at the ALS (Beamline 10.0.1). There, information gathering starts with a pinch of fullerene soot evaporated in an ion source. A fine beam of the resulting buckyball ions is accelerated from the ion source and turned 90 degrees to collide with a beam of ultraviolet photons. All but buckyballs of the desired charge state (+1 for most measurements, corresponding to a total of 239 valence electrons) are stripped out of the ion beam. The photon beam is tuned through a range of values, from 17 to 75 eV. Photoexcited ions are deflected to a detector; there the number of ions reaching the detector at different photon energies and their ion charge states are recorded.

The group's first experiment with buckyballs resulted in a clearer-than-ever picture of the giant resonance at 22 eV—evident as a sharp peak in a graph showing the number of photoionized buckyballs arriving at the detector as a function of the energy of the photon beam. But instead of falling off smoothly from this peak as photon energy was increased, there was a secondary rise, or shoulder, in the curve (Figure 4). The results were presented at a workshop in Berlin, where they were heard by theorists from the Max Planck Institute for Complex Systems, who had predicted such a higher-energy resonance but had not published their prediction because of a lack of experimental evidence.

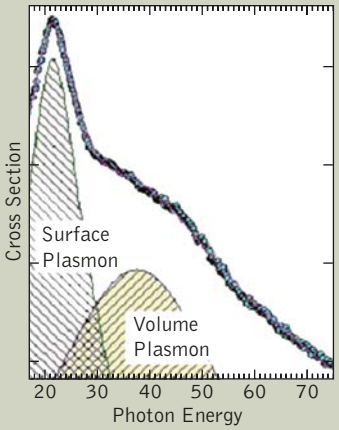

FIGURE 4
Absolute cross-section measurement of single photoionization of C-60 (open circles). The thin solid line results from the fit to the measured data of a linear background (not shown) plus the two separately displayed Lorentzian curves representing the surface and volume plasmons.

Combining their experimental observations and theoretical calculations, the collaborators interpreted the second resonance, occurring at a photon energy of 38 eV, as a volume plasmon, corresponding to a radial compression of the electron density, as opposed to the back-and-forth motion of a surface plasmon (Figure 5). The excitation of a volume plasmon in a solid conducting sphere is dipole forbidden, leading to its suppression in photoabsorption by metal clusters. However, a volume plasmon is possible in C-60 because of its shell geometry. The researchers' analysis considered the induced surface charges of the inner and outer surfaces of the shell. These surface charges can oscillate in two modes: one where they oscillate together relative to the shell, and one where they oscillate out of phase, creating local compression of the electron density with respect to the C-60 shell. This latter mode corresponds in effect to a dipole-allowed volume plasmon excitation.

When a 22-eV photon smacks into a charged buckyball, often the electron cloud surrounding it oscillates with enough energy to eject an electron. The same thing happens when a 38-eV photon smacks

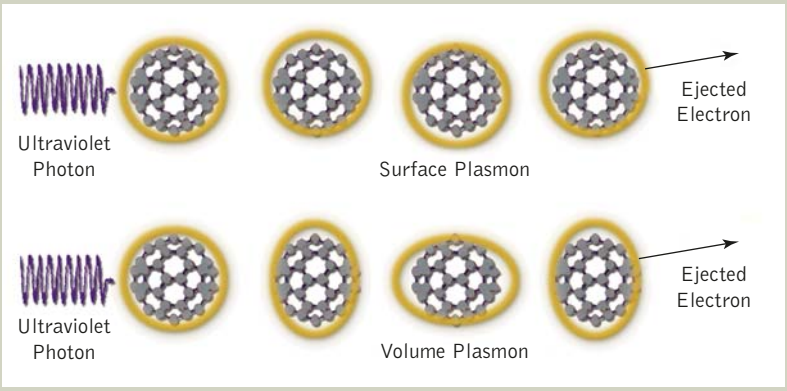

FIGURE 5
Top: When stimulated by photons at an energy of about 20 eV, a buckyball displays collective electron motion as a surface plasmon. Bottom: When stimulated by photons of about 40 eV, the result is a different mode of collective electron motion, a volume plasmon.

into a charged buckyball, except that the electron cloud wobbles in and out, penetrating the cage—a phenomenon unique to charged buckminsterfullerenes. Like hitting a big bronze bell with a clapper, it's a way to make the buckyballs ring.

Investigators

S.W.J. Scully, E.D. Emmons, M.F. Gharaibeh, and R.A. Phaneuf (University of Nevada, Reno); A.L.D. Kilcoyne and A.S. Schlachter (ALS); S. Schippers and A. Müller (Justus-Liebig-Universität, Germany); and H.S. Chakraborty, M.E. Madjet, and J.M. Rost (Max Planck Institute for the Physics of Complex Systems, Germany).

Publications

S.W.J. Scully, E.D. Emmons, M.F. Gharaibeh, R.A. Phaneuf, A.L.D. Kilcoyne, A.S. Schlachter, S. Schippers, A. Müller, H.S. Chakraborty, M.E. Madjet, and J.M. Rost, "Photoexcitation of a volume plasmon in C_{60} ions," *Phys. Rev. Lett.* **94,** 065503 (2005).

Funding

U.S. DOE BES, German Research Foundation, and Alexander von Humboldt Foundation.

Light Scattering of Ultrafine Silica Particles by VUV Synchrotron Radiation

In a dark room, microscopic dust particles suspended in air can be observed when a ray of bright light illuminates them. The light scattered from these small particles is described by a theory put forward by the German physicist Gustav Mie in 1908. This theory not only explains this phenomenon but has led to many practical techniques for detecting suspended particles in gases and fluids. Detecting a single suspended particle by monitoring scattered visible light can be achieved for smaller particles by using new, more intense light sources (lasers) and more efficient optics. However, there is a lower limit because the scattering efficiency of a particle decreases dramatically with the diameter of the particle. Since ultrafine particles have been implicated in climate change, give rise to scatter in interstellar clouds, and affect human health, their detection is of enormous interest. Shu et al. have shown that light scattering of ultrafine silica particles is observable with VUV synchrotron radiation. The experimental results demonstrate that the lower size limit for particle detection can be potentially greatly improved by probing with the much shorter wavelength VUV light.

There is enormous interest in the physics and chemistry of ultrafine particles because of their widespread importance in fields as far removed as climatology, astrophysics, and public health. Mie theory, put forward almost one hundred years ago, has been used to analyze visible-light scattering experiments, but no experimental study on VUV scattering by particles had been carried out. Such studies provide a new way to look at very small particles, since the scattering cross section of nanometer-sized particles increases at short VUV wavelengths. A Berkeley Lab–UC Berkeley team has now shown that VUV scattering by ultrafine silica particles does indeed follow Mie theory. Moreover, the experimental results show that VUV scattering is potentially a more sensitive probe for ultrafine particles than visible light.

The investigators performed their experiment at the ALS Chemical Dynamics Beamline (Beamline 9.0.2), which produces a high flux (10^{16} photons/s) of VUV light (8–30 eV) with a 2.2% bandwidth. Completed in 1995, the beamline remains one of the brightest VUV light sources in the world, enabling it to play a significant role in chemical dynamics investigations of molecules. Light scattering experiments are a substantially new capability for this beamline. In these experiments, a new aerosol endstation equipped with a light-scattering detector was coupled to the beamline. The apparatus consists of an aerosol-generation system and a VUV-scattering detector as well as a sampler to inject the aerosol into the machine.

The aerosol-generation system was used to produce spherical silica particles in situ for the scattering experiment. Silica particle images measured with a scanning electron microscope at Berkeley Lab's National Center for Electron

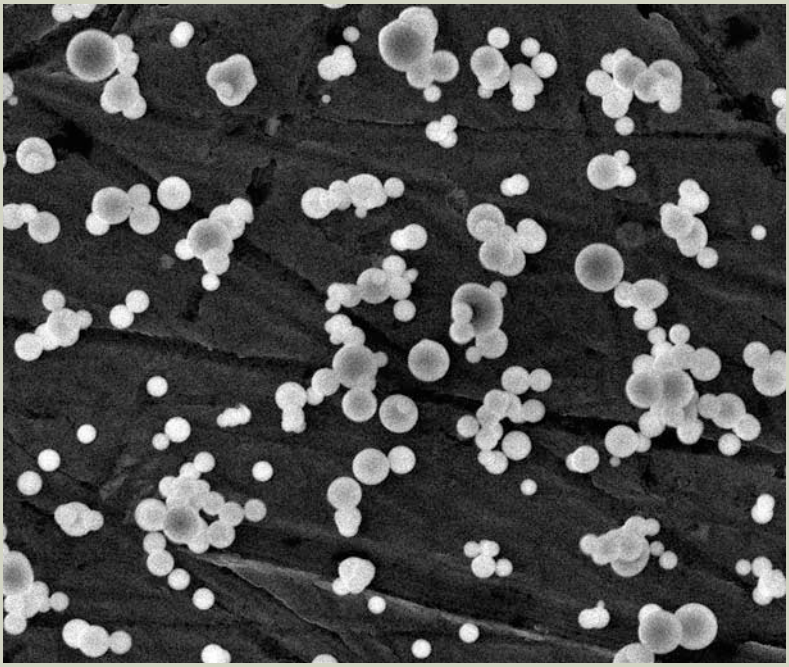

FIGURE 6
An image (area about 10 × 8 □m²) of silica particles measured with a scanning electron microscope verifies that the particles are spherical.

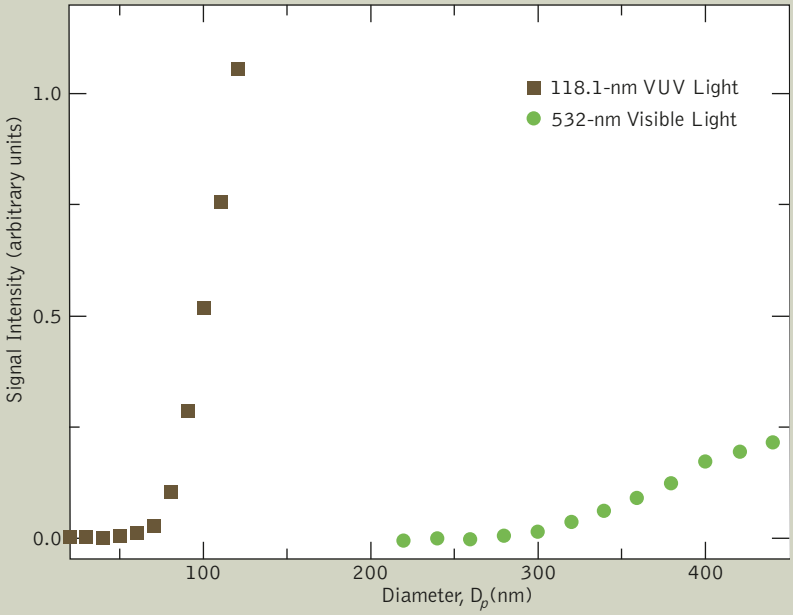

FIGURE 7
Scattering intensities for particles of different sizes illuminated with 118.1-nm (VUV) and 532-nm (visible) light show the enhanced sensitivity at VUV wavelengths..

Microscopy demonstrated that the silica particles were spherical (Figure 6). The scattering machine consists of a vacuum chamber, a rotatable VUV photon detector, and an aerosol sampler. After particles are size-selected by a differential mobility analyzer, they enter the vacuum chamber and are accelerated in a jet, forming a particle beam. The particle beam and VUV photon beam intersect in the vacuum chamber. Scattered photons from the intersection region were collected with a VUV photon detector.

Scattering intensities for particles of different sizes were measured at two wavelengths, 118.1 nm (VUV) and 532 nm (visible), under otherwise comparable conditions (e.g., scattering angle). The measurements revealed that the size-sensitivity curve of VUV scattering had an onset at about 70 nm (i.e., particles with sizes below 70 nm are not transmitted efficiently through the endstation). In contrast, visible scattering had an onset at about 250 nm (Figure 7). This illustrates that VUV scattering is more sensitive than visible-light scattering. Even though the result is not yet at the limits of detection, it clearly shows the potential to directly probe ultrafine particles by means of VUV scattering. Further improvements of this apparatus are possible and should push the detection limit below 70 nm.

The Berkeley group also measured the angular distributions of scattered signals from silica particles with diameters of 70 and 200 nm that were illuminated with VUV light at 118.1 nm and 145.9 nm and fit the data with calculations based on Mie theory (Figure 8). Comparing Mie theory expectations with experimental results for

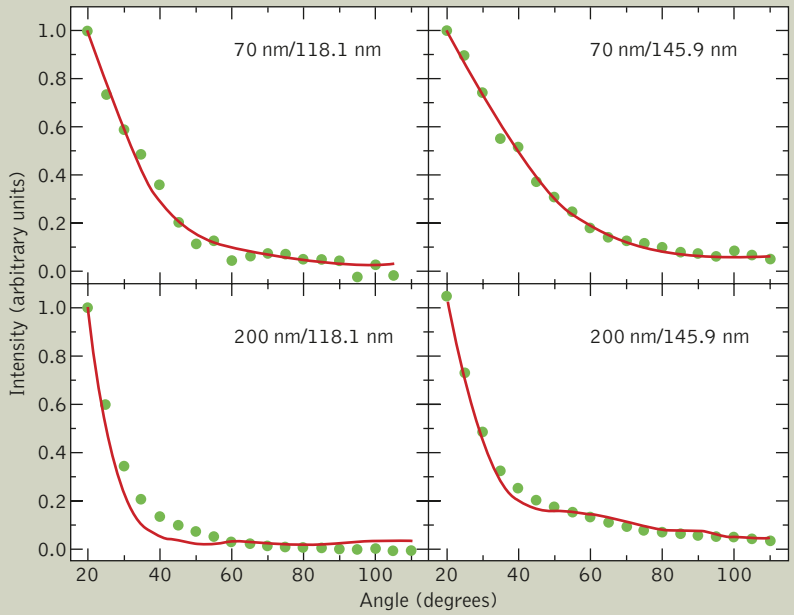

FIGURE 8
Angular distributions of scattered signals from 70- and 200-nm silica particles illuminated with 118.1 and 145.9-nm VUV light. The circles represent the experimental data. The red lines denote the fit of the Mie calculation. The diameter of particles was measured with a differential mobility analyzer that selects sizes via particle mobility (so that multiply charged particles that are larger can have the same mobility as smaller, singly charged particles).

scattering is important, since the optical properties of most matter change dramatically at VUV wavelengths. In particular, the particles become strongly absorbing. If the comparisons are good, then practical designs for scattering instruments can be based on the Mie calculation. The results show that VUV scattering of ultrafine particles does follow Mie theory, although there are small discrepancies between the fitting and experimental data that may result from inhomogeneities in the generated silica particles.

Additional experiments are in progress to benchmark the sensitivity for detection of ultrasmall particles.

Jinian Shu (Berkeley Lab).

INVESTIGATORS
J. Shu, K.R. Wilson, and M. Ahmed (Berkeley Lab); A.N. Arrowsmith (UC Berkeley and University of Colorado, Boulder); and S.R. Leone (Berkeley Lab and UC Berkeley).

PUBLICATIONS
J. Shu, K.R. Wilson, A. Arrowsmith, M. Ahmed, and S.R. Leone, "Light scattering of ultrafine silica particles by VUV synchrotron radiation," *Nano Lett.* **5,** 1009 (2005).

FUNDING
U.S. DOE BES.

Aerosol Time-of-Flight Mass Spectrometry for Organic Constituents

Imagine trying to determine the complete chemical composition of an aerosol particle, with a diameter of just 1 micrometer, a mass of only one tenth of one trillionth of a gram, and composition of more than 100 different organic compounds, many of which are very unstable and not commonly known. This is the challenge faced by environmental chemists in their quest to understand the origin, reactivities, and health effects of aerosol particles dispersed in the Earth's troposphere. Mass spectrometry has the required sensitivity, but the complex mixture of organic compounds, which can easily break apart in the ionization process required for mass analysis, greatly complicates the task. One of the gentlest methods for ionizing organic molecules is by VUV radiation, with the wavelength tuned to the exact energy needed to ionize the molecule. Mysak et al. have constructed an aerosol particle photoionization mass spectrometer to investigate the chemical composition of aerosol particles prepared in different ways. The intensity and variable wavelength (tunability) of synchrotron radiation is proving to be the ideal ionization source for such studies.

Mass spectrometric detection of aerosol particles in the atmosphere is a rapidly growing activity. Instruments sufficiently small to be deployed in various locations around the globe as well as in the nose cones of airplanes have been developed, and at least two commercial companies sell portable instruments. However, the detection of delicate organic molecules, which make up as much as 50% of tropospheric aerosols, requires a more delicate ionization method than used in these instruments. To meet this need, a group of researchers from the University of North Carolina, Chapel Hill, and Berkeley Lab have constructed an aerosol particle mass spectrometer for use at the ALS Chemical Dynamics Beamline (Beamline 9.0.2). The combination of the spectrometer and photoionization with tunable VUV light at a synchrotron source is proving an ideal tool for aerosol composition analysis.

Most commercial aerosol instruments use laser ablation or electron impact as the ionization source. More recently, researchers at the University of North Carolina pioneered VUV lasers as an ionization source. However, the difficulty in tuning the laser wavelength and its limitation to particles larger than 1 □m in diameter have prevented them from identifying many organic constituents as well as investigating the more interesting particles with diameters of 30 to 500 nm that are formed in the troposphere when, for instance, naturally emitted α-pinene reacts with man-made ozone.

In the new instrument, particles are generated in both pure form and as a result of gas-phase condensation or gas–surface reactions. The stream of particles enters the mass spectrometer through an aerodynamic lens that focuses the particles to an exit aperture, where they are accelerated into the first stage of the mass spectrometer (Figure 9). The particles then move into the high-vacuum part of the instrument, where they are vaporized by a heater located close to the ionization region, and the vapor molecules are ionized by the VUV beam for mass analysis by ion time of flight. Because the ALS beam is quasi-continuous, it is possible to investigate a continuous stream of small particles, thereby permitting the analysis of small and large particles.

Readily tunable VUV radiation (from 7 to 12 eV) and high photon flux (10^{15} photons/s) at Beamline 9.0.2 is essential. The resulting ability to ionize and detect delicate organic molecules is illustrated in the mass spectrum of oleic acid (Figure 10). The dominant peak is the parent ion, which is nearly absent in typical electron-impact-ionization mass spectra. The photoionization efficiency spectrum (ion signal versus photon energy) demonstrates the ability to determine ionization energies of nonvolatile compounds.

The advantage of using tunable VUV radiation is evident when an aerosol resulting from chemical reactions is investigated. These particles consist of numerous molecules ranging in mass from 50 to 500 amu. Their identification is greatly facilitated with tunable VUV radiation because the photon source can be tuned to below and above the ionization energy of a particular

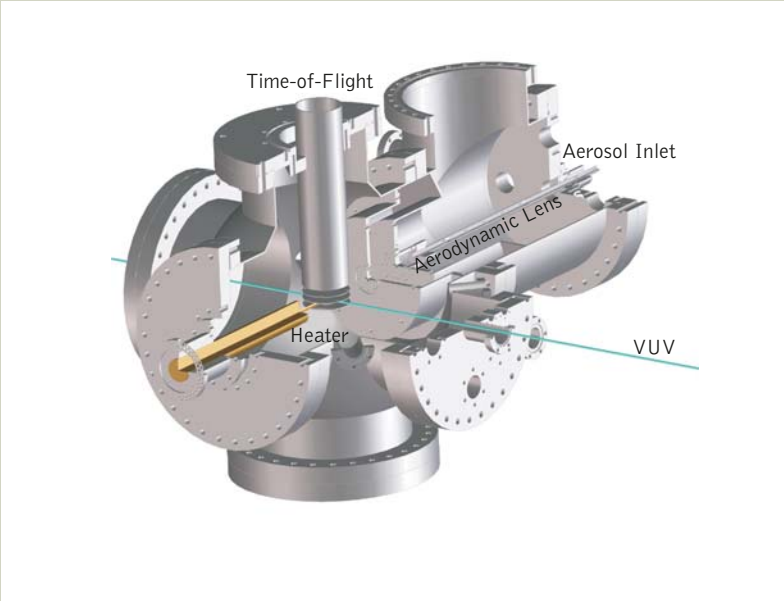

FIGURE 9
Schematic of aerosol time-of-flight mass spectrometer.

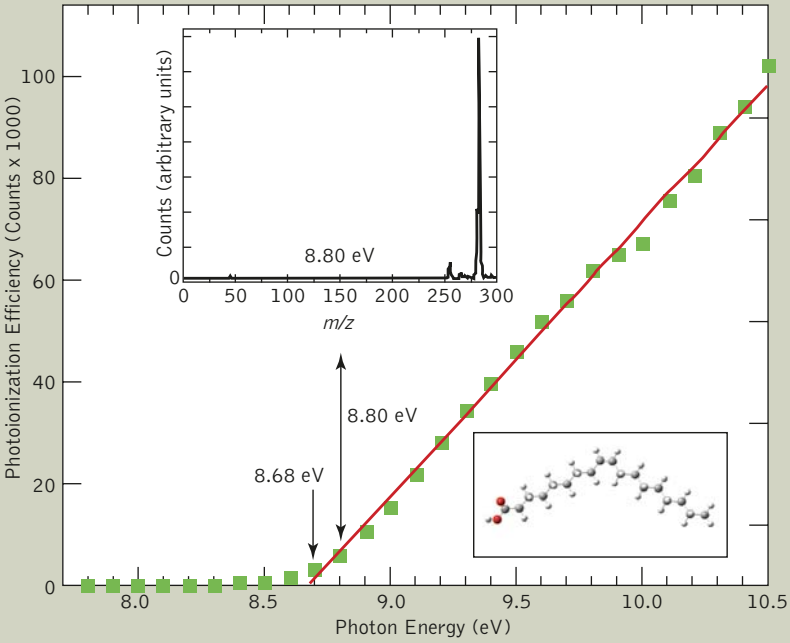

FIGURE 10
The photoionization efficiency curve for oleic acid (ball-and-stick structure shown in lower inset) indicates that its ionization potential is 8.68 eV. Upper inset: The dominant peak in the photoionization mass spectra of oleic acid at a photon energy of 8.80 eV is not present with electron-impact ionization.

molecule, thereby identifying it not only by its mass, but also by its ionization energy; that is, it is a two-dimensional analytical tool.

An example of the complex mass spectra that are typical of such chemical reactions was obtained by reacting ozone gas with α-pinene vapor (Figure 11). When this naturally occurring terpene reacts with ozone, the ozone attacks the α-pinene double bond, thereby initiating a complex series of reactions, the result of which is the production of molecules that contain alcohol and acid groups with much lower vapor pressure. These low-volatility species then nucleate into nanodroplets and quickly grow in diameter to 20 to 100 nm. Although many of the peaks are a result of dissociative photoionization, this mass spectrum clearly demonstrates that the number of molecular species generated in the ozone–pinene reaction is dauntingly large.

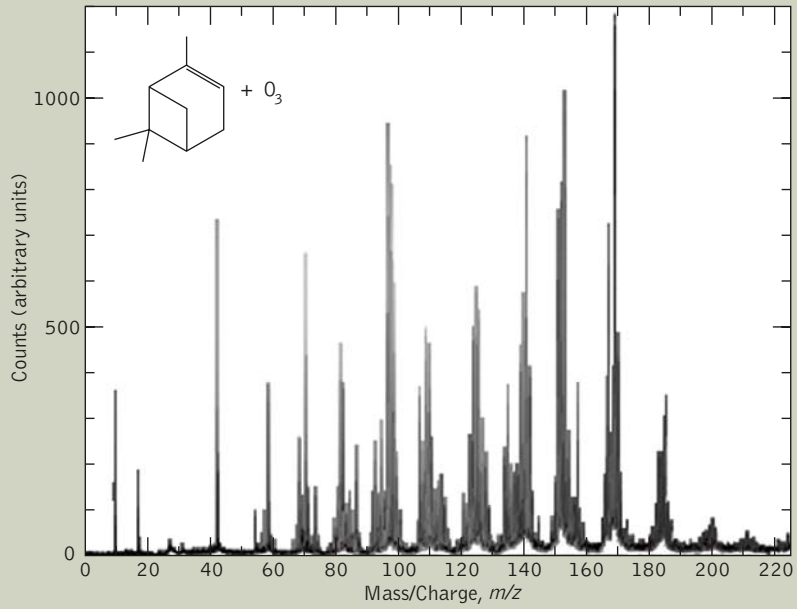

FIGURE 11
Oxidation by ozone of the terpene α-pinene (reacted in a flow tube and sampled into the aerosol time-of-flight mass spectrometer) shows the dauntingly complex mass spectrum obtained after 10 seconds of reaction time and a photon energy of 10.5 eV for ionizing the constituent molecules. Inset: Two gas-phase reactants, ozone and α-pinene, used to form liquid aerosols.

INVESTIGATORS

E.R.Mysak and T. Baer (University of North Carolina, Chapel Hill) and K.R. Wilson, M. Jimenez-Cruz, and M. Ahmed (Berkeley Lab).

PUBLICATIONS

E.R. Mysak, K.R. Wilson, M. Jimenez-Cruz, M. Ahmed, and T. Baer, "Synchrotron radiation based aerosol time-of-flight mass spectrometry for organic constituents," *Anal. Chem.* **77,** 5953 (2005).

FUNDING

U.S. National Science Foundation and U.S. DOE BES.

Tomas Baer and Erin Mysak (University of North Carolina, Chapel Hill).

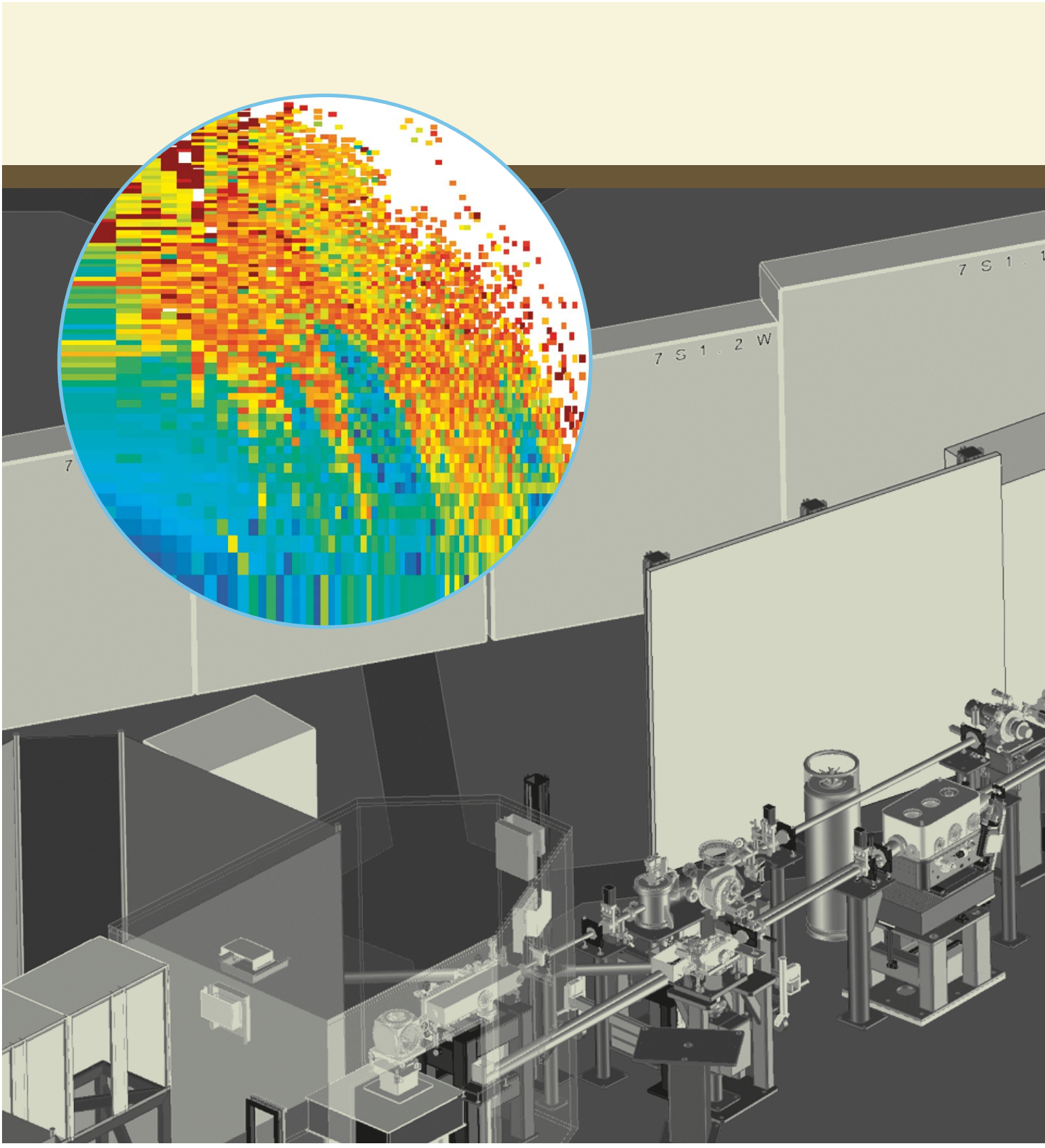
7 S 1 . 2 W

Facility Report

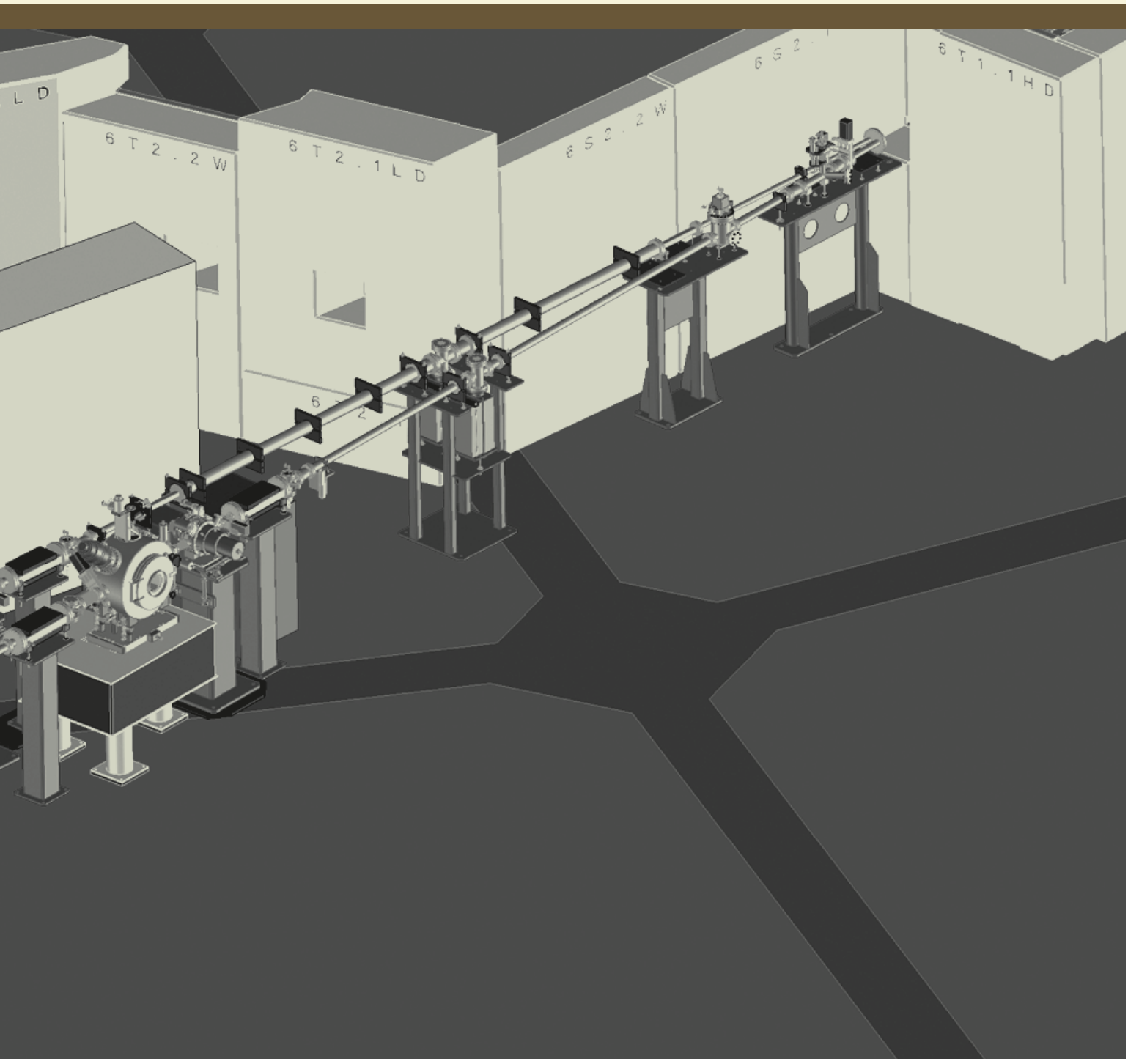

Operations

BEN FEINBERG, DIVISION DEPUTY FOR OPERATIONS

Operations and Availability

The mission of the ALS is to "support users in doing outstanding science in a safe environment." Critical to that support is the delivery of high-quality beam. The delivery of beam according to the published schedule, along with an efficient, effective safety program, allow ALS researchers to make maximum use of the limited beam time. In 2005, the ALS maintained its exemplary operations record while continuing to make significant improvements in beam quality and reliability. In addition, the Operations groups worked with the Experimental Systems Group (ESG) and other groups at Berkeley Lab to bring online a new beamline for examining materials using x-ray pump–probe experiments on the femtosecond time scale. This beamline, the first of two branches, makes use of the first in-vacuum undulator at the ALS designed to produce both soft and hard x rays.

The research community at the ALS has become accustomed to high operational efficiency and reliability, and it was not disappointed during this period. As shown in Figure 1, the ALS delivered beam to users over 96% of the time scheduled for user operations in fiscal year (FY) 2005, doing even better than the previous year.

As in years past, we look very carefully at our different systems to determine where to focus our resources to improve reliability. Figure 2 shows our "lost user-beam analysis" over the past several years. These figures allow us to pinpoint the most frequent causes of lost user-beam time. Reductions in beam time lost due to the longitudinal feedback system (LFB) in 2005 resulted from the installation of higher-order-mode (HOM) dampers since 2004.

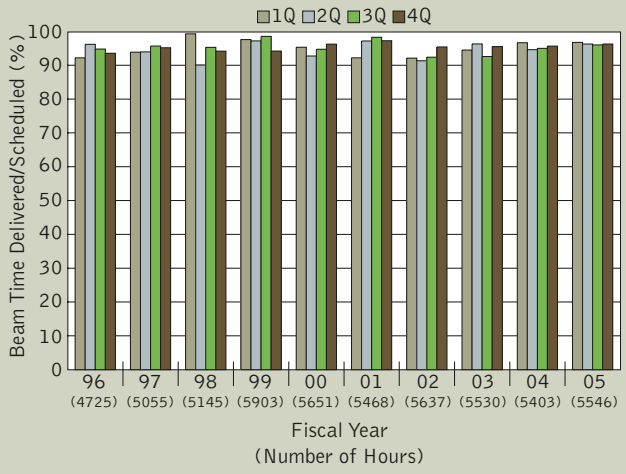

FIGURE 1
ALS operational availability (percentage of scheduled user-beam time actually delivered).

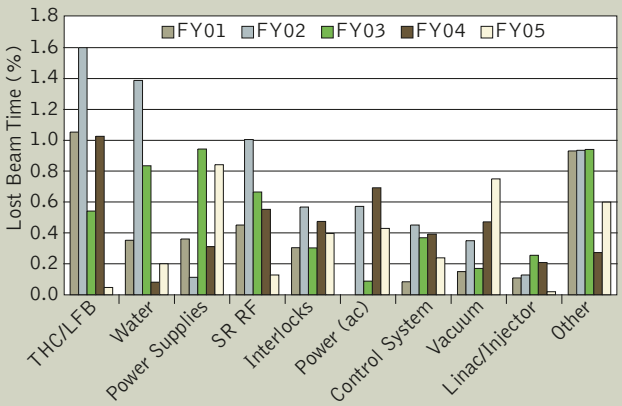

FIGURE 2
Lost user-beam analysis. The bars represent the percentage of user-beam time lost over the last five fiscal years, separating out the various machine systems responsible. THC/LFB = third-harmonic cavities/longitudinal feedback; SR RF = storage-ring rf power.

Facility Growth and Changes in User and Instrument Hours

This year we had one five-week installation shutdown primarily to install a new in-vacuum insertion device in Sector 6. This undulator will serve the femtosecond slicing source in that sector by providing both soft and hard x rays for two branch lines. The new insertion-device beamline, for femtosecond spectroscopy, received its first light to start the commissioning process. We also installed one of the HOM dampers in the storage-ring rf cavity to improve the stability of the beam and replaced the superbend cryogenic coolers, which require rebuilding annually.

The monthly operations schedule continued to include the minimum number of maintenance and installation periods consistent with safe, efficient operation. Allowing approximately three days per month for needed maintenance and installation of new instrumentation has provided the maximum number of hours for user operations. The delivered operating hours remained at about the same level in FY 05 as in previous years.

With the constant number of operating hours and the installation of new beamlines, we were able to increase the number of instrument hours (user hours multiplied by the number of beamlines that can simultaneously accept beam). We finished the fiscal year with 37 beamlines operating simultaneously, up from 36 at the beginning of the previous fiscal year. Figure 3 shows the growth in instrument hours since the first full year of ALS operations. This year's growth resulted in the delivery of almost 200,000 instrument hours, an increase of 4% over FY 04.

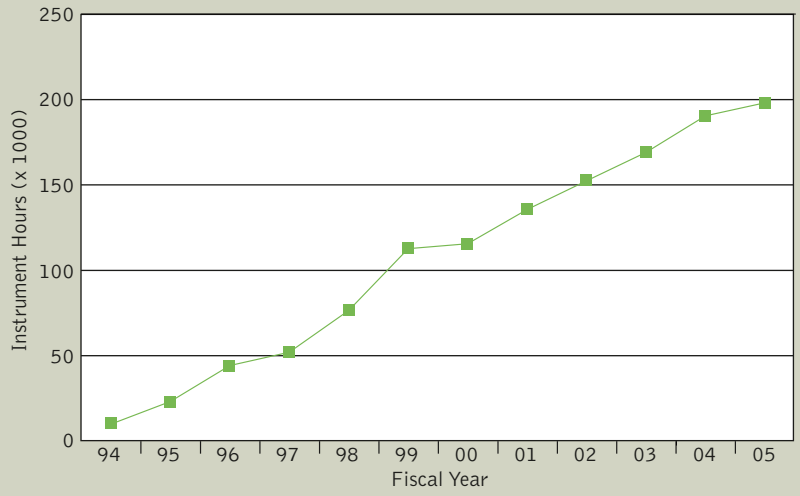

FIGURE 3
Growth in the number of instrument hours (user hours multiplied by the number of simultaneously running beamlines) from year to year.

Beam Quality and Accelerator Operations Improvements

Christoph Steier

During the last year, no large-scale upgrades were implemented at the ALS. However, there were many small and medium-sized projects that helped to improve the beam quality, the reliability of operations, or enabled new beamlines (namely the undulator femtosecond slicing source) to begin routine operation.

In-Vacuum Undulator and Local Dispersion Bump for Femtosecond Slicing

As explained in previous Activity Reports, the upgrade of the femtosecond slicing source, which uses an in-vacuum undulator as a radiator, requires a significant modification of the coupled ALS lattice to provide the necessary spatial separation of the energy-modulated bunch slices. The technique uses 10–12 skew quadrupole magnets in several arcs to generate a closed vertical dispersion bump while at the same time keeping global as well as local coupling at the in-vacuum undulator very small. To make this possible, several additional trim coils on sextupole magnets were rewired to provide enough skew quadrupole strength and flexibility. The lattice functions of the new lattice are shown in Figure 4. This new lattice has no measurable side effects for the nonfemtoslicing users and is now being used as the default lattice of the ALS.

The new in-vacuum undulator also constitutes the smallest vertical physical aperture in the ALS. Before it was installed, the smallest inner aperture of any insertion-device vacuum vessel was 8.9 mm. The new undulator allows a minimum magnetic gap of 5.5 mm, corresponding to a vacuum aperture of just over 5 mm. Over the last several years, many studies were carried out to predict the impact of such small apertures, particularly on beam lifetime. By optimizing control of the lattice symmetry, lowering the vertical beta functions in all straight sections, and refining control of global and local coupling as well as the vertical dispersion (see previous Activity Reports), it was possible to minimize the impact of the aperture reduction on the Touschek lifetime (Figure 5). We also studied the impact of the small gap on instability thresholds and found a small reduction in the vertical transverse-mode coupling instability (TMCI) threshold, which could easily be compensated for with the existing ALS fast feedback systems.

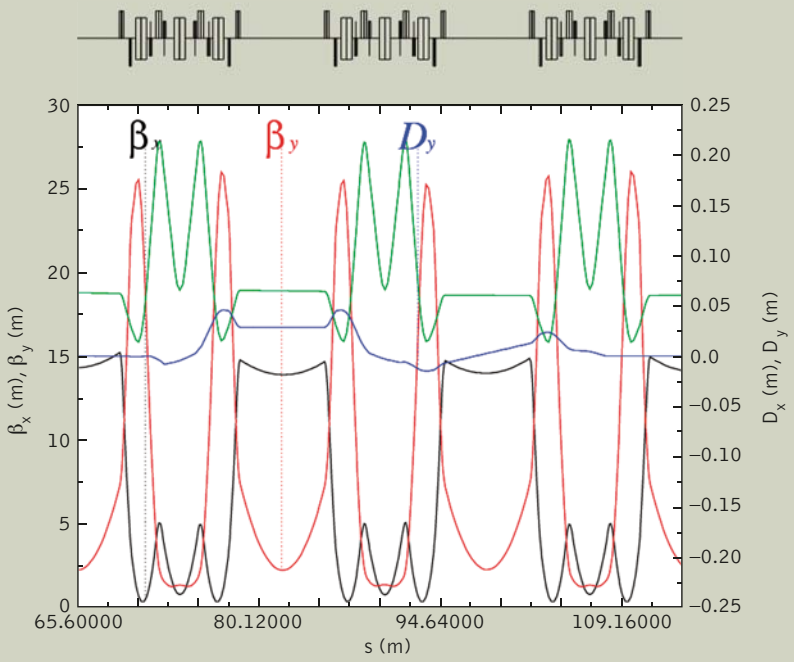

FIGURE 4
Lattice functions for ALS Sectors 5, 6, and 7 with the vertical dispersion bump for the undulator femtosecond slicing source. This has been used as the default user lattice since December 2005.

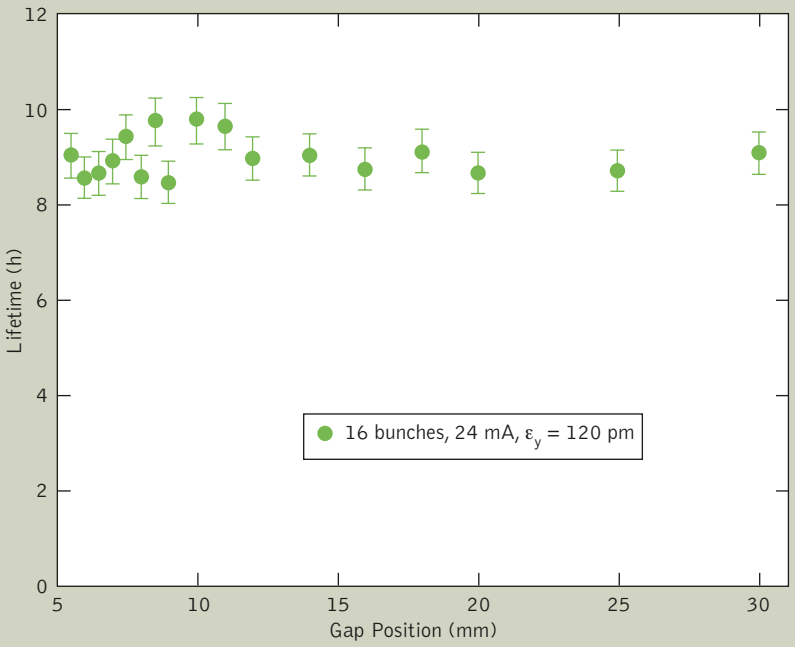

FIGURE 5
Touschek lifetime as a function of the magnetic gap of the in-vacuum undulator in Sector 6. Within the measurement errors, there is no reduction in Touschek lifetime down to the minimum magnetic gap of 5.5 mm.

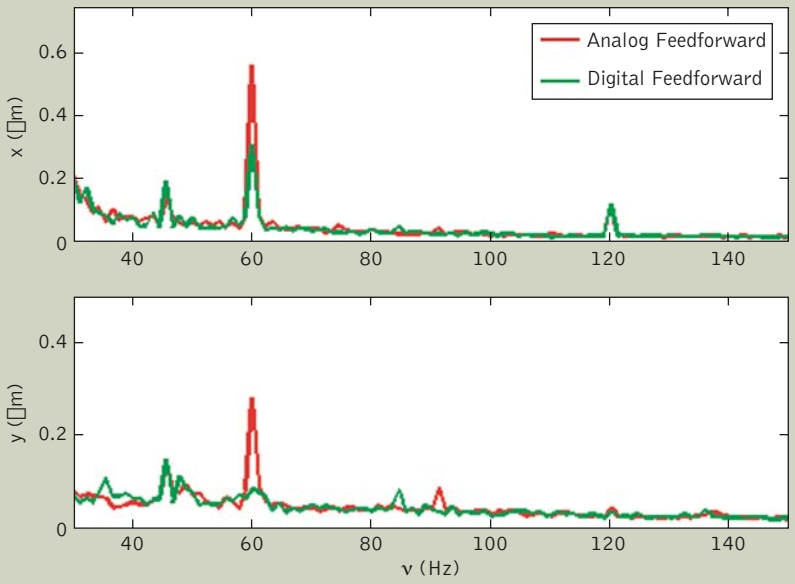

FIGURE 6
Comparison of the beam orbit noise spectrum of the ALS for frequencies between 30 and 150 Hz. The slow and fast orbit feedbacks were switched off. Replacing the fast analog feedforward significantly reduced the steady-state 60-Hz orbit noise.

Digital EPU Feedforward

To compensate for the orbit distortion caused by the fast-switching elliptically polarizing undulators (EPUs) at the ALS, a fast local feedforward system with two-dimensional compensation tables was implemented years ago, allowing fast EPU switching while ensuring transparent orbit stability for all other users. However, with the additional diagnostic capabilities of the fast orbit feedback system, it was determined that ground loops and noise, introduced into the fast corrector magnets in the analog feedforward system, significantly contributed to the steady-state 60-Hz orbit noise on the beam. With the advent of faster computer networks, it became feasible to replace the old analog systems, which used long signal cables, with a digital system that transmits set-point changes via the network. This new digital feedforward system reduced the steady-state 60-Hz orbit noise significantly—eliminating it nearly completely in the vertical plane even without additional fast feedback. Figure 6 compares the beam orbit noise spectrum of the ALS for frequencies between 30 and 150 Hz. The slow and fast orbit feedbacks were switched off for the measurement.

The performance of the digital feedforward system in terms of update rate (>100 Hz) and latency for the dipole correctors is the same as for the old analog system it replaced. In addition, it incorporates the skew quadrupole feedforward for all EPUs, which ensures the ALS beam-size stability, significantly improving its reliability and bandwidth.

Other Improvements

In the ongoing quest to provide better orbit stability, new input/output boards for the control system were designed, manufactured, and installed. These produce lower noise, smaller long-term analog drifts, and potentially faster operation of the fast orbit feedback system. They are now installed in all the main computer crates controlling storage-ring hardware. In addition, the networking hardware was upgraded to Gbit bandwidth to prepare for future upgrades of the fast feedback systems. As part of the improvements, many beam-position monitor (BPM) modules were replaced. The new modules have slightly lower noise figures, are easier to maintain and exchange, and provide flexible clock frequencies, allowing smaller latency times.

To improve beam-size stability and to partially mitigate the dynamic aperture effects of EPUs, a two-dimensional feedforward system to compensate for focusing effects was implemented with an update rate of 1 Hz. It supplements the existing fast systems for dipole and skew quadrupole compensation and provides correction of both tune shift and beta beating.

With the installation of the third EPU with a 5-cm period, dedicated to the new PEEM3 beamline (11.0.2), the Sector 11 straight section became the first chicaned straight section at the ALS filled with two insertion devices feeding completely independent beamlines. This arrangement provides additional capacity for high-brightness beamlines but adds potential complications to accelerator operations. As it turned out, the individual orbit, tune, and skew quadrupole compensations for both devices work fine together and the beamlines can be used in a fully transparent way. As part of this work, two additional skew quadrupole compensation coils were installed for the PEEM3 EPU and the upcoming longer-period MERLIN EPU.

As part of the top-off upgrade project, several (currently four) adjustable vertical collimators were designed and installed. Their purpose is to localize particle losses (both for injected and for Touschek- or gas-scattered particles) and thereby reduce the background radiation dose rates on the experiment floor as well as the potentially damaging dose rate for permanent-magnet insertion devices. Figure 7 shows an engineering drawing of one of the collimators. They were designed to provide small impedance and are water cooled for reliable operation. Initial tests with beam were successful and the collimators are already being used to reduce the dose rate for the EPU in Sector 4 as well as around beamline frontends.

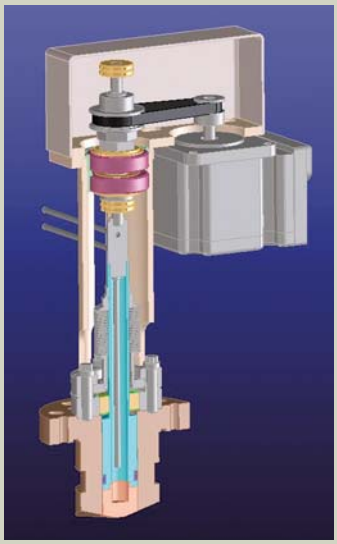

FIGURE 7
Layout of the adjustable vertical collimators that were installed to localize beam losses and therefore reduce the radiation exposure of insertion devices as well as the general radiation background dose rate on the experiment floor.

As it is every year, the storage ring was surveyed. An improved technique was used to stabilize the temperature in the storage-ring tunnel during the shutdown, when the tunnel is opened at many places. In addition, the adjustment of measured data on the temperature difference between conditions during the survey and normal operation was improved. The overall alignment of the girders was found to be sufficiently good not to require any realignment. Nevertheless, a partial realignment of individual magnets was performed for the first time since the initial installation of the ALS, resulting in smaller uncorrected gradient and skew gradient feed-down errors in sextupoles.

As mentioned above, during this year's shutdown a waveguide HOM damper was installed in one of the main rf cavities of the ALS, completing earlier work to damp higher-order modes. With this addition, the ALS beam is now nearly passively stable in the longitudinal plane at 1.9 GeV (for typical third-harmonic cavity settings). The final waveguide HOM damper for the second main rf cavity will be installed in the coming year. The improvements in the HOM spectrum of the rf cavities have basically eliminated problems with the multibunch feedback systems by reducing the load on them.

Finally, as part of top-off preparations, work was done to improve the method used to perform bunch cleaning in two-bunch mode. Further details can be found in the following Accelerator Physics section.

Accelerator Physics

DAVID ROBIN, ACCELERATOR PHYSICS GROUP LEADER

The Accelerator Physics Group plays several important roles in the ALS mission of supporting users in doing outstanding science in a safe environment. The first is to make certain that the ALS provides high-quality beam in a reliable manner to users. The second is to strive to understand and continually improve the performance of the facility, keeping it at the forefront of synchrotron radiation sources. The third is to ensure that machine upgrades are implemented smoothly with minimal adverse impact to users. The fourth is to study potential facility upgrades that will enhance the capabilities and capacities of the ALS.

This year significant gains were realized in understanding and improving the quality of the beams that were delivered to users. We continued to unravel the mysteries of the effect of the EPUs on the electron beam. Last year's Activity Report described how small but correlated motion of the EPU magnetic blocks was responsible for changes in the beam size. This year we investigated the degradation of injection efficiency due to EPU polarization settings. This effect, known as the dynamic multipole effect, is very important, particularly with top-off operation and for larger-period EPUs such as MERLIN. The dynamic multipole correction of EPUs is described below.

Another improvement related to beam quality was the development of a new technique for purifying the bunch fill pattern (so-called "bunch cleaning"). Previously, a purely frequency-based technique was used that was very effective but had some limitations. The new technique, first developed at SPring-8, has several advantages over the older bunch-purifying technique: it is faster, can target specific bunches, and is likely more compatible with top-off operation.

The technique involves mixing two signals. A schematic of the setup is shown in Figure 1. The first signal is generated by an existing sinusoidal signal generator. The second signal is a square wave that goes through zero whenever a bunch to be saved passes the kicker (Figure 2). It is generated by a fast, 500-MHz, multipurpose board developed by the ALS Electrical Engineering Instrumentation Group. The multipurpose board has a very large bandwidth (BW) and no timing drift. It is also very reliable and easy to program. An example of the effectiveness of the new bunch-cleaning technique is shown in Figure 3.

Our first in-vacuum insertion device (IVID) was installed in the ALS during the May 2005 shutdown. This device is part of the femtosecond slicing upgrade and acts as the radiator for the sliced beam. At the IVID's minimum gap, the vertical vacuum aperture is only 5 mm, the smallest vacuum gap of any ALS insertion device. Prior to the installation of the IVID, the smallest vacuum aperture was 8.9 mm. In

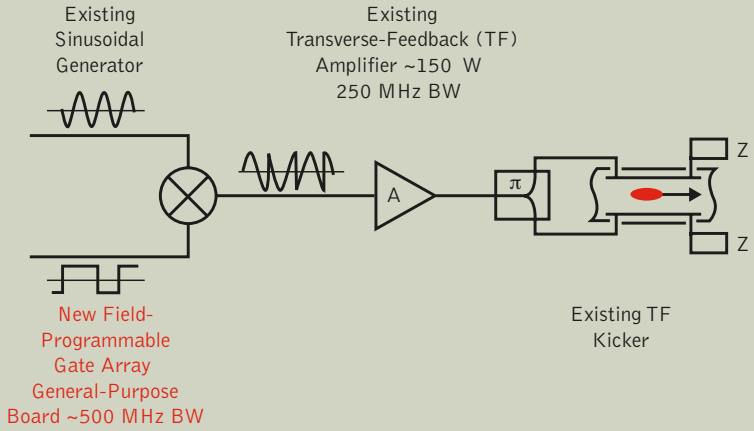

FIGURE 1
The mixed signal is amplified and sent to a transverse-feedback (TF) kicker to excite the beam.

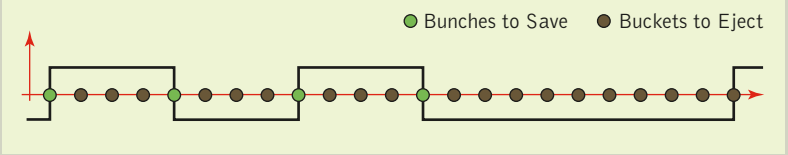

FIGURE 2
The signal from the multipurpose board has a zero crossing at each bunch to be saved.

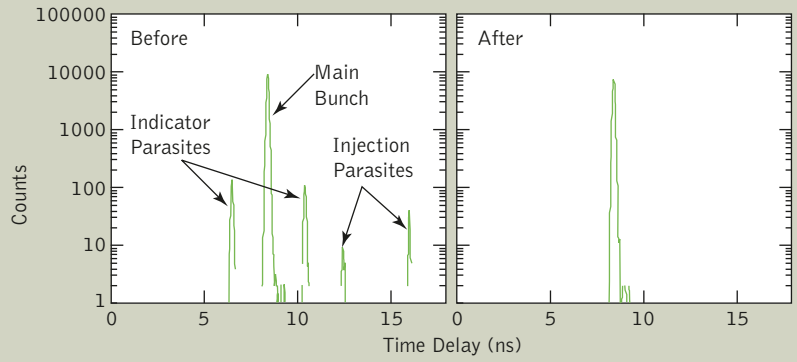

FIGURE 3
Bunch purity before and after cleaning as measured at Beamline 7.0.1 (courtesy of Anton Tremsin, Jinghua Guo, Chao-Wen Chiu).

addition, a new storage-ring magnetic lattice has been created that is compatible with femtosecond slicing. In this lattice, there is a vertical dispersion bump in the IVID. The effects of the IVID and the new lattice have been studied and show no significant impact on the performance of the ALS. The new lattice has been commissioned and is being used in normal ALS operation.

The highest near-term priority is the upgrade of ALS operation to continuous top-off injection. With top-off injection, the ALS will benefit from increased time-averaged current (in our case, a 100% increase) and much-improved beam stability due to a constant heat load on the accelerator vacuum chamber and especially on beamline optics. In preparation for top-off, many long-lead items were purchased in 2005. Also, several additions were made to the storage ring. In particular, four new scrapers were installed to localize losses and thus reduce radiation levels on the storage-ring floor.

Dynamic Multipole Correction of EPUs

SOREN PRESTEMON, CHRISTOPH STEIER, WEISHI WAN

The ALS has successfully installed a number of APPLE II-type EPUs capable of generating high-brightness photon beams with variable linear, elliptical, or circular polarization characteristics. The existing devices have a period of 50 mm. A 90-mm-period device is currently being designed and fabricated for the new ultrahigh-resolution MERLIN beamline under construction. The interaction of the existing devices with the stored electron beam has been intensely studied at the ALS because of the observation of strong polarization-dependent beam-dynamics effects, aided by very well understood beam behavior. The effects can be attributed to three distinct sources:

1. The original ALS EPU end design was developed to provide steering- and displacement-free behavior for all row-phase and gap configurations, assuming $m = 1$ permanent-magnet material. However, the nonunity relative permeability, $m \sim 1.15$, of the magnetic blocks introduces a row-phase-dependent dipole (steering) field. This effect has been significantly reduced for the most recent EPUs by introducing an optimized end design [1, 2]. For older devices, a fast feedforward system with multidimensional correction tables was implemented.
2. A shift-dependent skew-quadrupole term was found to emanate from micrometer-level magnetic-force-induced motion of the permanent-magnet blocks. Trim coils were installed on the vacuum chambers of the existing EPUs to allow for feedforward compensation of skew-quadrupole fields [3].
3. Beam-based measurements and simulations show that the trans-

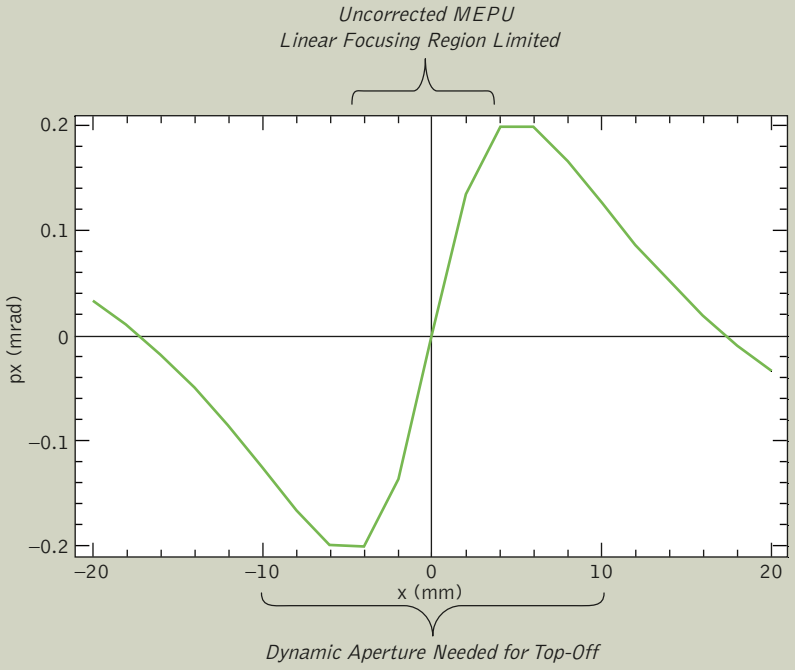

FIGURE 4
Angular deflection at the exit of the MEPU device operating in linear vertical polarization mode, based on particles with initial location (x,y = 0). Tracking was performed using Radia [6] and independently verified using COSY [7].

verse dynamic aperture of the ALS is reduced by EPU fields and that the reduction is shift-dependent. The effect is noticeable during existing ALS operation, but will become intolerable during top-off operation, when electrons will be injected with large offsets while the EPUs are in operation.

Basic design modifications are being implemented on the MERLIN EPU (MEPU) to address the first two issues. The dynamic aperture concern, however, is significantly exacerbated by the long period of the MEPU. To address the issue, we have performed detailed magnetic and tracking analysis of a passive correction method first proposed at the ESRF and later successfully tested at BESSY [4].

It is well known that undulator fields have focusing and defocusing effects on passing particles. The effect is not seen in integrated fields; it stems from variations in field strength as the particle "wiggles" through the structure. An ideal focusing element will provide an angular deflection proportional to the ray offset. Figure 4 shows the deflection angle for particles tracked through the MEPU device. The strongly nonlinear behavior for large (>5-mm) particle offsets results in a reduced dynamic aperture.

To address this issue, passive shims have been proposed [5] that act to linearize the angular kick with displacement over a broad range of phase-shift modes of operation. The shims are small pieces of magnetic steel, about 4 mm wide, 100–200 micrometers thick, extending the length of a block, and located on the beam-side face and inner wall of certain blocks (Figure 5). Detailed Radia [6] models were used to optimize the shim sizes, number, and distribution among the four MEPU quadrants so as to maximize the dynamic aperture for all polarization modes.

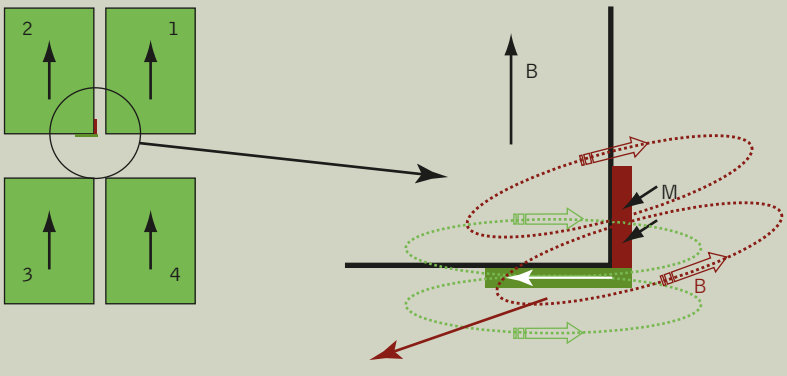

FIGURE 5
Sketch of passive magnetic steel shims (left) and the magnetization and resulting fields they produce (right). A combination of such shims, appropriately distributed on different blocks in all four quadrants, can produce fields that compensate for the nonlinear dynamic focusing.

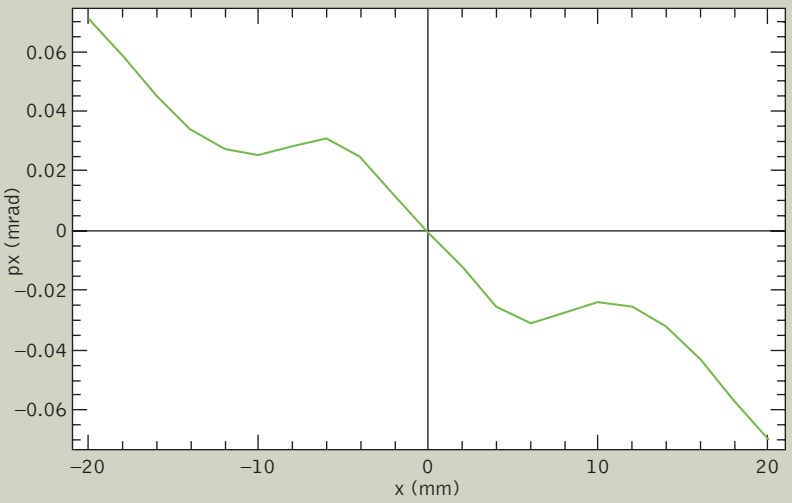

FIGURE 6
Angular deflection in linear vertical polarization mode, as defined in Figure 4, with optimized shims. Note the 60% reduction in peak angular kick and the nearly linear dependence of angle on offset.

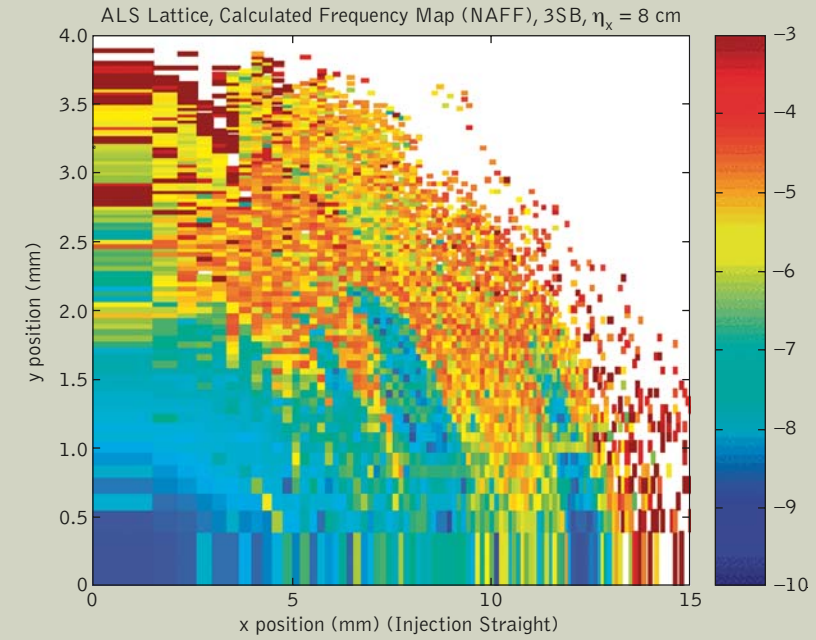

FIGURE 7
Frequency-map analysis of the MEPU device in vertical polarization mode. Top-off injection is at ~10 mm. Without passive shimming, the simulations show a remaining dynamic aperture of only about 3 mm.

Based on detailed tracking simulations, the final distribution of shims will provide sufficient dynamic aperture for operation in top-off mode in all elliptical modes and in vertical and horizontal polarization modes. Variable linear modes around 45° will not be allowed. This restriction is acceptable for the physics of interest to the MERLIN beamline.

As an example, Figure 6 shows the angular kick produced on the beam by the MEPU after shimming. Note the mostly linearized profile field dependence and the reduction in amplitude by a factor of about 3. Figure 7 shows a simulated frequency map of the shimmed device operating in linear vertical polarization mode, suggesting that injection at an offset of around 10 mm during top-off should be acceptable. As is the case for the existing unshimmed EPUs, adjacent normal quadrupoles will be used to compensate for the (linear) focusing effects.

Beam-based measurements and simulations suggest that shimming will also be required for the EPU50 devices for top-off operation, although the reduction in dynamic aperture is not as severe as for the MEPU device. The analysis work developed for the MEPU is currently being applied to the existing EPU50 devices at the ALS. An optimized set of shims will be developed and tested on the EPU50s in the next few months to validate the design concept and optimization process in anticipation of top-off operation.

References

1. J. Chavanne, P. Elleaume, and P. Van Vaerenbergh, "End field structures for linear/helical insertion devices," in *Proceedings of the 1999 Particle Accelerator Conference,* p. 2665 (1999); New York, New York, March 29–April 2, 1999.
2. R. Schlueter, S. Marks, and S. Prestemon, "Elliptically polarizing undulator end designs," presented at the 19th International Conference on Magnet Technology (MT19), Genoa, Italy, September 18–23, 2005.
3. C. Steier, S. Marks, S. Prestemon, D. Robin, R. Schlueter, and A. Wolski, "Study of row phase dependent skew quadrupole fields in Apple-II Type EPUs at the ALS," in *EPAC 2004,* p. 479 (2004); 9th European Particle Accelerator Conference, Lucerne, Switzerland, July 5–9, 2004.
4. P. Kuske, "Effects of fringe fields and insertion devices revealed through experimental frequency map analysis," in *Proceedings of the 2005 Particle Accelerator Conference,* p. 266 (2005); Knoxville, Tennessee, May 16–20, 2005.
5. J. Chavanne, P. Van Vaerenbergh , P. Elleaume, and T. Günzel, "Recent achievements and future prospect of ID activities at the ESRF," in *Proceedings of the 2000 European Particle Accelerator Conference,* p. 2346 (2000); Vienna, Austria, June 26–30, 2000.
6. P. Elleaume, O. Chubar, and J. Chavanne, "Computing 3D magnetic fields from insertion devices," in *Proceedings of the 1997 Particle Accelerator Conference,* p. 3509 (1997); Vancouver, Canada, May 12–16, 1997.
7. M. Berz, and K. Makimo, *COSY INFINITY Version 8.1 User's Guide and Reference Manual,* Technical Report MSUHEP-20704, Michigan State University (2001).

Pseudo-Single-Bunch Operation

Greg Portmann, Slawomir Kwiatkowski

Typically, storage-ring light sources operate with the maximum number of electron bunches possible, with a gap for ion clearing. By evenly distributing the beam current, the overall beam lifetime is maximized. The ALS has 2 nanoseconds between bunches and typically operates with 276 bunches out of a possible 328. For users doing timing experiments, this bunch separation is too small; they would prefer to see only one or two bunches in the ring. The ALS allocates four weeks every year for dedicated two-bunch operation.

To provide more flexible operations and substantially increase the amount of operating time for time-of-flight experimenters, a "pseudo-single-bunch" mode of operation was proposed as part of the ALS's strategic planning process. In this mode, the "camshaft" electron bunch (the use of which arose many years ago out of the needs of time-of-flight experimenters) would be kicked into a different vertical closed orbit. By spatially separating the light from this bunch from the main bunch train, the ALS could potentially offer single-bunch operation all year round. By putting this bunch in the middle of the ion-clearing gap, the required bandwidth of the kicker magnets is reduced. Using one kicker magnet running at the ring repetition rate (1.5 MHz), this bunch could be permanently put on a different closed orbit. Using multiple kicker magnets, this bunch could be locally offset at an arbitrary frequency. This pseudo-single-bunch mode of operation is revolutionary and has not been used or tested at any light source so far. Of course, many uncertainties exist and one important aspect of the beam tests will be to evaluate any potential negative impact on other experiments.

Possible Approaches

In principle, pseudo-single-bunch operational modes can be achieved with beamline choppers. In fact, accelerators such as those at the APS and ESRF can achieve similar functionality by installing choppers in the beamlines. However, even with state-of-the-art choppers, this solution requires relatively large gaps in the bunch train, so it is presently only feasible on large accelerators. It also requires each beamline to purchase a relatively expensive chopper that is often difficult to use and maintain. At the ALS, the largest gap in the bunch train is presently 104 nanoseconds, which is out of reach for mechanical x-ray choppers.

There are a number of beamlines at the ALS interested in exploring a pseudo-single-bunch operational mode. A major reason is that experiments using the camshaft bunch will not have to use gated detectors: the ability to use integrating detectors increases the variety and quality of the experiments that can be done. In the case of Beamline 6.0, the combination of the pseudo-single-

bunch mode and a chopper with an open time of just more than one turn will effectively allow single-bunch operation at 1 kHz.

By kicking the camshaft bunch to a different closed orbit, it may be possible to provide pseudo-single-bunch operation during a multibunch user run. There are a number of different ways the orbit of the camshaft bunch can be shaped depending on the number and location of the fast kicker magnets. The easiest thing to do is to install one kicker magnet and place the camshaft bunch on a different global closed orbit. This may not be optimal for all single-bunch or multibunch users, but it would be relatively easy to test the fundamental feasibility of the method. Another obvious possibility is to locally bump the camshaft bunch in one part of the ring. This would isolate the disturbance to a relatively small section of the ring. A third option is to install kicker magnets all around the ring and profile the orbit much like global orbit correction.

Global Orbit Distortions with a Single Kicker Magnet

Using one fast kicker magnet running at 1.5 MHz, the camshaft bunch can be permanently put on a different closed orbit. The figures at right show the change in the closed orbit for the camshaft bunch for a 60-μrad kick located at the end of straight section 2. As shown in Figures 8 and 9, this configuration would be suitable for a number of beamlines. Many of the beamlines numbered X.1.X and X.4.X (i.e., bend-magnet beamlines exiting the storage ring from ports 1 and 4) would see a sizeable separation. Some of the beamlines numbered X.0.X (insertion-device beamlines) and X.2.X and X.3.X (bend-magnet beamlines from ports 2 and 3) would see a sizeable separation as well.

Reduce the Repetition Rate by 1.5/n MHz

If a beamline is not in a favorable location with respect to the single kicker magnet in Sector 2 (Figure 8), it may not be the end of

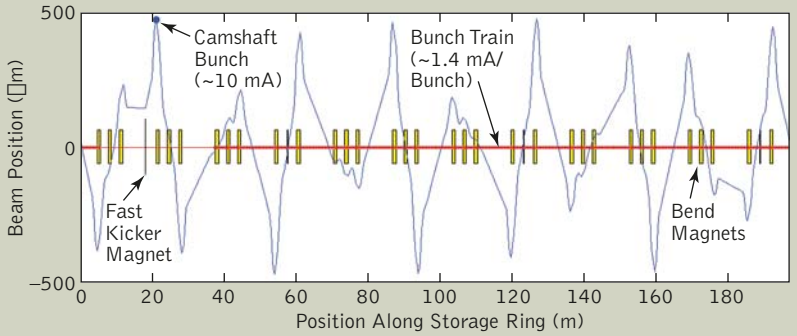

FIGURE 8
Single-kick magnet.

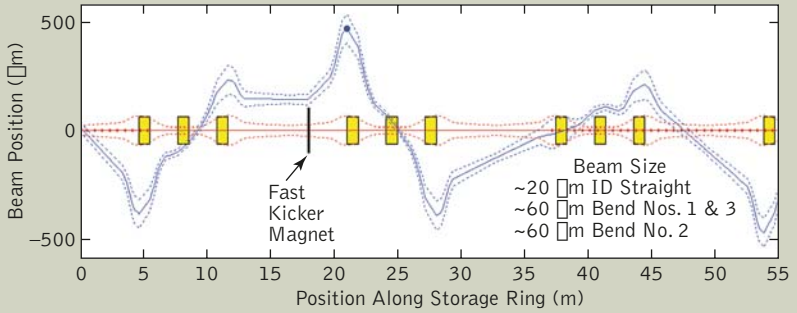

FIGURE 9
Single-kick magnet—first 3 sectors. Dotted lines are the 1σ beam size.

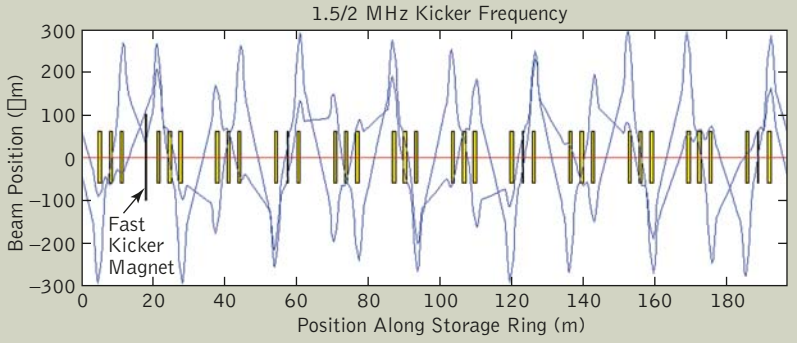

FIGURE 10
Kick every other turn.

the story. The ability to test this method on the X.0.X, X.2.X, and X.3.X beamlines is extremely important. Instead of adding more kicker magnets, one can produce interesting orbits by kicking at less than the revolution rate: 1.5/2 MHz, 1.5/3 MHz, 1.5/4 MHz, etc. Figures 10 and 11 show the closed orbits for kicking at 750 and 500 kHz. Notice that it takes 2, 3, 4, etc. turns for the orbit to close.

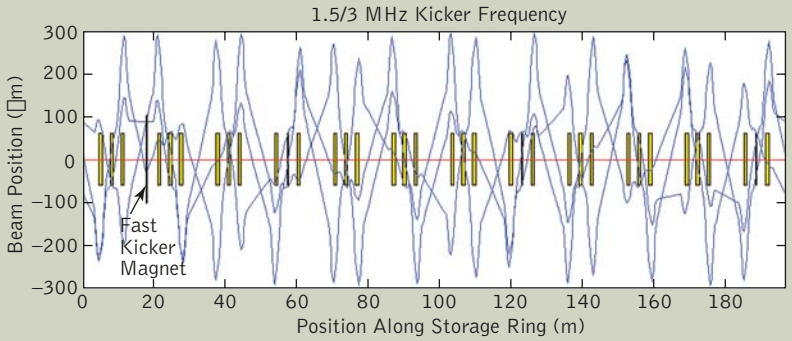

FIGURE 11
Kick every third turn.

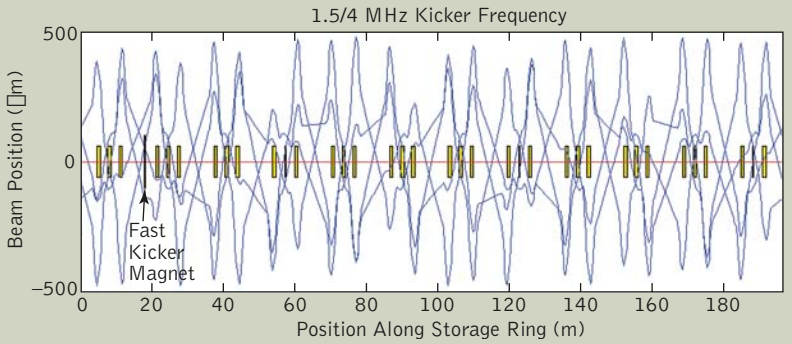

FIGURE 12
Kick every fourth turn.

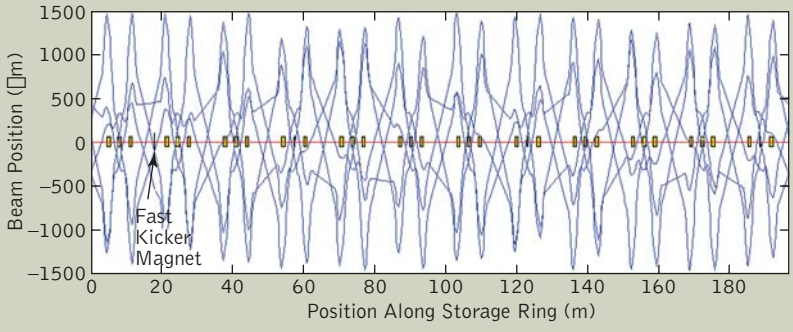

FIGURE 13
Kick every fifth turn.

The picture gets quite confusing if one skips too many turns before kicking (Figures 12 and 13). However, this method can extend the reach of a single kicker magnet. For instance, Beamline 6.0 (where users are very interested in this idea) sees mostly an angle change in Figure 8 but would see reasonable positional changes if kicking at every other or every fourth turn.

Global Orbit Profiling

By adding more kicker magnets (Figure 14), the global orbit of the camshaft bunch can be shaped more precisely. This is similar to global orbit correction except that the corrector magnets only select one bunch.

Local Orbit Bumps

If it is important to limit the separation of the camshaft from the main bunch train to a section of the accelerator, local bumps can be used. Three or four magnet bumps are easy to create and are commonly used in orbit control. The bump size could extend over a relatively small section, such as an arc or a straight section and neighboring arcs (Figures 15 and 16), or they can extend over many sectors. Very small bumps, over one straight section for example, will not be considered because they require large kick strength.

There are a myriad of possible bump shapes that could be used to reach various combinations of beamlines. Given that this system is being designed for a mature light source, it is going to be a challenge to reach all interested users using local bumps.

An advantage of using local bumps is that when the bump magnets are turned on, a new

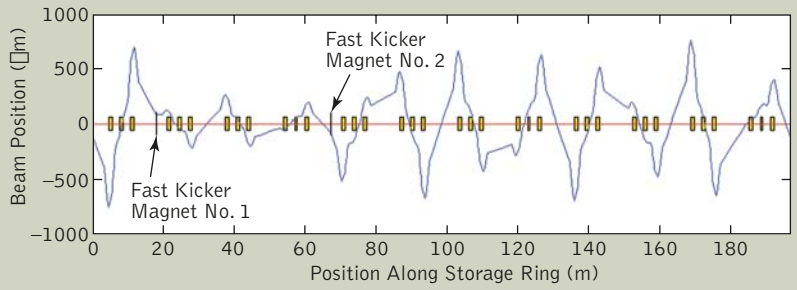

FIGURE 14
Kickers in Sectors 2 and 5.

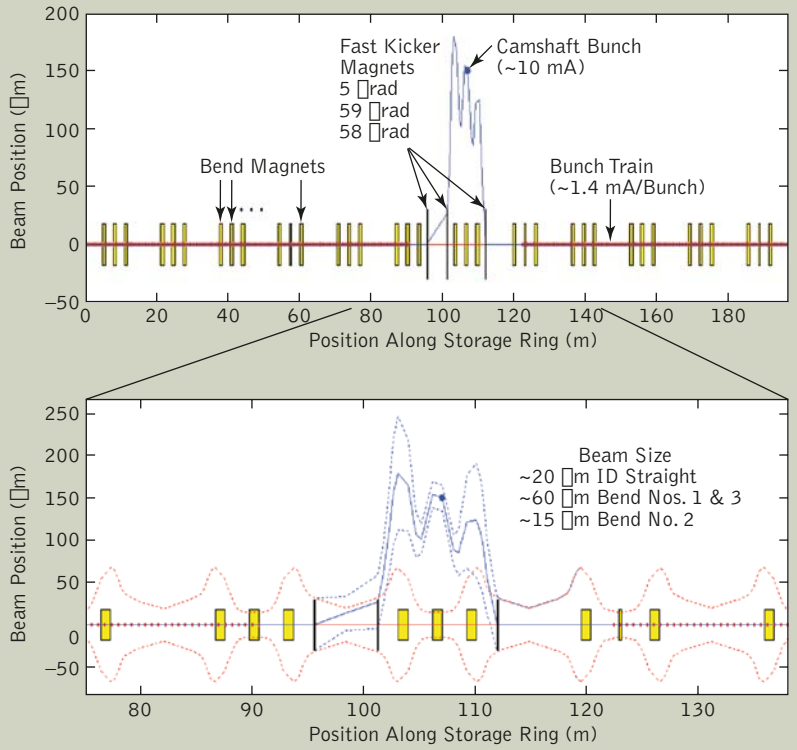

FIGURE 15
Arc sector bump. Dotted lines are the 1σ beam size.

closed orbit is obtained immediately. Hence, they can be turned on or off at any time without creating an orbit transient. For beamlines collecting data timed to a laser running at kilohertz frequencies, it is quite attractive to run the local bump at the same frequency.

Fast Kicker Magnet Design

The main parts of the fast kicker are the pulser and the magnet. The magnet has not been designed yet but will be a stripline kicker similar to the fast feedback kickers that have been designed at the ALS.

The pulser circuit provides the voltage to the kicker. The goal of the pulser is to supply high voltage when the camshaft bunch is present and zero volts otherwise. There was some hope of purchasing the pulser from industry, but the 1.5-MHz requirement puts too big a heat load on all commercial units investigated. For beamlines requiring a repetition rate of 10 kHz or less, there may be an off-the-shelf commercial unit with a rise/fall time fast enough to meet the specification. However, running at less than 1.5 MHz can only be done using local bumps.

Slawomir Kwiatkowski (Engineering Division, Berkeley Lab) has come up with a candidate design for the pulser running at 1.5 MHz (or less) and providing a 60-μrad kick (1.15 kV). Figure 17 shows the pulse shape. If the gap in the bunch train is reduced in the future, the length of the flat top will need to be reduced. It is unclear at this point if the 60-μrad kick can still be obtained with a shorter pulse.

Future Plans

We plan to install a fast kicker magnet in the Sector 2 straight section where some of the third-harmonic cavities have been removed. The downstream end of the wiggler in Sector 5 is the only other possible location. Both locations have vacuum chambers that are relatively easy to modify, but the vacuum chamber geometry in Sector 2 is more favorable. The magnet will provide at least a 60-μrad kick to the electron beam at 1.9 GeV at a repetition rate of 1.5 MHz (or less). The main goal is to study the benefits as well as

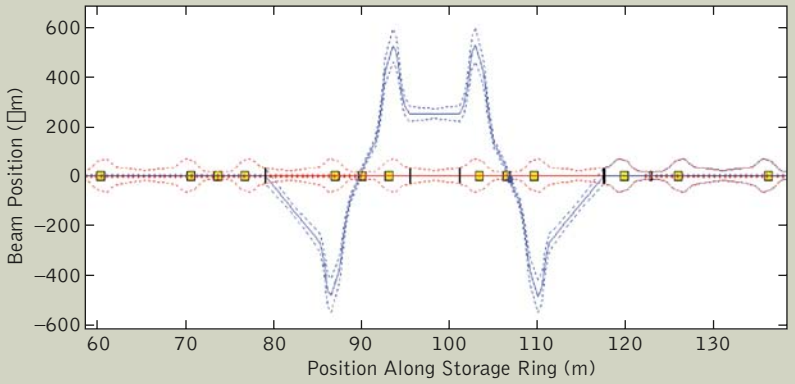

FIGURE 16
Straight section bump. Dotted lines are the 1σ beam size.

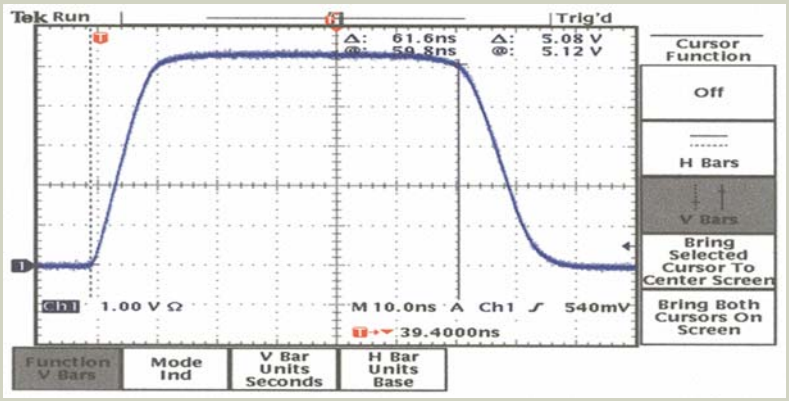

FIGURE 17
Fast kicker pulse.

unwanted side effects of pseudo-single-bunch mode. If the potential negative impacts on other beamlines turn out to be small enough, the system can also be run during user shifts. However, user operation is not part of the project goals at this initial stage.

Experimental Systems

Howard Padmore, Experimental Systems Group Leader

Introduction

The role of the ESG can be split into several categories: (1) to design and build beamlines and endstations based on the demands of the user program, (2) to conduct forefront research in science and instrumentation that will push the boundaries of the application of synchrotron radiation techniques, and (3) to give support to existing user programs, usually in areas of high technical complexity. Approximately 50% of this group's activity is in this latter area of direct user support. This short report gives several examples of work in the two former areas and summarizes the group's activity over the broader range of its work.

Beamline 11.0.1 and PEEM3

Beamline 11.0.1, a new undulator beamline for photoemission electron microscope (PEEM) studies at the ALS, is currently under commissioning. Initial measurements of flux, resolution, and other operational parameters confirm that the system is working to specification. The beamline is designed for optimal illumination of an aberration-corrected PEEM with an adjustable spot size (minimum size under 10 microns). The beamline's goal is to provide spectroscopic XMCD and XMLD imaging at nanometer resolution. As much of the noise in a dichroism spectrum is associated with wavelength jitter, a new system provides, for the first time, real-time measurement of the photon energy. The system provides a means of calculating the average photon energy within a defined time and a feedback mechanism to keep the energy constant. Very often we are now measuring dichroism of less than 10^{-4}, and this typically translates into energy shifts of an meV or so. The goal therefore was to measure these minute shifts in real time, and ultimately use this information for correction.

The overall layout of the beamline is shown in Figure 1. The first mirror of the optical system is a horizontally deflecting cylindrical mirror, focusing to the entrance slit in the vertical direction. The horizontal source size of the ALS is large in an insertion-device straight section (310 microns FWHM), and so high demagnification is necessary to reach the focal spot size demanded by PEEM3. This is done in two stages, first by a 20:1 horizontally deflecting elliptical mirror inside the monochromator, and then by a downstream horizontally deflecting elliptical mirror as part of the Kirkpatrick-Baez (K-B) pair. The monochromator is of a converging-beam variable-line-spacing (VLS) type (consisting of a vertically deflecting and focusing spherical mirror and VLS plane grating), which produces an image plane perpendicular to the central ray and puts the zero order in focus in the exit-slit plane. The position of the zero order is monitored to high precision using a YAG screen and optical microscope, and the centroid position with respect to the monochromatic slit position uniquely encodes the energy. The monochromator has achieved its design resolving power of 5000 at the 3d transition-metal L edges, and the goal is now to stabilize the

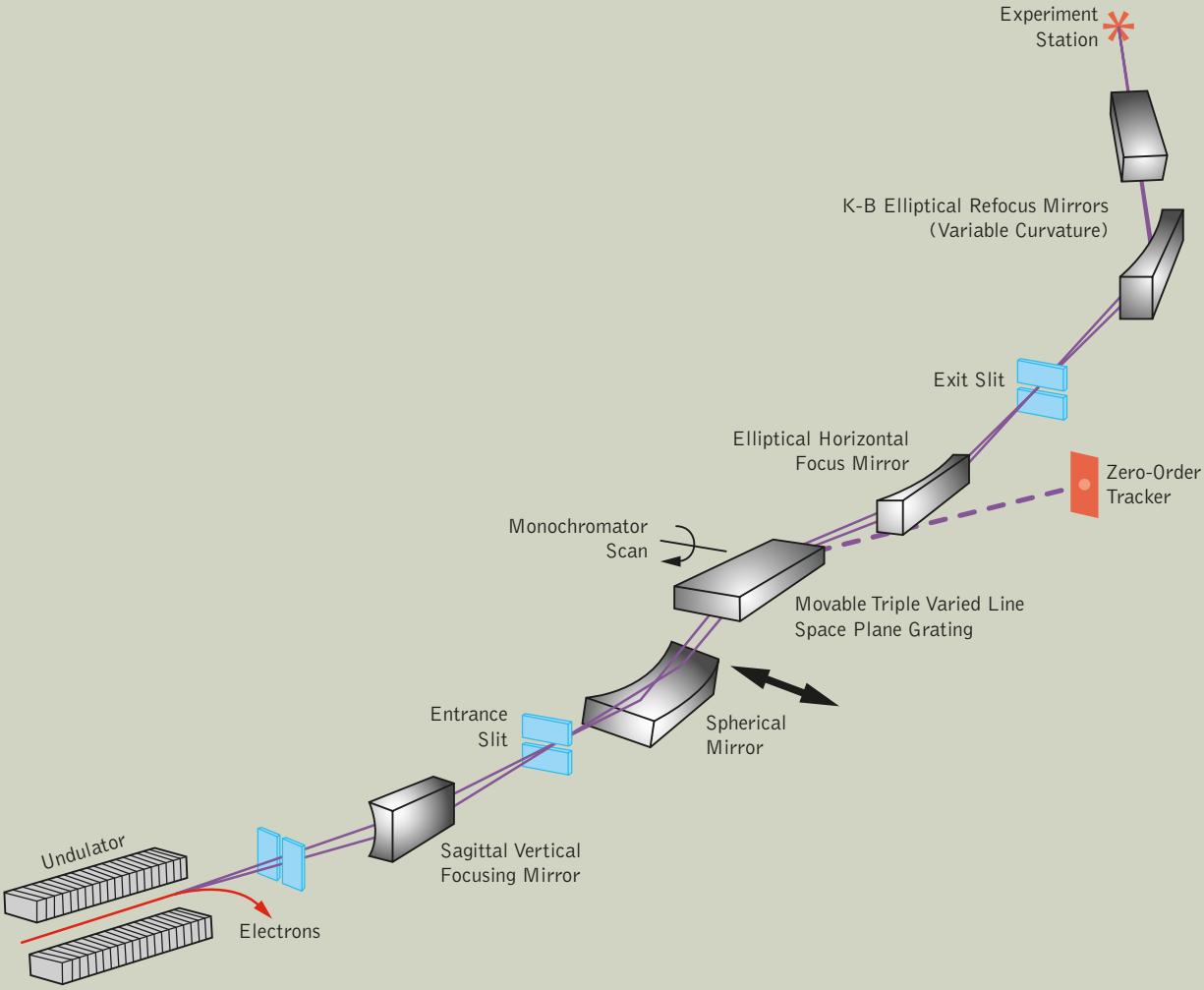

FIGURE 1
Layout of the PEEM3 beamline. The zero-order tracker is in the plane of the exit slit.

energy calibration to one part in 10^6 against relative thermal and structural motion of the slits and optics.

Figure 2 shows the operation of the zero-order tracker, which measures the vertical profile of the vertically focused zero-order light, visible on a single-crystal YAG scintillator below the exit slit. This measurement serves as an intensity monitor and, through the centroid of the profile, a high-precision monitor of the monochromator energy. Presently, the resolution of the photon energy centroid is 10^{-5} of the photon energy, limited by detector noise and pixelation. Simple improvements should allow our goal of 10^{-6} to be reached. Fluctuations in the photon energy over a range of frequencies can be seen at levels less than 10^{-4} and are being used to diagnose noise sources. In the near future, we will implement active feedback to reduce these energy fluctuations to a minimum.

The endstation, an aberration-corrected PEEM with a spatial resolution of approximately 5 nm, is being assembled and commissioned. A schematic of the electron

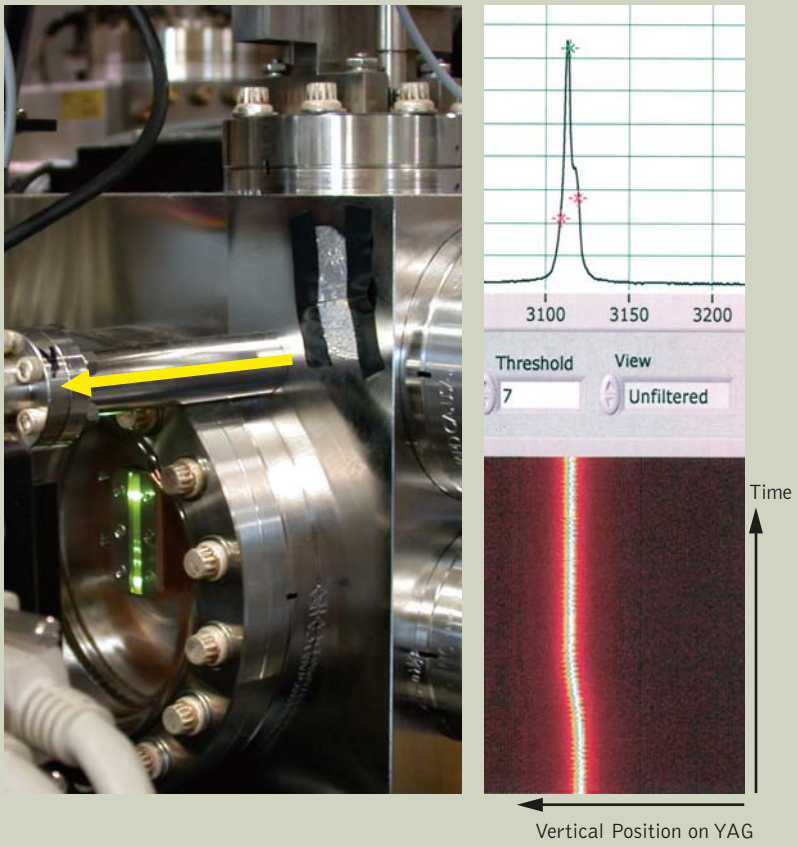

FIGURE 2
Exit-slit assembly at Beamline 11.0.1. The monochromatic x-ray beam (yellow arrow) passes to the experiment. The zero-order light is visible on a YAG screen in front of the microscope, along with unused undulator harmonics in first order. The image vertical line-scan history is shown on the right, capturing the monochromator as it steps 0.5 eV at 750 eV. The line-scan energy centroid is determined to 1 part in 100,000 after 1 second.

optics is shown in Figure 3. The sample is illuminated with soft x rays, and the emitted photoelectrons are accelerated to high kinetic energy (20 keV) in the gap between the sample and objective lens. The aberrations produced by this acceleration and subsequent focusing optics are balanced by the actions of an electron mirror, which has opposite low-order aberrations. To direct electrons to and from the electron mirror and to separate the beam paths, a dipole separator magnet is used.

As part of this project, we previously designed and built a prototype separator magnet that provided double focusing, was achromatic, and corrected all low-order aberrations. However, this combined-function magnet turned out to be very difficult to manufacture to the tolerances required. Much of the electron optics design has been a collaboration with the Accelerator Physics Group, and after identifying the issues with this conventional combined-function separator, we worked again with them on a new design. Led by Weishi Wan of Accelerator Physics, we are developing a new and much simpler separator magnet layout that separates the functions. That is, deflection is done by a dipole magnet, and focusing is done by a combination of electrostatic quadrupoles and a round lens. The chromatic dispersion introduced by the magnet is cancelled after reflection from the mirror and a second passage through the magnet, and low-order aberrations are cancelled or reduced to insignificance by symmetry. The system is now much more flexible, and any assembly or manufacturing errors can be eliminated by correct tuning.

The project is being staged in two phases. The first phase (without the magnetic separator and electron mirror) is currently being commissioned and will function in a manner similar to the existing PEEM2 instrument on bend-magnet Beamline 7.3.1.1, with a resolution of about 30 nm. The phase-one PEEM3 improves on PEEM2 by having a higher flux density from the insertion-device beamline (by a factor of 1000), polarization control, and a more sophisticated sample environment, including a novel five-axis, high-stability flexural sample stage that can be cooled to 60 K. Figure 4 shows the sample puck mounted on the five-axis sample stage with the objective-lens stack. The sample stage is designed to be stable and light to avoid drift and vibration effects that are general problems in electron microscopy. Initial measurements indicate that the natural stage vibration frequencies are

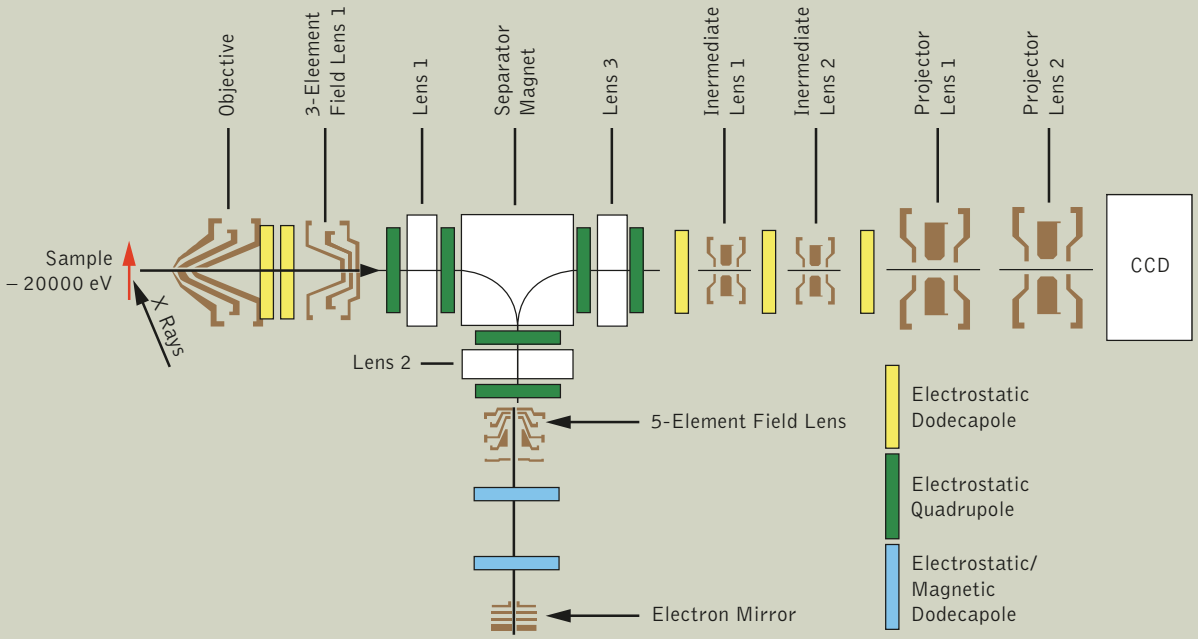

FIGURE 3
Schematic layout of the PEEM3 electron optic scheme. Photoelectrons from the sample are accelerated and focused by the objective lens and turned through the 90-degree separator magnet into the mirror arm. The electrons are reflected back through the separator and into the projector optics for final imaging on the CCD detector.

high—less than 200 Hz—demonstrating the stiffness of the structure. The sample transfer system, sample stage, and electron optics have had significant off-line mechanical alignment testing and are currently being assembled into the microscope vacuum tank itself. The vacuum tank has three layers of mu-metal magnetic shielding, which is necessary to reduce magnetic field strengths to less than 2×10^{-7} gauss. Such a low field is required as the path length is long (~1 m) for this microscope. This mode of microscope operation will last for about a year, until the summer of 2007. PEEM operation will then shift back to Beamline 7.3.1.1 (PEEM2) for six months, while the separator is added and the sample preparation facility is constructed.

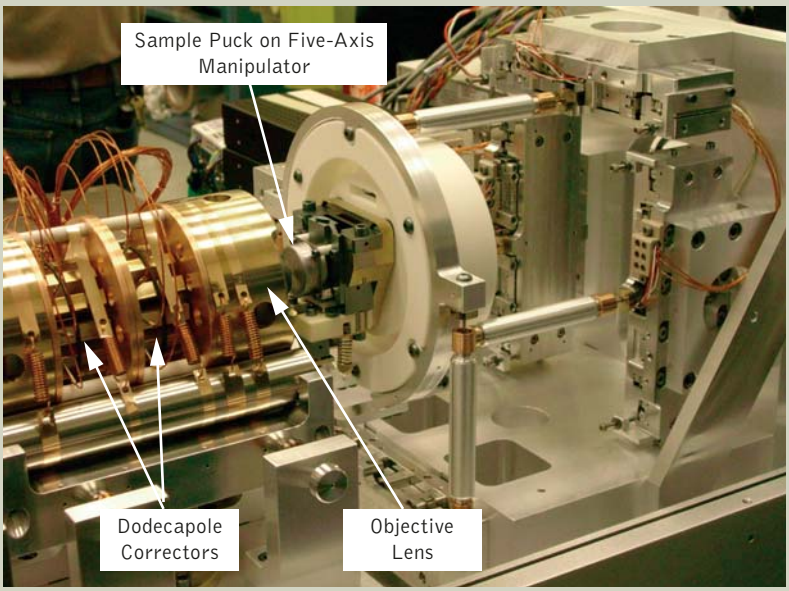

FIGURE 4
View of the sample puck mounted on the five-axis flexural sample stage. The objective lens and the first two sets of dodecapole correctors are visible on the left.

Ultrafast X-Ray Science Facility

Two beamlines, 6.0.1 and 6.0.2, are being developed for ultrafast x-ray science, based on beam slicing to create short x-ray pulses. This technique uses the interaction between a high-power laser and the electron beam to create an energy chirp in the electron beam, and this is used in combination with a dispersive field to deflect the electron beam. An optical system then images the position of the chirped beam, and a slit selects out the off-axis chirped short pulse. Pulses are expected to be about 200 fs wide FWHM. Beamline 6.0.2, the soft x-ray branch, will cover the photon energy range from 150–1800 eV while Beamline 6.0.1, the hard x-ray branch, will provide photons from 2.2–10 keV.

One of the challenges with the slicing technique is that the imaging system must have very low scatter and aberrations, so that the sliced beam, which represents about 1/10,000 of the intensity of a single bunch, can be distinguished from the unsliced beam. The beam is deflected in the vertical direction, and sagittal focusing from a cylindrical mirror is used in the vertical direction for high image quality. Extensive measurements were made to characterize the mirror scattering on other beamlines so that we could be sure that a particular mirror-manufacturing technique could be relied upon to produce the low levels of scattering required. We finally adopted a new polishing technique for cylindrical mirrors that emphasized the achievement of good

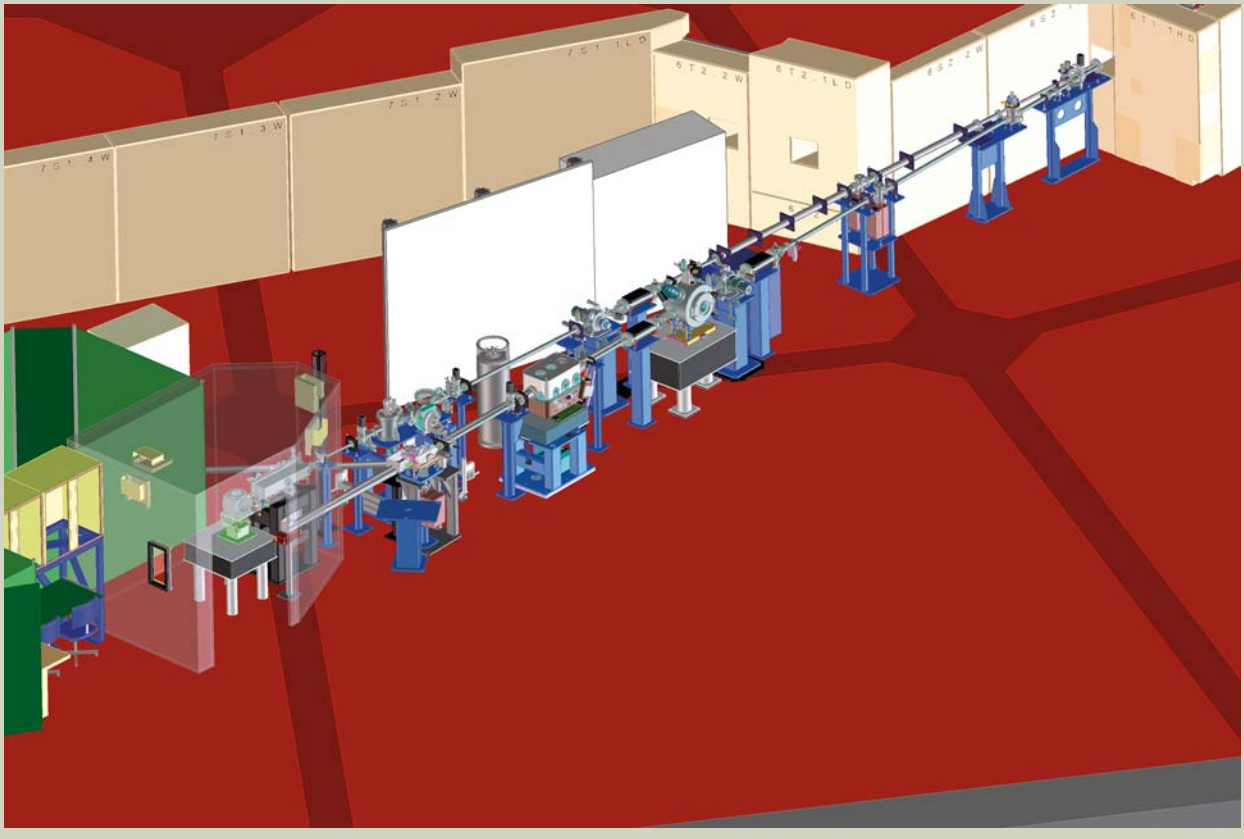

FIGURE 5
Schematic layout of femtosecond slicing beamlines in straight section 6, showing the soft x-ray beamline in the foreground and the hard x-ray beamline and hutch in the background.

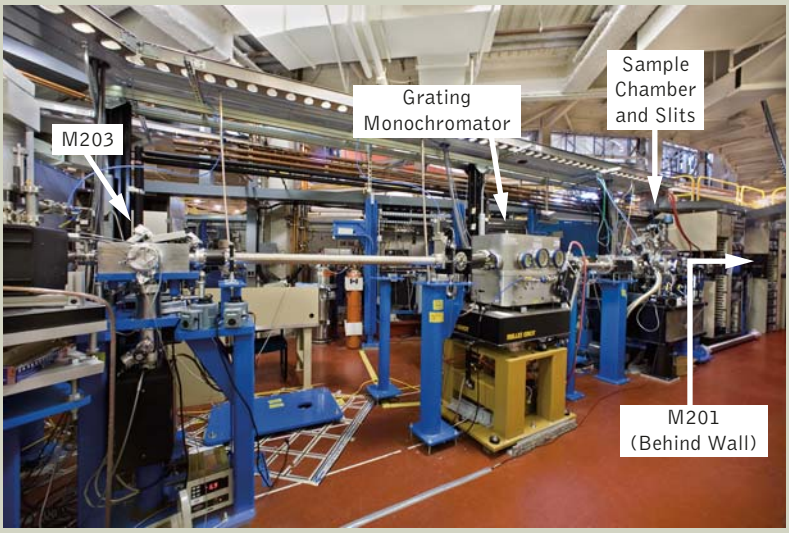

FIGURE 6
Soft x-ray femtosecond slicing Beamline 6.0.2, showing the beam emerging from the shield wall, the sample chamber and entrance slits, the grating spectrograph/monochromator and the refocusing mirror.

sagittal figure and exceptionally good microroughness.

The three-dimensional layout drawing of the beamlines is shown in Figure 5. The source is a 3-cm-period in-vacuum insertion device (minimum gap 5.5 mm) that occupies approximately 2 m of the straight section. The straight section is chicaned into two sections, and in the future, a 2-m-long 5-cm EPU will be used in conjunction with the soft x-ray beamline. The first section of the beamlines includes mirrors that image the x-ray source onto slits, which are used to select the vertically separated femtosecond x-ray pulses. High-speed choppers reduce the average power on samples in pink-beam mode and on the downstream optics. On the soft x-ray beamline, a sample chamber is positioned upstream of the monochromator in the pink beam, for dispersive transmission experiments. A soft x-ray spectrograph allows the measurement of an entire x-ray absorption spectrum at one time. A gateable imaging detector is used at the end of the beamline for detecting the absorption spectrum and for gating out nonsliced x-ray bunches. On the hard x-ray beamline, crystals produce a monochromatic beam for experiments inside a hutch. To interact with the electron beam and excite samples, a high-average-power femtosecond laser system has been built. The femtosecond laser system operates at a high repetition rate, 20 kHz, to increase the average flux of femtosecond x rays.

The soft x-ray beamline, Beamline 6.0.2, has been commissioned, and a photograph of the system is shown in Figure 6. We measured the dimensions of the intermediate focus to be 120 mm (FWHM) verti-

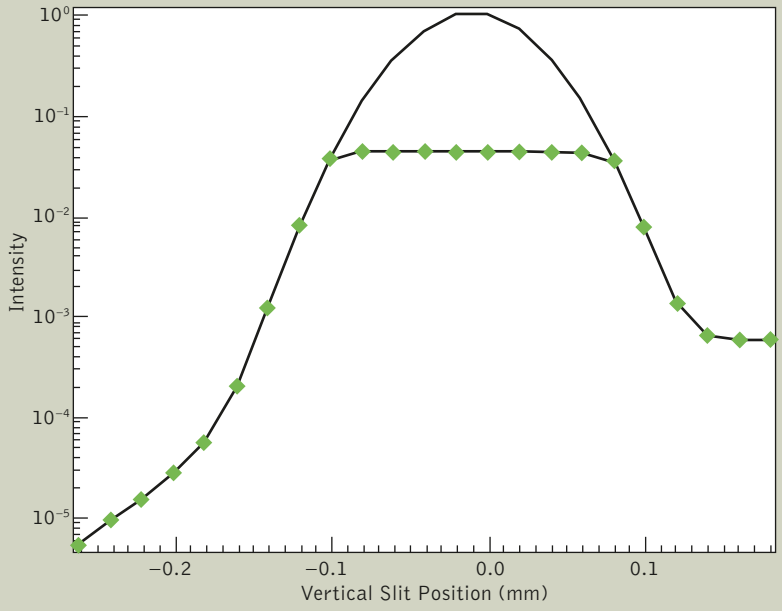

FIGURE 7
Vertical image profile at the monochromator entrance slits with 20% of the aperture clipped. For 3.45-cm dispersion, there is a 240-micron beam shift for 16.5-MeV energy modulation, at which point the scattered intensity is 10^{-5} of the peak intensity. The sliced intensity is about 10^{-4} of the main pulse.

cally and 540 mm (FWHM) horizontally, in agreement with calculations and modeling. The vertical profile of the x-ray focal spot is important in determining the slicing signal-to-background ratio and has been measured. Measurements of the vertical beam shape have been carried out under a range of different conditions to understand and minimize mirror scattering. Figure 7 shows the results from one of these measurements in which the vertical aperture inside the monochromator was closed slightly, reducing total flux by 20%. For a nominal dispersion of 3.45 cm, and for nominal laser conditions that should give a 16.5-MeV kick to the beam, the beam would be moved in the vertical direction by 240 μm, at which point the scattered signal is 10^{-5} of the peak intensity. The total intensity of the sliced beam will be around 10^{-4} of the main 80-ps x-ray pulse, and so under these conditions, it appears that we will have a good ratio of the sliced flux to the main-pulse flux.

We have measured flux and resolution, and the experimental program can commence once the fast chopper is installed. This is under test at a manufacturer and should be installed shortly. The hard x-ray beamline, Beamline 6.0.1, is in the assembly and installation phase and is scheduled for completion in the summer of 2006. The two beamlines will use radiation in a time-sharing mode from the existing 3-cm in-vacuum undulator, but the optics are designed so that with some minimal realignment, they can use radiation from two separate undulator sources. The second source would be a standard ALS EPU5, and we hope that this upgrade can be made in the near term.

X-Ray Microdiffraction on Superbend Beamline 12.3.2

A new x-ray microdiffraction endstation (Figure 8) is under commissioning on superbend Beamline 12.3.2, with a target user opening date of January 2007. The new facility will replace the successful x-ray microdiffraction program on bend-magnet Beamline 7.3.3, which has run now for three years as one of the few dedicated beamlines around the world routinely offering submicron white and monochromatic x-ray beam for diffraction experiments using a large-area CCD detector. Small submicron-sized beams are obtained by using a pair of elliptically bent K-B mirrors, and a four-bounce monochromator is used to rapidly switch between white and monochromatic beam while illuminating the same spot on the sample.

Scanning white-beam x-ray microdiffraction is a powerful technique that allows the mapping of grain orientation in polycrystalline samples with average grain sizes as small as a micron. Moreover, measurement of the tiny displacements of the diffraction peaks on the CCD detector allows the determination of strain and—through calculation—stress, with a spatial resolution given by the focused x-ray beam size.

The beamline currently provides a strain accuracy of about 10^{-4}, a crystal orientation sensitivity of 0.01°, and spatial resolution of 0.5 micron, with a diffraction-pattern acquisition time (including CCD readout) of about 8 s and an analysis time of about 10 s/frame for a typical polycrystalline copper thin-film sample. These numbers are greatly dependent on the type of material under investigation. The current limitations of the system include limited flux in monochromatic mode, CCD readout time being the limiting factor in data acquisition, data analysis speed, spatial resolution, orientation/strain sensitivity, limited energy range (presently about 6–12 keV), and bulk sensitivity.

To overcome many of these shortcomings, a group lead by Ersan Ustundag from Iowa State University and including scientists from UC Berkeley, UCLA, Caltech, Stanford, and the ALS have secured funding through an NSF grant for a major upgrade of the existing station. This involves moving the station to a superbend beamline, extending the available energy range to 24 keV. This will enhance orientation and strain sensitivity by an order of magnitude because these quantities are calculated using a nonlinear least-

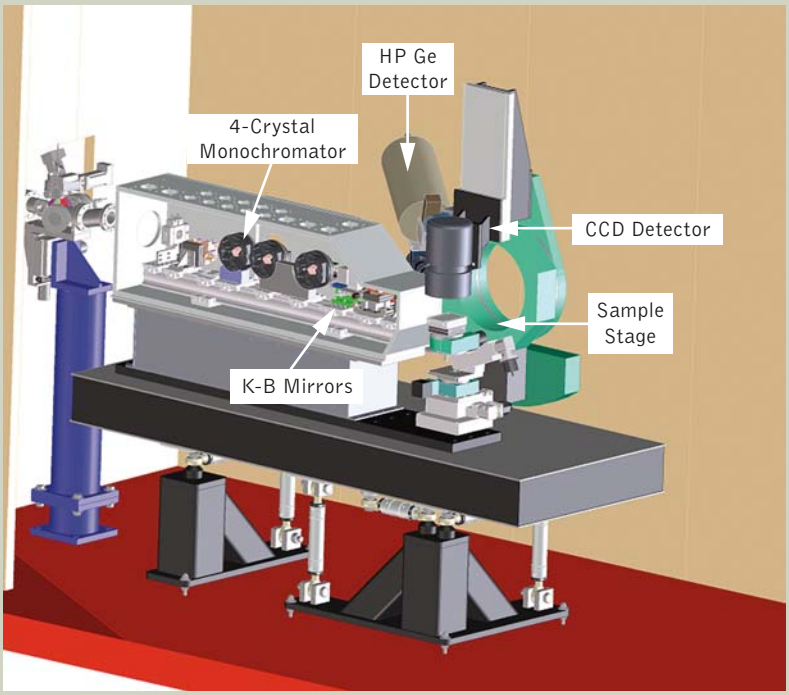

FIGURE 8
Schematic layout of the new x-ray microdiffraction endstation on superbend Beamline 12.3.2.

squares fit on the positions of the diffraction spots in the diffraction pattern; by increasing the number of spots in the pattern, the orientation and strain resolution is also increased. The superbend will also provide a significant increase in flux, which will allow a much wider use of monochromatic mode (including mineral phase mapping and fluorescence mapping of trace elements).

The Optical Metrology Lab, led by Valeriy Yashchuk, is working to provide enhanced K-B mirror capabilities, which should result in a focus size of about 100 nm. Higher energy also allows the study of not only thin films but also bulk samples, introducing the possibility of performing three-dimensional x-ray microdiffraction with depth-resolving capability. A 24-dual-processor-node Linux cluster has been purchased and set up to implement the very time-consuming two-dimensional and especially three-dimensional microdiffraction analysis codes. In parallel with these efforts, a very fast CCD detector is under development. Whereas the present 16-bit phosphor–fiber–CCD detector takes many seconds to read out, the new camera will read out in 5 ms due to use of a pseudocolumn parallel readout scheme. A prototype is under development, and we should have a version ready for experiments by the end of 2007.

The existing Beamline 7.3.3 x-ray microdiffraction facility has led to some helpful insights concerning the mechanical properties of thin metallic films. For example, tin and tin compounds are the most effective replacement for environmentally damaging lead in the microelectronics industry. However, tin has some unusual properties that can have severe consequences: its tendency to spontaneously grow "whiskers" can cause short circuits (tin whisker short-circuiting was found to be responsible for the total loss of three Galaxy telecommunication satellites!). A team lead by King-Ning Tu of UCLA has used the Beamline 7.3.3 endstation to unravel the mystery behind spontaneous whisker growth in tin. It was determined that whiskers grow from certain singularities in the loosely textured polycrystalline tin film, such as oddly oriented grains that cause cracks in the natural passivation layer. The growth of the whisker is then sustained by a compressive stress in the film due to the formation of an intermetallic compound at the interface between the tin and the copper substrate (Figure 9). Another unusual property of tin is a sudden initial 10% drop in resistance when current passes through. The same team has demonstrated that this drop is due to electromigration-induced grain growth. However, the mechanism is unique: tin is electrically very anisotropic, so that when current is passed inside a polycrystalline tin stripe, grains oriented less favorably (i.e., more resistive to the current flow) rotate to match the orientation of the more favorably oriented ones, giving the impression that the latter ones grow at the expense of the former. The grain rotations are triggered by opposite stress forces generated at grain

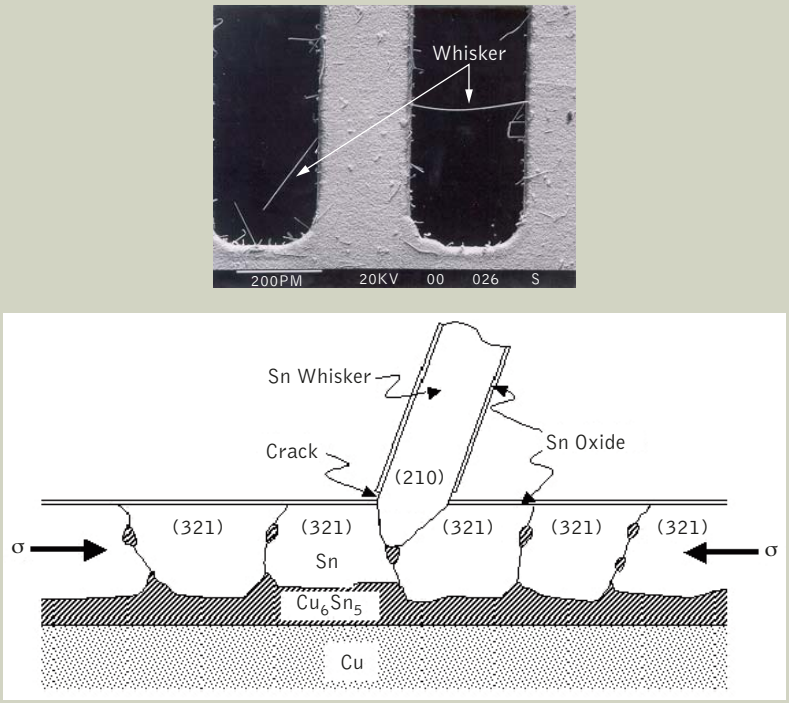

FIGURE 9
Top: A scanning electron microscope (SEM) image of tin whiskers. Bottom: Mechanism of whisker growth deduced from x-ray microdiffraction and SEM studies. The intermetallic compound Cu_6Sn_5 generated by the in-diffusion of Cu creates a compressive stress, extruding material out of the tin passivation layer through weak points.

boundaries by vacancy flux in opposite directions caused by anisotropic conductivity between grains.

The microdiffraction program covers very diverse areas of science and has been a tremendous success. The move to a high-energy superbend beamline with enhanced flux and high-energy coverage, combined with high-power computing, state-of-the-art detectors, and 100-nm spatial resolution, will result in a truly revolutionary facility, and we are set for a very bright future in applying the new system to the study of material microstructures.

Magnetization Dynamics Measured Using an X-Ray Streak Camera

Technology today makes extensive use of magnetic materials. Enormous amounts of data are stored either as magnetic domains in a continuous film (for example, on a hard disk) or as the magnetization of a nanostructured pattern (for example, in a magnetic random-access memory element). To write information into smaller and smaller volumes at higher and higher speed, new techniques for magnetic writing are being explored, using a combination of magnetic fields and optical excitation. Direct optical control of magnetism using short laser pulses is the ultimate goal, with the potential to increase the speed of magnetic writing by at least three orders of magnitude.

The physics of magnetic phase transitions is governed by the exchange of both energy and angular momentum between electrons and lattice, mediated by the spin–orbit and exchange interactions. In spite of the progress being made using femtosecond lasers, the ultrafast dynamics of many magnetic materials is not known, preventing us from understanding phenomena like damping, demagnetization, and magnetic switching. Furthermore, in a large class of interesting new materials, magnetic phase transi-

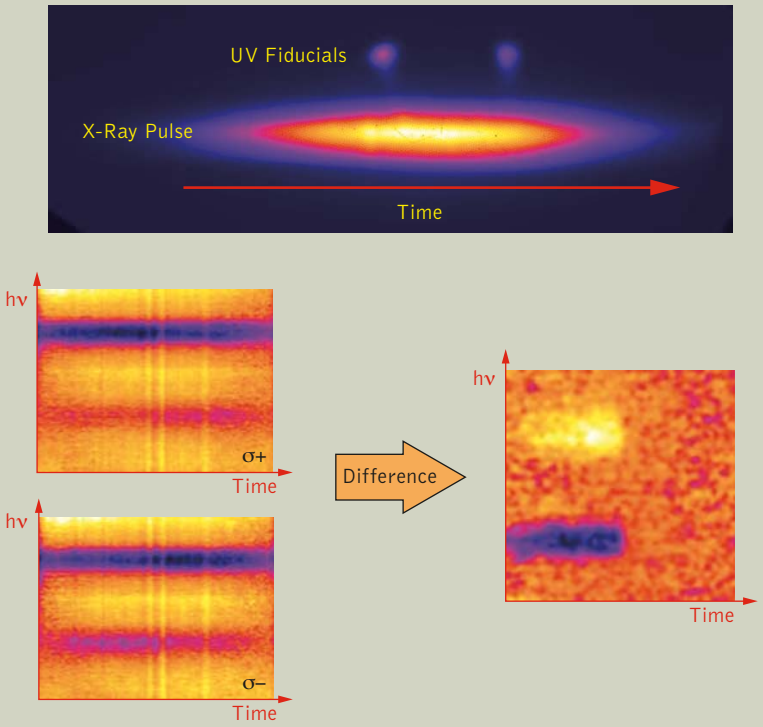

FIGURE 10
Top: Streak camera image of an 80-ps x-ray beam and two UV timing fiducials. Bottom left: X-ray absorption through a thin foil as a function of time and photon energy for right (σ^+) and left (σ^-) circular polarization. Bottom right: Difference between the two signals. The center of the image marks the point in time where the sample was pumped with a femtosecond laser.

tions are linked to other kinds of order such as orbital order, charge order, and ferroelectricity.

Time-resolved x-ray techniques offer new opportunities for investigating complex magnetic materials. X-ray techniques are sensitive to both ferro- and antiferromagnetism and are many orders of magnitude stronger than the Faraday and Kerr effects found in the visible spectrum. For transient magnetic studies, subpicosecond time resolution is required and can be obtained by using a streak camera as the detector. Significant progress was made over the last year to optimize an existing streak camera for magnetism studies. An x-ray streak camera maps the time information contained within an 80-ps x-ray pulse of the ALS onto one of the spatial coordinates of a two-dimensional detector (Figure 10). Electrons accelerated by a 10-kV potential off of the camera's photocathode are deflected by an electrical pulse on a pair of deflector plates (rise time ~100 ps) and imaged by a magnetic lens. The deflection pulse is derived from a 70-fs laser pulse hitting a ~300-V biased photoconductive GaAs switch at a 5-kHz repetition rate. Part of the same laser pulse is used as an infrared heating pulse initiating the dynamics of the sample. Two frequency-tripled UV pulses (~100 fs) derived from the same laser pulse are used for performance testing. The streak camera has achieved a time resolution of 0.6 ps in single-shot UV exposures. In x-ray experiments, the resolution is somewhat reduced (typically 2 ps) because of laser jitter, limitations of the current electron detector, and chromatic temporal aberrations.

The first measurements of the demagnetization initiated by ultrafast laser heating were conducted at Beamline 4.0.2 on Ni, FeNiPt, and FeGd systems. The project was sponsored by Berkeley Lab's Laboratory Directed Research and Development program. An almost complete demagnetization in response to a 20-mJ/cm^2 laser pulse was achieved in all three systems. The observed demagnetization rate in Ni appears to be limited by the x-ray time resolution of the setup, in agreement with literature data, which suggested a subpicosecond demagnetization. In Fe/Gd multilayers, we observed a slower rate of demagnetization, about 15% per ps (Figure 11). This surprisingly slow rate is most likely a result of the extraordinarily small anisotropy of the material and the vanishing spin–orbit coupling of the Gd layers. Spectroscopic data showed that the Fe and Gd magnetization vanished simultaneously, suggesting strong layer–layer coupling. The Fe orbital and spin magnetization also dropped at the same rate. No Gd orbital moment was observed, as expected for a half-filled valence shell.

A significant improvement in the x-ray time resolution can be achieved using an improved fast-readout CCD camera, allowing single-shot readout at the laser frequency.

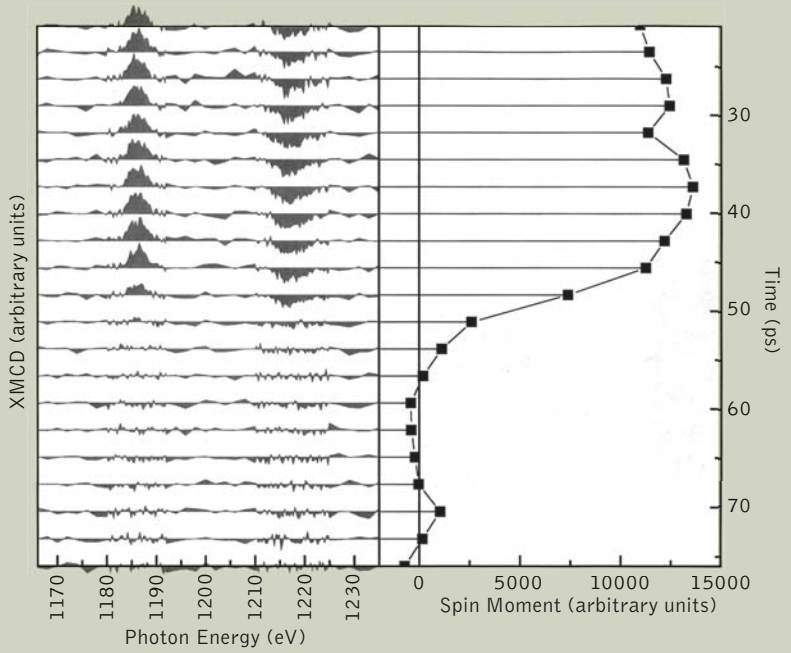

FIGURE 11
Time-resolved XMCD from Gd $M_{4,5}$ edges and resulting spin moment.

Automatic time fiducialization and single-electron center-of-gravity measurement should completely remove the effect of laser jitter and limited detector resolution, bringing the multishot x-ray resolution close to the resolution of single-shot UV exposures. The camera, readout electronics, and software are under development. Beyond that, the time resolution is dominated by temporal dispersion of energy-dispersed electrons from the photocathode. We will be upgrading the camera shortly to operate at far higher extraction and beam energies to overcome this problem with a goal of 250-fs resolution. In the longer term, working with the Accelerator Physics Group, we have designed an aberration corrector that should be capable of 50-fs temporal resolution.

Scientific Support

ZAHID HUSSAIN, SCIENTIFIC SUPPORT GROUP LEADER
ELI ROTENBERG, SCIENTIFIC SUPPORT GROUP DEPUTY LEADER

INTRODUCTION

The primary mission of the SSG is to support the efforts of researchers at the ALS through scientific and technical collaboration and scientific outreach. Working with the users, the SSG plays an important role in developing novel instrumentation that enables cutting-edge science. Depending on the needs of the user, the degree of collaboration can range from technical assistance with the beamline and instrumentation to full partnership in developing new research programs.

Scientific Outreach

The SSG strives to expand the scientific program of the ALS and broaden its user base through publications and presentations. The group organizes a variety of seminars, including the weekly ALS/CXRO seminar series and a targeted weekly SSG lecture series. The weekly lectures cover a wide range of topics and are given by world-renowned scientists. The group also organizes the quarterly ALS Colloquium.

Working together with the UEC, the SSG also helps to organize workshops exploring new scientific opportunities and needs for new beamlines or experimental facilities. During the 2005 ALS Users' Meeting, 12 such workshops were heavily attended by enthusiastic scientists, triggering many fruitful discussions that should spark further advances at the ALS.

The ALS Doctoral Fellowship in Residence program, established in 2001, has been very popular among doctoral students and has been received with much appreciation. Doctoral fellowships enable students to acquire hands-on scientific training and develop professional maturity for independent research. More details are given at the ALS Web site (www-als.lbl.gov/als/fellowships/). A selection committee consisting of Greg Denbeaux (chair, UEC), Erwin Poliakoff, Zahid Hussain, Sam Bader (chair, SAC), and Neville Smith recommended the following recipients for doctoral fellowships for academic year 2005–06: Yulin Chen (Stanford University, time-resolved photoemission spectroscopy); Ileana Dumitriu (Western Michigan University, inner-shell photodetachment of negative ions of C_{60} and nickel clusters); Amanda Hudson (UNLV, spin–orbit, ultrafast dissociation, and nondipole x-ray emission); Timothy Learmonth (Boston University, inelastic x-ray scattering and soft x-ray emission spectroscopy); Zhiqiang Li (UC San Diego, infrared microscopy of charge injection in organic field-effect transistors); Zhihui Pan (Boston College, photoemission study of strongly correlated electron systems); John Paul Strachan (Stanford University, condensed matter physics/magnetism); and Michelle Weinberger (UCLA, physical/materials chemistry under high pressure).

Support

SSG members are responsible for the operation, upgrade, and maintenance of most of the facility beamlines and many of the permanent endstations at the ALS. Each of the undulator-based beamlines—4.0.2, 7.0.1, 8.0.1, 10.0.1, a photoemission branchline on 12.0.1, and a coherent science branchline 12.0.2—typically have one or two SSG staff members responsible for their continued operation. This year the SSG has also taken responsibility for operation of Beamline 6.3.1, which was developed and operated by CXRO. The group is also playing an active role in optimizing the operation of the chemical dynamics complex (Beamline 9.0.2), which is operated by Berkeley Lab's Chemical Sciences Division under separate funding from DOE BES. Members of the SSG put great emphasis on making the development of novel instrumentation more efficient and user friendly. In 2005, the group designed and developed several new experimental systems, some of which are described bellow.

Member Research

Staff scientists within SSG are expected to maintain scientific and technical excellence in areas of synchrotron radiation research. Participation in active scientific programs is essential for such development, and all of the SSG scientists are active members of research programs at the ALS.

The Mini Magnet at Beamline 6.3.1

X-ray magnetic circular dichroism (XMCD) measures the difference in the absorption of x rays having helicity vectors parallel and antiparallel to the magnetization direction in a sample. XMCD is unique in its intrinsic element specificity and chemical-site sensitivity that allows separating the contributions of multiple magnetic species in alloys or layered systems. Most importantly, theoretically derived sum rules link XMCD intensities to spin and orbital magnetic moments, that is, sum rules enable the use of polarized x rays for quantitative magnetometry.

In a typical XMCD experiment, the magnetic moments are aligned along the x-ray beam by an external field, and field orientation or x-ray polarization are reversed to obtain the XMCD spectrum. To measure XMCD with very high precision, the new Mini Magnet endstation (Figure 1) was developed in collaboration between the ALS (Elke Arenholz, SSG) and Montana State University (Yves Idzerda) and installed at bending-magnet Beamline 6.3.1. Figure 2 shows that at the Mn $L_{3,2}$ edges, a change in x-ray absorption (measured in total electron yield mode) of 5×10^{-4} can easily be determined with a precision of 10^{-4} or better. Within the first month of operation, the system has already been used by three groups and contributed to publications.

FIGURE 1
Mini Magnet endstation installed at bending-magnet Beamline 6.3.1.

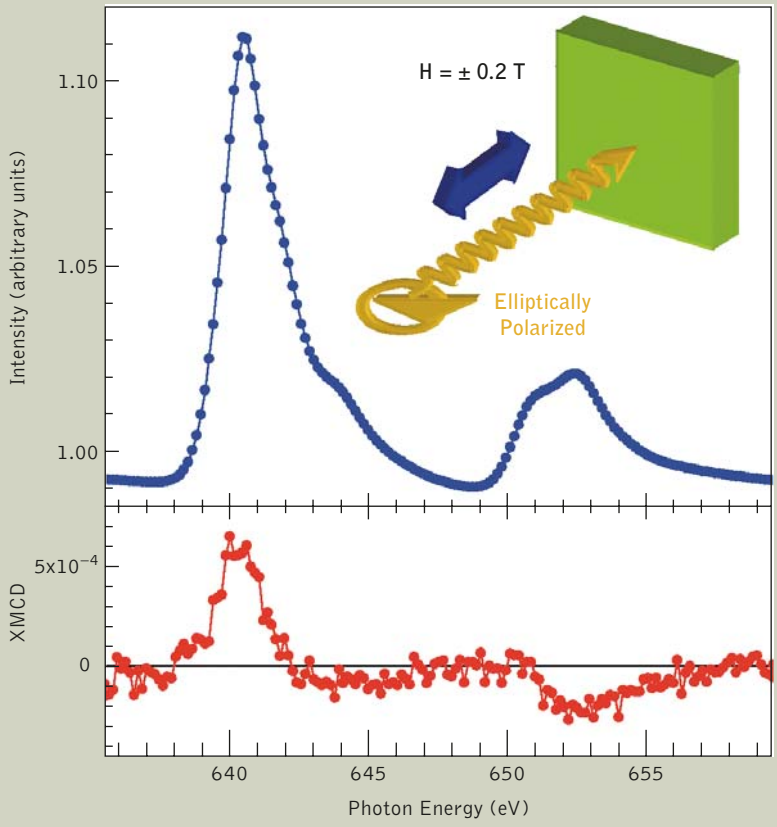

FIGURE 2
At the Mn $L_{3,2}$ edges, a change in x-ray absorption (measured in total electron yield mode) of 5×10^{-4} can easily be determined with a precision of 10^{-4} or better using the Mini Magnet endstation at Beamline 6.3.1 (data courtesy of Hendrik Ohldag,

Soft X-Ray Liquid-Flow Cell at Beamline 8.0.1

The group of Eberhard Umbach from the University of Würzburg, Germany, headed on the experimental side by Clemens Heske (now at UNLV), Oliver Fuchs, and Lothar Weinhardt, successfully commissioned a liquid-flow cell for soft x-ray spectroscopy at the Beamline 8.0.1 soft x-ray fluorescence (SXF) endstation. This apparatus, an extension of previous work performed on small (microliter) fixed-volume water cells, employs a continuously recirculating flow of liquid through a Teflon body behind a silicon nitride window (Figure 3). The transparency of the thin Si_3N_4 window to soft x rays, including those at the oxygen K edge, allows photon-in/photon-out measurements of x-ray absorption and emission using total fluorescence yield and grating spectrometer detectors. The advantages of the flow cell over the fixed-volume cell are the ability to rapidly switch liquid solutions, the precise control of the liquid temperature (monitored by a thermocouple at the back of the cell) and composition (e.g., pH value), and the reduction of beam-induced effects as a result of the constant refresh of the exposed liquid.

For the safety of the beamline monochromator and storage-ring vacuum in case of a rupture of the Si_3N_4 window, extra precautions were required beyond those needed for fixed-volume water-cell experiments. They include vacuum-interlocked fast fluid and vacuum valves, a differentially pumped branchline vacuum connection to the SXF chamber, multiple millimeter-sized apertures, a shock volume, and a fast-valve system identical to that employed at all ALS beamlines. A key goal was to prevent the beamline's fast sensor, only 2.5 m away from the endstation, from tripping, which would close the beamline's front-end fast valve and "dump" the beam in the storage ring.

For official commissioning of the flow-cell system, a demonstration rupture test was performed. A sharp point was purposefully pressed against the Si_3N_4 window to break it in order to monitor increases in ion-gauge pressure upstream along the beamline. A key effect that drastically mitigates the shock of vacuum exposure to water vapor for small window fractures is that the heat required for vaporization rapidly cools and freezes the remaining water, which collects as ice near the window and also blocks the initial leak.

One of the first experiments

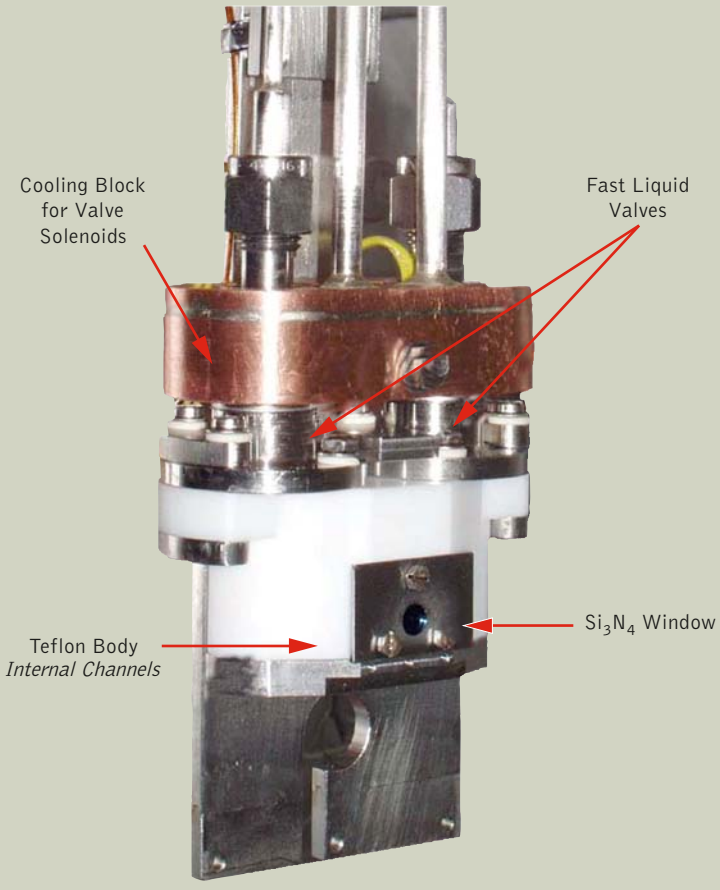

FIGURE 3
In-vacuum liquid-flow cell at Beamline 8.0.1 designed by the Umbach group.

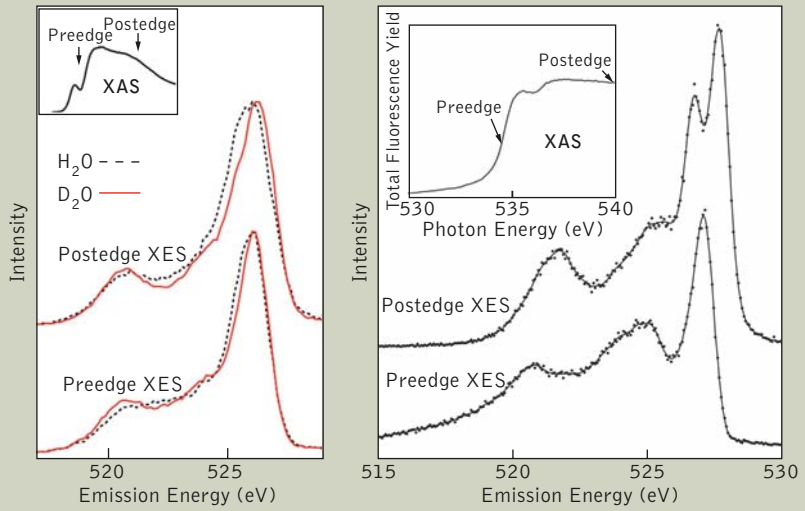

FIGURE 4
X-ray emission spectra of heavy water (D_2O) around the oxygen K edge obtained using a fixed-volume cell (left, red solid lines; spectra for H_2O are also shown as dashed black lines) and the new liquid-flow cell (right). The x-ray absorption spectra (XAS) for the oxygen K edge are shown in the insets.

performed with the liquid-flow cell measured the oxygen K-edge x-ray emission spectra (XES) of heavy water to confirm earlier measurements obtained using a fixed-volume water cell (see "Ultrafast Dynamics in Water" in the Environmental and Earth Science section of the Science Highlights). Since, in the meantime, the spectrometer detector was replaced and the software control was upgraded, significantly improved resolution could be obtained from the spectrometer. Figure 4 thus shows first results using the liquid-flow cell (with the above-listed advantages) with an obvious improvement in resolution.

High-Resolution Angle-Resolved Photoemission (HARP) Endstation at Beamline 12.0.1

The High-Resolution Angle-Resolved Photoemission (HARP) endstation at Beamline 12.0.1 has entered its second year of user operations with a solid general-user program devoted to photoemission studies of strongly correlated materials [1–4]. High demand for beam time at HARP has prompted us to search for yet remaining ways of improving its user friendliness and efficiency. We identified three problems: (1) a substantial amount of high-order light at low photon energies (typically below ~50 eV), (2) slight motion of the photon beam upon changing diffraction gratings, and (3) motion of the beam across the surface of the sample when the sample moves to the extreme positions during the angle scans. Below is an outline of our efforts aimed at correcting these issues.

To address the high-order light problem, we have installed thin-film filters (Mg, Al, Si, and B; comprehensive information about the filters can be found at http://www-cxro.lbl.gov/optical_constants/filter2.html). Depending on the photon energy, experimenters can select different filters or choose to run without any filters. Figure 5 displays the photoemission spectrum of $Bi_2Sr_2CaCu_2O_8$ measured at 28 eV with the unfiltered beam and with the beam passing through the Mg filter. The spectrum taken without the filter is superimposed on a high background produced by

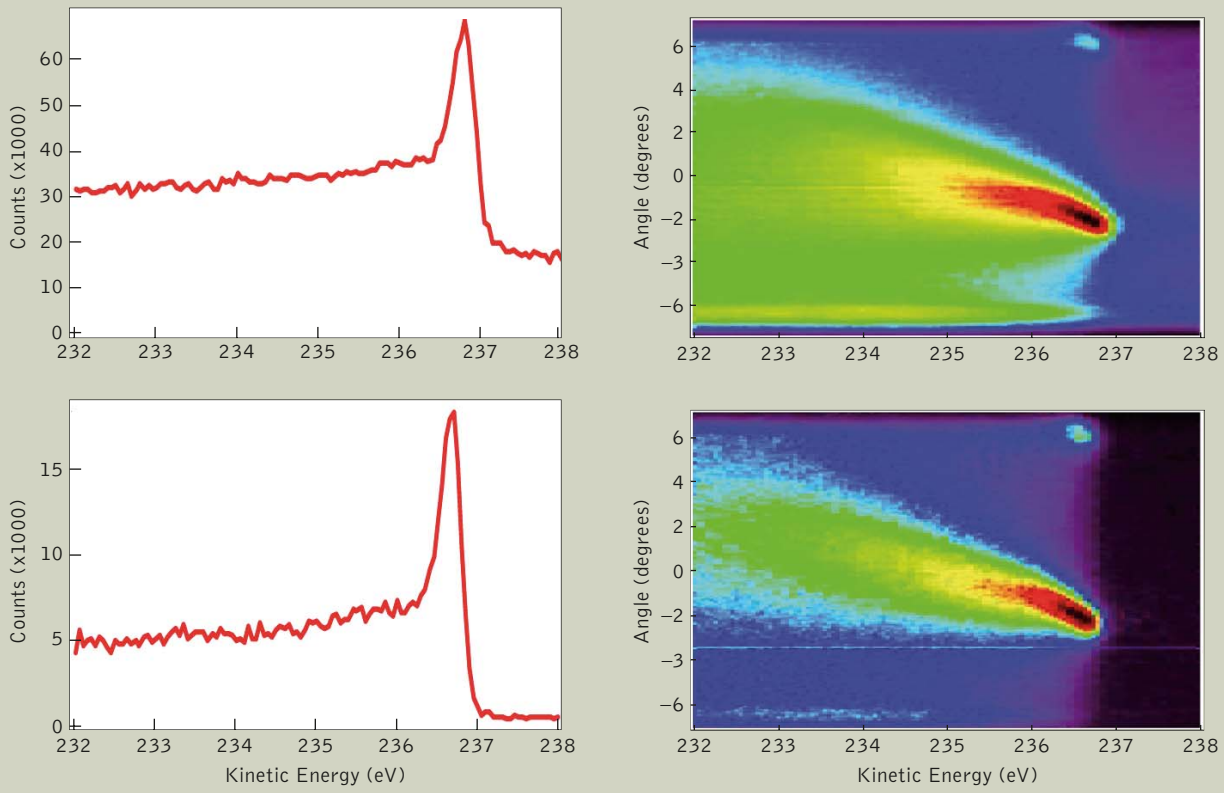

FIGURE 5
Photoemission spectrum of $Bi_2Sr_2CaCu_2O_8$ measured at 28 eV using a 300-line/mm grating. Top: Spectrum with the unfiltered beam (note high background due to high-order light). Bottom: Same spectrum measured after the high-order light was suppressed by the Mg filter.

the high-order light. Obtaining the true photoemission line shapes in this case is nearly impossible since the exact shape of the background is unknown. In contrast, the spectrum taken with the filter is very clean, with essentially no background due to the high-order light.

The second problem (beam motion) was treated by installing a beam-position monitor, a device that continually measures the profile of the photon beam along two orthogonal axes (x and y). This gives feedback to users and tells them whether they have to steer the photon beam by tilting horizontal and/or vertical mirrors in the K-B pair. Figure 6 shows a typical output signal: the sharp, tall peaks correspond to the beam profile along the x axis; the broad peaks represent the beam along the y axis; the extremely sharp blue peak is a reference signal.

The last problem was solved by implementing "compensated" angular scans of the sample. During the "compensated" scan (for automated Fermi-surface mapping, for example), the software keeps track of the sample position and automatically moves the sample along all coordinates to keep the photon beam at the same spot on the sample. Figure 7 displays the Fermi surface of a sample measured by Jonathan Denlinger (SSG) using

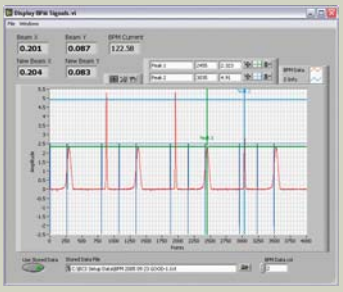

FIGURE 6
Output signal from a beam-position monitor (BPM) provides feedback to HARP users about beam motion.

compensated scans. Note the very "rocky" surface of the cleaved sample. It would have been extremely

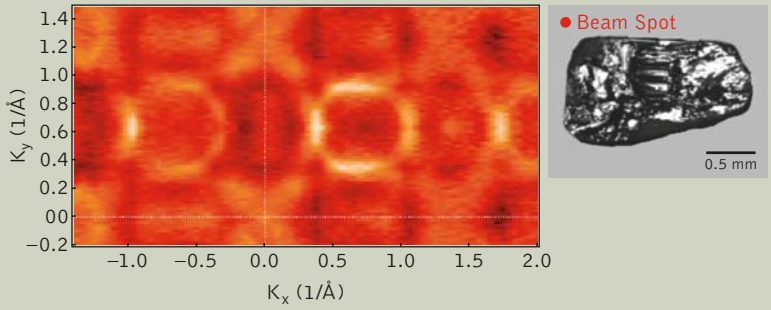

FIGURE 7
Fermi surface of a sample measured by Jonathan Denlinger (SSG) using compensated scans.

challenging, if not impossible, to measure the Fermi surface of such sample without the compensation.

Several Berkeley Lab staff members have made vital contributions to these developments: Eric Gullikson (CXRO) helped with the thin-film filters; John Pepper (ALS) developed and built the cryogenic sample manipulator; Ed Domning and Brian Smith (ALS) developed the software controlling the sample manipulator, BPM, and the beamline.

REFERENCES

1. M.Z. Hasan, Y.D. Chuang, D. Qian, Y.W. Li, Y. Kong, A. Kuprin, A.V. Fedorov, R. Kimmerling, E. Rotenberg, K. Rossnagel, Z. Hussain, H. Koh, N.S. Rogado, M.L. Foo, and R.J. Cava, "Fermi surface and quasiparticle dynamics of $Na_{0.7}CoO_2$ investigated by angle-resolved photoemission spectroscopy," *Phys. Rev. Lett.* **92,** 246402 (2004).
2. H.B. Yang, Z.H. Pan, A.K.P. Sekharan, T. Sato, S. Souma, T. Takahashi, R. Jin, B.C. Sales, D. Mandrus, A.V. Fedorov, Z. Wang, and H. Ding, "Fermi surface evolution and Luttinger theorem in Na_xCoO_2: A systematic photoemission study," *Phys. Rev. Lett.* **95,** 146401 (2005).
3. J.D. Koralek, J.F. Douglas, N.C. Plumb, Z. Sun, A.V. Fedorov, M.M. Murnane, H.C. Kapteyn, S.T. Cundiff, Y. Aiura, K. Oka, H. Eisaki, and D.S. Dessau, "Laser based angle-resolved photoemission, the sudden approximation, and quasiparticle-like spectral peaks in $Bi_2Sr_2CaCu_2O_{8+\delta}$," *Phys. Rev. Lett.* **96,** 017005 (2006).
4. D. Qian, L. Wray, D. Hsieh, D. Wu, J.L. Luo, N.L. Wang, A. Kuprin, A.V. Fedorov, R.J. Cava, L. Visiu, and M.Z. Hasan, "Quasiparticle dynamics in the vicinity of metal-insulator phase transition in Na_xCoO_2," *Phys. Rev. Lett.* **96,** 046407 (2006).

ADVANCED X-RAY INELASTIC SCATTERING FACILITY (AXIS) AT BEAMLINE 7.0.1

Photon-In/Photon-Out X-Ray Spectroscopy of DNA in Aqueous Solution

As part of a continuing, joint effort between Uppsala University and the ALS to study liquids using photon-in/photon-out x-ray spectroscopy, we investigated the nitrogen bonding structure of the DNA polymer, poly(dC)-poly(dG). Understanding protein functionality is of fundamental importance in biochemistry. Soft x-ray absorption and emission studies of poly(dC)-poly(dG) can elucidate the relationship between structure and functionality in proteins.

Since nitrogen atoms are found only in bases in DNA duplexes, photon-in/photon-out x-ray spectra extract the electronic orbital features of the bases in DNA. This would make it possible, for example, to learn whether electric conduction in DNA duplexes is due to charge hopping or charge transfer via delocalized states when electrons pass through the π* states of DNA bases. Three sharp peaks in the nitrogen absorption spectra at 398.5, 399.5, and 400.9 eV (Figure 8) indicate that absorption features originate from well-defined structures. From previous studies, we know that the 399.5-eV peak corresponds to the nitrile structure. Since the nitrile bond has predominantly π character, this peak appears strong in the π* region. The 398.5-eV

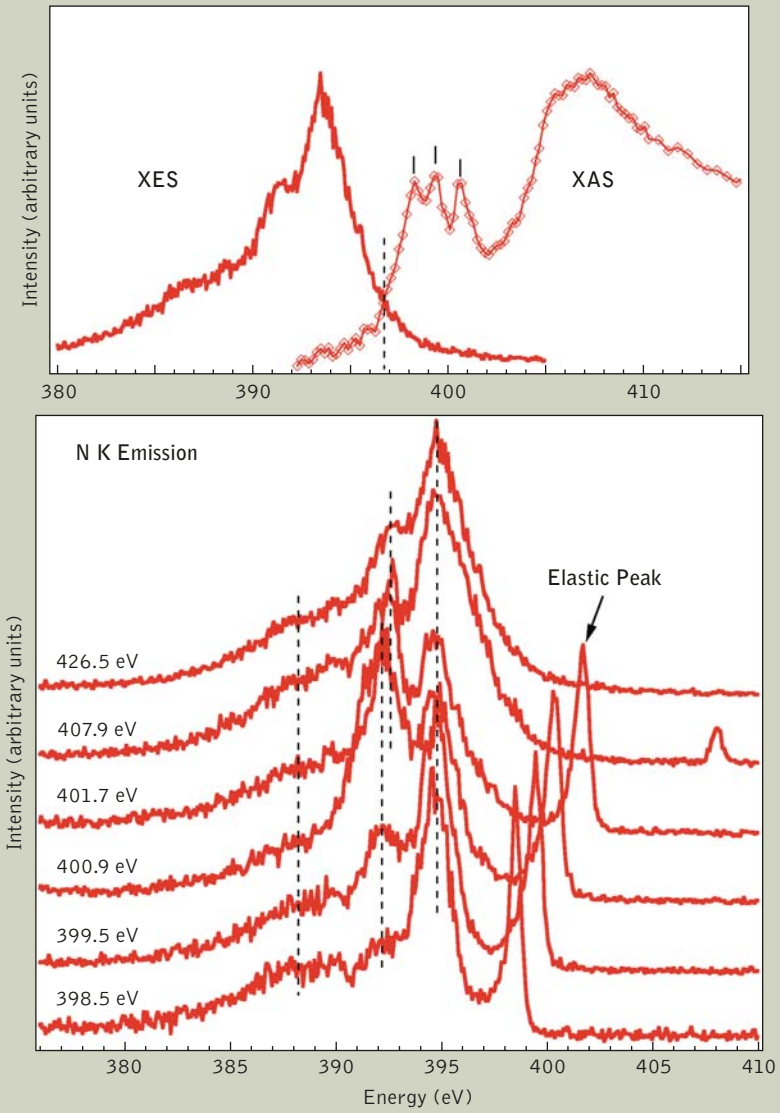

FIGURE 8
Top: Nitrogen K-edge absorption and emission spectra for poly(dC)-poly(dG). Bottom: Nitrogen K-edge emission spectra recorded at selected excitation energies.

peak corresponds to a pyridine-like structure. Graphite-like nitrogen produces a spectrum with a peak at 401.7 eV, with a shoulder to the low-energy side. This could be a low-energy σ* resonance; however, with the complex structure of DNA, it is difficult to separate the π and σ bonds. This structure, together with pyridine-like nitrogen, are possibly the origin of the 400.9-eV peak in the absorption spectrum.

Nitrogen K-edge emission spectra are also shown in Figure 8. The excitation energies were selected to correspond to the absorption features in the XAS spectrum. The fact that nitrogen atoms in different bonding environments are excited differently depending on the photon energy is clearly reflected by the differences in XES spectra. For the lowest excitation energy (398.5 eV), presumably corresponding to the 1s → π* transition of pyridine-like nitrogen, the main emission line is centered at 394.8 eV. The overall spectral shape is similar to that of pyridine. When the excitation energy is increased to 399.5 eV, mainly nitrogen in the nitrile structure should be excited. However, the emission spectra indicate that a large fraction of the pyridine-like nitrogen atoms are also excited at this energy. This can be explained by a relatively broad signal corresponding to pyridine-like nitrogen due to shifts that depend on the second-nearest neighbors. Thus the emission spectrum can be modeled by a superposition of the nitrile and pyridine-like spectra. The excitation energy of 400.9 eV, however, mainly excites the nitrile structure.

This effort is collaboration between Uppsala University (Johan Soderstrom, Joakim Andersson), the ALS (Jinghua Guo), Boston University (Per-Anders Glans, Timothy Learmonth, Kevin Smith), and the Northern California Institute for Research and Education (Hui Cheng, John McLeod Griffis).

Cryostat for Low-Temperature RIXS Experiments

The AXIS branch of Beamline 7.0.1 has been improved by the addition of an ALS-made cryostat and goniometer designed by John

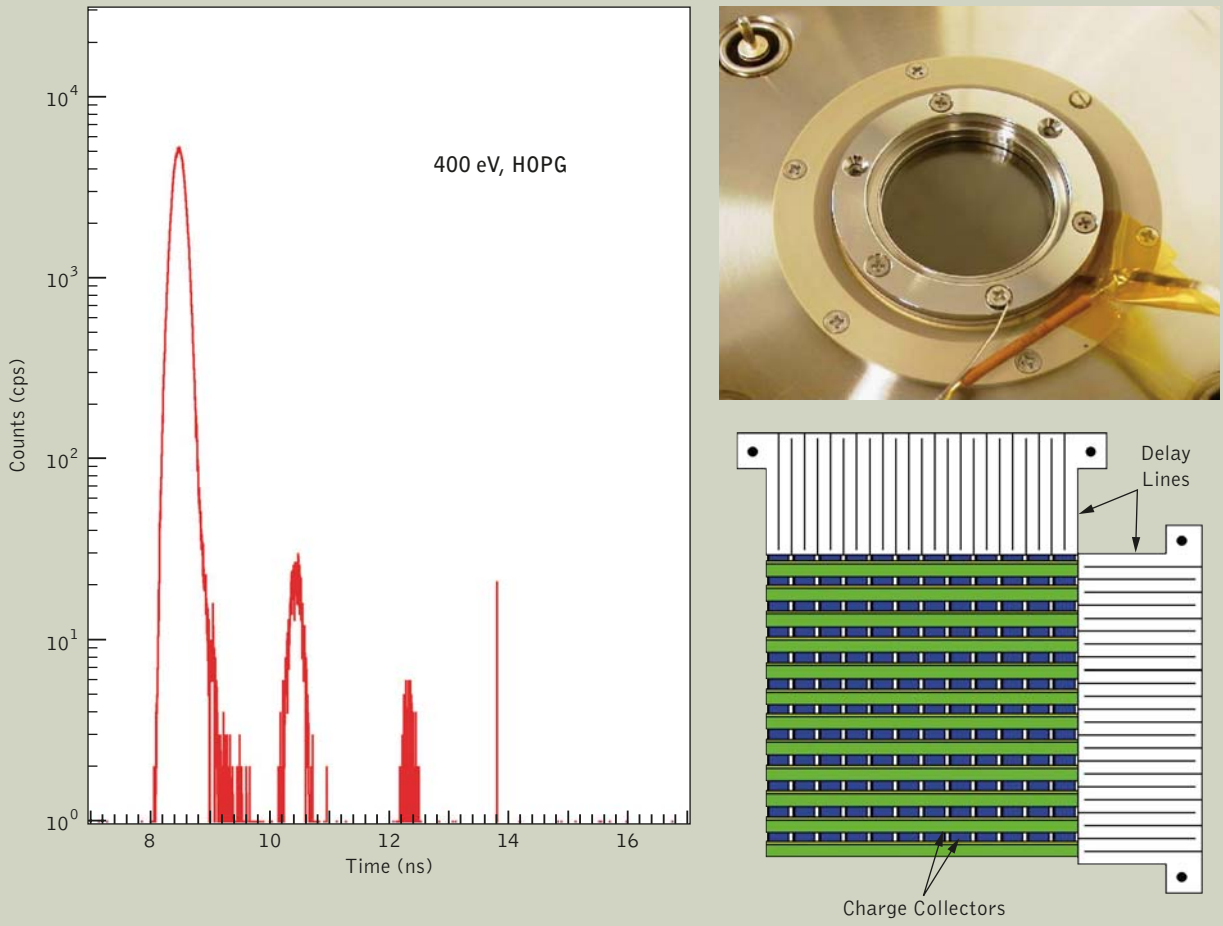

FIGURE 9
Left: Fluorescence signal detected from HOPG at an excitation energy of 400 eV. Right: The MCP detector (top) and cross delay-line readout scheme (bottom).

Pepper (Engineering Division) that allows resonant inelastic x-ray scattering (RIXS) experiments to be performed at temperatures as low as 10–15 K. Brian Smith (Controls Group) has also established a link between sample scanning control and data acquisition for the x-ray emission spectrometer, so it is now possible to obtain reliable x-ray absorption and emission spectra from soft materials such as polymers and biocomplex materials before photon-induced damage occurs.

Ultrafast MCP Detector Readout

In collaboration with the Space Sciences Laboratory of UC Berkeley, we have built an ultrafast multichannel plate (MCP) detector with a spatial resolution of 50 microns and a time resolution of 130 ps. The detector has been tested on Beamline 7.0.1 during two-bunch mode. The readout uses a cross delay-line design scheme, in which the MCP charge is divided between the upper and lower charge collectors. Event centroids are linearly proportional to the difference in signal arrival times at the ends of the delay lines. The full range on the time-to-digital converter was 17.68 ns, 41.68 ns, or 107.68 ns. Figure 9 shows the fluorescence signal from highly ordered pyrolytic graphite (HOPG). The first peak is coincident with the photons in the main bunch; the second peak appears closer to the

end of synchrotron run, when main bunch decays to the values seen when secondary bunch arrives, sometimes even the third one. The width of the main peak was measured to be 130 ps FWHM. The distance between the peaks is 2 ns, as it should be. The secondary peaks correspond to 2- and 4-ns delayed pulses, and thus are coming from the bunch behind the main one.

Ligand Field Multiplet Theory

To promote on-site activities involving theoretical calculations, we invited Frank de Groot (Utrecht University) to give a four-day course on Theo Thole multiplets. Ligand field multiplet theory can be used for x-ray absorption, XMCD, photoemission, resonant photoemission, Auger spectroscopy, and RIXS. Multiplet effects play an important role when there is a core hole in the L shell. Ligand field multiplet theory calculations are performed using Cowan's and Butler's codes, which were modified by Thole. In this approach, the interelectronic repulsions are introduced through Slater integrals, describing 3d–3d and 3d–2p Coulomb and (super) exchange interactions. Slater integrals and spin–orbit constants can be obtained using the Hartree-Fock method. The details of the course can be found at http://ssg.als.lbl.gov/ttcourse05/ttcourse05.htm.

There were over 50 attendees (Figure 10) from UC Berkeley, UC Davis, Stanford University, Montana State University, APS, Boston University, University of Saskatchewan, and University of British Colombia. Over 20 participants were from the ALS and different divisions of Berkeley Lab. The computer program provided by Frank has been installed on the SSG's super-PC in the SSG Library.

FIGURE 10
Participants of the Theo Thole Multiplets Course (September 27–30, 2005).

Left-Handed Nanoscale Meta-Materials: Towards the Optical Domain

Artificial meta-materials can be made that have a negative index of refraction, which allows a homogeneous flat slab of the material to behave as a "perfect" lens, possibly even creating sub-diffraction-limited focusing. The meta-materials consist of split-ring resonators that provide a negative □ and metal strips that provide a negative ε. The goal is to fabricate and measure left-handed nanoscale meta-materials taking advantage of the nanofabrication expertise within the CXRO.

We have begun the micro- and nanofabrication of these meta-material structures using gold on thin SiN windows (examples of split-ring resonators are shown in Figure 11, with dimensions as indicated). The SiN is thin enough that these are nearly free-standing structures, allowing us to fully characterize the index of refraction properties as a function of wavelength using Beamlines 1.4.2, 1.4.3, and 1.4.4.

We measured the polarized far-infrared (THz) spectral response of these meta-materials. Samples were measured in reflectance with variable angles of incidence between 5° and 80°. Figure 12 below shows an example of the measured and simulated magnetic resonance from the double split-ring resonator in the inset. The observed resonance frequency at about 37 cm^{-1} (~1.1 THz) is well predicted by the simulations. We have continued to push to smaller dimensions with structures having 60-nm dimensions using a nanowriter and are developing international collaborations to fully exploit these exciting meta-materials.

References

M.C. Martin, Z. Hao, A. Liddle, E.H. Anderson, W.J. Padilla, D. Schurig, and D.R. Smith, "Fabrication and optical measurements of nanoscale meta-materials: Terahertz and beyond," in *Proceedings of the Joint 30th International Conference on Infrared and Millimeter Waves and 13th International Conference on Terahertz Electronics* (IRMMW-THz 2005), Vol. 1, p. 34 (2005); Williamsburg, Virginia, September 19–23, 2005.

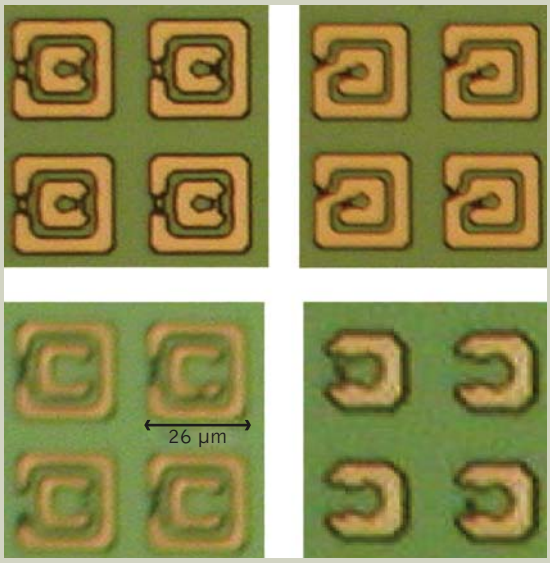

FIGURE 11
Micro- and nanofabrication of meta-material structures using gold on thin SiN windows (examples of split-ring resonators).

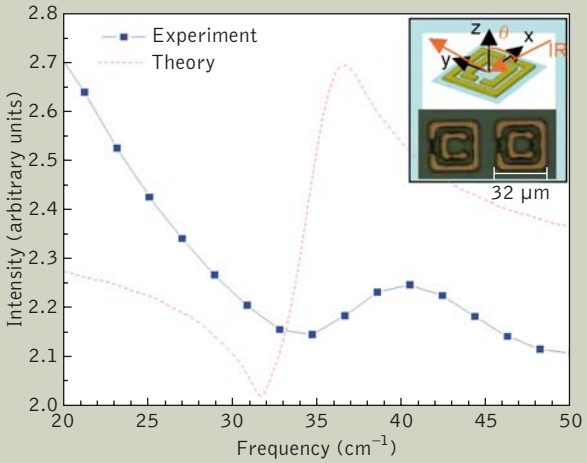

FIGURE 12
Example of the measured and simulated magnetic resonance from the double split-ring resonator in the inset.

Upgrade to the Electronic Structure Factory at Beamline 7.0.1

The Electronic Structure Factory (ESF) at Beamline 7.0.1 consists of an angle-resolved photoemission spectroscopy (ARPES) endstation together with an advanced molecular-beam epitaxy (MBE) chamber. In the past year, this endstation underwent a major upgrade to a new SES-R4000 analyzer with an order of magnitude more throughput than the previous detector for the same resolution. This improvement is achieved by the combination of a larger spectrometer size (200-mm mean radius instead of 100 mm) together with a larger angular acceptance (30° instead of 7°). As a result of the higher throughput, it is now possible to take three-dimensional band-structure data (energy, k_x, k_y) in minutes for publication-quality data or in practically real time for purposes of sample alignment and survey. Full surveys over the four-dimensional space (energy, k_x, k_y, k_z) can therefore be acquired for most materials in around 1.5–2.0 hours with reasonable statistics. Figure 13 shows a typical example of data that can be acquired using the new system. The band structure of Gd(0001), grown in situ on a W(110) crystal, was acquired over a region in k space comparable to the Brillouin zone dimensions in under three minutes. In addition, a major upgrade to the vacuum pumping has now let us achieve a routine base pressure of around 1.0×10^{-11} Torr without activating the cryostat. Sample storage and growth vacuum chambers are typically in the mid 10^{-11} Torr range.

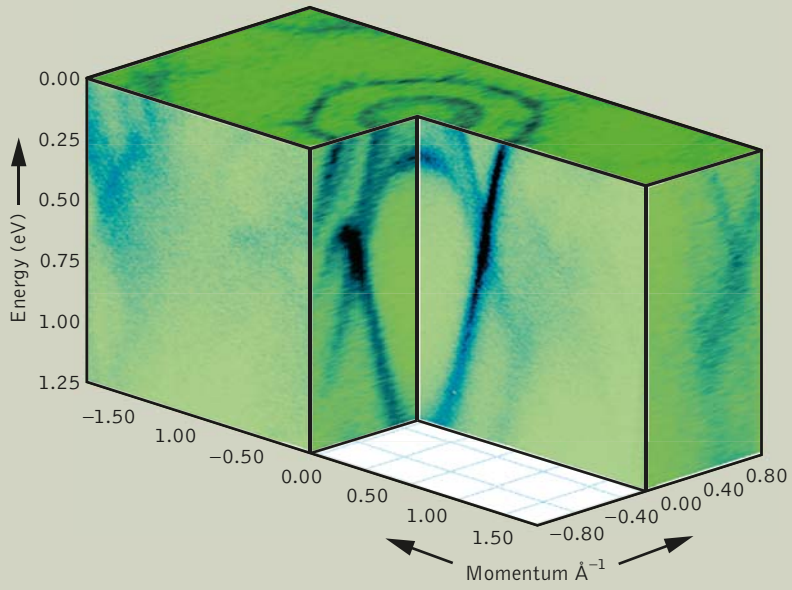

FIGURE 13
The band structure of Gd(0001) on W(110), acquired in 160 s at the Electronic Structure Factory. The instantaneously acquired data (energy-momentum planes covering ±1.5 $Å^{-1}$) are rastered over the orthogonal direction using the sample goniometer's motor (data courtesy of S.D. Kevan, University of Oregon).

Testing of New Endstation for Nanometer-Scale ARPES

The ALS strategic plan lays out the plan for new instrumentation capabilities. The highest-priority items include the development of small-spot ARPES for analysis of microcrystals and phase-segregated materials with a resolution on the order of 50 nm. To that end, a "nanoARPES" test chamber was constructed using a zone plate to focus the light down to around 300 nm, and ARPES measurements were conducted on a variety of test samples.

Figure 14 provides a dramatic demonstration of the capabilities we can expect to have routinely when nanoARPES is fully developed. The data show the individual crystalline grains in polycrystalline (HOPG) graphite. The contrast mechanism is neither topographical nor chemical (for which no contrast can be expected) but rather the valence-band intensity captured within a 12 × 1° solid angle. The method is roughly equivalent to a microdiffraction experiment in which grains can be oriented using an angular emission pattern (in this case, photoelectron emission rather than photon emission), but the information conveyed is electronic rather than structural. To highlight this electronic contrast, Figure 14 shows individual electronic bands acquired from different grains. Ultimately, such data could be used as a new kind of scanning probe sensitive to transport properties, many-body interactions, and other fundamental properties normally measured macroscopically using ARPES. Future goals for nanoARPES are to make the test endstation functional for user proposals and to design and attempt to raise funds for an optimized beamline and endstation.

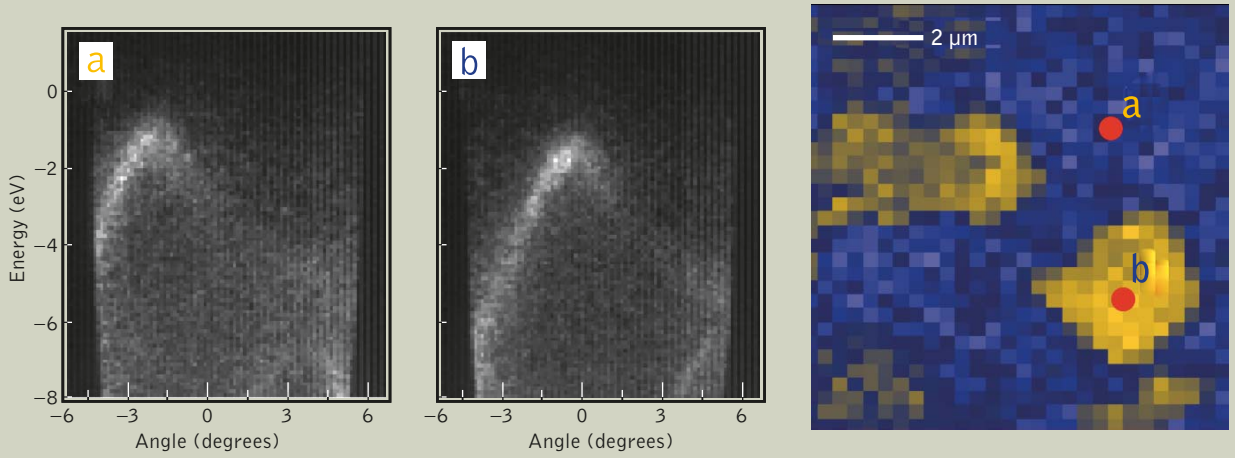

FIGURE 14
Electronic bands (12° wide angular window) of two different crystalline grains (labeled a and b) that were isolated from a polycrystalline (HOPG) graphite sample. The intensity map on the right is a micrograph of the sample's domain structure built up from such valence band maps.

User Services

Gary Krebs, User Services Group Leader

The User Services Group mission is to provide a friendly and efficient interface to the ALS, focusing on safety for users and visitors. The group is made up of four sections: the User Services Office, Beamline Coordination, Material Management, and Technical Information. These groups work together to provide the users with a wide range of services.

User Services Office

The User Services Office is staffed by administrative personnel who help new and continuing users with the registration and safety process. All registered users must carry an electronic identification key card, which allows them access to Berkeley Lab and the ALS experiment floor. Over 2000 users accessed the experiment floor in 2005. The experiment safety process is initiated at the office both with respect to general facility safety and specific experiment safety. New users can complete much of the processing before they arrive by preregistering on the ALS Web site (www.als.lbl.gov/4DCGI/WEB_GetForm/PGIFormEntry.shtml/Initialize).

General user proposals for beam time are received through the ALS Web site and are peer reviewed and ranked for scientific merit by the Proposal Study Panel (PSP). The User Services Office provides administrative and logistical support for the PSP. The proposal submission and beam time allocation process is described in greater detail on the ALS Web site (www.als.lbl.gov/als/quickguide/independinvest.html). In addition, the User Services Office provides administrative support to the UEC. The UEC, elected annually by the users, serves as the voice of that diverse group and represents them in the ALS strategic planning process.

FIGURE 1
Barbara Phillips, Olga Poblete, Jeff Troutman, Carmen Escobar, David Malone, Valerie Wysinger, and Gary Krebs.

For out-of-towners, the User Services Office can also help in finding a place to stay while working at the ALS. The office manages the ALS apartments; detailed information can be found on the Web at www.als.lbl.gov/als/quickguide/housing.html.

The User Services Office is managed by Jeff Troutman and includes Carmen Escobar, Sharon Fujimura, Barbara Phillips, Olga Poblete, and Valerie Wysinger (Figure 1).

Beamline Coordination

The Beamline Coordination section coordinates the safety inspection required for each experiment. All experiments are examined and documented in detail to ensure the safety of users, visitors, and operations personnel. Beamline coordi-

nators work closely with Berkeley Lab safety specialists in the areas of electrical, mechanical, chemical, radiation, seismic, and laser safety. The Beamline Coordination Section is led by Donna Hamamoto and includes John Pruyn and David Malone (Figure 2).

Material Management

The Material Management section provides shipping, receiving, temporary storage, and endstation setup services. The section maintains a stockroom of parts and equipment, including safety devices, commonly needed by ALS users and technicians (Figure 3). These supplies are accessible by key card 24 hours a day. The section is managed by Gary Giangrasso and includes Todd Anderson, Derrick Crofoot, and Jason De Ponte (Figure 4).

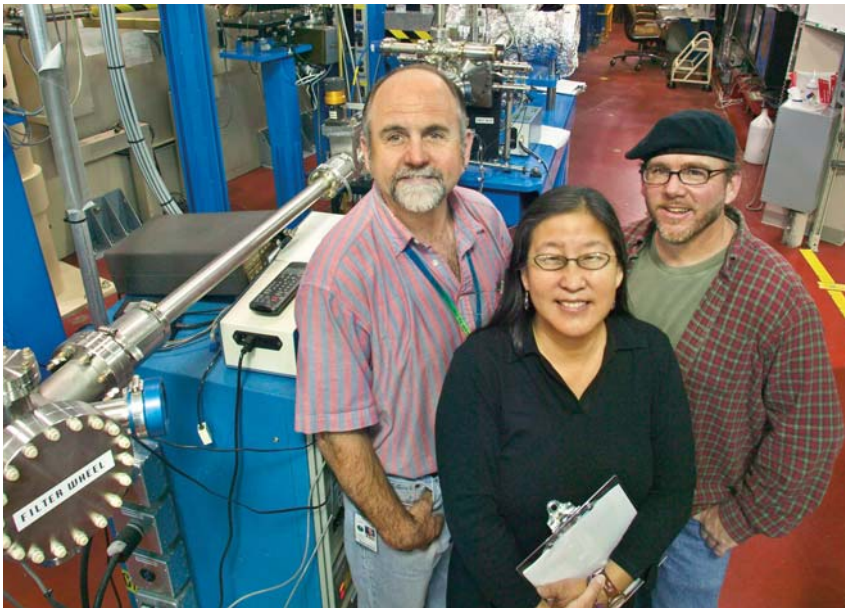

FIGURE 2
John Pruyn, Donna Hamamoto, and David Malone.

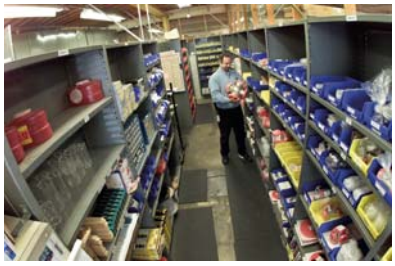

FIGURE 3
Commonly needed parts and equipment are kept in a user stock room available 24 hours a day by key card.

FIGURE 4
Gary Giangrasso, Jason De Ponte, Derrick Crofoot, and Todd Anderson.

Technical Information

The Technical Information section is responsible for producing this Activity Report as well as the ALS Web site, newsletter, science highlights, and countless special brochures and posters. The section provides science writing, graphic design, and Web expertise to help keep the ALS scientific and technical community, government officials, and the general public informed about the science carried out at the ALS. The group maintains strong ties to the educational community, both within the state of California, the U.S., and internationally. The section is led by Art Robinson and includes Elizabeth Moxon, Lori Tamura, and Greg Vierra.

User Demographics in 2005

The User Services Group collects user demographics and publication information, available in this Activity Report as well as online (http://www-als.lbl.gov/als/publications/). As a national user facility, the ALS is required to report these statistics annually to the U.S. Department of Energy. The ALS continued to grow rapidly in 2005. Figure 5 shows the growth in particular scientific fields and the overall user growth from 1997–2005. The breakdown of different institutions that make up our user base is shown in Figure 6. The growth of the user community over the past 10 years is mirrored by the growth in beamlines and publications, as shown in Figure 7. As the number of beamlines approaches the capacity of the storage ring, new beamlines will be created by chicaning straight sections and revamping some older bend-magnet beamlines.

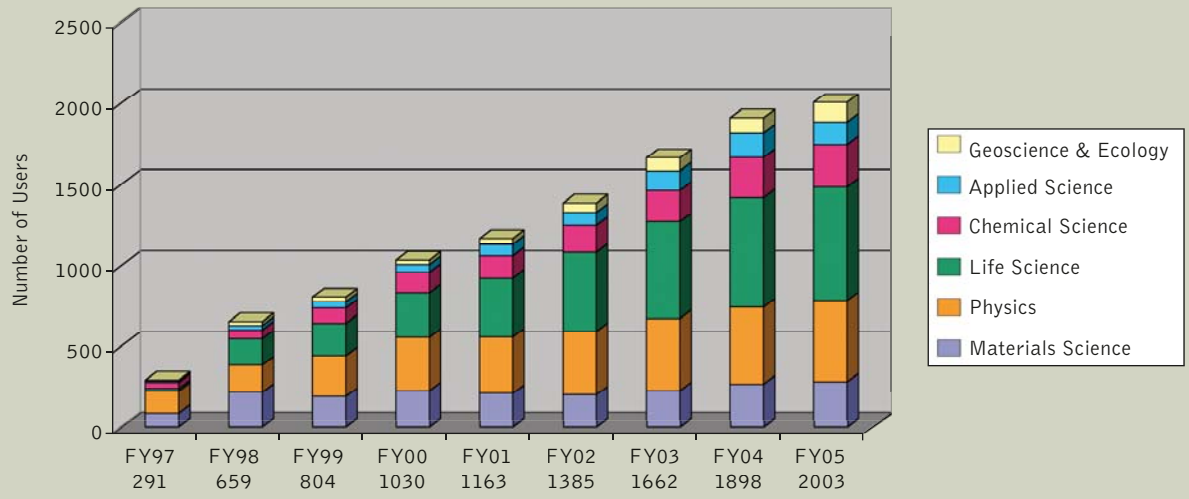

FIGURE 5
Bar graph showing growth in areas of science.

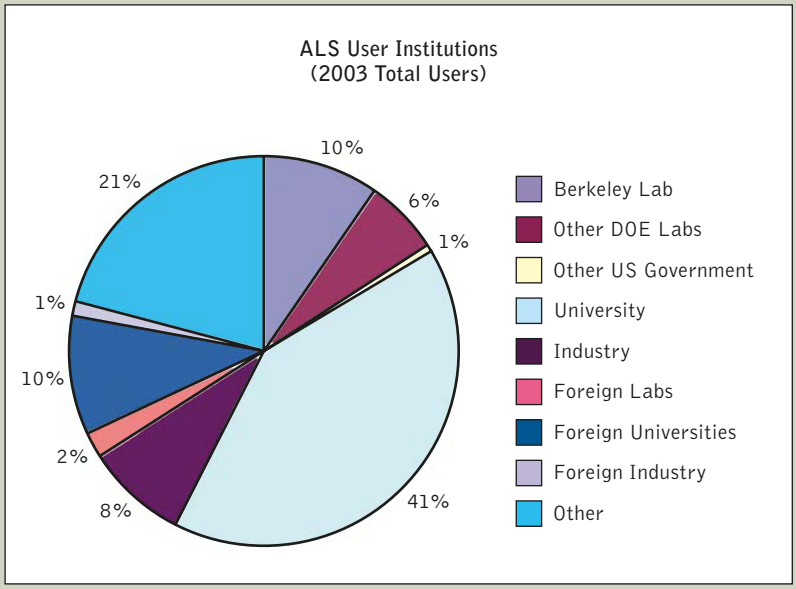

FIGURE 6
Pie chart showing percentages of different types of user institutions.

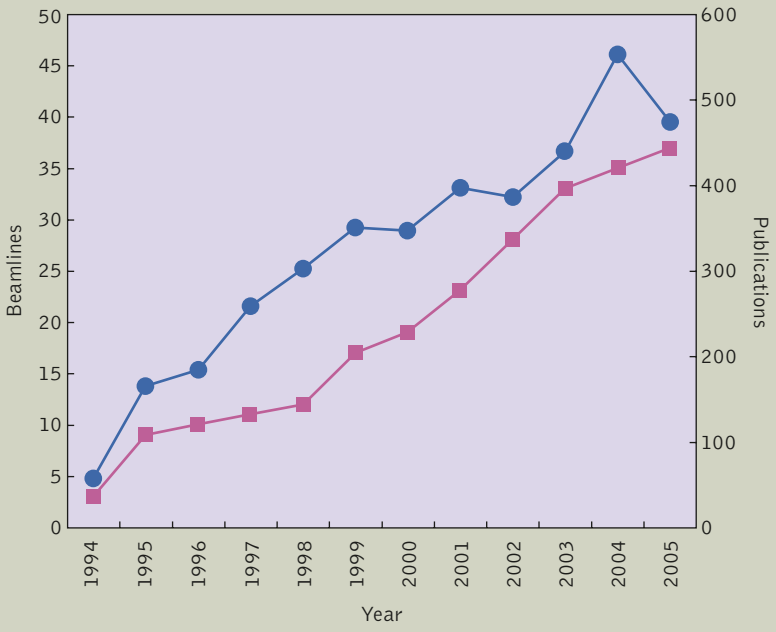

FIGURE 7
Graph of growth in beamlines (pink) and publications (blue). Note that publications for 2005 were still being collected at the time this section was being written.

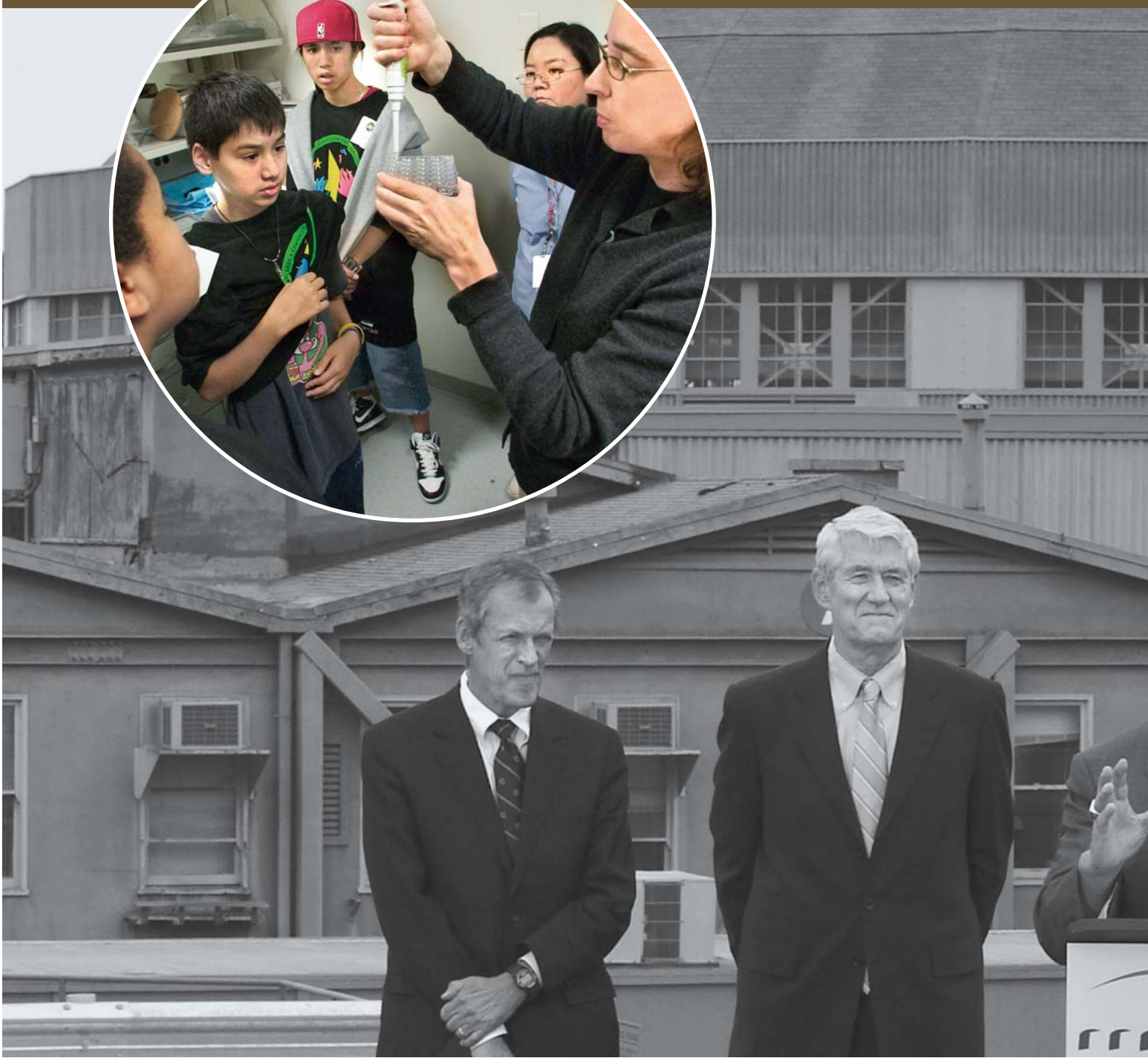

Special Events

Meetings and Workshops

2005 ALS Users' Meeting
October 20–22, 2006

After a welcome to meeting attendees from Berkeley Lab Director Steve Chu (left) and an ALS update from Acting Division Director Janos Kirz (below), Pat Dehmer, DOE BES Associate Director of Science, took questions from the floor following her "Perspectives from Washington" talk (lower left).

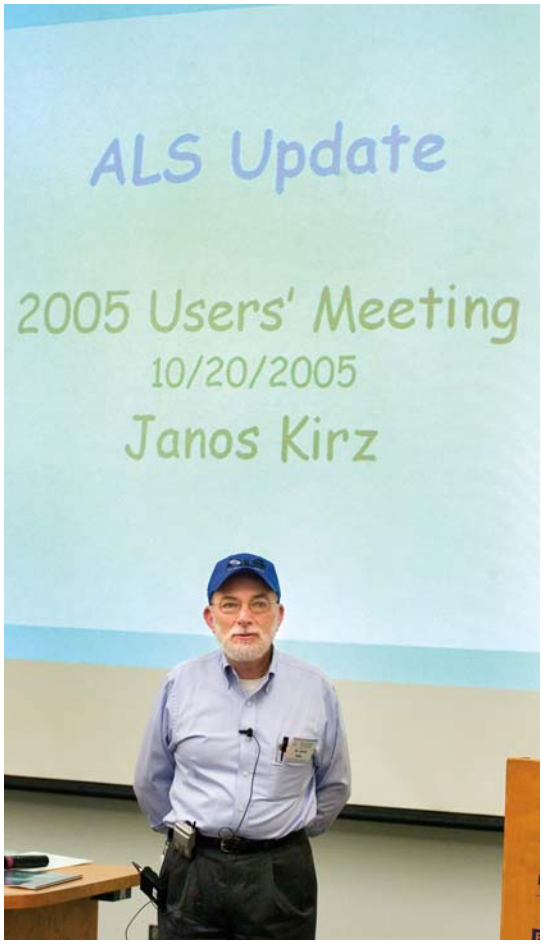

A historic moment occurred when Pat Dehmer awarded retiring ALS Division Director Daniel Chemla a DOE Distinguished Associates Award. After acknowledging Dr. Chemla's outstanding scientific and leadership contributions to Berkeley Lab and, in particular, to the ALS, she joined the audience in a prolonged standing ovation.

The plenary session of the meeting featured presentations covering the diverse areas of research at the ALS. During the Science Highlights session, Tonio Buonassisi (left) of Berkeley Lab discussed recent research into the metal impurity nanodefects that limit solar cell performance (see "Engineering Metal Impurities in Multicrystalline Silicon Solar Cells" in the Nano and Materials Science section of the Science Highlights). An earlier keynote address from Z.X. Shen of Stanford University (right) detailed photoemission studies of complex materials.

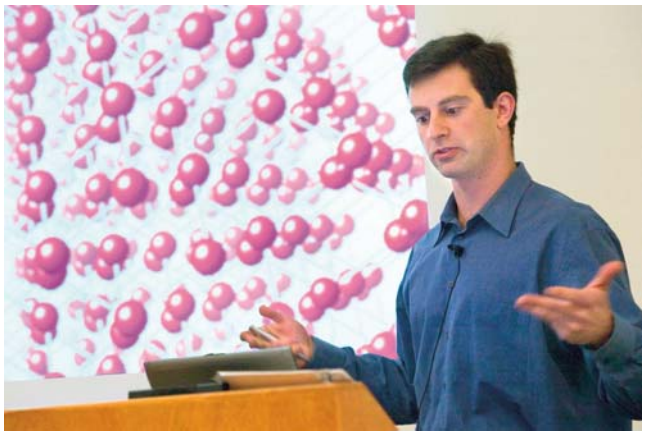

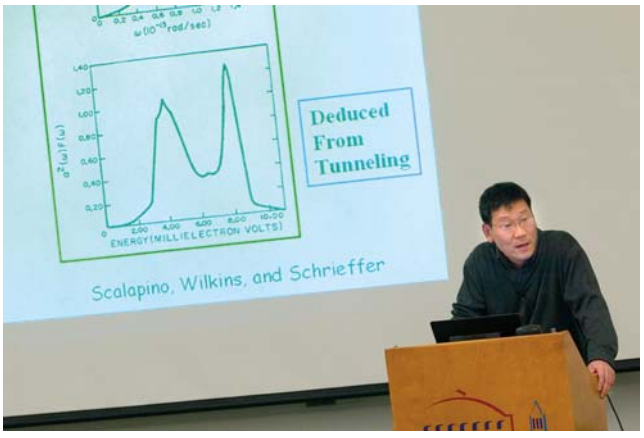

Meeting participants had the opportunity to view more than 120 posters (left) and the offerings of 28 exhibitors of synchrotron-related equipment during the popular reception for vendors (right).

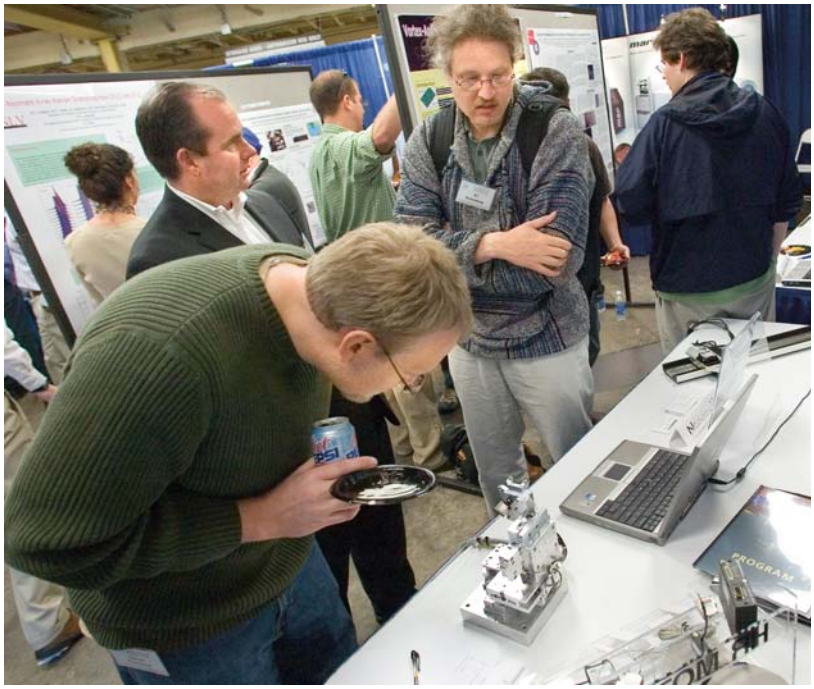

The awards banquet and barbecue filled the tents on the ALS patio on the final evening of the meeting.

AWARDS

Neville Smith presented the David A. Shirley Award for scientific achievement to Craig Taatjes (right) (Sandia National Laboratories), Terrill Cool (Cornell University), and Philip Westmoreland (University of Massachussetts) for their research that revealed enols in flames (see "Combustion Research Heats Up at the ALS," featured in the Science Highlights section).

The Klaus Halbach Award for innovative instrumentation was won by Soren Prestemon (Engineering Division) and Elke Arenholz (ALS) for the design and implementation of a vector magnetometer for soft x-ray studies. Soren (left) accepted the award from Acting ALS Director Janos Kirz on behalf of the team.

Users' Meeting program co-chair Jinghua Guo presented this year's student poster prizes to Michelle Weinberger (UCLA) who won first prize for her poster, "In Situ High-Pressure X-Ray Diffraction Experiments for the Determination of the Mechanical Properties of New Ultra-Incompressible, Ultrahard Materials," and to Benjamin Yuhas (UC Berkeley) who took second prize for the poster, "Synchrotron XRD and EXAFS of Transition-Metal Doped Zinc Oxide Nanowires."

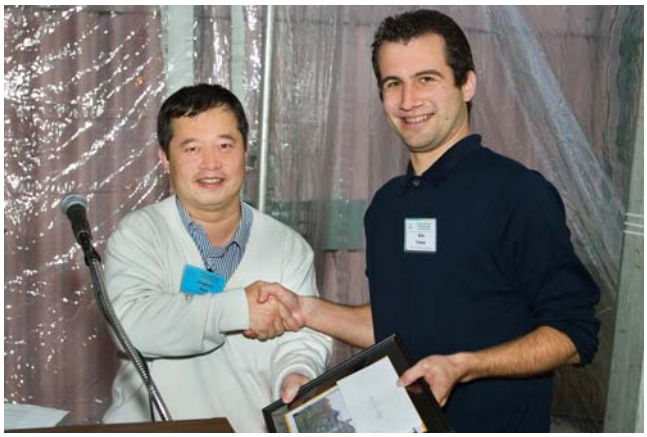

UEC Chair Greg Denbeaux presented Ed Wong (Mechanical Technology User Support) and Ron Slater (Electronic Maintenance) with the Tim Renner User Services Award for their outstanding support to the ALS user community.

A full complement of 12 workshops filled conference rooms around Berkeley Lab. Topics covered included soft and hard x-ray tomography, ultrafast science, atomic and molecular physics, bandmapping, microdiffraction, and macromolecular crystallography techniques.

A first ever Public Science Lecture was held as part of this year's Users' Meeting. Dr. Joachim (Jo) Stöhr, SSRL Director, engaged the capacity audience with his presentation of "The Magic of Magnetism: From Physical Attraction to Spin Doctors."

Molecular Nanoscience Workshop in Honor of Daniel Chemla's 65th Birthday November 21, 2006

A Molecular Nanoscience Workshop was held in November to celebrate the career and scientific achievements of retiring ALS Division Director Daniel Chemla. Colleagues past and present from around the world participated in a busy program of talks and presentations that acknowledged not only Daniel's accomplishments, but also his impact on the future directions of nanoscience research.

Daniel and his wife Berit during a break in the program.

Distinguished Visitors

In June, Ray Orbach (center), Director of DOE's Office of Science, stopped at Beamline 7.0.1 to talk about recent research with beamline scientist Eli Rotenberg (left) during a tour of the ALS with Acting Division Director Janos Kirz.

Members of the Scientific Advisory Committee paused during their July meeting for a photo on the ALS patio. The SAC meets annually to discuss strategic planning and organizational, scientific, and user issues at the ALS. From left, Sunil Sinha, Sam Bader, Jennifer Doudna, Yves Idzerda, Neil Ashcroft, Phil Bucksbaum, John Spence, Steve Kevan, Tony Starace, Don Sparks, Pascal Elleaume, and Greg Denbeaux.

California Governor Arnold Schwarzenegger (at podium) visited the ALS in August accompanied by (left to right) UC President Robert Dynes, UC Berkeley Chancellor Robert Birgeneau, and Berkeley Lab Director Steve Chu. After touring the facility, the governor held a press conference to discuss the importance of scientific research to the California economy.

Richard Blum (second from left), Vice Chairman of the UC Regents, visited the National Center for X-Ray Tomography (NCXT) beamline construction area and viewed examples of current research with NCXT Director Carolyn Larabell as Berkeley Lab Director Steve Chu (left), and ALS Scientific Director Neville Smith (right) look on.

During a September visit to the Berkeley Lab, Charles M. Vest, President Emeritus of the Massachusetts Institute of Technology (left), got an "overview" tour of the ALS atop the booster ring with ALS Scientific Director Neville Smith.

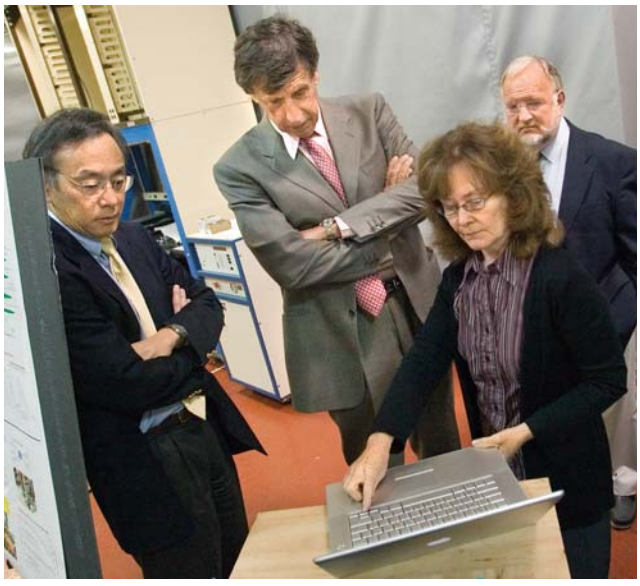

Education

Corie Ralston of the Physical Biosciences Division shows eager students how to prepare protein crystals for experiments as part of Daughters and Sons to Work Day at the ALS.

David Attwood of CXRO paused with students from UC's Summer Undergraduate Program in Engineering Research at Berkeley (SUPERB) after touring the ALS.

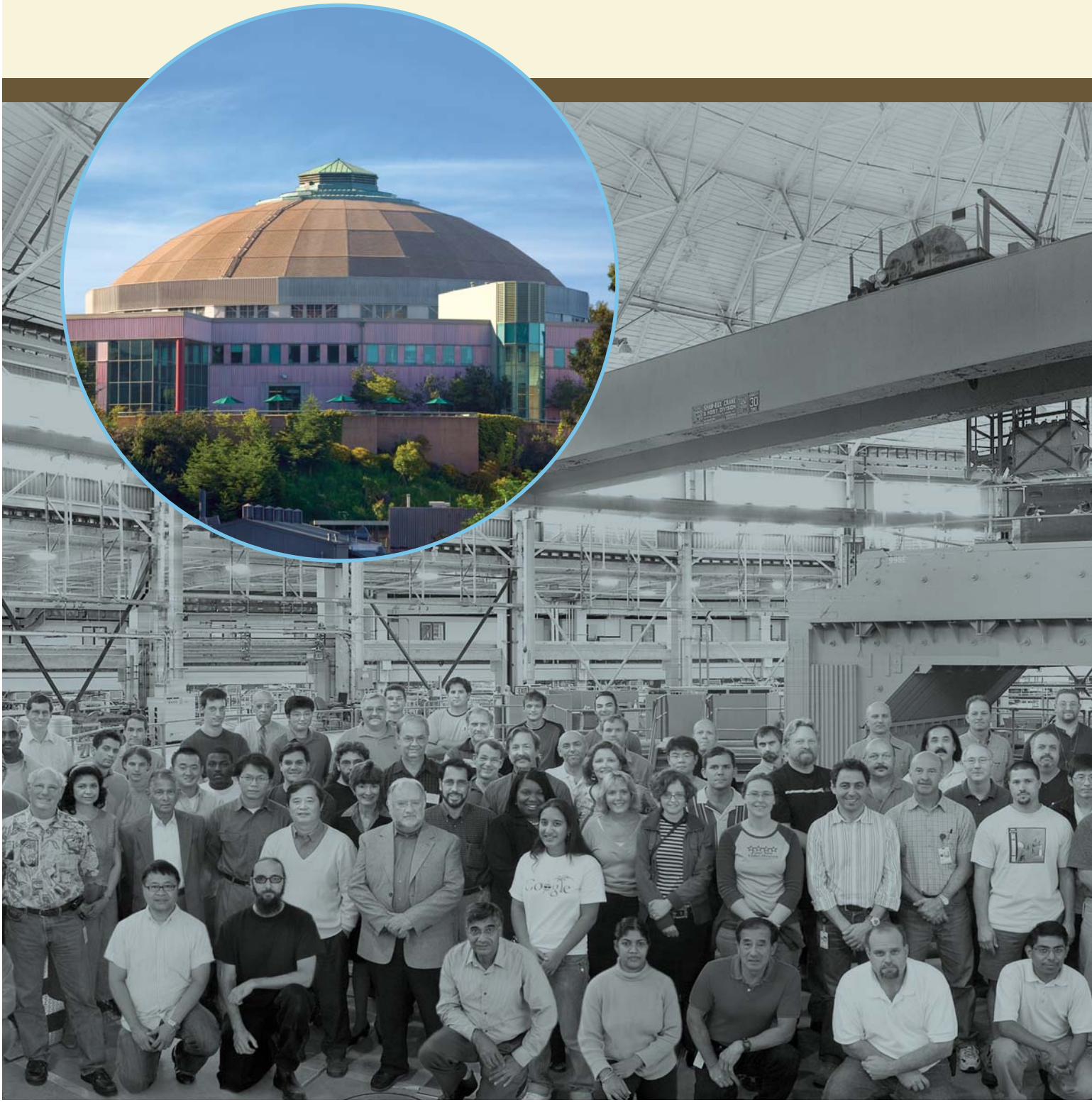

About the ALS

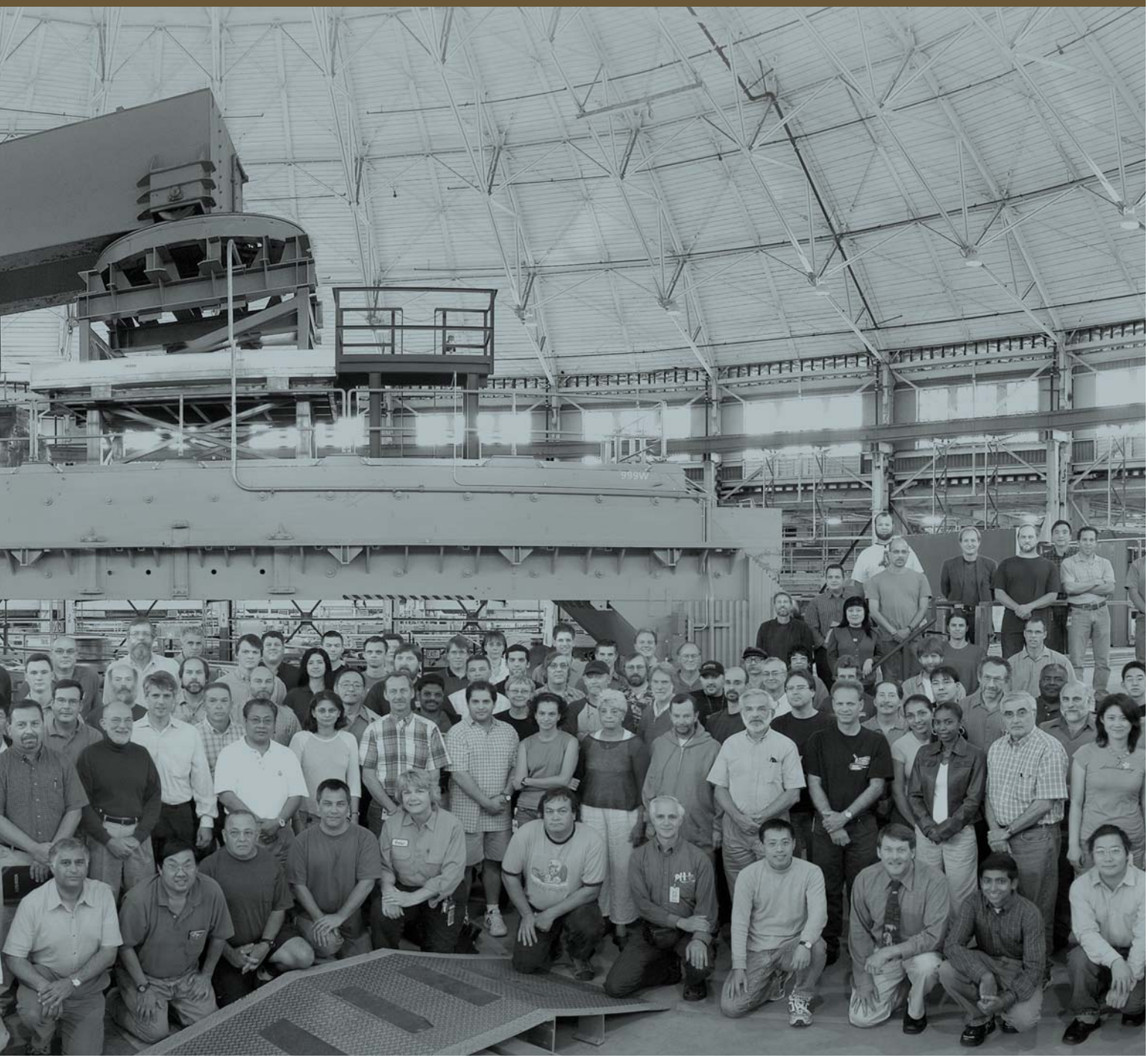

ALS Staff

This is a cumulative list of all those who worked at the ALS during the 2005 calendar year. The list includes visitors, students, as well as staff members from other divisions who were matrixed to the ALS.

Division Management

D. Chemla†
J. Kirz
B. Feinberg
J. Krupnick
N. Smith

Accelerator Physics

D. Robin, Group Leader
C. Steier, Deputy Leader
W. Byrne
A. Loftsdottir*
H. Nishimura
G. Portmann
H. Sannibale
T. Scarvie
W. Wan
W. Wittmer**

Administration

C. Cooper
A. Reza
N. Sallee
L. Senft

Budget

J. Coyne
J. Kekos
M. Lewis

Computer Protection

E. Williams

Controls

A. Biocca, Group Leader
C. Timossi, Deputy Leader
T. Campbell
E. Domning
H. Huang
C. Ikami
S. Jacobson
T. Kellog
A. Robb
B. Smith
J. Spring
R. Steele
J. Turner
M. Urashka
E. Williams

Electrical Engineering

W. Barry, Group Leader
G. Stover, Deputy Leader
B. Bailey
M. Balagot
K. Baptiste
M. Bell
R. Candelario
P. Casey
M. Chin
R. Colston
S. Cooper
P. Cull
J. Elkins
M. Fahmie
R. Gassaway
R. Gervasoni
A. Geyer
L. Holzer
J. Julian
B. Kelius
P. Kozy
T. Kuneli
S. Kwiatkowski
E. Lee
W. Mattson
P. Molinari
R. Mueller
J. Nomura
F. Ottens
S. Rogoff
P. Rosado
M. Sawada
A. Sippio
R. Slater
M. Szajbler
R. Velasco
D. Vandyke
M. Vinco
J. Weber
K. Woolfe

Environment, Safety, and Health

R. Baker
B. Fairchild
T. Kuneli
G. Perdue

Experimental Systems

H. Padmore, Group Leader
A. Warwick, Deputy Leader
R. Celestre
M. Church
S. Clark
A. Doran
S. Fakra
J. Feng
J. Glossinger
E. Glover
J. Hao
P. Heimann
M. Howells
S. Irick
T. Kellog
A. MacDowell
M. Marcus
W. McKinney
G. Morrison
S. Morton
J. Nasiatka
K. Opachich
A. Scholl
N. Tamura
B. Valek
V. Yashchuck
A. Young

Mechanical Engineering

R. Duarte, Group Leader
N. Andresen
R. Beggs
D. Calais
A. Catalano
M. Coleman
D. Colomb
C. Cummings
M. Decool
A. DeMello
S. Dimaggio
D. Ellis
J. Fischer
D. Fritz
A. Gavidia
D. Gibson
F. Gicquel
J. Haugrud
C. Hernikl
C. Hopkins
D. Horler
D. Hull
D. Jones
J.-Y. Jung
N. Kelez
S. Klingler
M. Kritscher
K. Krueger
A. Lim
A. Lobodovsky
R. Low
D. MacGill
S. Marks
P. McKean
H. Meyer
T. Miller
V. Moroz
G. Morrison
D. Munson
W. Ogelsby
M. Omerbashich
J. Osborn
E. Palmerston
J. Pepper
K. Peterman
P. Pipersky
D. Plate
S. Prestemon
A. Rawlins
D. Shuman
K. Sihler
A. Smith
T. Stevens
M. Thomas
W. Thur
M. Wingert
E. Wong
D. Yegian
F. Zucca

Operations

J. Pusina, Group Leader
W. Byrne, Deputy Leader
M. Beaudrow
D. Brothers
K. Osborne
A. Pearson
D. Richardson
D. Riley-Cole
S. Stricklin
M. Wolfe

Procedure Center

R. Jones

Project Management

A. Catalano
S. Rossi

Quality Assurance

D. Richardson

Scientific Support

Z. Hussain, Group Leader
J. Bozek, Deputy Leader
G. Ackerman
E. Arenholz
W. Bates
A. Bostwick
K. Chesnel**
Y.-D. Chuang**
J. Denlinger
A. Federov
J. Guo
A. Guy
C. Hauck
D. Kilcoyne
G. Lebedev
M. Martin
S. Mun
J. Pepper
M. Pfeifer**
E. Rotenberg
B. Rude
F. Schlachter
J. Spear
T. Tyliszczak

User Services

G. Krebs, Group Leader
A. Robinson, Deputy Leader
T. Anderson
J. De Ponte
C. Escobar
S. Fujimura
G. Giangrasso
D. Hamamoto
D. Malone
E. Moxon
B. Phillips
O. Poblete
J. Pruyn
J. Troutman
M. Tablan
L. Tamura
G. Vierra
V. Wysinger

Visitors and Students

T. Araki**
A. Bartelt**
H. Barth
B. Batterman
F. Baumberger**
R. Bilodeau**
A. Budiman
S. Caldwell
A. Chakmatov
S. Chourou
A. Comin**
C. Cui**
A. Das
P. Dietrich
B. Freelon**
E. Gann
P. Glans**
A. Gleason
M. Greaves
Z. Hao*
F. Himpsel
M. Hindi
S. Kashtanov
S. Kevan
A. Kouprine
M. Kunz
D. Lacy
K. Lee
M. Liberati**
A. MacPhee
N. Mannella**
J. McChesney
G. Meyer
B. Nellis
M. Nip
H. Ohldag
T. Ohta*
K. Opachich*
G. Paranthaman
J. Patel
M. Perri**
E. Poliakoff
D. Rolles
M. Rossi
S. Roy
H.-J. Shin
D. Shiraki
K. Smith
J. Soderstrom**
L. Sorenson
J. Spence
Z. Sun
M. Van Hove
D. Walker
M. Watanabe
M. Water
C. Won*
A. Wu
W. Yang
J. Zaanen
X. Zhou

ALS Doctoral Fellows

Y. Chen*
I. Dumitriu*
A. Hudson*
T. Learmonth*
Z. Li*
Z. Pan*
P. Strachan*
M. Weinberger*

†On leave
*Graduate Student Research Assistant
**Postdoc

ALS Advisory Panels

Scientific Advisory Committee

Neil Ashcroft, Cornell University
Samuel Bader (chair), Argonne National Laboratory
Phil Bucksbaum, University of Michigan
Greg Denbeaux (ex-officio), University at Albany, State University of New York
Jennifer Doudna, Berkeley Lab
Wolfgang Eberhardt, BESSY GmbH
Pascal Elleaume, European Synchrotron Facility Radiation Facility
Yves Idzerda (ex-officio), Montana State University
Stephen Kevan (past chair), University of Oregon
Carolyn Larabell, Berkeley Lab
John Parise, State University of New York
Erwin Poliakoff, Louisiana State University
Miquel Salmeron, Berkeley Lab
Sunil Sinha, University of California, San Diego
Don Sparks, University of Delaware
John Spence, Arizona State University
Tony Starace, University of Nebraska
J. Friso van der Veen, Paul Scherrer Institut
Linda Young, Argonne National Laboratory

Users' Executive Committee

Gregory Denbeaux (chair) University at Albany, State University of New York
Dan Dessau, University of Colorado
Jinghua Guo, Advanced Light Source, Berkeley Lab
Clemens Heske (vice chair), University of Nevada, Las Vegas
Amanda Hudson (student), University of Nevada, Las Vegas
Keith Jackson, Center for X-Ray Optics, Berkeley Lab
Dennis Lindle (past chair), University of Nevada, Las Vegas
Gary Mitchell, Dow Chemical Company
Yasuji Muramatsu, Japan Atomic Energy Research Institute
Corie Ralston, Physical Biosciences Division, Berkeley Lab
Tony van Buuren, Lawrence Livermore National Laboratory
Ed Westbrook, Molecular Biology Consortium

Science Policy Board

Massimo Altarelli, Elettra Synchrotron Light Laboratory
Samuel Bader, Argonne National Laboratory
Paul Fleury, Yale University
Franz Himpsel, University of Wisconsin, Madison
Walter Kohn, University of California, Santa Barbara
Yuan T. Lee, Academia Sinica, Tawian
Albert Narath, Lockheed Martin Corporation (retired)
Yves Petroff, European Synchrotron Radiation Facility
Alan Schriesheim, Argonne National Laboratory
Robert Tijan, University of California, Berkeley
Eberhardt Umbach, University of Würzburg

Facts and Figures

Using the Advanced Light Source

The ALS, a DOE national user facility, welcomes researchers from universities, industry, and government laboratories. Qualified users have access to the ALS as general users or as members of either a participating research team (PRT) or approved program (AP). PRTs and APs (groups of researchers with related interests from one or more institutions) construct and operate beamlines and have primary responsibility for experiment endstation equipment. They are entitled to a certain percentage of their beamline's operating time commensurate with the resources that they have contributed to the beamline. Through a peer-reviewed proposal process, the remaining beamtime is granted to general users, who may provide their own endstation or negotiate access to a PRT- or AP-owned endstation.

The ALS does not charge users for beam access if their research is nonproprietary. Users performing proprietary research are charged a fee based on full cost recovery. All users are responsible for the day-to-day costs of research (e.g., supplies, phone calls, technical support).

The nominal operating energy of the ALS storage ring is 1.9 GeV, although it can run from 1.0 to 1.9 GeV, allowing flexibility for user operations. At 1.9 GeV, the normal maximum operating current is 400 mA in multibunch operation. The spectral range of undulator and wiggler beamlines extends from photon energies of roughly 5 eV to 21 keV; on superbend beamlines the range is between 2.4 and 60 keV. Bend magnets produce radiation from the infrared to about 20 keV.

The ALS is capable of accommodating approximately 50 beamlines and more than 100 endstations. The first user beamlines began operation in October 1993, and there were 37 operating beamlines, with several more under construction, by the end of 2005.

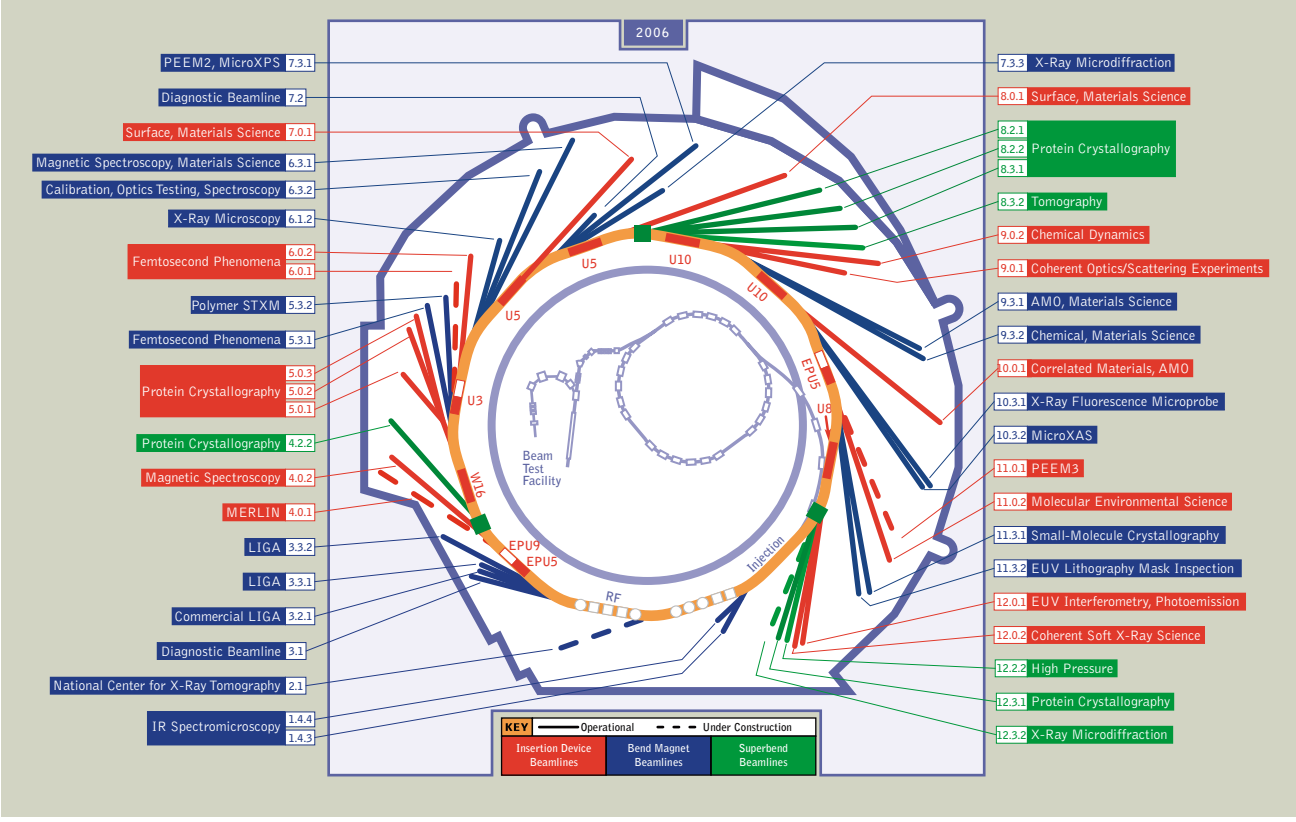

ALS Beamlines[a]

Beamline	Source	Areas of Research/Techniques	Monochromator	Energy Range	Operational
1.4.3	Bend	Infrared spectromicroscopy	Interferometer	0.05–1.2 eV (600–10,000 cm^{-1})	Now
1.4.4	Bend	Infrared spectromicroscopy	Interferometer	0.05–1.5 eV (400–12,000 cm^{-1})	Now
2.1	Bend	National Center for X-Ray Tomography (XM-2)	Zone-plate linear	200 eV–7 keV	2006
3.1	Bend	Diagnostic beamline	Mirror/filter	1–2 keV	Now
3.2.1	Bend	Commercial deep-etch x-ray lithography (LIGA)	None	3–12 keV	Now
3.3.1	Bend	Deep-etch x-ray lithography (LIGA)	None	3–12 keV	Now
3.3.2	Bend	Deep-etch x-ray lithography (LIGA)	None	3–12 keV	Now
4.0.1	EPU9	High-resolution spectroscopy of complex materials (MERLIN)	Variable-included-angle SGM	8–150 eV	2006
4.0.2	EPU5	Magnetic spectroscopy			
		Advanced photoelectron spectrometer/ diffractometer	Variable-included-angle PGM	52–1900 eV	Now
		L-edge chamber with superconducting spectrometer	Variable-included-angle PGM	52–1900 eV	Now
		XMCD chamber (6 T, 2 K)	Variable-included-angle PGM	52–1900 eV	Now
		Eight-pole electromagnet	Variable-included-angle PGM	52–1900 eV	Now
4.2.2	SB	Multiple-wavelength anomalous diffraction (MAD) and monochromatic protein crystallography	Double crystal	5–17 keV	Now
5.0.1	W11	Monochromatic protein crystallography	Curved crystal	12.4 keV	Now
5.0.2	W11	Multiple-wavelength anomalous diffraction (MAD) and monochromatic protein crystallography	Double crystal	3.5–14 keV	Now
5.0.3	W11	Monochromatic protein crystallography	Curved crystal	12.4 keV	Now
5.3.1	Bend	Femtosecond phenomena	Double crystal	1.8–12 keV	Now
5.3.2	Bend	Polymer scanning transmission x-ray microscopy	SGM	250–700 eV	Now
6.0.1	U3	Femtosecond phenomena	Double crystal	2–10 keV	2006
6.0.2	U3	Femtosecond phenomena	VLS-PGM	200–1800 eV	Now
6.1.2	Bend	High-resolution zone-plate microscopy	Zone-plate linear	300–1300 eV	Now
6.3.1	Bend	Magnetic spectroscopy and materials science			
		Mini Magnet	VLS-PGM	300–2000 eV	Now
		Reflectometer	VLS-PGM	300–2000 eV	Now
6.3.2	Bend	Calibration and standards; EUV optics testing; atomic, molecular, and materials science	VLS-PGM	50–1300 eV	Now
7.0.1	U5	Surface and materials science, spectromicroscopy			
		Scanning photoemission microscope (SPEM)	SGM	100–800 eV	Now
		Electronic Structure Factory (ESF)	SGM	60–1200 eV	Now
		Advanced X-Ray Inelastic Scattering (AXIS)	SGM	80–1200 eV	Now
7.2	Bend	Diagnostic beamline	Filter/none	Far IR–17 keV	Now
7.3.1	Bend	Magnetic microscopy, spectromicroscopy	SGM	175–1500 eV	Now
7.3.3	Bend	X-ray microdiffraction	White light, two or four crystal	6–12 keV	Now
8.0.1	U5	Surface and materials science, imaging photoelectron spectroscopy, soft x-ray fluorescence			
		Ellipsoidal-mirror electron energy analyzer (EMA)	SGM	65–1400 eV	Now
		Soft x-ray fluorescence spectrometer (SXF)	SGM	65–1400 eV	Now
8.2.1	SB	Multiple-wavelength anomalous diffraction (MAD) and monochromatic protein crystallography	Double crystal	5–17 keV	Now
8.2.2	SB	Multiple-wavelength anomalous diffraction (MAD) and monochromatic protein crystallography	Double crystal	5–17 keV	Now
8.3.1	SB	Multiple-wavelength anomalous diffraction (MAD) and monochromatic protein crystallography	Double crystal	2.4–18 keV	Now
8.3.2	SB	Tomography	Double crystal	3–60 keV	Now

Beamline	Source	Areas of Research/Techniques	Monochromator	Energy Range	Operational
9.0.1	U10	Coherent optics/scattering experiments	None or off-axis zone plate	10–800 eV	Now
9.0.2	U10	Chemical dynamics			
		Molecular-beam photoelectron/photoion imaging and spectroscopy	White light, Off-plane Eagle	5–30 eV	Now
		Flame chamber	White light, Off-plane Eagle	5–30 eV	Now
		Ablation chamber	White light, Off-plane Eagle	5–30 eV	Now
		Aerosol chamber	White light, Off-plane Eagle	5–30 eV	Now
		Kinetics machine	White light, Off-plane Eagle	5–30 eV	Now
9.3.1	Bend	Atomic, molecular, and materials science			
		Angle-resolved time-of-flight electron spectrometer	Double crystal	2.2–5.5 keV	Now
		Ion time-of-flight spectrometer	Double crystal	2.2–5.5 keV	Now
		Magnetic mass analyzer	Double crystal	2.2–5.5 keV	Now
		Polarized-x-ray emission spectrometer	Double crystal	2.2–5.5 keV	Now
		X-ray absorption cell	Double crystal	2.2–5.5 keV	Now
		XAFS station	Double crystal	2.2–5.5 keV	Now
9.3.2	Bend	Chemical and materials science, circular dichroism, spin resolution			
		Advanced materials chamber (AMC)	SGM	30–1400 eV	Now
		Ambient pressure photoemission	SGM	30–1400 eV	Now
10.0.1	U10	Photoemission of highly correlated materials; high-resolution atomic, molecular, and optical physics			
		High-energy-resolution spectrometer (HERS)	SGM	17–340 eV	Now
		High-resolution atomic and molecular electron spectrometer (HiRAMES)	SGM	17–340 eV	Now
		Ion-photon beamline (IPB)	SGM	17–340 eV	Now
		Electron spin polarization (ESP)	SGM	17–340 eV	Now
10.3.1	Bend	X-ray fluorescence microprobe	White light, multilayer mirrors	3–20 keV	Now
10.3.2	Bend	Environmental and materials science, micro x-ray absorption spectroscopy	White light, two crystal	2.5–17 keV	Now
11.0.1	EPU5	Magnetic microscopy, spectromicroscopy (PEEM3)	VLS-PGM	100–2000 eV	2006
11.0.2	EPU5	Molecular environmental science			
		Wet spectroscopy	Variable-included-angle PGM	95–2000 eV	Now
		High-pressure photoemission spectroscopy	Variable-included-angle PGM	95–2000 eV	Now
		Scanning transmission x-ray microscope (STXM)	Variable-included-angle PGM	130–2000 eV	Now
11.3.1	Bend	Small-molecule crystallography	Channel-cut Si(111)	6–17 keV	Now
11.3.2	Bend	Inspection of EUV lithography masks	VLS-PGM	50–1000 eV	Now
12.0.1	U8	EUV optics testing and interferometry, angle- and spin-resolved photoemission			
		EUV interferometer (2 available)	VLS-PGM	60–320 eV	Now
		Angle- and spin-resolved photoemission	VLS-PGM	20–320 eV	Now
12.0.2	U8	Coherent soft x-ray science			
		Coherent optics	VLS-PGM	200–1000 eV	Now
		Coherent scattering	VLS-PGM	200–1000 eV	Now
12.2.2	SB	California High-Pressure Science Observatory (CALIPSO)			
		Nanoscience/materials chemistry	Double crystal	6–40 keV	Now
		Solid-state physics/geoscience	Double crystal	6–40 keV	Now
12.3.1	SB	Structurally Integrated Biology for Life Sciences (SIBYLS)	Double crystal and double multilayer	5.5–17 keV	Now
12.3.2	SB	X-ray microdiffraction	White light and four crystal	6–22 keV	2006
BTF	Linac	Beam Test Facility	None	50-MeV electrons	Now

[a]The information in this table is valid as of May 2006. The most current information about ALS beamlines is available on the Web at www-als.lbl.gov/als/als_users_bl/bl_table.html.

Bend = bend magnet SB = superconducting bend magnet EPUx = x-cm-period EPU Ux = x-cm-period undulator Wx = x-cm-period wiggler

ALS Insertion Device Parameters[a]

Device Beamline	Status	Energy Range at 1.5 GeV (eV)	Energy Range at 1.9 GeV (eV)	Period (cm)	No. of Periods	Operating Gap Range (cm)	Effective Field Range (T)
U3	6.0.2	Operational	73–3100	120–5000 4000–11000[b]	3.0	50	0.55–2.7
U5	8.0.1	Operational	50–1900	80–3000	5.0	89	1.4–4.5
U5	7.0.1	Operational	50–1900	80–3000	5.0	89	1.4–4.5
U8	12.0.1	Operational	18–1200	20–1900	8.0	55	2.47–8.3
U10	9.0.1	Operational	5–950	8–1500	10.0	43	2.27–11.6
U10	10.0.1	Operational	8–950	12–1500	10.0	43	2.31–11.6
EPU5	4.0.2	Operational	47–1000[c]	75–3000[c]	5.0	37	1.40–5.5[d] 0.58–0.10[e]
EPU5	11.0.1	Operational	50–1000[c]	80–3000[c]	5.0	36.5	1.44–5.5[d] 0.57–0.10[e]
EPU5	11.0.2	Operational	47–1000[c]	75–3000[c]	5.0	37	1.38–5.5[d] 0.58–0.10[e]
W11	5.0.2	Operational	6000–13000[b]	6000–21000[b]	11.4	29	1.25–18.0

[a]The information in this table is valid as of December 2005.
[b]Wiggler mode. [c]Elliptical polarization mode.
[d]Vertical field. [e]Horizontal field.

ALS Storage Ring Parameters[a]

Parameter	Value
Beam particle	Electron
Beam energy	1.0–1.9 GeV
Injection energy	1.0–1.5 GeV
Beam current	
multibunch mode	400 mA
two-bunch mode	2 × 25 mA
Filling pattern (multibunch mode)	276 to 320 bunches possibility of 10-mA "camshaft" bunch in filling gap
Bunch spacing	
multibunch mode	2 ns
two-bunch mode	328 ns
Circumference	196.8 m
Number of straight sections	12
Current number of insertion devices	10
Radio frequency	499.642 MHz
Beam size in straight sections, rms	
(1.9 GeV multibunch mode)	310 microns horiz. × 16 microns vert.

Parameter	Value at 1.5 GeV	Value at 1.9 GeV
Beam lifetime		
multibunch mode	~3.5 hours at 400 mA	~8.0 hours at 400 mA
two-bunch mode	not used	~60 min. at 40 mA
Horizontal emittance	4.2 nm-rad	6.3 nm-rad
Vertical emittance [b]	0.2 nm-rad	0.13 nm-rad
Energy spread (ΔE/E, rms)	8×10^{-4}	1×10^{-3} [c]
Pulse length (FWHM)	65 ps	70 ps [d]

[a]The information in this table is valid as of December 2005.
[b]Vertical emittance is deliberately increased to improve beam lifetime.
[c]Above 8 mA per bunch in two-bunch mode, the energy spread increases because of the microwave instability.
[d]In multibunch mode, the bunch length is deliberately increased using harmonic cavities to improve the beam lifetime. In two-bunch mode, the bunch length is current dependent and decreases from about 70 ps at high bunch current to below 40 ps at small current.

Publications

Listed below are publications (e.g., journal articles, conference papers, theses, and book chapters) that were published in calendar year 2005 and are based on data obtained in whole or in part at the ALS as well as publications containing descriptions of experiment, beamline, or accelerator systems developed at the ALS.

Aagaard, A., P. Listwan, N. Cowieson, T. Huber, T. Ravasi, C. Wells, J.U. Flanagan, S. Kellie, D.A. Hume, B. Kobe, and J.L. Martin, "An inflammatory role for the mammalian carboxypeptidase inhibitor latexin: Relationship to cystatins and the tumour suppressor TIG1," *Structure* 13, 309 (2005).

Abendroth, J., P. Murphy, M. Sandkvist, M. Bagdasarian, and W.G.J. Hol, "The x-ray structure of the type II secretion system complex formed by the N-terminal domain of EpsE and the cytoplasmic domain of EpsL of *Vibrio cholerae*," *J. Mol. Biol.* 348, 845 (2005).

Abu-Samha, M., K.J. Børve, L.J. Sæthre, and T.D. Thomas, "Conformational effects in inner-shell photoelectron spectroscopy of ethanol," *Phys. Rev. Lett.* 95, 103002 (2005).

Accardi, A., M. Walden, W. Nguitragool, H. Jayaram, C. Williams, and C. Miller, "Separate ion pathways in a Cl^-/H^+ exchanger," *Journal of General Physiology* 126, 563 (2005).

Acrivos, J.V., "$YBa_2Cu_3O_7$ electromagnetic optic effects in Ba $L_{2,3}$ x-ray absorption near T_c," *Microchemical Journal* 81, 98 (2005).

Adams, E.J., Y.H. Chien, and K.C. Garcia, "Structure of a γδ T cell receptor in complex with the nonclassical MHC T22," *Science* 308, 227 (2005).

Adams, J.A., A. Bostwick, T. Ohta, F.S. Ohuchi, and M.A. Olmstead, "Heterointerface formation of aluminum selenide with silicon: Electronic and atomic structure of Si(111):AlSe," *Phys. Rev. B* 71, 195308 (2005).

Addlagatta, A., X. Hu, J.O. Liu, and B.W. Matthews, "Structural basis for the functional differences between Type I and Type II human methionine aminopeptidases," *Biochemistry* 44, 14741 (2005).

Aertgeerts, K., I. Levin, L. Shi, G.P. Snell, A. Jennings, G.S. Prasad, Y. Zhang, M.L. Kraus, S. Salakian, V. Sridhar, R. Wijnands, and M.G. Tennant, "Structural and kinetic analysis of the substrate specificity of human fibroblast activation protein α," *J. Biol. Chem.* 280, 19441 (2005).

Aguilar, A., E.D. Emmons, M.F. Gharaibeh, A.M. Covington, J.D. Bozek, G. Ackerman, S. Canton, B. Rude, A.S. Schlachter, G. Hinojosa, I. Alvarez, C. Cisneros, B.M. McLaughlin, and R.A. Phaneuf, "Photoionization of ions of the nitrogen isoelectronic sequence: Experiment and theory for F^{2+} and Ne^{3+}," *J. Phys. B–At. Mol. Opt.* 38, 343 (2005).

Akey, D.L., and J.M. Berger, "Structure of the nuclease domain of ribonuclease III from *M. tuberculosis* at 2.1 Å," *Protein Sci.* 14, 2744 (2005).

Aldaz, H., L.M. Rice, T. Stearns, and D.A. Agard, "Insights into microtubule nucleation from the crystal structure of human γ-tubulin," *Nature* 435, 523 (2005).

Andersson, K., A. Gomez, C. Glover, D. Nordlunc, H. Ostrom, T. Schiros, O. Takahasi, H. Ogasawara, L.G.M. Pettersson, and A. Nilsson, "Molecularly intact and dissociative adsorption of water on clean Cu(110): A comparison with the water/Ru(001) system," *Surface Science Letters* 585, L183 (2005).

Apiyo, D., L. Zhao, M.D. Tsai, and T.L. Selby, "X-ray structure of the R69D phosphatidylinositol-specific phospholipase C enzyme: Insight into the role of calcium and surrounding amino acids in active site geometry and catalysis," *Biochemistry* 44, 9980 (2005).

Araki, T., A.P. Hitchcock, F. Shen, P.L. Chang, M. Wang, and R.F. Childs, "Quantitative chemical mapping of sodium acrylate- and N-vinylpyrrolidone-enhanced alginate microcapsules," *J. Biomater. Sci., Polym. Ed.* 16, 611 (2005).

Arenholz, E., and K. Liu, "Angular dependence of the magnetization reversal in exchange biased Fe/MnF_2," *Appl. Phys. Lett.* 87, 132501 (2005).

Arenholz, E., and S. Prestemon, "Design and performance of an eight pole resistive magnet for soft x-ray magnetic dichroism measurements," *Rev. Sci. Instrum.* 76, 83908 (2005).

Aston, D.J., D.J. Payne, A.J.H. Green, R.G. Egdell, D.S.L. Law, J.H. Guo, P.A. Glans, T. Learmonth, and K.E. Smith, "High-

resolution x-ray spectroscopic study of the electronic structure of the prototypical p-type transparent conducting oxide $CuAlO_2$," *Phys. Rev. B* 72, 195115 (2005).

Augustsson, A., G.V. Zhuang, S.M. Butorin, J.M. Osorio-Guillén, C.L. Dong, R. Ahuja, C.L. Chang, P.N. Ross, J. Nordgren, and J.H. Guo, "Electronic structure of phospho-olivines Li_xFePO_4 (x=0,1) from soft-x-ray-absorption and -emission spectroscopy," *J. Chem. Phys.* 123, 184717 (2005).

Bajt, S., Z.R. Dai, E.J. Nelson, M.A. Wall, J. Alameda, N. Nguyen, S. Baker, J.C. Robinson, J.S. Taylor, M. Clift, A. Aquila, E.M. Gullikson, and N.V.G. Edwards, "Oxidation resistance of Ru-capped EUV multilayers," *Proc. SPIE*, 5751, 118 (2005); Microlithography 2005, San Jose, California, February 27–March 4, 2004.

Balooch, G., M. Balooch, R.K. Nalla, S. Schilling, E.H. Filvaroff, G. Marshall, S.J. Marshall, R.O. Ritchie, R. Derynck, and T. Alliston, "TGF-β regulates the mechanical properties and composition of bone matrix," *Proc. Natl. Acad. Sci. USA* 102, 18813 (2005).

Barabash, R.I., G.E. Ice, N. Tamura, B.C. Valek, J.C. Bravman, and J.R. Patel, "White beam analysis of coupling between precipitation and plastic deformation during electromigration in a passivated Al(0.5wt.% Cu) interconnect," *Metallofizika i Noveishie Tekhnologii* 27, 75 (2005).

Barney, M., "Plastic deformation of constrained systems: Boundary effects and their implications for strain gradient plasticity," Ph.D. thesis, University of California, Berkeley (2005).

Barry, W., M. Chin, D. Robin, F. Sannibale, T. Scarvie, and C. Steier, "Diagnostic systems plan for the Advanced Light Source top-off upgrade," in *Proceedings of 2005 Particle Accelerator Conference* (PAC 05), p. 4066 (2005); Knoxville, Tennessee, May 16–20, 2005.

Bartelt, A., A. Comin, J. Feng, J. Nasiatka, H. Padmore, A. Scholl, and A. Young, "Ultrafast magnetization dynamics studies using an x-ray streak camera," *Proc. SPIE* 5920, 263 (2005); Ultrafast X-Ray Detectors, High-Speed Imaging, and Applications, San Diego, California, July 31–August 4, 2005.

Barty, A., Y. Liu, E. Gulllikson, J.S. Taylor, and O.R. Wood, II, "Actinic inspection of multilayer defects on EUV masks," *Proc. SPIE* 5751, 651 (2005); Emerging Lithographic Technologies IX, San Jose, California, March 1–3, 2005.

Baumann, T.F., S.O. Kucheyev, A.E. Gash, and J.H. Satcher, "Facile synthesis of a crystalline, high-surface-area SnO_2 aerogel," *Adv. Mater.* 17, 1546 (2005).

Beeby, M., B.D. O'Connor, C. Ryttersgaard, D.R. Boutz, L.J. Perry, and T.O. Yeates, "The genomics of disulfide bonding and protein stabilization in thermophiles," *PLoS Biology* 3, 1549 (2005).

Beetz, T., M.R. Howells, C. Jacobsen, C.C. Kao, J. Kirz, E. Lima, T.O. Mentes, H. Miao, C. Sanchez-Hanke, D. Sayre, and D. Shapiro, "Apparatus for x-ray diffraction microscopy and tomography of cryo specimens," *Nucl. Instrum. Meth. A* 545, 459 (2005).

Benzerara, K., T.H. Yoon, N. Menguy, T. Tyliszczak, and G.E. Brown, Jr., "Nanoscale environments associated with bioweathering of a meteoritic Mg-Fe-pyroxene," *Proc. Natl. Acad. Sci. USA* 102, 979 (2005).

Bernstein, N.K., R.S. Williams, M.L. Rakovszky, D. Cui, R. Green, F. Karim-Busheri, R.S. Mani, S. Galicia, C.A. Koch, C.E. Cass, D. Durocher, M. Weinfeld, and J.N. Glover, "The molecular architecture of the mammalian DNA repair enzyme, polynucleotide kinase," *Mol. Cell* 17, 657 (2005).

Berrah, N., R.C. Bilodeau, J.D. Bozek, G. Turri, and G.D. Ackerman, "Double photodetachment in He^-: Feshbach and triply excited resonances," *J. Electron Spectrosc.* 144–147, 19 (2005).

Bertero, M.G., R.A. Rothery, N. Boroumand, M. Palak, F. Blasco, N. Ginet, J.H. Weiner, and N.C.J. Strynadka, "Structural and biochemical characterization of a quinol binding site of *Escherichia coli* nitrate reductase A," *J. Biol. Chem.* 280, 14836 (2005).

Biagioni, P., A. Brambilla, M. Portalupi, N. Rougemaille, A.K. Schmid, A. Lanzara, P. Vavassori, M. Zani, M. Finazzi, L. Duò, and F. Ciccacci, "Magnetic properties of Fe/NiO/Fe(001) trilayers," *J. Magn. Magn. Mater.* 290–291, 153 (2005).

Bilodeau, R.C., J.D. Bozek, N.D. Gibson, C.W. Walter, G.D. Ackerman, I. Dumitriu, and N. Berrah, "Inner-shell photodetachment thresholds: Unexpected long-range validity of the Wigner law," *Phys. Rev. Lett.* 95, 083001 (2005).

Bilodeau, R.C., N.D. Gibson, J.D. Bozek, C.W. Walter, G.D. Ackerman, P. Andersson, J.G. Heredia, M. Perri, and N. Berrah, "High-charge-state formation following inner-shell photodetach-

ment from S^-," *Phys. Rev. A* 72, 050701(R) (2005).

Biswal, B.K., M.M. Cherney, M. Wang, C. Garen, and M.N. James, "Structures of *Mycobacterium tuberculosis* pyridoxine 5'-phosphate oxidase and its complexes with flavin mononucleotide and pyridoxal 5'-phosphate," *Acta Crystallogr. D* D61, 1492 (2005).

Biswal, B.K., M.M. Cherney, M.T. Wang, L. Chan, C.G. Yannopoulos, D. Bilimoria, O. Nicolas, J. Bedard, and M.N.G. James, "Crystal structures of the RNA-dependent RNA polymerase genotype 2a of hepatitis C virus reveal two conformations and suggest mechanisms of inhibition by non-nucleoside inhibitors," *J. Biol. Chem.* 280, 18202 (2005).

Blomqvist, P., K.M. Krishnan, and H. Ohldag, "Direct imaging of asymmetric magnetization reversal in exchange-biased Fe/MnPd bilayers by x-ray photoemission electron microscopy," *Phys. Rev. Lett.* 94, 107203 (2005).

Bolte, M., R. Eiselt, T. Eimueller, P. Fischer, and G. Meier, "Micromagnetic simulation as a bridge between magnetic-force and magnetic-transmission x-ray microscopy," *J. Magn. Magn. Mater.* 290–291, 723 (2005).

Boysen, R.B., "Development of palladium L-edge x-ray absorption spectroscopy and its application on chloro palladium complexes," masters thesis, Montana State University (2005).

Bradley, J., Z.R. Dai, R. Erni, N. Browning, G. Graham, P. Weber, J. Smith, I. Hutcheon, H. Ishii, S. Bajt, C. Floss, F. Stadermann, and S. Sanford, "An astronomical 2175 Å feature in interplanetary dust particles," *Science* 307, 244 (2005).

Braun, A., "Carbon speciation in airborne particulate matter with C (1s) NEXAFS spectroscopy," *J. Environ. Monit.* 7, 1059 (2005).

Braun, A., F.E. Huggins, N. Shah, Y. Chen, S. Wirick, S.B. Mun, C. Jacobsen, and G.P. Huffman, "Advantages of soft x-ray absorption over TEM-EELS for solid carbon studies—a comparative study on diesel soot with EELS and NEXAFS," *Carbon* 43, 117 (2005).

Brena, B., G.V. Zhuang, A. Augustsson, G. Liu, J. Nordgren, J.H. Guo, P.N. Ross, and Y. Luo, "Conformation dependence of electronic structure of poly(ethylene oxide)," *J. Phys. Chem. B* 109, 7907 (2005).

Brown, P.N., M.A.A. Mathews, L.A. Joss, C.P. Hill, and D.F. Blair, "Crystal structure of the flagellar rotor protein FliN from *Thermotoga maritima*," *J. Bacteriol.* 187, 2890 (2005).

Buchanan, K.S., K.Y. Guslienko, A. Doran, A. Scholl, S.D. Bader, and V. Novosad, "Magnetic remanent states and magnetizationion reversal in patterned trilayer nanodots," *Phys. Rev. B* 72, 134415 (2005).

Buonassisi, T., "Transition metals in multicrystalline silicon solar cells: Understanding the nature, origins, and impacts of metal contamination in multicrystalline Si and minimizing its impact on solar cell performance," Ph.D. thesis, University of California, Berkeley (2005).

Buonassisi, T., A.A. Istratov, M. Heuer, M.A. Marcus, R. Jonczyk, J. Isenberg, B. Lai, Z.H. Cai, S. Heald, W. Warta, R. Schindler, G. Willeke, and E.R. Weber, "Synchrotron-based investigations of the nature and impact of iron contamination in multicrystalline silicon solar cells," *J. Appl. Phys.* 97, 074901 (2005).

Buonassisi, T., A.A. Istratov, M.A. Marcus, B. Lai, Z. Cai, S.M. Heald, and E.R. Weber, "Engineering metal-impurity nanodefects for low-cost solar cells," *Nature Materials* 4, 676 (2005).

Buonassisi, T., A.A. Istratov, M.A. Marcus, M. Heuer, M.D. Pickett, B. Lai, Z. Cai, S.M. Heald, and E.R. Weber, "Local measurements of diffusion length and chemical character of metal clusters in multicrystalline silicon," *Solid State Phenomena* 108–109, 577 (2005).

Buonassisi, T., A.A. Istratov, M.A. Marcus, S. Peters, C. Ballif, M. Heuer, T.F. Ciszek, Z. Cai, B. Lai, R. Schindler, and E.R. Weber, "Synchrotron-based investigations into metallic impurity distribution and defect engineering in multicrystalline silicon via thermal treatments," in *Conference Record of the 31st IEEE Photovoltaic Specialist Conference*, IEEE Product. No. CH37608, p. 1027 (2005); Lake Buena Vista, Florida, January 3–7, 2005.

Buonassisi, T., A.A. Istratov, M.D. Pickett, M.A. Marcus, G. Hahn, S. Riepe, J. Isenberg, W. Warta, G. Willeke, T.F. Ciszek, and E.R. Weber, "Quantifying the effect of metal-rich precipitates on minority carrier diffusion length in multicrystalline silicon using synchrotron-based spectrally-resolved x-ray beam induced current," *Appl. Phys. Lett.* 87, 044101 (2005).

Buonassisi, T., M.A. Marcus, A.A. Istratov, M. Heuer, T.F. Ciszek, B. Lai, Z. Cai, and E.R. Weber,

"Analysis of copper-rich precipitates in silicon: Chemical state, gettering, and impact on multicrystalline silicon solar cell material," *J. Appl. Phys.* 97, 063503 (2005).

Butorin, S.M., C. Sathe, A. Agui, F. Saalem, J.A. Alonso, and J. Nordgren, "Intra- versus inter-site electronic excitations in $NdNiO_3$ by resonant inelastic ultra-soft x-ray scattering at Ni 3p edge," *Solid State Commun.* 135, 716 (2005).

Byrd, J.M., Z. Hao, M. Martin, D.S. Robin, F. Sannibale, R.W. Schoenlein, A. Zholents, and M. Zolotorev, "Terahertz coherent synchrotron radiation from femtosecond laser modulation of the electron beam at the Advanced Light Source," in *Proceedings of 2005 Particle Accelerator Conference* (PAC 05), p. 3682 (2005); Knoxville Tennessee, May 16–20, 2005.

Calarese, D.A., H.K. Lee, C.Y. Huang, M.D. Best, R.D. Astronomo, R.L. Stanfield, H. Katinger, D.R. Burton, C.H. Wong, and I.A. Wilson, "Dissection of the carbohydrate specificity of the broadly neutralizing anti-HIV-1 antibody 2G12," *Proc. Natl. Acad. Sci. USA* 102, 13372 (2005).

Callaghan, A.J., M.J. Marcaida, J.A. Stead, K.J. McDowall, W.G. Scott, and B.F. Luisi, "Structure of *Escherichia coli* RNase E catalytic domain and implications for RNA turnover," *Nature* 437, 1187 (2005).

Cappa, C.D., "Water isotopes, clouds and aqueous solutions," Ph.D. thesis, University of California, Berkeley (2005).

Cappa, C.D., J.D. Smith, K.R. Wilson, B.M. Messer, M.K. Gilles, R.C. Cohen, and R.J. Saykally, "Effects of alkali metal halide salts on the hydrogen bond network of liquid water," *J. Phys. Chem. B* 109, 7046 (2005).

Cappa, C.D., W.S. Drisdell, J.D. Smith, R.J. Saykally, and R.C. Cohen, "Isotope fractionation of water during evaporation without condensation," *J. Phys. Chem. B* 109, 24391 (2005).

Card, G.L., L. Blasdel, B.P. England, C. Zhang, Y. Suzuki, S. Gillette, D. Fong, P.N. Ibrahim, D.R. Artis, G. Bollag, M.V. Milburn, S.H. Kim, J. Schlessinger, and K.Y.J. Zhang, "A family of phosphodiesterase inhibitors discovered by cocrystallography and scaffold-based drug design," *Nat. Biotechnol.* 23, 201 (2005).

Caruthers, J.M., F. Zucker, E. Worthey, P.J. Myler, F. Buckner, W. Van Voorhis, C. Mehlin, E. Boni, T. Feist, J. Luft, S. Gulde, A. Lauricella, O. Kaluzhniy, L. Anderson, I. LeTrong, M.A. Holmes, E. Thomas, M. Soltis, K.O. Hodgson, W.G.J. Hol, and E.A. Merritt, "Crystal structures and proposed structural/functional classification of three protozoan proteins from the isochorismatase superfamily," *Protein Sci.* 14, 2887 (2005).

Castro, J., D. Dingwell, A. Nichols, and J. Gardner, "New insights on the origin of flow bands in obsidian," *Special Paper 396: Kinematics and dynamics of lava flows*, p. 55, Geological Society of America (2005).

Castro, J.M., M. Manga, and M.C. Martin, "Vesiculation rates of obsidian domes inferred from H_2O concentration profiles," *Geophys. Res. Lett.* 32, L21307 (2005).

Cavalleri, A., M. Rini, H.H.W. Chong, S. Fourmaux, T.E. Glover, P.A. Heimann, J.C. Kieffer, and R.W. Schoenlein, "Band-selective measurements of electron dynamics in VO_2 using femtosecond near-edge x-ray absorption," *Phys. Rev. Lett.* 95, 067405 (2005).

Cavalleri, M., M. Odelius, D. Nordlund, A. Nilsson, and L.G.M. Pettersson, "Half or full core hole in density functional theory x-ray absorption spectrum calculations of water?" *Phys. Chem. Chem. Phys.* 7, 2854 (2005).

Chakravarthy, S., S.K.Y. Gundimella, C. Caron, P.Y. Perche J.R. Pehrson, S. Khochbin, and K. Luger, "Structural characterization of the histone variant macroH2A," *Molecular and Cellular Biology* 25, 7616 (2005).

Chamberlain, P.P., M.L. Sandberg, K. Sauer, M.P. Cooke, S.A. Lesley, and G. Spraggon, "Structural insights into enzyme regulation for inositol 1,4,5-trisphosphate 3-kinase B," *Biochemistry* 44, 14486 (2005).

Chao, J., J. Lee, B.R. Chapados, E.W. Debbler, A. Schneemann, and J.R. Williamson, "Dual modes of RNA silencing suppression by Flock House virus protein B2," *Nat. Struct. Mol. Biol.* 12, 952 (2005).

Chao, W.L., "Resolution characterization and nanofabrication for soft x-ray zone plate microscopy," Ph.D. thesis, University of California, Berkeley (2005).

Chao, W.L., B.D. Harteneck, J.A. Liddle, E.H. Anderson, and D.T. Attwood, "Soft x-ray microscopy at a spatial resolution better than 15 nm," *Nature* 435, 1210 (2005).

Chen, W., C. Xiao, Q. Yang, A. Moewes, and A. Hirose, "The effects of bias polarity on diamond

deposition by hot filament chemical vapour deposition," *Can. J. Phys.* 83, 753 (2005).

Chen, Y., B. Shoichet, and R. Bonnet, "Structure, function, and inhibition along the reaction coordinate of CTX-M β-lactamases," *J. Am. Chem. Soc.* 127, 5423 (2005).

Chen, Y., J. Delmas, J. Sirot, B. Shoichet, and R. Bonnet, "Atomic resolution structures of CTX-M β-lactamases: Extended spectrum activities from increased mobility and decreased stability," *J. Mol. Biol.* 348, 349 (2005).

Chen, Z., W.D. Singer, P.C. Sternweis, and S.R. Sprang, "Structure of the p115RhoGEF rgRGS domain—Gα13/il chimera complex suggests convergent evolution of a GTPase activator," *Nat. Struct. Mol. Biol.* 12, 191 (2005).

Chiou, J.W., H.M. Tsai, C.W. Pao, C.L. Dong, C.L. Chang, F.Z. Chien, W.F. Pong, M.H. Tsai, S.C. Shi, C.F. Chen, L.C. Chen, K.H. Chen, I.H. Hong, C.H. Chen, H.J. Lin, J.H. Guo, "Comparison of the electronic structures of AlN nanotips grown on p- and n-type Si substrates," *J. Phys.: Condens. Matter* 17, 7523 (2005).

Choi, H.J., and W.I. Weis, "Structure of the armadillo repeat domain of plakophilin 1," *J. Mol. Biol.* 346, 367 (2005).

Chu, C.C., G.L. Hwang, J.W. Chiou, W.T. Pong, C.L. Lin, C.Y. Tsai, H.M. Lin, Y.C. Chang, C.S. Chang, A.H. Hsu, W.L. Huang, J.H. Guo, P.H. Chen, and T.Y. Luh, "Polymerization of a confined π-system: Chemical synthesis of tetrahedral amorphous carbon nanoballs from graphitic carbon nanocapsules," *Adv. Mater.* 17, 2707(2005).

Clark, S.M., and R. Jeanloz, "A new paradigm to extend diffraction measurements beyond the megabar regime," *J. Synchrotron Rad.* 12, 632 (2005).

Clark, S.M., S.G. Prilliman, C.K. Erdonmez, and A.P. Alivisatos, "Size dependence of the pressure-induced γ to α structural transition in iron oxide nanocrystals," *Nanotechnology* 16, 2813 (2005).

Compaan, D.M., L.C. Gonzalez, I. Tom, K.M. Loyet, D. Eaton, and S.G. Hymowitz, "Attenuating lymphocyte activity: The crystal structure of the BTLA-HVEM complex," *J. Biol. Chem.* 280, 39553 (2005).

Cool, T.A., A. McIlroy, F. Qi, P.R. Westmoreland, L. Poisson, D.S. Peterka, and M. Ahmed, "Photoionization mass spectrometer for studies of flame chemistry with a synchrotron light source," *Rev. Sci. Instrum.* 76, 094102 (2005).

Cool, T.A., J. Wang, K. Nakajima, C.A. Taatjes, and A. McIlroy, "Photoionization cross sections for reaction intermediates in hydrocarbon combustion," *Int. J. Mass Spectrom.* 247, 18 (2005).

Cool, T.A., K. Nakajima, C.A. Taatjes, A. McIlroy, P.R. Westmoreland, M.E. Law, and A. Morel, "Studies of a fuel-rich propane flame with photoionization mass spectrometry," *Proceedings of the Combustion Institute* 30, 1681 (2005).

Corbett, K.D., A.J. Schoeffler, N.D. Thomsen, and J.M. Berger, "The structural basis for substrate specificity in DNA topoisomerase IV," *J. Mol. Biol.* 351, 545 (2005).

Corbett, K.D., and J.M. Berger, "Structural dissection of ATP turnover in the prototypical GHL ATPase topoVI," *Structure* 13, 873 (2005).

Corn, J.E., P.J. Pease, G.L. Hura, and J.M. Berger, "Crosstalk between primase subunits can act to regulate primer synthesis in trans," *Mol. Cell* 20, 391 (2005).

Credle, J.J., J.S. Finer-Moore, F.R. Papa, R.M. Stroud, and P. Walter, "On the mechanism of sensing unfolded protein in the endoplasmic rericulum," *Proc. Natl. Acad. Sci. USA* 102, 18773 (2005).

Croll, L.M., H.D.H. Stover, and A.P. Hitchcock, "Composite tectocapsules containing porous polymer microspheres as release gates," *Macromolecules* 38, 2903 (2005).

Cumberland, R., "Solid-state routes to optoelectronic and ultrahard materials," Ph.D. thesis, University of California, Los Angeles (2005).

Cumberland, R.W., M.B. Weinberger, J.J. Gilman, S.M. Clark, S.H. Tolbert, and R.B. Kaner, "Osmium diboride, an ultra-incompressible, hard material," *J. Am. Chem. Soc.* 127, 7264 (2005).

Czasch, A., L.P.H. Schmidt, T. Jahnke, T. Weber, O. Jagutzki, S. Schössler, M.S. Schöffler, R. Dörner, and H. Schmidt-Böcking, "Photo induced multiple fragmentation of atoms and molecules: Dynamics of coulombic many-particle systems studied with the COLTRIMS reaction microscope," *Phys. Lett. A* 347, 95 (2005).

Das, D., N. Oganesyan, H. Yokota, R. Pufan, R. Kim, and S.H. Kim, "Crystal structure of the conserved hypothetical protein MPN330 (GI: 1674200) from *Mycoplasma pneumoniae*," *Proteins: Structure, Function, and Bioinformatics* 58, 504 (2005).

Davis, M.I., M.J. Bennett, L.M. Thomas, and P.J. Bjorkman, "Crystal structure of prostrate-specific membrane antigen, a tumor marker and peptidase," *Proc. Natl. Acad. Sci. USA* 102, 5981 (2005).

Davis, T.L., T.M. Bonacci, S.R. Sprang, and A.V. Smrcka, "Structural and molecular characterization of a preferred protein interaction surface on G protein βγ subunits," *Biochemistry* 44, 10593 (2005).

Davis, V.T., A. Aguilar, A.M. Covington, J.S. Thompson, D. Calabrese, C. Cisneros, M.S. Gulley, M. Halka, D. Hanstorp, J. Sandström, B.M. McLaughlin, G.F. Gribakin, and D.J. Pegg, "Photo-double detachment from the F^- ion," *J. Phys. B–At. Mol. Opt.* 38, 2579 (2005).

De Stasio, G., D. Rajesh, P. Casalbore, M.J. Daniels, R.J. Erhardt, B.H. Frazer, L.M. Wiese, K.L. Richter, B.R. Sonderegger, B. Gilbert, S. Schaub, R.J. Cannara, J.F. Crawford, M.K. Gilles, T. Tyliszczak, J.F. Fowler, L.M. Larocca, S.P. Howard, D. Mercanti, M.P. Mehta, and R. Pallini, "Are gadolinium contrast agents suitable for gadolinium neutron capture therapy?" *Neurological Research* 27, 387 (2005).

Debler, E.W., S. Ito, F.P. Seebeck, A. Heine, D. Hilvert, and I.A. Wilson, "Structural origins of efficient proton abstraction from carbon by a catalytic antibody," *Proc. Natl. Acad. Sci. USA* 102, 4984 (2005).

DeLaBarre, B., and A.T. Brunger, "Nucleotide dependent motion and mechanism of action of p97/VCP," *J. Mol. Biol.* 347, 437 (2005).

Deng, J., N. Lewis Ernst, S. Turley, and W.G.J. Hol, "Structural basis for UTP specificity of RNA editing TUTases from *Trypanosoma brucei*," *EMBO J.* 24, 4007 (2005).

Dong, C.L., A. Augustsson, C.L. Chen, C.L. Chang, Y.Y. Chen, and J.H. Guo, "Electronic structure and valence state of $CeAl_2$ from x-ray absorption and emission spectroscopy," *J. Electron Spectrosc.* 144–147, 581 (2005).

Doucleff, M., B. Chen, A.E. Maris, D.E. Wemmer, E. Kondrashkina, and B.T. Nixon, "Negative regulation of AAA+ ATPase assembly by two component receiver domains: A transcription activation mechanism that is conserved in mesophilic and extremely hyperthermophilic bacteria," *J. Mol. Biol.* 353, 242 (2005).

Drake, I.J., "Fundamental investigation into the structure and function of Cu for catalyzed synthesis of dimethyl carbonate," Ph.D. thesis, University of California, Berkeley (2005).

Drake, I.J., K.L. Fujdala, A.T. Bell, and T.D. Tilley, "Dimethyl carbonate production via the oxidative carbonylation of methanol over Cu/SiO_2 catalysts prepared via molecular precursor grafting and chemical vapor deposition approaches," *J. Catal.* 230, 14 (2005).

Du, Z.H., J.K. Lee, R. Tjhen, S. Li, H. Pan, R.M. Stroud, and T.L. James, "Crystal structure of the first KH domain of human poly (C)-binding protein-2 in complex with a C-rich strand of human telomeric DNA at 1.7 Å," *J. Biol. Chem.* 280, 38823 (2005).

Edwards, D.C., and S.C.B. Myneni, "Hard and soft x-ray absorption spectroscopic investigation of aqueous Fe(III)-hydroxamate siderophore complexes," *J. Phys. Chem. A* 109, 10249 (2005).

Emmons, E.D., A. Aguilar, M.F. Gharaibeh, S.W.J. Scully, R.A. Phaneuf, A.L.D. Kilcoyne, A.S. Schlachter, I. Alvarez, C. Cisneros, and G. Hinojosa, "Photoionization and electron-impact ionization of Xe^{3+}," *Phys. Rev. A* 71, 042704 (2005).

Estebanez-Perpina, E., J.M.R. Moore, E. Mar, E. Delgado-Rodrigues, P. Nguyen, J.D. Baxter, B.M. Buehrer, P. Webb, R.J. Fletterick, and R.K. Guy, "The molecular mechanisms of coactivator utilization in ligand-dependent transactivation by the androgen receptor," *J. Biol. Chem.* 280, 8060 (2005).

Fadley, C.S., "X-ray photoelectron spectroscopy and diffraction in the hard x-ray regime: Fundamental considerations and future possibilities," *Nucl. Instrum. Meth. A* 547, 24(2005).

Faham, S., G.L. Boulting, E.A. Massey, S. Yohannan, D. Yang, and J.U. Bowie, "Crystallization of bacteriorhodopsin from bicelle formulations at room temperature," *Protein Sci.* 14, 836 (2005).

Feinberg, H., Y. Guo, D.A. Mitchell, K. Drickamer, and W.I. Weis, "Extended neck regions stabilize tetramers of the receptors DC-SIGN and DC-SIGNR," *J. Biol. Chem.* 280, 1327 (2005).

Feldman, R.I., J.M. Wu, M.A. Polokoff, M.J. Kochanny, H. Dinter, D. Zhu, S.L. Biroc, B. Alicke, J. Bryant, S. Yuan, B.O. Buckman, D. Lentz, M. Ferrer, M. Whitlow, M. Adler, S. Finster, Z. Chang, D.O. Arnaiz, "Novel small

molecule inhibitors of 3-phosphoinositide-dependent kinase-1," *J. Biol. Chem.* 280, 19867 (2005).

Fellouse, F.A., "Usage d'anticorps synthetiques pour explorer les principes de base de reconnaissance moleculaire," Ph.D. thesis, University of Marseille, France (2005).

Felts, R.L., T.J. Reilly, and J.J. Tanner, "Crystallization of AcpA, a respiratory burst-inhibiting acid phosphatase from *Francisella tularensis*," *Biochim. Biophys. Acta* 1752, 107 (2005).

Feng, J., W. Wan, J. Qiang, A. Bartelt, A. Comin, A. Scholl, J. Byrd, R. Falcone, G. Huang, A. MacPhee, J. Nasiatka, K. Opachich, D. Weinstein, T. Young, and H. Padmore, "An ultrafast x-ray streak camera for the study of magnetization dynamics," *Proc. SPIE 5920*, 73 (2005); Ultrafast X-Ray Detectors, High-Speed Imaging, and Applications, San Diego, California, July 31–August 4, 2005.

Fennell-Fezzie, R., S.D. Gradia, D. Akey, and J.M. Berger, "The MukF subunit of *Escherichia coli* condensin: Architecture and functional relationship to kleisins," *EMBO J.* 24, 1921 (2005).

Feulner, P., M. Ecker, P. Jakob, R. Romberg, R. Weimar, D. Menzel, A. Fohlisch, W. Wurth, S.H. Yang, C.S. Fadley, R. Larciprete, S. Lizzit, K.L. Kostov, and G. Tyuliev, "Search for a local effect in multiatom resonant core excitation in a surface species: Photoemission and photon-stimulated desorption from N_2 on Ni(111)," *Phys. Rev. B* 71, 5409 (2005).

Finer-Moore, J.S., A.C. Anderson, R.H. O'Neil, M.P. Costi, S. Ferrari, J. Krucinski, and R.M. Stroud, "The structure of *Cryptococcus neoformans* thymidylate synthase suggests strategies for using target dynamics for species-specific inhibition," *Acta Crystallogr. D* D61, 1320 (2005).

Fischer, P., M.Y. Im, T. Eimuller, G. Schutz, and S.C. Shin, "Magnetization reversal behaviour of nanogranular CoCrPt alloy thin films studied with magnetic transmission x-ray microscopy," *J. Magn. Magn. Mater.* 286, 311 (2005).

Fu, J., and S.G. Urquhart, "Linear dichroism in the x-ray absorption spectra of linear *n*-alkanes," *J. Phys. Chem. A* 109, 11724 (2005).

Fujii, S., S.P. Armes, T. Araki, and H. Ade, "Direct imaging and spectroscopic characterization of stimulus-responsive microgels," *J. Am. Chem. Soc.* 127, 16808 (2005).

Gatzeva-Topalova, P.Z., "Biophysical and biochemical characterization of ArnA—A required enzyme in the polymixin resistance pathway," Ph.D. thesis, University of Colorado at Boulder, (2005).

Gatzeva-Topalova, P.Z., A. May, and M.C. Sousa, "Structure and mechanism of ArnA: Conformational change implies ordered dehydrogenase mechanism in key enzyme for polymyxin resistance," *Structure* 13, 929 (2005).

Gatzeva-Topalova, P.Z., A.P. May, and M.C. Sousa, "Crystal structure and mechanism of the *Escherichia coli* ArnA (PmrI) transformylase domain. An enzyme for lipid A modification with 4-amino-4-deoxy-L-arabinose and polymyxin resistance," *Biochemistry* 44, 5328 (2005).

Gawelda, W., C. Bressler, M. Saes, M. Kaiser, A.N. Tarnovsky, D. Grolimund, S.L. Johnson, R. Abela, and M. Chergui, "Picosecond time resolved x-ray absorption spectroscopy of solvated organometallic complexes," *Phys. Scr.* T115, 102 (2005).

Gharaibeh, M.F., "Systematic photoionization study along the iron isonuclear sequence," Ph.D. thesis, University of Nevada, Reno (2005).

Ghosal, S., J.C. Hemminger, H. Bluhm, B.S. Mun, E.L.D. Hebenstreit, G. Ketteler, D.F. Ogletree, F.G. Requejo, and M. Salmeron, "Electron spectroscopy of aqueous solution interfaces reveals surface enhancement of halides," *Science* 307, 563 (2005).

Ginder-Vogel, M.A., T. Borch, M.A. Mayes, P.M. Jardine, and S. Fendorf, "Chromate reduction and retention processes within arid environments," *Environ. Sci. Technol.* 39, 7833 (2005).

Glans, P.A., T. Learmonth, K.E. Smith, J.H. Guo, A. Walsh, G.W. Watson, F. Terzi, and R.G. Egdell, "Experimental and theoretical study of the electronic structure of HgO and Tl_2O_3," *Phys. Rev. B* 71, 235109 (2005).

Goudeau, P., N. Tamura, B. Lavelle, S. Rigo, T. Masri, A. Bosseboeuf, T. Sarnet, J.A. Petit, and J.M. Desmarres, "X-ray diffraction characterization of suspended structures for MEMS applications," *MRS Proc.* 875, O4.11 (2005); 2005 MRS Spring Meeting, San Francisco, California, March 28–April 1, 2005.

Goudeau, P., N. Tamura, G. Parry, J. Colin, C. Coupeau, F. Cleymand, and H. Padmore, "Strain mapping on gold thin film buckling and sili-

con blistering," *MRS Proc.* 875, O10.4 (2005); 2005 MRS Spring Meeting, San Francisco, California, March 28–April 1, 2005.

Goudeau, P., N. Tamura, R. Spolenak, and H.A. Padmore, "Application of the white/monochromatic x-ray □-diffraction technique to the study of texture and triaxial strain at the submicron level," *Mater. Sci. Forum* 490–491, 672 (2005).

Graf, J., C. Jozwiak, A.K. Schimd, Z. Hussain, and A. Lanzara, "Mapping spin-dependent electron reflectivity in Fe and Co ferromagnetic thin films," *Phys. Rev. B* 71, 144429 (2005).

Grant, A., T.J. Wilkinson, D.R. Holman, and M. Martin, "Identification of recently handled materials by analysis of latent human fingerprints using infrared spectromicroscopy," *Appl. Spectrosc.* 59, 1182 (2005).

Greenstein, A.E., C. Grundner, N. Echols, L.M. Gay, T.N. Lombana, C.A. Miecskowski, K.E. Pullen, P. Sung, and T. Alber, "Structure/function studies of Ser/Thr and Tyr protein phosphorylation in *Mycobacterium tuberculosis*," *J. Mol. Microbiol. Biotechnol.* 9, 167 (2005).

Grimsley, J.K., B. Calamini, J.R. Wild, and A.D. Mesecar, "Structural and mutational studies of organophosphorus hydrolase reveal a cryptic and functional allosteric-binding site," *Arch. Biochem. Biophys.* 442, 169 (2005).

Grundner, C., H.L. Ng, and T. Alber, "*Mycobacterium tuberculosis* protein tyrosine phosphatase PtpB structure reveals a diverged fold and a buried active site," *Structure* 13, 1625 (2005).

Guay, D., J. Stewart-Ornstein, X. Zhang, and A.P. Hitchcock, "In situ spatial and time resolved studies of electrochemical reactions by scanning transmission x-ray microscopy," *Anal. Chem.* 77, 3479 (2005).

Guillemin, R., O. Hemmers, D.W. Lindle, and S.T. Manson, "Experimental investigation of nondipole effects in photoemission at the Advanced Light Source," *Radiat. Phys. Chem.* 73, 311 (2005).

Guillemin, R., W.C. Stolte, L.T.N. Dang, S.W. Yu, and D.W. Lindle, "Fragmentation dynamics of H_2S following S 2p photoexcitation," *J. Chem. Phys.* 122, 94318 (2005).

Gunawan, J., D. Simard, M. Gilbert, A.L. Lovering, W.W. Wakarchuk, M.E. Tanner, and N.C.J. Strynadka, "Structural and mechanistic analysis of sialic acid synthase NeuB from *Neisseria meningitidis* in complex with Mn^{2+}, phosphoenolpyruvate, and N-acetylmannosaminitol," *J. Biol. Chem.* 280, 3555 (2005).

Guo, J.H., "Soft-x-ray spectroscopic study of nanoscale materials," *Proc. SPIE* 5929, 59290K (2005); Optics & Photonics 2005: SPIE 50th Annual Meeting, San Diego, California, July 31–August 4, 2005.

Guo, J.H., A. Augustsson, S. Kashtanov, D. Spangberg, J. Nordgren, K. Hermansson, and Y. Luo, "The interaction of cations and liquid water studied by resonant soft-x-ray absorption and emission spectroscopy," *J. Electron Spectrosc.* 144–147, 287 (2005).

Hague, C.F., J.H. Underwood, A. Avila, A. Delaunay, H. Ringuenet, M. Marsi, and M. Sacchi, "Plane-grating flat-field soft x-ray spectrometer," *Rev. Sci. Instrum.* 76, 023110 (2005).

Hamburger, A.E., A.P. West, Jr., Z.A. Hamburger, P. Hamburger, and P.J. Bjorkman, "Crystal structure of a secreted insect ferritin reveals a symmetrical arrangement of heavy and light chains," *J. Mol. Biol.* 349, 558 (2005).

Hamilton, T., "Determining the sp2/sp3 bonding concentrations of carbon films," masters thesis, University of Saskatchewan, Canada (2005).

Hamma, T., S.L. Reichow, G. Varani, and A.R. Ferré-D'Amaré, "The Cbf5-Nop10 complex is a molecular bracket that organizes box H/ACA RNPs," *Nat. Struct. Mol. Biol.* 12, 1101 (2005).

Hansen, S.B., "Ligand specificity and conformational states of the acetylcholine binding protein, a nicotinic receptor surrogate," Ph.D. thesis, University of California, San Diego (2005).

Hansen, S.B., G. Sulzenbacher, T. Huxford, P. Marchot, P. Taylor, and Y. Bourne, "Structures of *Aplysia* AChBP complexes with nicotinic agonists and antagonists reveal distinctive binding interfaces and conformations," *EMBO J.* 24, 3635 (2005).

Harton, S.E., T. Koga, F.A. Stevie, T. Araki, and H. Ade, "Investigation of blend miscibility of a ternary PS/PCHMA/PMMA system using SIMS and mean-field theory," *Macromolecules* 38, 10511 (2005).

Hatters, D.M., C.A. Peters-Libeu, and K.H. Weisgraber, "Engineering conformational destabilization into mouse apolipoprotein E: A model for a unique property of human apolipoprotein E4," *J. Biol. Chem.* 280, 26477 (2005).

Heideker, C.J., "An investigation of a homolog from *Aquifex aeolicus* of the two component response regulator NtrC by NMR," masters thesis, Universität Würzburg, Germany (2005).

Heimann, P., M. Koike, and H. Padmore, "Dispersive x-ray absorption spectroscopy with gratings above 2 keV," *Rev. Sci. Instrum.* 76, 063102 (2005).

Hellgren, N., J.H. Guo, Y. Luo, C. Sathe, A. Agui, S. Kashtanov, J. Nordgren, H. Agren, and J.E. Sundgren, "Electronic structure of carbon nitride thin films studied by x-ray spectroscopy techniques," *Thin Solid Films* 471, 19 (2005).

Hemmers, O., R. Guillemin, A. Wolska, D.W. Lindle, D. Rolles, K.T. Cheng, W.R. Johnson, H.L. Zhou, and S.T. Manson, "Nondipole effects in Xe 4d photoemission," *J. Electron Spectrosc.* 144–147, 51 (2005).

Hemmers, O., R. Guillemin, D. Rolles, A. Wolska, D.W. Lindle, E.P. Kanter, B. Krassig, S.H. Southworth, R. Wehlitz, P.W. Langhoff, V. McKoy, and B. Zimmerman, "Nondipole effects in molecular nitrogen valence shell photoionization," *J. Electron Spectrosc.* 144–147, 155 (2005).

Higgins, L.J., F. Yan, P. Liu, H.W. Liu, and C.L. Drennan, "Structural insight into antibiotic fosfomycin biosynthesis by a mononuclear iron enzyme," *Nature* 437, 838 (2005).

Hinojosa, G., M.M. Sant'Anna, A.M. Covington, R.A. Phaneuf, I.R. Covington, I. Dominguez, A.S. Schlachter, I. Alvarez, and C. Cisneros, "Photofragmentation of ionic carbon monoxide," *J. Phys. B–At. Mol. Opt.* 38, 2701 (2005).

Hitchcock, A.P., C. Morin, X. Zhang, T. Araki, J.J. Dynes, H. Stover, J. Brash, J.R. Lawrence, and G.G. Leppard, "Soft x-ray spectromicroscopy of biological and synthetic polymer systems," *J. Electron Spectrosc.* 144–147, 259 (2005).

Hitchcock, A.P., H.D.H. Stover, L.M. Croll, and R.F. Childs, "Chemical mapping of polymer microstructure using soft x-ray spectromicroscopy," *Aust. J. Chem.* 58, 423 (2005).

Hochlaf, M., T. Baer, X.M. Qian, and N.Y. Ng, "A vacuum ultraviolet pulsed field ionization-photoelectron study of cyanogen cation in the energy range of 13.2–15.9 eV," *J. Chem. Phys.* 123, 144302 (2005).

Holm, A.P., T.C. Ozawa, S.M. Kauzlarich, S.A. Morton, G.D. Waddill, and J.G. Tobin, "X-ray photoelectron spectroscopy studies of $Yb_{14}MnSb_{11}$ and $Yb_{14}ZnSb_{11}$," *J. Solid State Chem.* 178, 262 (2005).

Holmes, M.A., W. Paulsene, J. Xu, C. Ratledge, and R.K. Strong, "Siderocalin (Lcn 2) also binds carboxymycobactins, potentially defending against mycobacterial infections through iron sequestration," *Structure* 13, 29 (2005).

Hong, M., M. Fuangthong, J.D. Helmann, and R.G. Brennan, "Structure of an OhrR-*ohrA* operator complex reveals the DNA binding mechanism of the MarR family," *Mol. Cell* 20, 131 (2005).

Hosfield, D.J., Y.Q. Wu, R.J. Skene, M. Hilgers, A. Jennings, G.P. Snell, and K. Aertgeerts, "Conformational flexibility in crystal structures of human 11^{β}-hydroxysteroid dehydrogenase type I provide insights into glucocorticoid interconversion and enzyme regulation," *J. Biol. Chem.* 280, 4639 (2005).

Huang, D.T., A. Paydar, M. Zhuang, M.B. Waddell, J.M. Holton, and B.A. Schulman, "Structural basis for recruitment of Ubc12 by an E2 binding domain in NEDD8's E1," *Mol. Cell* 17, 341 (2005).

Huang, L.S., D. Cobessi, E.Y. Tung, and E.A. Berry, "Binding of the respiratory chain inhibitor antimycin to the mitochondrial bc_1 complex: A new crystal structure reveals an altered intramolecular hydrogen-bonding pattern," *J. Mol. Biol.* 351, 573 (2005).

Huang, L.S., T.M. Borders, J.T. Shen, C.J. Wang, and E.A. Berry, "Crystallization of mitochondrial respiratory complex II from chicken heart: A membrane-protein complex diffracting to 2.0 Å," *Acta Crystallogr. D* D61, 380 (2005).

Hudson, C.E., J.B. West, K.L. Bell, A. Aguilar, R.A. Phaneuf, F. Folkmann, H. Kjeldsen, J. Bozek, A.S. Schlachter, and C. Cisneros, "A theoretical and experimental study of the photoionization of Al II," *J. Phys. B–At. Mol. Opt.* 38, 2911 (2005).

Hunt, A., A. Moewes, W.Y. Ching, and Y.M. Chiang, "An indirect probe of the half-metallic nature of $LiFePO_4$ using resonant inelastic x-ray scattering," *J. Phys. Chem. Solids* 66, 2290 (2005).

Hunt, A., D. Muir, and A. Moewes, "Studying 4d–4f transitions in Er using resonant inelastic scattering," *J. Electron Spectrosc.* 144–147, 573 (2005).

Hütten, A., S. Kämmerer, J. Schmalhorst, and G. Reiss, "Heusler alloyed electrodes integrated in magnetic tunnel-junctions," in *Half-metallic Alloys: Fundamentals and Applications,*

Lecture Notes in Physics, Vol. 676, p. 241 (Springer Berlin/Heidelberg, 2005).

Iihara, J., Y. Muramatsu, T. Takebe, A. Sawamura, A. Namba, T. Imai, J. Denlinger, and R.C. Perera, "Element-selective observation of electronic structure transition between semiconducting and metallic states in boron-doped diamond using soft x-ray emission and absorption spectroscopy," Jpn. *J. Appl. Phys.* 44, 6612 (2005).

Ioanoviciu, A., S. Antony, Y. Pommier, B.L. Staker, L. Stewart, and M. Cushman, "Synthesis and mechanism of action studies of a series of norindenoisoquinoline topoisomerase I poisons reveal an inhibitor with a flipped orientation in the ternary DNA-enzyme-inhibitor complex as determined by x-ray crystallographic analysis," *J. Med. Chem.* 48, 4803 (2005).

Isaure, M.P., A. Manceau, N. Geoffroy, A. Laboudigue, N. Tamura, and M.A. Marcus, "Zinc mobility and speciation in soil covered by contaminated dredged sediment using micrometer-scale and bulk-averaging x-ray fluorescence, absorption and diffraction techniques," *Geochim. Cosmochim. Acta* 69, 1173 (2005).

Iyer, R.B., R. Silaghi-Dumitrescu, D.M. Kurtz, and W.N. Lanzilotta, "High-resolution crystal structures of *Desulfovibrio vulgaris* (Hildenborough) nigerythrin: Facile, redox-dependent iron movement, domain interface variability, and peroxidase activity in the rubrerythrins," *J. Biol. Inorg. Chem.* 10, 592 (2005).

Jacobs, M.D., J. Black, O. Futer, L. Swenson, B. Hare, M. Fleming, and K. Saxena, "Pim-1 ligand-bound structures reveal the mechanism of serine/threonine kinase inhibition by LY294002," *J. Biol. Chem.* 280, 13728 (2005).

Jahnke, T., "'Interatomic coulombic decay'—Experimentelle Untersuchung eines neuartigen, interatomaren Abregungsmechanismus," Ph.D. thesis, Institut für Kernphysik, Germany (2005).

Jalil, P.A., M.S. Kariapper, M. Faiz, N. Tabet, N.M. Hamdan, J. Diaz, and Z. Hussain, "Surface and bulk investigation of ZSM5 and Al-MCM-41 using synchotron XPS, XANES, and hexane cracking," *Appl. Catal., A* 290, 159 (2005).

Jiang, H., "Inner shell excitation spectroscopy of amino acids and small peptides," masters thesis, McMaster University, Canada (2005).

Johnson, E., D. Cascio, M.R. Sawaya, M. Gingery, and I. Schröder, "Crystal structures of a tetrahedral open pore ferritin from the hyperthermophilic archaeon *Archaeoglobus fulgidus*," *Structure* 13, 637 (2005).

Johnson, S.L., P.A. Heimann, A.G. MacPhee, A.M. Lindenberg, O.R. Monteiro, Z. Chang, R.W. Lee, and R.W. Falcone, "Bonding in liquid carbon studied by time-resolved x-ray absorption spectroscopy," *Phys. Rev. Lett.* 94, 057407 (2005).

Joo, H.D., J.S. Kim, C.W. Bark, J.Y. Kim, Y.M. Koo, and N. Tamura, "Microdiffraction study of polycrystalline copper during uniaxial tension deformation using a synchrotron x-ray source," *Mater. Sci. Forum* 475–479, 4149 (2005).

Juenger, M.C.G., P.J.M. Monteiro, E.M. Gartner, and G.P. Denbeaux, "A soft x-ray microscope investigation into the effects of calcium chloride on tricalcium silicate hydration," *Cem. Concr. Res.* 35, 19 (2005).

Kabasawa, E., J. Nakamura, T. Morimoto, N. Yamada, K. Kuroki, H. Yamazaki, K. Okada, K. Oka, Y. Tezuka, J.D. Denlinger, and R.C.C. Perera, "X-ray spectroscopy study on the electronic structure of hole-doped edge-shared chains in $Ca_{2+xY2-x}Cu_{5O10}$," *J. Electron Spectrosc.* 148, 65 (2005).

Kaiser, S.E., J.H. Brickner, A.R. Reilein, T.D. Fenn, P. Walter, and A.T. Brunger, "Structural basis of FFAT motif-mediated ER targeting," *Structure* 13, 1035 (2005).

Kaner, R.B., J.J. Gilman, and S.H. Tolbert, "Materials science: Designing superhard materials," *Science* 308, 1268 (2005).

Kang, B.S., D.H. Kim, E. Anderson, P. Fischer, and G. Cho, "Polarization modulated magnetic soft x-ray transmission microscopy," *J. Appl. Phys.* 98, 093907 (2005).

Kang, S.J., Y. Yi, C.Y. Kim, K.H. Yoo, A. Moewes, M.H. Cho, J.D. Denlinger, C.N. Wang, and G.S. Chang, "Chemical reaction at the interface between pentacene and HfO_2," *Phys. Rev. B* 72, 205328 (2005).

Kashtanov, S., "Theoretical modeling of x-ray spectroscopy of liquids," Ph.D. thesis, The Royal Institute of Technology, Sweden (2005).

Kashtanov, S., A. Augustsson, J.E. Rubensson, J. Nordgren, H. Agren, J.H. Guo, and Y. Luo, "Chemical and electronic structures of liquid methanol from x-ray emission

spectroscopy and density functional theory," *Phys. Rev. B* 71, 104205 (2005).

Kazantsev, A.V., A.A. Krivenko, D.J. Harrington, S.R. Holbrook, P.D. Adams, and N.R. Pace, "Crystal structure of a bacterial ribonuclease P RNA," *Proc. Natl. Acad. Sci. USA* 102, 13392 (2005).

Keenan, R.J., D.L. Siehl, R. Gorton, and L.A. Castle, "DNA shuffling as a tool for protein crystallization," *Proc. Natl. Acad. Sci. USA* 102, 8887 (2005).

Kerfeld, C.A., M.R. Sawaya, S. Tanaka, C.V. Nguyen, M. Phillips, M. Beeby, and T.O. Yeates, "Protein structures forming the shell of primitive bacterial organelles," *Science* 309, 936 (2005).

Ketteler, G., D.F. Ogletree, H. Bluhm, H.J. Liu, E.L.D. Hebenstreit, and M. Salmeron, "In situ spectroscopic study of the oxidation and reduction of Pd(111)," *J. Am. Chem. Soc.* 127, 18269 (2005).

Kim, C., N.H. Xuong, and S.S. Taylor, "Crystal structure of a complex between the catalytic and regulatory (Rlα) subunits of PKA," *Science* 307, 690 (2005).

Kim, C.S., "Speciation of mercury using synchrotron radiation," in *Mercury: Sources, Measurements, Cycles, and Effects*, Vol. 34, p. 95 (Mineralogical Association of Canada, 2005).

Kim, D.H., B. Kang, W. Chao, P. Fischer, E. Anderson, S.B. Choe, M.Y. Im, and S.C. Shin, "Direct spatial-temporal observation of Barkhausen avalanche in low dimensional ferromagnetic system," *Proc. SPIE* 5843, 40 (2005); Third SPIE International Symposium Fluctuations and Noise in Materials, Austin, Texas, May 24–26, 2005.

Kim, H.S., S.M. Damo, S.Y. Lee, D. Wemmer, and J.P. Klinman, "Structure and hydride transfer mechanism of a moderate thermophilic dihydrofolate reductase from *Bacillus stearothermophilus* and comparison to its mesophilic and hyperthermophilic homologues," *Biochemistry* 44, 11428 (2005).

Kim, J.S., A. DeGiovanni, J. Jancarik, P.D. Adams, H. Yokota, R. Kim, and S.H. Kim, "Crystal structure of DNA sequence specificity subunit of a type I restriction-modification enzyme and its functional implications," *Proc. Natl. Acad. Sci. USA* 102, 3248 (2005).

Kim, P.S.G., S.J. Naftel, T.K. Sham, I. Coulthard, Y.F. Hu, A. Moewes, and J.W. Freeland, "Photon-in photon-out studies of Alq_3 (tris-aluminum-8-hydroxyquinolinate): Synchrotron light excited optical luminescence and x-ray emission," *J. Electron Spectrosc.* 144–147, 901 (2005).

Kim, S.K., K.S. Lee, J.B. Kortright, and S.C. Shin, "Soft x-ray resonant Kerr rotation measurement and simulation of element-resolved and interface-sensitive magnetization reversals in a NiFe/FeMn/Co trilayer structure," *Appl. Phys. Lett.* 86, 102502 (2005).

Kim, S.K., K.S. Lee, B.W. Kang, K.J. Lee, and J.B. Kortright, "Vortex-antivortex assisted magnetization dynamics in a semi-continuous thin-film model system studied by micromagnetic simulations," *Appl. Phys. Lett.* 86, 2504 (2005).

Kinney, J.H., J.S. Stölken, T.S. Smith, J.T. Ryaby, and N.E. Lane, "An orientation distribution function for trabecular bone," *Bone* 36, 193 (2005).

Kinney, J.H., R.K. Nalla, J.A. Pople, T.M. Breunig, and R.O. Ritchie, "Age related transparent root dentin: Mineral concentration, crystallite size, and mechanical properties," *Biomaterials* 26, 3363 (2005).

Knapp, A., A. Kheifets, I. Bray, T. Weber, A.L. Landers, S. Schössler, T. Jahnke, J. Nickles, S. Kammer, O. Jagutzki, L.P.H. Schmidt, M. Schöffler, T. Osipov, M.H. Prior, H. Schmidt-Böcking, C.L. Cocke, and R. Dörner, "Photo double ionization of helium 100 eV and 450 eV above threshold: II. Circularly polarized light," *J. Phys. B–At. Mol. Opt.* 38, 635 (2005).

Kollman, J.M., and R.F. Doolittle, "Unusual non-crystallographic symmetry in crystals of a 420 kDa crustacean clottable protein," *Acta Crystallogr. D* D61, 485 (2005).

Korkegian, A., M.E. Black, D. Baker, and B.L. Stoddard, "Computational thermostabilization of an enzyme," *Science* 308, 857 (2005).

Korlann, S.D., A.E Riley, B.L. Kirsch, B. Mun, and S.H. Tolbert, "Chemical tuning of the electronic properties in a periodic surfactant-templated nanostructured semiconductor," *J. Am. Chem. Soc.* 127, 12516 (2005).

Kortright, J., "Resonant soft x-ray techniques to study nanoscale magnetism," in *Modern Techniques for Characterizing Magnetic Materials*, p. 159 (Kluwer Academic Publishers 2005).

Kortright, J.B., O. Hellwig, K. Chesnel, S. Sun, and E.E. Fullerton, "Interparticle magnetic

correlations in dense Co nanoparticle assemblies," *Phys. Rev. B* 71, 012402 (2005).

Kreidi, K., "Photodoppelionisation von H_2—eine analogie zum doppelspalt," masters thesis, Institut für Kernphysik, Germany (2005).

Kreusch, A., S. Han, A. Brinker, V. Zhou, H.S. Choi, Y. He, S.A. Lesley, J. Caldwell, and X.J. Gu, "Crystal structures of human Hsp90α-complexed with dihydroxyphenylpyrazoles," *Bioorg. Med. Chem. Lett.* 15, 1475 (2005).

Krylova, I.N., E.P. Sablin, J. Moore, R.X. Xu, G.M. Waitt, J.A. Mackay, D. Juzumiene, J.M. Bynum, K. Madauss, V. Montana, L. Lebedeva, M. Suzawa, J.D. Williams, S.P. Williams, R.K. Guy, J.W. Thornton, R.J. Fletterick, T.M. Willson and H.A. Ingraham, "Structural analyses reveal phosphatidyl inositols as ligands for the NR5 orphan receptors SF-1 and LRH-1," *Cell* 120, 343 (2005).

Kucheyev, S.O., J. Biener, J.W. Tringe, Y.M. Wang, P.B. Mirkarimi, T. van Buuren, S.L. Baker, A.V. Hamza, K. Bruhne, and H. Fecht, "Ultrathick, low-stress nanostructured diamond films," *Appl. Phys. Lett.* 86, 221914 (2005).

Kucheyev, S.O., J. Biener, Y.M. Wang, T.F. Baumann, K.J. Wu, T. van Buuren, A.V. Hamza, J.H. Satcher, J.W. Elam, and M.J. Pellin, "Atomic layer deposition of ZnO on ultralow-density nanoporous silica aerogel monoliths," *Appl. Phys. Lett.* 86, 083108 (2005).

Kucheyev, S.O., T.F. Baumann, P.A. Sterne, Y.M. Wang, T. van Buuren, A.V. Hamza, L.J. Terminello, and T.M. Willey, "Surface electronic states in three-dimensional SnO_2 nanostructures," *Phys. Rev. B* 72, 035404 (2005).

Kucheyev, S.O., T.F. Baumann, Y.M. Wang, T. van Buuren, and J.H. Satcher, "Synthesis and electronic structure of low-density monoliths of nanoporous nanocrystalline anatase TiO_2," *J. Electron Spectrosc.* 144–147, 609 (2005).

Kudryashov, D.S., M.R. Sawaya, H. Adisetiyo, T. Norcross, G. Hegyi, E. Reisler, and T.O. Yeates, "The crystal structure of a cross-linked actin dimer suggests a detailed molecular interface in F-actin," *Proc. Natl. Acad. Sci. USA* 102, 13105 (2005).

Kuepper, K., "Electronic and magnetic properties of transition metal compounds: An x-ray spectroscopic study," Ph.D. thesis, University of Osnabrück, Germany (2005).

Kuepper, K., M. Kadiroglu, V. Postnikov, K.C. Prince, M. Matteucci, V.R. Galakhov, H. Hesse, G. Borstel, and M. Neumann, "Electronic structure of highly ordered Sr_2FeMoO_6: XPS and XES studies," *J. Phys.: Condens. Matter* 17, 4309 (2005).

Kuepper, K., M.C. Falub, K.C. Prince, V.R. Galakhov, I.O. Troyanchuk, S.G. Chiuzbaian, M. Matteucci, D. Wett, R. Szargan, N.A. Ovechkina, Y.M. Mukovskii, and M. Neumann, "Electronic structure of A- and B-site doped lanthanum manganites: A combined x-ray spectroscopic study," *J. Phys. Chem. B* 109, 9354 (2005).

Kumar, A., V. Mandiyan, Y. Suzuki, C. Zhang, J. Rice, J. Tsai, D.R. Artis, P. Ibrahim, and R. Bremer, "Crystal structures of proto-oncogene kinase pim1: A target of aberrant somatic hypermutations in diffuse large cell lymphoma," *J. Mol. Biol.* 348, 183 (2005).

Kunz, M., A.M. MacDowell, W.A. Caldwell, D. Cambie, R.S. Celestre, E.E. Domning, R.M. Duarte, A.E. Gleason, J.M. Glossinger, N. Kelez, D.W. Plate, T. Yu, J.M. Zuag, H.A. Padmore, R. Jeanloz, A.P. Alivisatos, S.M. Clark, "A beamline for high-pressure studies at the Advanced Light Source with a superconducting bending magnet as the source," *J. Synchrotron Rad.* 12, 650 (2005).

Kuprin, A., Z. Hasan, Y.D. Chuang, Z. Hussain, D. Qian, M. Foo, and R.J. Cava, "Angle-resolved photoemission spectroscopy (ARPES) of $Na_{0.7}CoO_2$," *Int. J. Mod. Phys. B* 19, 345 (2005).

Kurmaev, E.Z., A. Moewes, R. Wilks, L.D. Lechkina, D.A. Zatsepin, T. Kawashima, and E. Takayama-Muromachi, "Local environment of fluorine atoms in $Sr_2Ca_{n-1}Cu_nO_{2n+\delta}F_{2\pm y}$ {n=2,3} high-temperature superconductors grown under high pressure," *Physics of the Solid State* 47, 1211 (2005).

Kurmaev, E.Z., A.L. Ankudinov, J.J. Rehr, L.D. Finkelstein, P.F. Karimov, and A. Moewes, "L_2:L_3 intensity ratio in soft x-ray emission spectra of 3d-metals," *J. Electron Spectrosc.* 148, 1 (2005).

Kurmaev, E.Z., N.A. Skorikov, A.V. Galakhov, P.F. Karimov, V.R. Galakhov, V.A. Trofimova, Y.M. Yarmoshenko, A. Moewes, and S.Y. Paranchich, "Electronic structure of carbosulfide superconductors," *Phys. Rev. B* 71, 0245281 (2005).

Lago, A.F., A.C.F. Santos, W.C. Stolte, A.S. Schlachter, and G.G.B. de Souza, "Ionic fragmentation of

deep core-level (Cl 1s) excited chloroform molecule," *J. Electron Spectrosc.* 144–147, 161 (2005).

Lam, P.J., "Marine particulate matter in the Twilight Zone: Insights on iron cycling and remineralization of particulate organic carbon in the ocean," Ph.D. thesis, University of California, Berkeley (2005).

Lario, P.I., R.A. Pfuetzner, E.A. Frey, L. Creagh, C. Haynes, A.T. Maurelli, and N.C.J. Strynadka, "Structure and biochemical analysis of a secretin pilot protein," *EMBO J.* 24, 1111 (2005).

Larson, S.B., J.S. Day, S. Glaser, G. Braslawsky, and A. McPherson, "The structure of an antitumor C_H2-domain-deleted humanized antibody," *J. Mol. Biol.* 348, 1177 (2005).

Larson, S.B., R.W. Lucas, and A. McPherson, "Crystallographic structure of the T=1 particle of brome mosaic virus," *J. Mol. Biol.* 346, 815 (2005).

Law, M.E., "Molecular-beam mass spectrometry of ethylene and cyclohexane flames," Ph.D. thesis, University of Massachusetts, Amherst (2005).

Le Gros, M.A., G. McDermott, and C.A. Larabell, "X-ray tomography of whole cells," *Curr. Opin. Struct. Biol.* 15, 593 (2005).

Lee, D.S., E. Flachsova, M. Bodnarova, B. Demeler, P. Martasek, and C.S. Raman, "Structural basis of hereditary coproporphyria," *Proc. Natl. Acad. Sci. USA* 102, 14232 (2005).

Lee, J.K., D. Kozono, J. Remis, Y. Kitagawa, P. Agre, and R.M. Stroud, "Structural basis for conductance by the archaeal aquaporin AqpM at 1.68 Å," *Proc. Natl. Acad. Sci. USA* 102, 18932 (2005).

Lee, K.S., D.E. Jeong, S.K. Kim, and J.B. Kortright, "Soft x-ray resonant magneto-optical Kerr effect as a depth-sensitive probe of magnetic heterogeneity: A simulation approach," *J. Appl. Phys.* 97, 083519 (2005).

Lee, K.S., S.K. Kim, and J.B. Kortright, "Soft x-ray resonant magneto-optical Kerr effect as a depth-sensitive probe of magnetic heterogeneity: Its application to resolve helical spin structures using linear *p* polarization," *J. Appl. Phys.* 96, 7414 (2005).

Lee, M.S., R.A. Edwards, G.L. Thede, and J.N. Glover, "Structure of the BRCT repeat domain of MDC1 and its specificity for the free COOH-terminal end of the γ-H2AX histone tail," *J. Biol. Chem.* 280, 32053 (2005).

Lee, S.Y., A. Lee, J. Chen, and R. MacKinnon, "Structure of the KvAP voltage-dependent K^+ channel and its dependence on the lipid membrane," *Proc. Natl. Acad. Sci. USA* 102, 15441 (2005).

Lee, T.T., S. Agarwalla, and R.M. Stroud, "A unique RNA fold in the RumA-RNA-cofactor ternary complex contributes to substrate selectivity and enzymatic function," *Cell* 120, 599 (2005).

Lee, T.W., M.M. Cherney, C. Huitema, J. Liu, K.E. James, J.C. Powers, L.D. Eltis, and M.N.G. James, "Crystal structures of the main peptidase from the SARS coronavirus inhibited by a substrate-like aza-peptide epoxide," *J. Mol. Biol.* 353, 1137 (2005).

Leitch, S., "Spectroscopic analysis of selected silicon ceramics," masters thesis, University of Saskatchewan, Canada (2005).

Levin, I., M.D. Miller, R. Schwarzenbacher, D. McMullan, P. Abdubek, E. Ambing, T. Biorac, J. Cambell, J.M. Canaves, H.J. Chiu, A.M. Deacon, M. DiDonato, M.A. Elsliger, A. Godzik, C. Grittini, S.K. Grzechnik, J. Hale, E. Hampton, G.W. Han, J. Haugen, M. Hornsby, L. Jaroszewski, C. Karlak, H.E. Klock, E. Koesema, A. Kreusch, P. Kuhn, S.A. Lesley, A. Morse, K. Moy, E. Nigoghossian, J. Ouyang, R. Page, K. Quijano, R. Reyes, A. Robb, E. Sims, G. Spraggon, R.C. Stevens, H. van den Bedem, J. Velasquez, J. Vincent, X. Wang, B. West, G. Wolf, Q. Xu, O. Zagnitko, K.O. Hodgson, J. Wooley, and I.A. Wilson, "Crystal structure of an indigoidine synthase A (IndA)-like protein (TM1464) from *Thermotoga maritima* at 1.90 Å resolution reveals a new fold," *Proteins: Structure, Function, and Bioinformatics* 59, 864 (2005).

Levin, J.I., J.M. Chen, L.M. Laakso, M. Du, X. Du, A.M. Venkatesan, V. Sandanayaka, A. Zask, J. Xu, W. Xu, Y. Zhang, and J.S. Skotnicki, "Acetylenic TACE inhibitors. Part 2: SAR of six-membered cyclic sulfonamide hydroxamates," *Bioorg. Med. Chem. Lett.* 15, 4345 (2005).

Li, F., W. Li, M. Farzan, and S.C. Harrison, "Structure of SARS coronavirus spike receptor-binding domain complexed with receptor," *Science* 309, 1864 (2005).

Li, H., M.L. Flinspanch, J. Igarashi, J. Jamal, W. Yang, J.A. Gomez-Vidal, E.A. Litzinger, H. Huang, E.P. Erdal, R.B. Silverman, and T.L. Poulos, "Exploring the binding conformations of bulkier dipeptide amide inhibitors in con-

stitutive nitric oxide synthases," *Biochemistry* 44, 15222 (2005).

Li, H., M.R. Sawaya, F.R. Tabita, and D. Eisenberg, "Crystal structure of a RuBisCO-like protein from the green sulfur bacterium *Chlorobium tepidum*," *Structure* 13, 779 (2005).

Li, S., N.A. Peterson, M.Y. Kim, C.Y. Kim, L.W. Hung, M. Yu, T. Lekin, B.W. Segelke, J.S. Lott, and E.N. Baker, "Crystal structure of AhpE from *Mycobacterium tuberculosis*, a 1-Cys peroxiredoxin," *J. Mol. Biol.* 346, 1035 (2005).

Li, Z.Q., G.M. Wang, K.J. Mikolaitis, D. Moses, A.J. Heeger, and D.N. Basov, "An infrared probe of tunable dielectrics in metal-oxide-semiconductor structures," *Appl. Phys. Lett.* 86, 223506 (2005).

Lindenberg, A.M., Y. Acremann, D.P. Lowney, P.A. Heimann, T.K. Allison, T.R. Matthews, and R.W. Falcone, "Time-resolved measurements of the structure of water at constant density," *J. Chem. Phys.* 122, 204507 (2005).

Liu, J., C. Huang, D.H. Shin, H. Yokota, J. Jancarik, J.S. Kim, P.D. Adams, R. Kim, and S.H. Kim, "Crystal structure of a heat-inducible transcriptional repressor HrcA from *Thermotoga maritima*: Structural insight into DNA binding and dimerization," *J. Mol. Biol.* 350, 987 (2005).

Liu, J., Y. Lou, H. Yokota, P.D. Adams, R. Kim, and S.H. Kim, "Crystal structure of a PhoU protein homologue: A new class of metalloprotein containing multinuclear iron clusters," *J. Biol. Chem.* 280, 15960 (2005).

Lodowski, D.T., J.F. Barnhill, R.M. Pyskadlo, R. Ghirlando, R. Sterne-Marr, and J.J.G. Tesmer, "The role of Gβγ and domain interfaces in the activation of G protein-coupled receptor kinase 2," *Biochemistry* 44, 6958 (2005).

Lovering, A.L., S.S. Lee, Y.W. Kim, S.G. Withers, and N.C.J. Strynadka, "Mechanistic and structural analysis of a family 31 α-glycosidase and its glycosyl-enzyme intermediate," *J. Biol. Chem.* 280, 2105 (2005).

Lowery, T.J., M. Doucleff, E.J. Ruiz, S.M. Rubin, A. Pines, and D.E. Wemmer, "Distinguishing multiple chemotaxis Y protein conformations with laser-polarized ^{129}Xe NMR," *Protein Sci.* 14, 848 (2005).

Lu, H., D.J. Chang, B. Baratte, L. Meijer, and U. Schulze-Gahmen, "Crystal structure of a human cyclin-dependent kinase 6 complex with a flavonol inhibitor, fisetin," *J. Med. Chem.* 48, 737 (2005).

Lussier, A., "Ferromagnetism in cobalt-doped titanium," Ph.D. thesis, Montana State University, (2005).

Ma, Y., J. Dostie, G. Dreyfuss, and G.D. Van Duyne, "The Gemin6-Gemin7 heterodimer from the survival of motor neurons complex has an Sm protein-like structure," *Structure* 13, 883 (2005).

MacNaughton, J., A. Moewes, and E.Z. Kurmaev, "Electronic structure of the nucleobases," *J. Phys. Chem. B* 109, 7749 (2005).

MacNaughton, J.B., A. Moewes, R.G. Wilks, X.T. Zhou, T.K. Sham, T. Taniguchi, C.Y. Chan, W.J. Zhang, I. Bello, S.T. Lee, H. Hofsass, and K. Watanabe, "The electronic structure of boron nitride single crystals and films," *Phys. Rev. B* 72, 195113 (2005).

Magid, K.R., E.T. Lilleodden, N. Tamura, J.N. Florando, D.H. Lassila, M.M. Leblanc, R.I. Barabash, and J.W. Morris, Jr., "X-ray microdiffraction characterization of deformation heterogeneities in BCC crystals," *MRS Proc.* 840, Q7.2 (2005); 2004 MRS Fall Meeting, Boston, Massachusetts, November 28–December 3, 2004.

Manceau, A., C. Tommaseo, S. Rihs, N. Geoffroy, D. Chateigner, M. Schlegel, D. Tisserand, M.A. Marcus, N. Tamura, and Z.S. Chen, "Natural speciation of Mn, Ni and Zn at a micrometer scale in a clayey paddy soil using x-ray fluorescence, absorption and diffraction," *Geochim. Cosmochim. Acta* 69, 4007 (2005).

Mannella, N., A. Rosenhahn, M. Watanabe, B. Sell, A. Nambu, S.B. Ritchey, E. Arenholz, A. Young, Y. Tomioka, and C.S. Fadley, "Temperature-dependent x-ray absorption spectroscopy of colossal magnetoresistive perovskites," *Phys. Rev. B* 71, 5117 (2005).

Mannella, N., W. Yang, X.J. Zhou, H. Zheng, J.F. Mitchell, J. Zaanen, T.P. Devereaux, N. Nagaosa, Z. Hussain, and Z.X. Shen, "Nodal quasiparticles in pseudo-gapped colossal magnetoresistive manganites," *Nature* 438, 474 (2005).

Mao, X., Z.Y. Ren, G.N. Parker, H. Sondermann, M.A. Pastorello, W. Wang, J.S. McMurray, B. Demeier, J.E. Darnell, and X.M. Chen, "Structural bases of unphosphorylated STAT1 association and receptor binding," *Mol. Cell* 17, 761 (2005).

Martinez, S.E., S. Bruder, A. Schultz, N. Zheng, J.E. Schultz, J.A. Beavo, and J.U. Linder,

"Crystal structure of the tandem GAF domains from a cyanobacterial adenylyl cyclase: Modes of ligand binding and dimerization," *Proc. Natl. Acad. Sci. USA* 102, 3082 (2005).

Mathews, I., R. Schwarzenbacher, D. McMullan, P. Abdubek, E. Ambing, H. Axelrod, T. Biorac, J.M. Canaves, H.J. Chiu, A.M. Deacon, M. DiDonato, M.A. Elsliger, A. Godzik, C. Grittini, S.K. Grzechnik, J. Hale, E. Hampton, G.W. Han, J. Haugen, M. Hornsby, L. Jaroszewski, H.E. Klock, E. Koesema, A. Kreusch, P. Kuhn, S.A. Lesley, I. Levin, M.D. Miller, K. Moy, E. Nigoghossian, J. Ouyang, J. Paulsen, K. Quijano, R. Reyes, G. Spraggon, R.C. Stevens, H. van den Bedem, J. Velasquez, J. Vincent, A. White, G. Wolf, Q. Xu, K.O. Hodgson, J. Wooley, I.A. Wilson, "Crystal structure of S-adenosylmethionine:tRNA ribosyltransferase-isomerase (QueA) from *Thermotoga maritima* at 2.0 Å resolution reveals a new fold," *Proteins: Structure, Function, and Bioinformatics* 59, 869 (2005).

Maynard, J., K. Petersson, D.H. Wilson, E.J. Adams, S.E. Blondelle, M.J. Boulanger, D.B. Wilson, and K.C. Garcia, "Structure of an autoimmune T cell receptor complexed with class II peptide-MHC: Insights into MHC bias and antigen specificity," *Immunity* 22, 81 (2005).

Maynes, J.T., M.M. Cherney, M.A. Qasim, M. Laskowski, and M.N. James, "Structure of the subtilisin Carlsberg-OMTKY3 complex reveals two different ovomucoid conformations," *Acta Crystallogr. D* D61, 580 (2005).

McCunn, L.R., M.J. Krisch, Y. Liu, L.J. Butler, and J. Shu, "A study of the unimolecular dissociation of the 2-buten-2-yl radical via the 193 nm photodissociation of 2-chloro-2-butene," *J. Phys. Chem. A* 109, 6430 (2005).

McNear, D.H., R. Tappero, and D.L. Sparks, "Shining light on metals in the environment," *Elements* 1, 211 (2005).

Melcher, C.L., S. Friedrich, S.P. Cramer, M.A. Spurrier, P. Szupryczynski, and R. Nutt, "Cerium oxidation state in LSO:Ce scintillators," *IEEE Trans. Nucl. Sci.* 52, 1809 (2005).

Messer, B.M., "X-ray absorption spectroscopy of aqueous amino acids," Ph.D. thesis, University of California, Berkeley (2005).

Messer, B.M., C.D. Cappa, J.D. Smith, K.R. Wilson, M.K. Gilles, R.C. Cohen, and R.J. Saykally, "pH dependence of the electronic structure of glycine," *J. Phys. Chem. B* 109, 5375 (2005).

Messer, B.M., C.D. Cappa, J.D. Smith, W.S. Drisdell, C.P. Schwartz, R.C. Cohen, and R.J. Saykally, "Local hydration environments of amino acids and dipeptides studied by x-ray spectroscopy of liquid microjets," *J. Phys. Chem. B* 109, 21640 (2005).

Metz, R.B., C. Nicolas, M. Ahmed, and S.R. Leone, "Direct determination of the ionization energies of FeO and CuO with VUV radiation," *J. Chem. Phys.* 123, 114313 (2005).

Miller, G.J., M.P. Wilson, P.W. Majerus, and J.H. Hurley, "Specificity determinants in inositol polyphosphate synthesis: Crystal structure of inositol 1,3,4-trisphosphate 5/6-kinase ," *Mol. Cell* 18, 201 (2005).

Miller, J.L., M.J. Krisch, L.J. Butler, and J.N. Shu, "Dissociation channels of the 1-buten-2-yl radical and its photolytic precursor 2-bromo-1-butene," *J. Phys. Chem. A* 109, 4038 (2005).

Moewes, A., R. Wilks, A.G. Kochur, and E.Z. Kurmaev, "Monitoring 5p–4d soft x-ray emission of La when exciting through the low-lying 3d–4f threshold," *J. Electron Spectrosc.* 144–147, 577 (2005).

Moewes, A., R. Wilks, A.G. Kochur, and E.Z. Kurmaev, "Resonantly excited cascade x-ray emission from La," *Phys. Rev. B* 72, 075129 (2005).

Mooers, B.H., J.S. Logue, and J.A. Berglund, "The structural basis of myotonic dystrophy from the crystal structure of CUG repeats," *Proc. Natl. Acad. Sci. USA* 102, 16626 (2005).

Morel, A., "Molecular-beam mass spectrometer measurements and modeling of propene and related flames," masters thesis, University of Massachusetts, Amherst (2005).

Müller, P., M.R. Sawaya, I. Pashkov, S. Chan, C. Nguyen, Y. Wu, L.J. Perry, and D. Eisenberg, "The 1.70 Å x-ray crystal structure of *Mycobacterium tuberculosis* phosphoglycerate mutase," *Acta Crystallogr. D* D61, 309 (2005).

Mun, B.G., M. Watanabe, M. Rossi, V. Stamenkovic, N.M. Markovic, and P.N. Ross, "A study of electronic structures of Pt_3M (M=Ti,V,Cr,Fe,Co,Ni) polycrystalline alloys with valence-band photoemission spectroscopy," *J. Chem. Phys.* 123, 204717 (2005).

Mun, B.S., C. Lee, V. Stamenkovic, N.M. Markovic, and P.N. Ross,

"Electronic structure of Pd thin films on Re(0001) studied by high-resolution core-level and valence-band photoemission," *Phys. Rev. B* **71**, 115420 (2005).

Mun, B.S., C. Lee, V. Stamenkovic, N.M. Markovic, and P.N. Ross, "A photoemission study of Pd ultra-thin films on Pt(111)," *J. Chem. Phys.* **122**, 184712 (2005).

Muntean, L., R. Planques, A.L.D. Kilcoyne, S.R. Leone, M.K. Gilles, and W.D. Hinsberg, "Chemical mapping of polymer photoresists by scanning transmission x-ray microscopy," *J. Vac. Sci. Technol. B* **23**, 1630 (2005).

Muramatsu, Y., T. Yamamoto, J.D. Denlinger, and R.C.C. Perera, "Soft x-ray emission spectra of argons atoms doped in solid matrices," *J. Electron Spectrosc.* **144–147**, 799 (2005).

Muramatsu, Y., M. Yamashita, M. Motoyama, M. Hirose, J. Denlinger, E.M. Gullikson, and R.C. Perera, "Characterization of surface carbon films on weathered Japanese roof tiles by soft x-ray spectroscopy," *X-Ray Spectrom.* **34**, 509 (2005).

Mysak, E.R., K.R. Wilson, M. Jimenez-Cruz, M. Ahmed, and T. Baer, "Synchrotron radiation based aerosol time-of-flight mass spectrometry for organic constituents," *Anal. Chem.* **77**, 5953 (2005).

Nachimuthu, P., S. Thevuthasan, E.M. Adams, W.J. Weber, B.D. Begg, B.S. Mun, D.K. Shuh, D.W. Lindle, E.M. Gullikson, and R.C. Perera, "Near-edge x-ray absorption fine structure study of disordering in $Gd_2(Ti_{1-y}Zr_y)_2O_7$ pyrochlores," *J. Phys. Chem. B* **109**, 1337 (2005).

Nachtegaal, M.H., M.A. Marcus, J.E. Sonke, J. Vangronsveld, K.J.T. Livi, D. van Der Lelie, and D.L. Sparks, "Effects of in situ remediation on the speciation and bioavailability of zinc in a smelter contaminated soil," *Geochim. Cosmochim. Acta* **69**, 4649 (2005).

Naslund, L.A., D.C. Edwards, P. Wernet, U. Bergmann, H. Ogasawara, L.G.M. Pettersson, S. Myneni, and A. Nilsson, "X-ray absorption spectroscopy study of the hydrogen bond network in the bulk water of aqueous solutions," *J. Phys. Chem. A* **109**, 5995 (2005).

Naslund, L.A., J. Luning, Y. Ufuktepe, H. Ogasawara, P. Wernet, U. Bergmann, L.G.M. Pettersson, and A. Nilsson, "X-ray absorption spectroscopy measurements of liquid water," *J. Phys. Chem. B* **109**, 13835 (2005).

Navacerrada, M.A., A. Mehta, H. Sahibudeen, and J. Acrivos, "Comparative study of structural properties of $YBa_2Cu_3O_7$ thin films on $SrTiO_3$ single crystal and bicrystal substrates by x-ray diffraction," *MRS Proc.* **868E**, C8.2 (2005); 2005 MRS Spring Meeting, San Francisco, California, March 28–April 1, 2005.

Negres, R.A., S.O. Kucheyev, P. DeMange, C. Bostedt, T. van Buuren, A.J. Nelson, and S.G. Demos, "Decomposition of KH_2PO_4 crystals during laser-induced breakdown," *Appl. Phys. Lett.* **86**, 171107 (2005).

Newberry, K.J., S. Nakano, P. Zuber, and R.G. Brennan, "Crystal structure of the *Bacillus subtilis* anti-alpha, global transcriptional regulator, Spx, in complex with the α C-terminal domain of RNA polymerase," *Proc. Natl. Acad. Sci. USA* **102**, 15839 (2005).

Newhouse, Y., C. Peters-Libeu, and K.H. Weisgraber, "Crystallization and preliminary x-ray diffraction analysis of apolipoprotein E-containing lipoprotein particles," *Acta Crystallogr. F* **F61**, 981 (2005).

Ng, C.Y., "Two-color photoionization and photoelectron studies by combining infrared and vacuum ultraviolet," *J. Electron Spectrosc.* **142**, 179 (2005).

Nikitin, A., H. Ogasawara, D. Mann, R. Denecke, Z. Zhang, H. Dai, K. Cho, and A. Nilsson, "Hydrogenation of single-walled carbon nanotubes," *Phys. Rev. Lett.* **95**, 225507 (2005).

Nilsson, H.J., T. Tyliszczak, R.E. Wilson, L. Werme, and D.K. Shuh, "Soft x-ray scanning transmission x-ray microscopy (STXM) of actinide particles," *Anal. Bioanal. Chem.* **383**, 41 (2005).

Nordlinder, S., "Nanotubes for battery applications," Ph.D. thesis, Uppsala University, Sweden (2005).

Nurmi, J.T., P.G. Tranyek, V. Sarathy, D.R. Baer, J.E. Amonetter, K. Pecher, C. Wang, J.C. Linehan, D.W. Matson, R.L. Penn, and M.D. Driessen, "Characterization and properties of metallic iron and iron-oxide nanoparticles: Spectroscopy, electrochemistry, and kinetics," *Environ. Sci. Technol.* **39**, 1221 (2005).

Odelius, M., H. Ogasawara, D. Nordlund, O. Fuchs, L. Weinhardt, F. Maier, E. Umbach, C. Heske, Y. Zubavichus, M. Grunze, J.D. Denlinger, L.G.M. Pettersson, and A. Nilsson, "Ultrafast core-hole-induced dynamics in water probed

by x-ray emission spectroscopy," *Phys. Rev. Lett.* 94, 227401 (2005).

Oganesyan, V., N. Oganesyan, P.D. Adams, J. Jancarik, H.A. Yokota, R. Kim, and S.H. Kim, "Crystal structure of the 'PhoU-Like' phosphate uptake regulator from *Aquifex aeolicus*," *J. Bacteriol.* 187, 4238 (2005).

Ohta, T., D.A. Schmidt, S. Meng, A. Klust, A. Bostwick, Q. Yu, M.A. Olmstead, and F.S. Ohuchi, "Intrinsic vacancy-induced nanoscale wire structure in heteroepitaxial Ga_2Se_3/Si(001)," *Phys. Rev. Lett.* 94, 116102 (2005).

Okulov, V.I., L.D. Sabirzyanova, E.Z. Kurmaev, L.D. Finkelstein, R.F. Karimov, A. Moewes, and S.Y. Paranchich, "Experimental evidence of the hybridization of the electron states of an impurity and the conduction band in the HgSe:Fe system," *JETP Letters* 81, 72 (2005).

Olamit, J., E. Arenholz, Z.P. Li, O. Petracic, I.V. Roshchin, R. Morales, X. Batlle, I.K. Schuller, and K. Liu, "Loop bifurcation and magnetization rotation in exchange biased Ni/FeF_2," *Phys. Rev. B* 72, 012408 (2005).

Olson, R., K.E. Huey-Tubman, C. Dulac, and P.J. Bjorkman, "Structure of a pheromone receptor-associated MHC molecule with an open and empty groove," *PLoS Biology* 3, 1436 (2005).

O'Neal, C.J., M.J. Jobling, R.K. Holmes, and W.G.J. Hol, "Structural basis for the activation of cholera toxin by human ARF6-GTP," *Science* 309, 1093 (2005).

Osipov, T., A.S. Alnaser, S. Voss, M.H. Prior, T. Weber, O. Jagutzki, L. Schmidt, H. Schmidt-Böcking, R. Dörner, A. Landers, E. Wells, B. Shan, C. Maharjan, B. Ulrich, P. Ranitovic, X.M. Tong, C.D. Lin, C.L. Cocke, "Photon-ion collisions and molecular clocks," *J. Mod. Opt.* 52, 439 (2005).

Ostheimer, G.J., H. Hadjivasiliou, D.P. Kloer, A. Barkan, and B.W. Matthews, "Structural analysis of the Group II intron splicing factor CRS2 yields insights into its protein and RNA interaction surfaces," *J. Mol. Biol.* 345, 51 (2005).

Paddock, M.L., C. Chang, Q. Xu, E.C. Abresch, H.L. Axelrod, G. Feher, and M.Y. Okamura, "Quinone (Q_B) reduction by B-branch electron transfer in mutant bacterial reaction centers from Rhodobacter sphaeroides: Quantum efficiency and x-ray structure," *Biochemistry* 44, 6920 (2005).

Panfili, F., A. Manceau, G. Sarret, L. Spadini, T. Kirpichtchikova, V. Bert, A. Laboudigue, M.A. Marcus, N. Ahamdach, and M.F. Libert, "The effect of phytostabilization on Zn speciation in a dredged contaminated sediment using scanning electron microscopy, x-ray fluorescence, EXAFS spectroscopy and principal components analysis," *Geochim. Cosmochim. Acta* 69, 2265 (2005).

Parry, S., "The effect of pressure upon the structure of talc and 10A phase: In-situ experiments using synchrotron x-ray diffraction and infrared spectroscopy," Ph.D. thesis, University of Manchester, UK (2005).

Parsonage, D., D.S. Youngblood, G.N. Sarma, Z.A. Wood, P.A. Karplus, and L.B. Poole, "Analysis of the link between enzymatic activity and oligomeric state in AhpC, a bacterial peroxiredoxin," *Biochemistry* 44, 10583 (2005).

Pegan, S., C. Arrabit, W. Zhou, W. Kwiatkowski, A. Collins, P.A. Slesinger, and S. Choe, "Cytoplasmic domain structures of Kir2.1 and Kir3.1 show sites for modulating gating and rectification," *Nature Neuroscience* 8, 279 (2005).

Peterka, D.S., "Imaging chemical dynamics with the vacuum ultraviolet," Ph.D. thesis, University of California, Berkeley (2005).

Peters-Libeu, C., Y. Newhouse, P. Krishnan, K. Cheung, E. Brooks, K. Weisgraber, and S. Finkbeiner, "Crystallization and diffraction properties of the Fab fragment of 3B5H10, an antibody specific for disease-causing polyglutamine stretches," *Acta Crystallogr. F* F61, 1065 (2005).

Piancastelli, M.N., W.C. Stolte, R. Guillemin, A. Wolska, S.W. Yu, M.M. Sant'Anna, and D.W. Lindle, "Anion and cation-yield spectroscopy of core-excited SF_6," *J. Chem. Phys.* 122, 094312 (2005).

Pierce, M.S., C.R. Buechler, L.B. Sorenson, J.J. Turner, S.D. Kevan, E.A. Jagla, J.M. Deutsch, T. Mai, O. Nayaran, J.E. Davies, K. Liu, J.H. Dunn, K.M. Chesnel, J.B. Kortright, O. Hellwig, and E.E. Fullerton, "Disorder-induced microscopic magnetic memory," *Phys. Rev. Lett.* 94, 7202 (2005).

Pleshe, E., J. Truesdell, and R.T. Batey, "Structure of a class II TrmH tRNA-modifying enzyme from *Aquifex aeolicus*," *Acta Crystallogr. F* F61, 722 (2005).

Prince, K.C., M. Matteucci, K. Kuepper, S.G. Chiuzbaian, S. Bartkowski, and M. Neumann,

"Core-level spectroscopic study of FeO and FeS_2," *Phys. Rev. B* 71, 085102 (2005).

Puzic, A., B. Van Wayenberge, K.W. Chou, P. Fischer, H. Stoll, G. Schutz, T. Tyliszczak, K. Rott, H. Bruckl, G. Reiss, I. Neudecker, T. Haug, M. Buess, and C.H. Back, "Spatially resolved ferromagnetic resonance: Imaging of ferromagnetic eigenmodes," *J. Appl. Phys.* 97, 10E704 (2005).

Puzic, A., H. Stoll, P. Fischer, B. van Waeyenberge, J. Raabe, G. Denbeaux, T. Haug, D. Weiss, and G. Schutz, "Implementing subns time resolution into magnetic xray microscopies," *Phys. Scr.* T115, 1029 (2005).

Radisky, E.S., C.J.K. Lu, G. Kwan, and D.E. Koshland, Jr., "Role of the intramolecular hydrogen bond network in the inhibitory power of chymotrypsin inhibitor 2," *Biochemistry* 44, 6823 (2005).

Rathbone, G.J., E.D. Poliakoff, J.D. Bozek, and R.R. Lucchese, "Electronically forbidden ($5\sigma_u \rightarrow k\sigma_u$) photoionization of CS_2: Mode-specific electronic-vibrational coupling," *J. Chem. Phys.* 122, 064308 (2005).

Rathbone, G.J., E.D. Poliakoff, J.D. Bozek, D. Toffoli, and R.R. Lucchese, "Photoelectron trapping in N_2O $7\sigma \rightarrow k\sigma$ resonant ionization," *J. Chem. Phys.* 123, 014307 (2005).

Reményi, A., M.C. Good, R.P. Bhattacharyya, and W.A. Lim, "The role of docking interactions in mediating signaling input, output, and discrimination in the yeast MAPK network," *Mol. Cell* 20, 951 (2005).

Reyes, C.L., and G. Chang, "Structure of the ABC transporter MsbA in complex with ADP-vanadate and lipopolysaccharide," *Science* 308, 1028 (2005).

Roberts, B.R., Z.A. Wood, T.J. Jonnson, L.B. Poole, and P.A. Karplus, "Oxidized and synchrotron cleaved structures of the disulfide redox center in the N-terminal domain of *Salmonella typhimurium* AhpF," *Protein Sci.* 14, 2414 (2005).

Robin, D., J. Krupnick, R. Schlueter, C. Steier, S. Marks, B. Wang, J. Zbasnik, R. Benjegerdes, A. Biocca, P. Bish, W. Brown, W. Byrne, J. Chen, W. Decking, J. DeVries, W.R. DeMarco, M. Fahmie, A. Geyer, J. Harkins, T. Henderson, J. Hinkson, E. Hoyer, D. Hull, S. Jacobson, J. McDonald, P. Molinari, R. Mueller, L. Nadolski, H. Nishimura, K. Nishimura, F. Ottens, J.A. Paterson, P. Pipersky, G. Portmann, A. Ritchie, S. Rossi, B. Salvant, T. Scarvie, A. Schmidt, J. Spring, C. Taylor, W. Thur, C. Timossi, and A. Wandesforde, "Superbend upgrade on the Advanced Light Source," *Nucl. Instrum. Meth. A* 538, 65 (2005).

Robin, D.S., J.M. Byrd, P. Heimann, S. Kwiatkowski, D. Li, F. Sannibale, C. Steier, W. Wan, A. Zholents, and W. Wittmer, "Generation of picosecond x-ray pulses in the ALS using rf orbit," in *Proceedings of 2005 Particle Accelerator Conference* (PAC 05), p. 3659 (2005); Knoxville Tennessee, May 16–20, 2005.

Robinson, J.C., N.E. Sveum, S.J. Goncher, and D.M. Neumark, "Photofragment translational spectroscopy of allene, propyne, and propyne-d_3 at 193 nm," *Mol. Phys.* 103, 1765 (2005).

Rosenberg, O.S., S. Deindl, R.J. Sung, A.C. Nairn, and J. Kuriyan, "Structure of the autoinhibited kinase domain of CaMKII and SAXS analysis of the holoenzyme," *Cell* 123, 849 (2005).

Rossnagel, K., E. Rotenberg, H. Koh, N.V. Smith, and L. Kipp, "Continuous tuning of electronic correlations by alkali adsorption on layered 1T-TaS_2," *Phys. Rev. Lett.* 95, 126403 (2005).

Rossnagel, K., E. Rotenberg, H. Koh, N.V. Smith, and L. Kipp, "Fermi surface, charge-density-wave gap, and kinks in 2H-$TaSe_2$," *Phys. Rev. B* 72, 121103R (2005).

Roy, S., M.R. Fitzsimmons, S. Park, M. Dorn, O. Petracic, I.V. Roshchin, Z.P. Li, X. Batlle, R. Morales, A. Misra, X. Zhang, K. Chesnel, J.B. Kortright, S.K. Sinha, and I.K. Schuller, "Depth profile of uncompensated spins in an exchange bias system," *Phys. Rev. Lett.* 95, 047201 (2005).

Ryser, A.L., D.G. Strawn, M.A. Marcus, J.L. Johnson-Maynard, M.E. Gunter, and G. Moller, "Micro-spectroscopic investigation of selenium-bearing minerals from the Western US Phosphate Resource Area," *Geochem. Trans.* 6, 1 (2005).

Sacchi, M., F. Offi, P. Torelli, A. Fondacaro, C. Spezzani, G. Cautero, M. Cautero, S. Huotari, M. Grioni, R. Delaunay, M. Fabrizioli, G. Vankó, G. Monaco, G. Paolicelli, G. Stefani, G. Panaccione, "Quantifying the effective attenuation length in high-energy photoemission experiments," *Phys. Rev. B* 71, 155117 (2005).

Sahibudeen, H.S., M.A. Navacerrada, and J.V. Acrivos, "Theory and experiments on periodic lattice distortions that explain 1D conductivity along the CuO_2

plane ab and a-b diagonals in $YBa_2Cu_3O_7$ (YBCO) 50 nm film with a 24 DEG grain boundary (GB)," in *Nanotech 2005*, Vol. 2, Ch. 8, p. 573 (2005); 2005 NSTI Nanotechnology Conference and Trade Show, Anaheim, California, May 8–12, 2005.

Sampathkumar, P., S. Turley, J.E. Ulmer, H.G. Rhie, C.H. Sibley, and W.G.J. Hol, "Structure of the *Mycobacterium tuberculosis* flavin dependent thymidylate synthase (MtbThyX) at 2.0 Å resolution," *J. Mol. Biol.* 352, 1091 (2005).

Sandström, J., I. Alvarez, D. Calabrese, C. Cisneros, A.M. Covington, V.T. Davis, M.S. Gulley, M. Halka, D. Hanstorp, F.S. Schlachter, J.S. Thompson, and D.J. Pegg, "Triple photodetachment from the Cl^- ion," *Phys. Rev. A* 72, 034702 (2005).

Santillion, J., "The incorporation of carbon and phosphorus in the deep Earth," Ph.D. thesis, University of California, Santa Cruz (2005).

Sarma, G.N., C. Nickel, S. Rahlfs, M. Fischer, K. Becker, and P.A. Karplus, "Crystal structure of a novel plasmodium falciparum 1-Cys peroxiredoxin," *J. Mol. Biol.* 346, 1021 (2005).

Sarma, G.N., V.A. Manning, L.M. Ciuffetti, and P.A. Karplus, "Structure of Ptr ToxA: An RGD-containing host-selective toxin from *Pyrenophora tritici-repentis*," *Plant Cell* 17, 3190 (2005).

Sasagawa, T., A. Lanzara, G.H. Gweon, S. Zhou, J. Graf, Suryadijaya, and H. Takagi, "Oxygen isotope effect on electron dynamics in $Bi_2Sr_2CaCu_2O_y$: Angle-resolved photoemission spectroscopy," *Physica C* 426, 436 (2005).

Sauer, K., J. Yano, and V.K. Yachandra, "X-ray spectroscopy of the Mn_4Ca cluster in the water-oxidation complex of Photosystem II," *Photosynth. Res.* 85, 73 (2005).

Schade, U., K. Holldack, M. Martin, and D. Fried, "THz near-field imaging of biological tissues employing synchrotron radiation," *Proc. SPIE* 5725, 46 (2005); SPIE Photonics West, San Jose California, January 22–27, 2005.

Schmalhorst, J., M.D. Sacher, A. Thomas, H. Bruckl, G. Reiss, and K. Starke, "X-ray absorption and magnetic circular dichroism studies of annealed magnetic tunnel junctions," *J. Appl. Phys.* 97, 123711 (2005).

Schmidt, A.E., H.S. Chand, D. Cascio, W. Kisiel, and S.P. Bajaj, "Crystal structure of Kunitz domain 1 (KD1) of tissue factor pathway inhibitor-2 in complex with trypsin: Implications for KD1 specificity of inhibition," *J. Biol. Chem.* 280, 27832 (2005).

Schuler, T. M., R.A. Stern, R. McNorton, S.D. Willoughby, J.M. MacLaren, D.L. Ederer, V. Perez-Dieste, F.J. Himpsel, S.A. Lopez-Rivera, and T.A. Callcott, "Electronic structure of the dilute magnetic semiconductor $Zn_{0.90}Mn_{0.10}S$ obtained by soft x-ray spectroscopy and first principles calculations," *Phys. Rev. B* 72, 045211 (2005).

Schuler, T.M., D.L. Ederer, S. Itza-Ortiz, G.T. Woods, T.A. Callcott, and J.C. Woicik, "Character of the insulating state in NiO: A mixture of charge-transfer and Mott-Hubbard character," *Phys. Rev. B* 71, 115113 (2005).

Schulze-Gahmen, U., S. Aono, S. Chen, H. Yokota, R. Kim, and S.H. Kim, "Structure of the hypothetical *Mycoplasma* protein MPN555 suggests a chaperone function," *Acta Crystallogr. D* D61, 1343 (2005).

Schumacher, M., K. Mizuno, and H.P. Bächinger, "The crystal structure of the collagen-like polypeptide (glycyl-4(R)-hydroxyprolyl-4(R)-hydroxyprolyl)$_9$ at 1.55 Å resolution shows up-puckering of the proline ring in the Xaa position," *J. Biol. Chem.* 280, 20397 (2005).

Schumacher, M.A., and B.E. Funnell, "Structures of ParB bound to DNA reveal mechanism of partition complex formation," *Nature* 438, 516 (2005).

Schuwirth, B.S., M.A. Borovinskaya, C.W. Hau, W. Zhang, A. Vila-Sanjurjo, J.M. Holton, and J.H. Doudna Cate, "Structures of the bacterial ribosome at 3.5 Å resolution," *Science* 310, 827 (2005).

Scully, S.WJ., A. Aguilar, E.D. Emmoms, R.A. Phaneuf, D. Leitner, J.C. Levin, M.S. Lubbell, R. Puettner, A.S. Schlachter, A.M. Covington, S. Schippers, A. Mueller, and B.M. McLaughlin, "K-shell photoionization of Be-like carbon ions: Experiment and theory for C^{2+}," *J. Phys. B–At. Mol. Opt.* 38, 1967 (2005).

Scully, S.W J., E.D. Emmons, M.F. Gharaibeh, R.A. Phaneuf, A.L.D. Kilcoyne, A.S. Schlachter, S. Schippers, A. Mueller, H.S. Chakraborty, M.E. Madjet, and J.M. Rost, "Photoexcitation of a volume plasmon in C_{60} ions," *Phys. Rev. Lett.* 94, 065503 (2005).

Seidel, A., and D.H. Lee, "The Luther-Emery liquid: Spin gap and anomalous flux period," *Phys. Rev. B* 71, 0451133 (2005).

Seidel, A., H.H. Lin, and D.H. Lee, "Phonons in Hubbard ladders studied within the framework of the one-loop renormalization group," *Phys. Rev. B* 71, 22051 (2005).

Shan, L., I.I. Mathews, and C. Khosla, "Structural and mechanistic analysis of two prolyl endopeptidases: Role of interdomain dynamics in catalysis and specificity," *Proc. Natl. Acad. Sci. USA* 102, 3599 (2005).

Shapiro, D., P. Thibault, T. Beetz, V. Elser, M. Howells, C. Jacobsen, J. Kirz, E. Lima, H. Miao, A.M. Neiman, and D. Sayre, "Biological imaging of soft x-ray diffraction microscopy," *Proc. Natl. Acad. Sci. USA* 102, 15343 (2005).

Sherman, D.M., "Electronic structures of iron(III) and manganese(IV) (hydr)oxides: Thermodynamics of photochemical reductive dissolution in aquatic environments," *Geochim. Cosmochim. Acta* 69, 3249 (2005).

Shi, K., C.K. Brown, Z.Y. Gu, B.K. Kozlowicz, G.M. Dunny, D.H. Ohlendorf, and C.A. Earhart, "Structure of peptide sex pheromone receptor PrgX and PrgX/pheromone complexes and regulation of conjugation in *Enterococcus faecalis*," *Proc. Natl. Acad. Sci. USA* 102, 18596 (2005).

Shia, S., J. Stamos, D. Kirchhofer, B. Fan, J. Wu, R.T. Corpuz, L. Santell, R.A. Lazarus, and C. Eigenbrot, "Conformational lability in serine protease active sites: Structures of hepatocyte growth factor activator (HGFA) alone and with the inhibitory domain of HGFA inhibitor-1B," *J. Mol. Biol.* 346, 1335 (2005).

Shin, D.H., N. Oganesyan, J. Jancarik, H. Yokota, R. Kim, and S.H. Kim, "Crystal structure of a nicotinate phosphoribosyltransferase from *Thermoplasma acidophilum*," *J. Biol. Chem.* 280, 18326 (2005).

Shin, D.W., S.X. Wang, A.F. Marshall, W. Kimura, C. Dong, A. Augustsson, and J.H. Guo, "Growth and characterization of copper nanoclusters embedded in SiC matrix," *Thin Solid Films* 473, 267 (2005).

Shin, S., R. El-Diwany, S. Schaffert, E.J. Adams, K.C. Garcia, P. Pereira, and Y.H. Chien, "Antigen recognition determinants of γδ T cell receptors," *Science* 308, 252 (2005).

Shu, J., K.R. Wilson, A.N. Arrowsmith, M. Ahmed, and S.R. Leone, "Light scattering of ultrafine silica particles by VUV synchrotron radiation," *Nano Lett.* 5, 1009 (2005).

Shuman, D., W. Barry, S. Prestemon, R. Schlueter, C. Steier, and G. Stover, "Stray field reduction of als eddy current septum magnets," in *Proceedings of 2005 Particle Accelerator Conference* (PAC 05), p. 3718 (2005); Knoxville Tennessee, May 16–20, 2005.

Silaghi-Dumitrescu, R., D.M. Kurtz, Jr., L.G. Ljungdahl, and W.N. Lanzilotta, "X-ray crystal structures of *Moorella thermoacetica* FprA. Novel diiron site structure and mechanistic insights into a scavenging nitric oxide reductase," *Biochemistry* 44, 6492 (2005).

Silva, D.A., and P.J.M. Monteiro, "ESEM analysis of polymeric film in EVA-modified cement paste," *Cem. Concr. Res.* 35, 2047 (2005).

Silva, D.A., and P.J.M. Monteiro, "Hydration evolution of C_3S–EVA composites analyzed by soft x-ray microscopy," *Cem. Concr. Res.* 35, 351 (2005).

Skordalakes, E., A.R. Brogan, B.S. Park, H. Kohn, and J.M. Berger, "Structural mechanism of inhibition of the Rho transcription termination factor by the antibiotic bicyclomycin," *Structure* 13, 99 (2005).

Slep, K.C., S. L. Rogers, S.L. Elliott, H. Ohkura, P.A. Kolodziej, and R.D. Vale, "Structural determinants for EB1-mediated recruitment of APC and spectraplakins to the microtubule plus end," *J. Cell Biol.* 168, 587 (2005).

Slovic, A.M., S.E. Stayrook, B. North, and W.F. DeGrado, "X-ray structure of a water-soluble analog of the membrane protein phospholamban: Sequence determinants defining the topology of tetrameric and pentameric coiled coils," *J. Mol. Biol.* 348, 777 (2005).

Smith, J.D., C.D. Cappa, B.M. Messer, R.C. Cohen, and R.J. Saykally, "Response to comment on 'Energetics of hydrogen bond network rearrangements in liquid water,'" *Science* 308, 793b (2005).

Smith, J.D., C.D. Cappa, K.R. Wilson, R.C. Cohen, P.L. Geissler, and R.J. Saykally, "Unified description of temperature-dependent hydrogen-bond rearrangements in liquid water," *Proc. Natl. Acad. Sci. USA* 102, 14171 (2005).

Soderstrom, J., J. Grasjo, S. Kashtanov, C. Bergstrom, M. Agaker, T. Schmitt, A. Augustsson, L. Duda, J.H. Guo, J. Nordgren, Y. Luo, P. Artursson, and J.E. Rubensson, "X-ray yield and selectively excited x-ray emission spectra of atenolol and nadolol," *J. Electron Spectrosc.* 144–147, 283 (2005).

Soldatov, A.V., A.N. Kratsova, E.N. Fedorovich, A. Ankudinov, A. Moewes, and E.Z. Kurmaev, "Analysis of the electronic structure of human hemoglobin from soft x-ray emission," *J. Electron Spectrosc.* 144–147, 279 (2005).

Spangenberg, M., J.R. Neal, T.H. Shen, S.A. Morton, J.G. Tobin, G.D. Waddill, J.A.D. Matthew, D. Greig, A.E.R. Malins, E.A. Seddon, and M. Hopkinson, "Observation of a low Curie temperature ferromagnetic phase of ultrathin epitaxial Fe films on GaAs(001)," *J. Magn. Magn. Mater.* 292, 241 (2005).

Spear, J.D., "Shot noise in x-ray measurements with *p-i-n* diodes," *Rev. Sci. Instrum.* 76, 076101 (2005).

Spence, J.C., K. Schmidt, J.S. Wu, G. Hembree, U. Weierstall, B. Doak, and P. Fromme, "Diffraction and imaging from a beam of laser-aligned proteins: Resolution limits," *Acta Crystallogr. A* A61, 237 (2005).

Speziale, S., A.A. Milner, V.E. Lee, S.M. Clark, M.P. Pasternak, and R. Jeanloz, "Iron spin transition in Earth's mantle," *Proc. Natl. Acad. Sci. USA* 102, 17918 (2005).

Spolenak, R., "X-ray diffraction as a probe for elastic strain: Micro- and nanoscale investigation of thin metal films," *MRS Proc.* 840, Q3.4 (2005); 2004 MRS Fall Meeting, Boston, Massachusetts, November 28–December 3, 2004.

Spraggon, G., D. Pantazatos, H.E. Klock, I.A. Wilson, V.L. Woods, Jr., and S.A. Lesley, "On the use of DXMS to produce more crystallizable proteins: Structures of the *T. maritima* proteins TM0160 and TM1171," *Protein Sci.* 14, 168 (2005).

Staker, B.L., M.D. Feese, M. Cushman, Y. Pommier, D. Zembower, L. Stewart, and A.B. Burgin, "Structures of three classes of anticancer agents bound to the human topoisomerase I-DNA covalent complex," *J. Med. Chem.* 48, 2336 (2005).

Starodub, D., R.B. Doak, K. Schmidt, U. Weierstall, J.S. Wu, J. Spence, M. Howells, M. Marcus, D. Shapiro, A. Barty, and H. Chapman, "Damped and thermal motion of laser-aligned hydrated macromolecule beams for diffraction," *J. Chem. Phys.* 123, 244304 (2005).

Stolte, W.C., R. Guillemin, A. Wolska, R. Feng, I.C. Tran, and D.W. Lindle, "Photofragmentation of SO_2 following photoexcitation near the sulfur $L_{2,3}$ ionization thresholds," *J. Electron Spectrosc.* 144–147, 157 (2005).

Stover, G.D., K.M. Baptiste, W. Barry, W. Gath, J. Julian, S. Kwiatkowski, S. Prestemon, R. Schlueter, D. Shuman, and C. Steier, "Investigation, experiments, and implications for using existing pulse magnets for 'topoff' operation at the Advanced Light Source," in *Proceedings of 2005 Particle Accelerator Conference* (PAC 05) p. 3727 (2005); Knoxville Tennessee, May 16–20, 2005.

Sun, J.P., W.Q. Wang, H. Yang, S. Liu, F. Liang, A.A. Fedorov, S.C. Almo, and Z.Y. Zhang, "Structure and biochemical properties of PRL-1, a phosphatase implicated in cell growth, differentiation, and tumor invasion," *Biochemistry* 44, 12009 (2005).

Surleraux, D.L., A. Tahri, W.G. Verschueren, G.M. Pille, H.A. de Kock, T.H. Jonckers, A. Peeters, S. De Meyer, H. Azijn, R. Pauwels, M. de Bethune, N.M. King, M. Prabu-Jeyabalan, C.A. Schiffer, and P.B. Wigerinck, "Discovery and selection of TMC114, a next generation HIV-1 protease inhibitor," *J. Med. Chem.* 48, 1813 (2005).

Szilagyi, R.K., and D.E. Schwab, "Sulfur K-edge x-ray absorption spectroscopy as an experimental probe for S-nitroso proteins," *Biochem. Biophys. Res. Commun.* 330, 60 (2005).

Taatjes, C.A., N. Hansen, A. McIlroy, J.A. Miller, J.P. Senosiain, S.J. Klippenstein, F. Qi, L. Sheng, Y. Zhang, T.A. Cool, J. Wang, P.R. Westmoreland, M.E. Law, T. Kasper, and K. Kohse-Höinghaus, "Enols are common intermediates in hydrocarbon oxidation," *Science* 308, 1887 (2005).

Taatjes, C.A., S.J. Klippenstein, N. Hansen, J.A. Miller, T.A. Cool, J. Wang, M.E. Law, and P.R. Westmoreland, "Synchrotron photoionization measurements of combustion intermediates: Photoionization efficiency and identification of C_3H_2 isomers," *Phys. Chem. Chem. Phys.* 7, 806 (2005).

Takekoh, R., M. Okubo, T. Araki, H.D.H. Stover, and A.P. Hitchcock, "Quantitative chemical mapping of nano-structured 'onion-like' poly(methyl methacrylate)/polystyrene composite particles by soft x-ray microscopy," *Macromolecules* 38, 542 (2005).

Takenaka, H., S. Ichimaru, and E.M. Gullikson, "EUV beam splitter for use in the wavelength region around 6 nm," *J. Electron Spectrosc.* 144–147, 1043 (2005).

Takenaka, H., S. Ichimaru, T. Ohchi, and E.M. Gullikson, "Soft-x-ray reflectivity and heat resist-

ance of SiC/Mg multilayer," *J. Electron Spectrosc.* 144–147, 1047 (2005).

Tamayo, N., L. Liao, M. Goldberg, D. Powers, Y.Y. Tudor, V. Yu, L.M. Wong, B. Henkle, S. Middleton, R. Syed, T. Harvey, G. Jang, R. Hungate, and C. Dominguez, "Design and synthesis of potent pyridazine inhibitors of p38 MAP kinase," *Bioorg. Med. Chem. Lett.* 15, 2409 (2005).

Tamura, N., H.A. Padmore, and J.R. Patel, "High spatial resolution stress measurements using synchrotron based scanning x-ray microdiffraction with white or monochromatic beam," *Mater. Sci. Eng. A* 399, 92 (2005).

Tanaka, M., R. Bateman, D. Rauh, E. Valsberg, S. Ramachandani, C. Zhang, K.C. Hansen, A.L. Burlingame, J.K. Trautman, K.M. Shokat, and C.L. Adams, "An unbiased cell morphology-based screen for new, biologically active small molecules," *PLoS Biology* 3, 764 (2005).

Tang, J., C.L. Yu, S.R. Williams, E. Springman, D. Jeffery, P.A. Sprengeler, A. Estevez, J. Sampang, W. Shrader, J. Spencer, W. Young, M. McGrath, and B.A. Katz, "Expression, crystallization, and three-dimensional structure of the catalytic domain of human plasma kallikrein," *J. Biol. Chem.* 280, 41077 (2005).

Tang, X.N., H. Xu, T. Zhang, Y. Hou, C. Chang, C.Y. Ng, Y. Chiu, R.A. Dressler, and D.J. Lavandier, "A pulsed-field ionization photoelectron secondary ion coincidence study of the $H_2^+(X,\ v^+=0–15,\ N^+=1)$ + He proton transfer reaction," *J. Chem. Phys.* 122, 164301 (2005).

Tang, X.N., Y. Hou, C.Y. Ng, and B. Ruscic, "Pulsed field ionization photoelectron–photoion coincidence study of the process $N_2 + h\nu \rightarrow N^+ + N + e^-$: Bond dissociation energies of N_2 and N_2^+," *J. Chem. Phys.* 123, 074330 (2005).

Tesmer, V.M., T. Kawano, A. Shankaranarayanan, T. Kozasa, and J.J.G. Tesmer, "Snapshot of activated G proteins at the membrane: The $G\alpha_q$–GRK2–$G\beta\gamma$ complex," *Science* 310, 1686 (2005).

Tezcan, F.A., J.T. Kaiser, D. Mustafi, M.Y. Walton, J.B. Howard, and D.C. Rees, "Nitrogenase complexes: Multiple docking sites for a nucleotide switch protein," *Science* 309, 1377 (2005).

Thomas, L., C. Rettner, M. Hayashi, M.G. Samant, S.S. Parkin, A. Doran, and A. Scholl, "Observation of injection and pinning of domain walls in magnetic nanowires using photoemission electron microscopy," *Appl. Phys. Lett.* 87, 262501 (2005).

Thomas, T.D., L.J. Sæthre, K.J. Børve, M. Gundersen, and E. Kukk, "Reactivity and core-ionization energies in conjugated dienes. Carbon 1s photoelectron spectroscopy of 1,3-pentadiene," *J. Phys. Chem. A* 109, 5085 (2005).

Tian, G.D., J.X. Xu, and L.F. Rao, "Optical absorption and structure of a highly symmetrical neptunium(V) diamide complex," Angew. *Chem. Int. Ed.* 44, 6200 (2005).

Tondi, D., F. Morandi, R. Bonnet, M.P. Costi, and B.K. Shoichet, "Structure-based optimization of a non-β-lactam lead results in inhibitors that do not up-regulate β-lactamase expression in cell culture," *J. Am. Chem. Soc.* 127, 4632 (2005).

Toner, B., A. Manceau, M.A.. Marcus, D.B. Millet, and G. Sposito, "Zinc sorption by a bacterial biofilm," *Environ. Sci. Technol.* 39, 8288 (2005).

Toner, B., S. Fakra, M. Villalobos, T. Warwick, and G. Sposito, "Spatially resolved characterization of biogenic manganese oxide production within a bacterial biofilm," *Appl. Environ. Microbiol.* 71, 1300 (2005).

Tu, D., G. Blaha, P.B . Moore, and T.A. Steitz, "Structures of MLS_BK antibiotics bound to mutated large ribosomal subunits provide a structural explanation for resistance," *Cell* 121, 257 (2005).

Tu, K.N., J.O. Suh, A.T.C. Wu, N. Tamura, and C.H. Tung, "Mechanism and prevention of spontaneous tin whisker growth," *Mater. Trans.* 46, 2300 (2005).

Tubbs, J.L., "Controlling chromophore structural chemistry and environment by structure-based design," Ph.D. thesis, The Scripps Research Institute (2005).

Tubbs, J.L., J.A. Tainer, and E.D. Getzoff, "Crystallographic structures of discosoma red fluorescent protein with immature and mature chromophores: Linking peptide bond trans-cis isomerization and acylimine formation in chromophore maturation," *Biochemistry* 44, 9833 (2005).

Tulumello, D., G. Cooper, I. Koprinarov, A.P. Hitchcock, E.G. Rightor, G.E. Mitchell, S. Rozeveld, G.F. Meyers, and T.M. Stokich, "Inner-shell excitation spectroscopy and x-ray photoemission electron microscopy of adhesion promoters," *J. Phys. Chem. B* 109, 6343 (2005).

Ustundag, E., R.C. Rogan, M.R. Daymond, N. Tamura, L. Margulies, and H. Poulsen, "Multiscale study of internal stress and texture in ferroelectrics," *Mater. Sci. Forum* 490–491, 28 (2005).

Van Hoewyk, D., G.F. Garifullina, A.R. Ackley, S.E. Abdel-Ghany, M.A. Marcus, S. Fakra, K. Ishiyama, E. Inoue, M. Pilon, H. Takahashi, and E.A.H. Pilon-Smits, "Overexpression of AtCpNifS enhances selenium tolerance and accumulation in arabidopsis," *Plant Physiol.* 139, 1518 (2005).

Van Petegem, F., F.C. Chatelain, and D.L. Minor, "Insights into voltage-gated calcium channel regulation from the structure of the $Ca_v1.2$ IQ domain–Ca^{2+}/calmodulin complex," *Nat. Struct. Mol. Biol.* 12, 1108(2005).

Vayssieres, L., C. Sathe, S.M. Butorin, D.K. Shuh, J. Nordgren, and J.H. Guo, "One-dimensional quantum-confinement effect in α-Fe_2O_3 ultrafine nanorod arrays," *Adv. Mater.* 17, 2320 (2005).

Vedula, L.S., M.J. Rynkiewicz, H.J. Pyun, R.M. Coates, D.E. Cane, and D.W. Christianson, "Molecular recognition of the substrate diphosphate group governs product diversity in trichodiene synthase mutants," *Biochemistry* 44, 6153 (2005).

Vinogradova, M.V., D.B. Stone, G.G. Malanina, C. Karatzaferi, R. Cooke, R.A. Mendelson, and R.J. Fletterick, "Ca^{2+}-regulated structural changes in troponin," *Proc. Natl. Acad. Sci. USA* 102, 5038 (2005).

Voegelin, A., S. Pfister, A.C. Scheinost, M.A. Marcus, and R. Kretzschmar, "Changes in zinc speciation in field soil after contamination with zinc oxide," *Environ. Sci. Technol.* 39, 6616 (2005).

Walker, D., P.K. Verma, L.M.D. Cranswick, S.M. Clark, R.L. Jones, and S. Buhre, "Halite-sylvite thermoconsolution," *Am. Mineral.* 90, 229 (2005).

Walker, R.J., and D. Walker, "Does the core leak?" *Eos, Trans. Am. Geophys. Un.* 86, 237 (2005).

Wang, C., T. Araki, and H. Ade, "Soft x-ray resonant reflectivity of low Z material thin films," *Appl. Phys. Lett.* 87, 4109 (2005).

Wang, L., A. Gamez, C.N. Sarkissian, M. Straub, M.G. Patch, G.W. Han, S. Striepeke, P. Fitzpatrick, C.R. Scriver, and R.C. Stevens, "Structure-based chemical modification strategy for enzyme replacement treatment of phenylketonuria," *Mol. Genet. Metab.* 86, 134 (2005).

Wang, W., C. Zhang, A. Marimuthu, H.I. Krupka, M. Tabrizizad, R. Shelloe, U. Mehra, K. Eng, H. Nguyen, C. Settachatgul, B. Powell, M.V. Milburn, and B.L. West, "The crystal structures of human steroidogenic factor-1 and liver receptor homologue-1," *Proc. Natl. Acad. Sci. USA* 102, 7505 (2005).

Waychunas, G.A., C.S. Kim, and J.F. Banfield, "Nanoparticulate oxide minerals in soils and sediments: Unique properties and contaminant scavenging mechanisms," *J. Nanopart. Res.* 7, 409 (2005).

Webb, S.M., G.J. Dick, J.R. Bargar, and B.M. Tebo, "Evidence for the presence of Mn(III) intermediates in the bacterial oxidation of Mn(II)," *Proc. Natl. Acad. Sci. USA* 102, 5558 (2005).

Webby, C.J., H.M. Baker, J.S. Lott, E.N. Baker, and E.J. Parker, "The structure of 3-deoxy-D-*arabino*-heptulosonate 7-phosphate synthase from *Mycobacterium tuberculosis* reveals a common catalytic scaffold and ancestry for type I and type II enzymes," *J. Mol. Biol.* 354, 927 (2005).

Wex, B., "Photochemical, photophysical and electronic properties of fused ring systems with alternating benzene and thiophene units," Ph.D. thesis, Bowling Green State University (2005).

White, T.A., and J.J. Tanner, "Cloning, purification and crystallization of *Thermus thermophilus* proline dehydrogenase," *Acta Crystallogr. F* F61, 737 (2005).

Wilks, R.G., "Experimental and theoretical investigation of the electronic structures of ferrocene-peptide conjugates," masters thesis, University of Saskatchewan, Canada (2005).

Wilks, R.G., E.Z. Kurmaev, J.C. Pivin, A. Hunt, M.V. Yablonskikh, D.A. Zatsepin, A. Moewes, S. Shin, P. Palade, and G. Principi, "Ion irradiation induced reduction of Fe^{3+} to Fe^{2+} and Fe^0 in triethoxysilane films," *J. Phys.: Condens. Matter* 17, 7023 (2005).

Wilson, D.K., D. Cerna, and E. Chew, "The 1.1-Å structure of the spindle checkpoint protein Bub3p reveals functional regions," *J. Biol. Chem.* 280, 13944 (2005).

Wilson, K.R., M. Cavalleri, B.S. Rude, R.D. Shaller, T. Catalono, A. Nilsson, R.J. Saykally, and L.G.M. Pettersson, "X-ray absorption spectroscopy of liquid methanol microjets: Bulk electronic structure and hydrogen bonding network," *J. Phys. Chem. B* 109, 10194 (2005).

Wisedchaisri, G., "Structural basis for transcription regulations in *Mycobacterium tuberculosis* by iron-dependent regulator and dormancy survival regulator," Ph.D. thesis, University of Washington, Seattle (2005).

Wisedchaisri, G., M. Wu, A.E. Rice, D.M. Roberts, D.R. Sherman, and W.G.J. Hol, "Structures of *Mycobacterium tuberculosis* DosR and DosR-DNA complex involved in gene activation during adaptation to hypoxic latency," *J. Mol. Biol.* 354, 630 (2005).

Won, C., Y.Z. Wu, J. Choi, W. Kim, A. Scholl, A. Doran, T. Owens, J. Wu, X. F. Jin, H.W. Zhao, and Z.Q. Qiu, "Magnetic stripe melting at the spin reorientation transition in Fe/Ni/Cu(001)," *Phys. Rev. B* 71, 224429 (2005).

Won, C., Y.Z. Wu, H.W. Hao, A. Scholl, A. Doran, W. Kim, T.L. Owens, X.F. Jin, and Z.Q. Qiu, "Studies of FeMn/Co/Cu(001) films using photoemission electron microscopy and surface magneto-optic Kerr effect," *Phys. Rev. B* 71, 24406 (2005).

Wu, S.Y., S.Q. Mehta, F. Pichaud, H.J. Bellen, and F.A. Quiocho, "Sec15 interacts with Rab11 via a novel domain and affects Rab11 localization in vivo," *Nat. Struct. Mol. Biol.* 12, 879 (2005).

Yablonskikh, M.V., Y.M. Yarmoshenko, I.V. Solovyev, E.Z. Kurmaev, L.C. Duda, T. Schmitt, M. Magnuson, J. Nordgen, and A. Moewes, "Resonant $L_{\alpha,\beta}$ x-ray emission and $L_{3,2}$ x-ray absorption spectra of 3d metals in Co_2MnZ (Z=Al, Ga, Sn, Sb) Heusler alloys as an element-selective probe of spin character of valence band," *J. Electron Spectrosc.* 144–147, 765 (2005).

Yamashita, A., S.K. Singh, T. Kawate, Y. Jin, and E. Gouaux, "Crystal structure of a bacterial homologue of Na^+/Cl^--dependent neurotransmitter transporters," *Nature* 437, 215 (2005).

Yang, H.B., Z.H. Pan, A.K. Sekharan, T. Sato, T. Takahashi, R. Jin, B.C. Sales, D. Mandrus, A.V. Fedorov, Z. Wang, H. Ding, and T. Souma, "Fermi surface evolution and Luttinger theorem in Na_xCoO_2: A systematic photoemission study," *Phys. Rev. Lett.* 95, 146401 (2005).

Yang, J., Y.X. Mo, K.C. La, Y. Song, X.M. Qian, and C.Y. Ng, "A combined vacuum ultraviolet laser and synchrotron pulsed field ionization study of BCl_3," *Phys. Chem. Chem. Phys.* 7, 1518 (2005).

Yin, J., E.M. Bergmann, M.M. Cherney, M.S. Lall, R.P. Jain, J.C. Vederas, and M.N.G. James, "Dual modes of modification of hepatitis A virus 3C protease by a serine-derived β-lactone: Selective crystallization and formation of a functional catalytic triad in the active site," *J. Mol. Biol.* 354, 854(2005).

Yip, C.K., B.B. Finlay, and N.C. Strynadka, "Structural characterization of a type III secretion system filament protein in complex with its chaperone," *Nat. Struct. Mol. Biol.* 12, 75 (2005).

Yip, C.K., T.G. Kimbrough, H.B. Felise, M. Vuckovic, N.A. Thomas, R.A. Pfuetzner, E.A. Frey, B.B. Finlay, S.I. Miller, and N.C.J. Strynadka, "Structural characterization of the molecular platform for type III secretion system assembly," *Nature* 435, 702 (2005).

Youn, B.Y., S.G.A. Moinuldin, L.B. Davin, N.G. Lewis, and C. Kang, "Crystal structures of apo-form and binary/ternary complexes of *Podophyllum* secoisolariciresinol dehydrogenase, an enzyme involved in formation of health-protecting and plant defense lignans," *J. Biol. Chem.* 280, 12917 (2005).

Yu, E.W., J.R. Aires, G. McDermott, and H. Nikaido, "A periplasmic drug-binding site of the AcrB multidrug efflux pump: A crystallographic and site-directed mutagenesis study," *J. Bacteriol.* 187, 6804 (2005).

Yu, K.M., W. Walukiewicz, T. Wojtowicz, J. Denlinger, M.A. Scarpulla, X. Liu, and J.K. Furdyna, "Effect of film thickness on the incorporation of Mn interstitials in $Ga_{1-x}Mn_xAs$," *Appl. Phys. Lett.* 86, 042102 (2005).

Zajonc, D.M., C. Cantu, III, J. Mattner, D. Zhou, P.B. Savage, A. Bendelac, I.A. Wilson, and L. Teyton, "Structure and function of a potent agonist for the semi-invariant natural killer T cell receptor," *Nat. Immunol.* 6, 810 (2005).

Zhang, J., T.D. Osslund, M.H. Plant, C.L. Clogston, R.E. Nybo, F. Xiong, J.M. Delaney, and S.R. Jordan, "Crystal structure of murine 11^{β}-hydroxysteroid dehydrogenase 1: An important therapeutic target for diabetes," *Biochemistry* 44, 6948 (2005).

Zhang, T., C.Y. Ng, F. Qi, C.S. Lam, and W.K. Li, "A 193 nm laser photofragmentation time-of-flight mass spectrometric study of chloroiodomethane," *J. Chem. Phys.* 123, 174316 (2005).

Zhang, Y., L. Wang, P.G. Schultz, and I.A. Wilson, "Crystal structures of apo wild-type *M-jannaschii* tyrosyl-tRNA synthetase (TyrRS) and an engineered TyrRS specific for O-methyl-L-tyrosine," *Protein Sci.* 14, 1340 (2005).

Zharnikov, M., A. Shaporenko, A. Paul, A. Golzhauser, and A. Scholl, "X-ray absorption spectromicroscopy studies for the development of lithography with a monomolecular resist," *J. Phys. Chem. B* 109, 5168 (2005).

Zheng, F., V. Pérez-Dieste, J.L. McChesney, Y.Y Luk, N.L. Abbott, and F.J. Himpsel, "Detection and switching of the oxidation state of Fe in a self-assembled monolayer," *Surf. Sci.* 587, L191 (2005).

Zhou, S.Y., G.H. Gweon, C.D. Spataru, J. Graf, D.H. Lee, S.G. Louie, and A. Lanzara, "Coexistence of sharp quasiparticle dispersions and disorder features in polycrystalline graphite," *Phys. Rev. B* 71, 161403(R) (2005).

Zhou, X.J., B. Wannberg, W.L. Yang, V. Brouet, Z. Sun, J.F. Douglas, D. Dessau, Z. Hussain, and Z.X. Shen, "Space charge effect and mirror charge effect in photoemission spectroscopy," *J. Electron Spectrosc.* 142, 27 (2005).

Zhou, X.J., J.R. Shi,T. Yoshida, T. Cuk, W.L. Yang, V. Brouet, J. Nakamura, N. Mannella, S. Komiya, Y. Ando, F. Zhou, W.X. Ti, J.W. Xiong, Z.X. Zhao, T. Sasagawa, T. Kakeshita, H. Eisaki, S. Uchida, A. Fujimori, Z.Y. Zhang, E.W. Plummer, R.B. Laughlin, Z. Hussain, and Z.X. Shen, "Multiple bosonic mode coupling in the electron self-energy of $(La_{2-x}Sr_x)CuO_4$," *Phys. Rev. Lett.* 95, 117001 (2005).

Zhu, Y., W. Huang, S.S.K. Lee, and W. Xu, "Crystal structure of a polyphosphate kinase and its implications for polyphosphate synthesis," *EMBO J.* 6, 681 (2005).

Zolotorev, M., R.W. Schoenlein, and A.A. Zholents, "Beam slicing by femtosecond laser," in *Femtosecond Beam Science*, p. 202 (Imperial College Press, 2005).

Acronyms and Abbreviations

ABC . . . . . ATP-binding cassette

ADP . . . . . adenosine diphosphate

ALS . . . . . Advanced Light Source

AMO . . . . atomic, molecular, and optical

amu . . . . . atomic mass unit

AP . . . . . approved program

APS . . . . . Advanced Photon Source

ARF . . . . . adenosine diphosphate ribosylation factor

ARPES . . . angle-resolved photoemission spectroscopy

ATP . . . . . adenosine triphosphate

AXIS . . . . . Advanced X-Ray Inelastic Scattering

BCS . . . . . Bardeen-Cooper-Schrieffer

BES . . . . . Basic Energy Sciences, DOE Office of

BESSY . . . Berliner Elektronenspeicherring-Gesellschaft für Synchrotronstrahlung

BPM . . . . . beam-position monitor

BW . . . . . bandwidth

CaMKII . . Ca^{2+}/calmodulin-activated protein kinase II

cAMP . . . . cyclic adenosine monophosphate

CAT . . . . . computed axial tomography

CBD . . . . . cAMP-binding domain

CCD . . . . . charge-coupled device

CMR . . . . . colossal magnetoresistance

CTA1 . . . . cholera toxin A1 subunit

CXRO . . . . Center for X-Ray Optics

DNA . . . . . deoxyribonucleic acid

DOE . . . . . Department of Energy

DOS . . . . . density of states

EDC . . . . . energy distribution curve

EPU . . . . . elliptically polarizing undulator

ESF . . . . . Electronic Structure Factory

ESG . . . . . Experiemental Systems Group

ESRF . . . . European Synchrotron Radiation Facility

EUV . . . . . extreme ultraviolet

EXAFS . . . extended x-ray absorption fine structure

FS . . . . . Fermi surface

FWHM . . . full width at half maximum

FY . . . . . fiscal year

G protein . . GTP-binding protein

GAP . . . . . GTPase-activating protein

GDP . . . . . guanosine diphosphate

GPCR . . . . G-protein-coupled receptor

GRK . . . . . G-protein-coupled receptor kinase

GTP . . . . . guanosine triphosphate

HARP . . . . High-Resolution Angle-Resolved Photoemission

HERS . . . . High-Energy-Resolution Spectrometer

HOM . . . . higher-order-mode (dampers)

HOPG . . . highly ordered pyrolytic graphite

HTH . . . . . helix-turn-helix (domain)

IR . . . . . infrared

IVID . . . . . in-vacuum insertion device

K-B . . . . . Kirkpatrick-Baez

LDA . . . . . local density approximation

LFB . . . . . longitudinal feedback system

LIGA . . . . German acronym for lithography, electroplating, and molding

LSCO . . . . $(La_{2-x}Sr_x)CuO_4$

LSMO . . . . $La_{0.7}Sr_{0.3}MnO_3$

MAD . . . . multiple-wavelength anomalous diffraction

MBE . . . . . molecular-beam epitaxy

MBMS . . . molecular beam mass sampling

MCO . . . . multicopper oxidase

MCP . . . . . multichannel plate

mc-Si . . . . multicrystalline silicon

MEPU . . . MERLIN elliptically polarizing undulator

MERLIN . . meV-resolution beamline

mRNA . . . messenger RNA

MZP . . . . . micro zone plate

NCXT . . . . National Center for X-Ray Tomography

NEXAFS . . near-edge x-ray absorption fine-structure spectroscopy

NSF . . . . . National Science Foundation

NSLS . . . . National Synchrotron Light Source

PAH . . . . . polycyclic aromatic hydrocarbon

PBC . . . . . phosphate binding cassette

PED . . . . . photoemission diffraction

PEEM . . . . photoemission electron microscope

PES . . . . . photoemission spectoscopy

PGM . . . . . plane grating monochromator

PIE . . . . . photoionization efficiency

PKA . . . . . protein kinase A

PLCβ . . . . phospholipase Cβ

PNNL . . . . Pacific Northwest National Laboratory

PP . . . . . pyrophosphate (P_2O_7)

PRT . . . . . participating research team

PSP . . . . . Proposal Study Panel

rf . . . . . radiofrequency

RGS . . . . . regulator of G-protein signaling

RH . . . . . relative humidity

RIXS . . . . resonant inelastic x-ray scattering

RNA . . . . . ribonucleic acid

SAC . . . . . Scientific Advisory Committee

SAXS . . . . small-angle x-ray scattering

SEM . . . . . scanning electron microscope/ microscopy

SGM . . . . . spherical grating monochromator

SIBYLS . . . Structurally Integrated Biology for Life Sciences

SPring-8 . . . Super Photon ring, 8 GeV (Large-Scale Synchrotron Radiation Facility, Japan)

SSG . . . . . Scientific Support Group

SSRL . . . . . Stanford Synchrotron Radiation Laboratory

STM . . . . . scanning tunneling microscopy

STXM . . . . scanning transmission x-ray microscopy

SWCN . . . . single-walled carbon nanotubes

SXF . . . . . soft x-ray fluorescence

TEM . . . . . transmission electron microscope/ microscopy

TF . . . . . transverse feedback

THC . . . . . third-harmonic cavity

TMCI . . . . transverse-mode coupling instability

TOMFS . . . time-of-flight mass spectrometer

TTSS . . . . . type III secretion system

UC . . . . . University of California

UCLA . . . . University of California, Los Angeles

UCSD . . . . University of California, San Diego

UEC . . . . . Users' Executive Committee

UNLV . . . . University of Nevada, Las Vegas

UV . . . . . ultraviolet

UW . . . . . University of Washington

VLS . . . . . variable line spacing

VUV . . . . . vacuum ultraviolet

XANES . . . x-ray absorption near-edge spectroscopy

XAS . . . . . x-ray absorption spectra/spectroscopy

XDM . . . . x-ray diffraction microscopy

XES . . . . . x-ray emission spectra/spectroscopy

XMCD . . . x-ray magnetic circular dichroism

XMLD . . . x-ray magnetic linear dichroism

XPS . . . . . x-ray photoelectron spectroscopy

XRD . . . . . x-ray diffraction

XRF . . . . . x-ray fluorescence

YAG . . . . . $Y_3Al_5O_{12}$

For More Information

For information about using the ALS, contact

Gary Krebs
User Services Group Leader
Advanced Light Source
Lawrence Berkeley National Laboratory
MS 6R2100
Berkeley, CA 94720-8226
Tel: (510) 486-7727
Fax: (510) 486-4773
Email: gfkrebs@lbl.gov

For all other information concerning the ALS, contact

Jeffrey Troutman
User Services Administrator
Advanced Light Source
Lawrence Berkeley National Laboratory
MS 6R2100
Berkeley, CA 94720-8226
Tel: (510) 495-2001
Fax: (510) 486-4773
Email: alsuser@lbl.gov

ALS home page

http://www-als.lbl.gov/

Supported by the U.S. Department of Energy under Contract No. DE-AC02-05CH11231

advanced light source
Ernest Orlando Lawrence Berkeley National Laboratory
University of California • Berkeley, California, 94720